

The paleoceanography of the southern Coral Sea across the Mid-Pleistocene Transition



Thomas Ford Russon

MA_(Cantab) MSci

Thesis submitted for the degree of Doctor of Philosophy

University of Edinburgh

2010

Abstract

A comprehensive theory explaining the relationship between periodic variations in the Earth's orbital parameters and the response of the climate system remains elusive. One of the key challenges is that of the Mid-Pleistocene Transition (MPT), during which the dominant mode of glacial/interglacial climatic variability shifted without any corresponding change in the mode of orbital forcing. Subtropical climate on orbital time-scales is sensitive to variability in both the low-latitude ocean/atmosphere circulation regime and the global carbon-cycle (through its effect on atmospheric greenhouse gas levels), both of which may have played a role in the shift in mode of global climate response to orbital forcing during the MPT. This thesis presents a series of multi-proxy (foraminiferal stable isotope and trace-metal) paleoceanographic reconstructions from the subtropical southwest Pacific, as seen in marine sediment core MD06-3018, from 2470m water depth and 23°S in the New Caledonia Trough, southern Coral Sea. The core age-model, based upon magnetic stratigraphy and orbital tuning, yields a mean sedimentation rate at the site of 20mm/ka and a core-bottom age of 1600ka.

The MD06-3018 reconstruction of New Caledonia Trough deep water chemistry, based on benthic $\delta^{13}\text{C}$ measurements, shows that the spatial chemistry gradient within the Southern Ocean between deep waters entering the Tasman Sea and the open Pacific was greater during glacial (relative to interglacial) stages over at least the past 1100ka. This gradient was, however, generally reduced on the >100kyr time-scale across the MPT, consistent with it being a period of reduced deep water ventilation in both hemispheres.

The MD06-3018 Mg/Ca-derived reconstruction of subtropical southwest Pacific Sea Surface Temperature (SST) shows glacial/interglacial variability of 2-3°C but no significant trends on the >100kyr time-scale over the duration of the record. An estimate of the uncertainty associated with the SST reconstruction demonstrates that no significant changes in reconstructed southern Coral Sea mean-annual SST can be identified between interglacial stages across the MPT. It is, therefore, unlikely that

regional climatic change constituted the main cause for the observed middle Pleistocene expansion of coral reef systems. The >100kyr time-scale stability of southern Coral Sea SST means that the position of the southern boundary of the Pacific warm pool has also been stable over at least the past 1500ka. Comparison with other low-latitude Pacific reconstructions shows that the early Pleistocene warm pool was consequently more hemispherically asymmetric than its present configuration, with the latter being established by ~1000ka and implying significant changes in meridional atmospheric heat and moisture fluxes prior to the MPT.

On orbital time-scales, the SST reconstruction shows a clear shift from dominant 40kyr to 100kyr modes of variability over the MPT, although significant 40kyr structure is also retained into the middle/late Pleistocene. In contrast, reconstructed hydrological cycle variability (based on coupled $\delta^{18}\text{O}$ -Mg/Ca measurements) shows only limited coherence with the obliquity cycle and a stronger relationship with the precession cycle. The decoupling of the reconstructed subtropical SST and hydrological cycle responses places constraints on the extent of orbitally paced fluctuations in the low-latitude ocean/atmosphere system. Instead, comparison of the MD06-3018 SST reconstruction with others from across the low-latitude Pacific supports a dominant role for greenhouse gas forcing in low-latitude western Pacific glacial/interglacial SST variability across the Pleistocene.

The subtropical multi-proxy climate reconstructions presented here show that the timing and sense of long-term (>100kyr time-scale) changes in the low-latitude ocean/atmosphere circulation regime are consistent with that system having been important in the expansion of northern hemisphere ice-volume during the early part of the MPT. However, the subtropical reconstructions also suggest that neither the low-latitude ocean/atmosphere circulation system nor the global carbon-cycle underwent a fundamental change in mode of response to orbital forcing during the transition. Instead, the origin of the 100kyr glacial/interglacial mode was most likely related to thresholds in the dynamics of the expanding northern hemisphere ice-sheets, leading in turn to the existence of significant inter-hemispheric asymmetry in the orbital time-scale climate response over the middle/late Pleistocene.

Summary for non-specialists

Over the past five million years of its history, the Earth's climate has undergone a series of regular, or nearly regular, fluctuations between warmer and colder states. These fluctuations take tens to hundreds of thousands of years to occur and are known as the 'glacial/interglacial cycles' on account of the associated changes in ice-sheet extent in the high-latitudes. The origin of these cycles is widely held to be the regular variations in form of the Earth's orbit around the sun. In spite of decades of research, however, no complete 'orbital theory of climate' exists, mainly because the patterns of past climate variability, as reconstructed using 'proxies' for variables such as surface temperature, is much more complex than that of the orbital variations themselves. It follows that processes within the Earth system, especially those associated with large ice-sheets, the carbon-cycle and the ocean circulation system, act to substantially modify the climate response to the orbital variations. Over the past ten years, new observations from both ice-cores and low-latitude marine sediment cores have suggested that the dominant system(s) involved in setting the Earth's response to the orbital variations may potentially be the carbon-cycle and/or the low-latitude ocean/atmosphere circulation regime rather than high-latitude ice-sheet dynamics, as was generally supposed previously. If this new view is correct, it has profound implications for the general sensitivity of the climate to the carbon-cycle on a range of time-scales - making its evaluation a scientific objective of considerable current importance.

This thesis presents a series of reconstructions of aspects of climate and carbon-cycle variability for the subtropical southwest Pacific, as based on proxy measurements in a marine sediment core that spans the past 1,600,000 years at around 5000 year resolution. The key focus is on an interval called the 'Mid-Pleistocene Transition', during which time the mode of glacial/interglacial variability changed, indicating a fundamental change in one or more aspects of the response to the orbital forcing. The study site is well placed to investigate variability in both the carbon-cycle and low-latitude ocean circulation over the climatic transition as it lies between the Southern Ocean, a key source of carbon-cycle variability and the

equatorial Pacific, where the modern El-Niño system arises. By characterizing variability in these systems, the potential role played by both systems in causing the change in mode of glacial/interglacial variability can be evaluated.

The key findings of the thesis are that; firstly, changes in the long-term state of the low-latitude ocean circulation system may well have been important for the expansion of northern hemisphere ice-sheets during the early part of the Mid-Pleistocene Transition. Secondly, it provides further support for a close connection between variability in the carbon-cycle and low-latitude climate on orbital time-scales but suggests that there is no clear evidence for either system undergoing a fundamental change in sensitivity to the orbital forcing during the transition. This implies that whilst paleoclimate records can potentially provide useful constraints on climate sensitivity to greenhouse gas forcing, it was the changing dynamics of the newly expanded northern hemisphere ice-sheets that led to the change in dominant glacial/interglacial periodicity during the Mid-Pleistocene Transition.

Declaration

This thesis has been composed by myself and represents my own work. I acknowledge the contributions of my co-authors in chapters 3 through 6, which are presented in paper format. I am, however, lead author on all of these papers and as such wrote the text, composed the figures and developed the arguments presented therein. All lab-work and data analysis was also undertaken by me, except where this is clearly highlighted at the beginning of the relevant chapter. The published papers, which are included within the electronic version of the thesis, were all done so through journals published by the AGU, who hold the relevant copyrights but have agreed to their inclusion in this thesis. This work has not been submitted for any other degree of professional qualification.

Thomas Ford Russon

Edinburgh, August 2010



Blank Page

Acknowledgements

This thesis would not have been possible without the help and support of a wide variety of people. The first and fullest thanks go, without reservations, to my principle supervisor Mary Elliot, who, in spite of this having been a very busy time in her own life, has always found time to discuss things and keep a focus on the wider importance of the work. I would also like to extend particular thanks to Aleksey Sadekov, who went beyond the call of duty in assisting me with the trace metal method development work. Without him there is simply no way this important aspect of the work presented here would have got done anytime soon. I would also like to thank my thesis examiners, Prof. Ian Hall and Prof. Dick Kroon, for their very constructive critique and discussion of this work.

Following this, I would like to thank my other supervisors and paper co-authors for their timely and insightful comments on the work. They are Sandy Tudhope, Thierry Corrège, Guy Cabioch, Patrick De Deckker and Catherine Kissel. For additional academic and laboratory support I thank many of the other academic and technical staff, post-docs and PhD students in our research group at Edinburgh. They are; Kate Darling, Tom Crowley, Raja Ganeshram, Walter Geibert, Laetitia Pichevin, Elsa Arrelano-Torres, Damien Carson, Amber Annett, Kev Welsh, Matt Unterman, Colin Chilcott, Ann Mennim, Alan Pike, Jim Smith and Sophie Tankere-Muller. Outside of the immediate project partners, Helen Bostock, Erin McClymont, Ros Rickaby, Steve Barker and Tim Barrows have all provided useful input on the science in this thesis and are gratefully thanked for their time and stimulating discussions. The reviewers of the published papers, anonymous and otherwise have also all contributed to the substantial improvement of those aspects of the work. I would also like to thank the five final year undergraduate students, here at Edinburgh, whose projects (to varying degrees related to this thesis) I have helped to supervise over the course of my PhD; Aidan Farrow, Sian Henley, Rosanna Greenop, Kindra Harris and Angharad Jenkins. Although none of our work together is presented explicitly in the thesis, it has certainly informed some of the ideas herein and it has been both a great privilege and lots of fun to have worked with them all.

In terms of the logistics of the project, I am very grateful to Catherine Kissel and others at the LSCE, France, for allowing myself and Mary to make use of various labs there at various times during the project. The crew, scientists and Yvon Balut from the R/V *Marion Dufresne*, Yves Lafoy (Dimenc, New Caledonia), A.M. Sémah and D. Wirrmann (IRD) are gratefully thanked for the original cruise that led to the collection of MD06-3018. Our collective thanks are expressed to the French Zonéco program, IPEV and IRD for contributing to the grants to obtain the core. My PhD funding was supplied by NERC (studentship NER/S/A/2006/14325), who have always been extremely supportive.

I am also very grateful to Didier Paillard and his research group, again of the LSCE, for providing me with the chance to go and do some modelling work in France during a six month break from my PhD in 2008. This work was funded by the Entente Cordiale scholarships programme (a joint UK/French government initiative), to whom I extend my warmest thanks. The time at LSCE was an exceptional opportunity for me and led directly to the carbon-cycle box-modelling paper, published with *Global Biogeochemical Cycles* in 2010, which is referred to in the discussion section of this thesis and is included in the electronic version.

Last, but in no way least, I would like to thank my friends, housemates and colleagues, in Edinburgh, Paris and elsewhere, for their support and excellent friendship over the past four years. This list is certainly not exhaustive but must include; Dan Hopley, Alex Whittaker, Rich Taylor, Tim Ivanic, Alex Stewart, Luke Ridley, Jenny Rapp, Louise Barron, Tanya Jude-Eton, Rhian Meara, Kate Briggs, Mohammed Alburaki, Christine Molina, Nathaëlle Bouttes, Malaak Kallache, Céline Montcourtois, Grant Nicoll, Jen Roberts, Rudra Kapila and Niklas Heinemann. Finally, especial thanks are for my best friend, Gillian McCay and for my ever patient parents.

This thesis is dedicated to the hope for a more understanding and mutually beneficial relationship between science, especially climate science, and wider society over the years to come.

Contents

Figure List	xiv
Table List	xvi
Word Count	xvi
Abbreviations List	xvii
Chapter 1: General Introduction	1
1.1 Thesis overview	1
1.2 Chapter overview	3
1.3 The science of paleoceanography	4
1.4 Paleoceanographic proxies and age-models	6
1.5 Plio-Pleistocene evolution of the climate system	9
1.6 The Milankovitch paradigm – orbital time-scale variability in the climate system	12
1.7 The Mid-Pleistocene Transition	16
1.7.1 Potential origins of the early Pleistocene intensification of northern hemisphere glaciation	17
1.7.2 The ‘100kyr problem’	20
1.7.3 Orbital time-scale variability in the carbon-cycle and the low-latitude ocean/atmosphere circulation system	23
1.8 Rationale and motivation for thesis	25
1.9 Aims of thesis	29
1.10 Structure of thesis	31
Chapter 2: Setting and sedimentology of giant piston core MD06-3018	33
2.1 Chapter overview	33
2.2 Core location and geological setting	34
2.3 Modern oceanography	37
2.4 Modern climatology	40
2.5 History of ocean drilling in the region	42
2.6 Core description and sampling	43
2.7 Core photographs	44
2.8 Composite core depth scale	44
2.9 Core sedimentology	47
2.10 Indices of down-core carbonate preservation	48
2.10.1 Scanning electron microscope images	49
2.10.2 Planktonic foraminifera shell weights	50
2.10.3 Weight% CaCO ₃	51
2.11 Discussion	53
2.12 Conclusions	54

Chapter 3:	Subtropical southwest Pacific deep water circulation across the Mid-Pleistocene Transition	55
3.1	Chapter overview	56
3.2	Introduction	57
3.3	Modern deep water circulation and mixing in the subtropical southwest Pacific	60
3.4	Modern deep water mass $\delta^{13}\text{C}_{\text{DIC}}$ in the subtropical southwest Pacific	63
3.5	Methods	64
3.5.1	Benthic stable isotope measurements	64
3.5.2	Magnetic measurements	65
3.6	Results	65
3.6.1	Benthic stable isotope measurements	65
3.6.2	Magnetic measurements	66
3.7	MD06-3018 age-model	67
3.8	Discussion	70
3.8.1	Does $\delta^{13}\text{C}_{\text{benthic}}$ at site MD06-3018 record $\delta^{13}\text{C}_{\text{DIC}}$?	70
3.8.2	Glacial/interglacial variability in the regional deep water mixing regime	71
3.8.3	Glacial decoupling of Deep Western Boundary Current to Central Pacific Basin deep waters	77
3.8.4	Glacial stage deep water chemistry gradients in the southwest Pacific	82
3.8.5	Pleistocene evolution of deep water circulation and mixing	84
3.9	Conclusions	86
Chapter 4:	Sources of uncertainty in the Mg/Ca paleothermometer: did climate change limit the middle Pleistocene expansion of reefs in the southern Coral Sea?	89
4.1	Chapter overview	90
4.2	Introduction	91
4.3	Methods	95
4.3.1	Planktic foraminiferal Mg/Ca measurements and Mg/Ca paleothermometry	95
4.3.2	Transfer function estimates of SST	98
4.3.3	Proposed down-core corrections to the Mg/Ca paleothermometer	100
4.4	Results	103
4.4.1	The MD06-3018 Mg/Ca-derived reconstruction of southern Coral Sea SST	103
4.4.2	The down-core effects of the salinity and Mg/Ca(sw) corrections	105
4.4.2	Transfer function estimates of seasonal SST compared to high-resolution Mg/Ca paleothermometry across glacial terminations	106

4.5	Discussion	108
4.5.1	Does the MD06-3018 Mg/Ca-derived SST record mean-annual SST?	108
4.5.2	Assessing the validity of the proposed Mg/Ca corrections	110
4.5.3	The 'combined uncertainty' associated with the Mg/Ca-derived SST reconstruction	111
4.5.4	Did regional climate change limit middle Pleistocene reef expansion in the Coral Sea?	114
4.6	Conclusions	117
Chapter 5: Inter-hemispheric asymmetry in the early Pleistocene Pacific warm pool		119
5.1	Chapter overview	120
5.2	Introduction	121
5.3	Comparison of the MD06-3018 SST reconstruction to others from the low-latitude Pacific	124
5.4	Discussion	127
5.5	Conclusions	130
Chapter 6: The Mid-Pleistocene Transition in subtropical southwest Pacific climate		131
6.1	Chapter overview	132
6.2	Introduction	133
6.3	Methods	137
6.3.1	Planktic stable isotope measurements	137
6.3.2	Calculation of $\delta^{18}\text{O}_{\text{sw}}$	137
6.4	Results	140
6.5	Discussion	145
6.5.1	Orbital influences on subtropical southwest Pacific SST variability	145
6.5.2	Orbital influences on subtropical southwest Pacific hydrological cycle variability	150
6.5.3	Constraints on 'super-ENSO' over the MPT	152
6.5.4	Low-latitude Pacific SST forcing mechanisms over the MPT	154
6.6	Conclusions	158

Chapter 7: General Discussion	161
7.1 Chapter overview	161
7.2 Orbital time-scale variability in the low-latitude ocean/atmosphere system: constraints from the meridional extent of the Pacific warm pool	162
7.3 Orbital and >100kyr time-scale variability in the carbon-cycle: constraints from subtropical southwest Pacific deep water circulation	170
7.4 Orbital and >100kyr time-scale variability in the carbon-cycle: the role of neritic calcification	172
7.5 Climate sensitivity to pCO ₂ on orbital time-scales	175
7.6 The origins of the early Pleistocene intensification of northern hemisphere glaciation	179
7.7 The '100kyr' problem revisited	182
7.8 Inter-hemispheric asymmetry in the glacial/interglacial climate response across the Mid-Pleistocene Transition	186
7.9 Research questions arising from this thesis	189
7.10 Pleistocene paleoceanography: future research directions	192
Chapter 8: Conclusions	195
8.1 Chapter overview	195
8.2 Marine sediment core MD06-3018 as an archive for subtropical southwest Pacific paleoceanography	196
8.3 Deep water circulation in the subtropical southwest Pacific on orbital and >100kyr time-scales	196
8.4 The paleoceanography and paleoclimatology of the southern Coral Sea on orbital and >100kyr time-scales	197
8.5 Limitations of the Mg/Ca paleothermometer in reconstructing southern Coral Sea paleoceanography: implications for the causes of middle Pleistocene reef expansion	198
8.6 Subtropical Pacific constraints on >100kyr time-scale variability in the low-latitude ocean/atmosphere circulation system: implications for the origins of the Mid-Pleistocene Transition	199
8.7 Subtropical Pacific constraints on orbital time-scale variability in the low-latitude ocean/atmosphere circulation system and the carbon-cycle: implications for the structure of the Mid-Pleistocene Transition	200

References		205
Appendices		229
Appendix 1	Principles of the foraminiferal stable isotope and Mg/Ca trace-metal proxy systems	229
A1.1	Stable oxygen isotopes in foraminiferal calcite	229
A1.2	Stable carbon isotopes in foraminiferal calcite	232
A1.3	Mg/Ca ratios in foraminiferal calcite	234
Appendix 2	Laboratory method, ICP-OES settings, calibration standards, reference materials and sample rejection criteria used for trace-metal analysis	237
A2.1	Trace metal sample preparation method	237
A2.2	Operating conditions for the Varian VISTA (Axial) ICP-OES	239
A2.3	Choice of ICP-OES spectral lines	239
A2.4	Trace-metal calibration standards	240
A2.5	Trace-metal reference materials and long-term reproducibility	241
A2.6	Trace-metal sample rejection criteria	242
Appendix 3	Laboratory method, reference materials and sample rejection criteria used for stable isotope analysis	243
A3.1	Stable isotope sample preparation method	243
A3.2	Stable isotope reference materials and long-term reproducibility	243
A3.3	Stable isotope sample rejection criteria	244
Appendix 4	Down-core MD06-3018 stable isotope and trace-metal data	245
Appendix 5	Down-core plots of stable isotope, trace metal and magnetic inclination data versus core depth	254
Appendix 6	High resolution stable isotope and trace-metal data for selected glacial terminations	255
A6.1	LGM/Hol	255
A6.2	MIS 12/11	257
A6.3	MIS 38/37	259
Appendix 7	MD06-3018 planktic foraminiferal faunal counts	260

Figure List

Chapter 1

1.1	Compilation of globally distributed $\delta^{18}\text{O}_{\text{benthic}}$ and $\delta^{13}\text{C}_{\text{benthic}}$ reconstructions over the past 65Ma	10
1.2	Plot and wavelet decomposition of LR04 $\delta^{18}\text{O}_{\text{benthic}}$ stack over the past 5000ka	13
1.3	Comparison of the LR04 $\delta^{18}\text{O}_{\text{benthic}}$ stack with selected equatorial Pacific SST reconstructions over the past 5000ka	19

Chapter 2

2.1	Geographic location of core MD06-3018	35
2.2	Schematic circulation regimes in the subtropical southwest Pacific for selected water-masses.	38
2.3	Mean-annual water column profiles for temperature and salinity from WOA2005 data for the central New Caledonia Trough	39
2.4	Core section photographs	45
2.5	SEM images of core-top specimens of <i>G. ruber</i> and <i>C. wuellerstorfi</i>	49
2.6	Down-core plot of bulk weight% CaCO_3 from coulometer measurements and values calculated from a colour index based model	51

Chapter 3

3.1	Bathymetric map of the subtropical southwest Pacific region with the location of cores MD06-3018, ODP 1123 and ODP 806B	59
3.2	Water-mass properties and schematic deep water circulation in the subtropical southwest Pacific	62
3.3	Benthic stable isotopes and magnetic inclination versus core depth	66
3.4	MD06-3018 age model	68
3.5	Benthic stable isotopes versus core age model with MIS assignment	69
3.6	Comparison of benthic stable isotope records from MD06-3018 and ODP 1123	73
3.7	Comparison of benthic stable isotope records from MD06-3018 and ODP 849	79
3.8	Plot of the composite minimum value estimate to $\Delta\delta^{13}\text{C}_{\text{NCT-CPBDW}}$	81

Chapter 4

4.1	Map of Coral Sea region with position of modern coral reef systems highlighted	92
4.2	Plots of the MD06-3018 SST reconstruction, both uncorrected and using the proposed salinity and $\text{Mg}/\text{Ca}_{(\text{sw})}$ corrections	104
4.3	Comparison of Mg/Ca-derived and MAT transfer function SST estimates across LGM/Holocene, MIS 12/11 and MIS 38/37 terminations	107
4.4	MD06-3018 Mg/Ca-and MAT-derived SST reconstruction compared to the seasonal difference in insolation at 23°S over the past 1600ka	109
4.5	Plots of the 'revised' MD06-3018 SST reconstruction with associated estimates of combined uncertainty.	113

Chapter 5

5.1	Map of Pacific SST distribution with core locations of MD06-3018, MD97-2140, ODP 846 and ODP 1147.	122
5.2	Pleistocene SST reconstructions from MD06-3018, MD97-2140, ODP 846 and ODP 1147 and derived reconstructions of low-latitude SST gradients	125

Chapter 6

6.1	Contour map of the correlation index between mean-annual SST and the Southern Ocean Index within the low-latitude Pacific with the core locations of MD06-3018, MD97-140 and ODP 846 shown	136
6.2	MD06-3018 $\delta^{18}\text{O}_{\text{planktic}}$, Mg/Ca-derived SST, calculated $\delta^{18}\text{O}_{\text{sw}}$ and calculated $\Delta\delta^{18}\text{O}_{\text{local}}$ plotted against age	141
6.3	Wavelet decomposition plots of the variables shown in Figure 5.2	142
6.4	Wavelet transform coherence plots of MD06-3018 SST and $\Delta\delta^{18}\text{O}_{\text{local}}$ reconstructions with orbital obliquity and precession index	146
6.5	MD06-3018 SST and $\delta^{18}\text{O}_{\text{benthic}}$ records compared to LR04 $\delta^{18}\text{O}_{\text{benthic}}$ stack, Antarctic ice-core δD and orbital obliquity over the past 800ka	148
6.6	Comparison of variance trends between the MD06-3018, MD97-2140 and ODP 846 SST reconstructions	155
6.7	Wavelet decomposition plots of the SST reconstructions shown in Figure 5.6	156

Chapter 7

7.1	Difference between the MD97-2140 and MD06-3018 SST reconstructions (ΔSST) and wavelet decomposition	164
7.2	Cross wavelet transform analysis of ΔSST record with orbital obliquity and precession index	165
7.3	EPICA composite pCO_2 and LR04 stacked $\delta^{18}\text{O}_{\text{benthic}}$ over the past 800ka	173
7.4	Plots of normalized difference from the mean of ice-core and geochemical reconstructions of pCO_2 variability and MD06-3018 Mg/Ca-derived SST over the past 1600ka.	177

Table List

Table 2.1	<i>G. ruber</i> shell weights for selected down-core intervals	50
Table 3.1	Comparison of orbital and magnetic age-models for MD06-3018	68
Table 3.2	Locations of sediment core records used in chapter 3	72
Table 3.3	Terms used in the comparison of regional $\delta^{13}\text{C}$ records	75
Table 4.1	Locations of sediment core records used in chapter 4	93
Table 5.1	Locations of sediment core records used in chapters 5 and 6	124
Table 7.1	% abundance for <i>G. ruber</i> and <i>G. inflata</i> for selected MIS	168

Word count

There are 47,100 words in the main body of this thesis and an additional 10,900 words in the references and appendices combined.

List of abbreviations used in the text

AAIW	Antarctic Intermediate Water
CDW	Circumpolar Deep Water
ChRM	Characteristic Remnant Magnetization
CPBDW	Central Pacific Basin Deep Water
DIC	Dissolved Inorganic Carbon
DSDP	Deep Sea Drilling Project
DWBC	Deep Western Boundary Current
DWT	Deep Water Temperature
EEP	Eastern Equatorial Pacific
ENSO	El-Niño Southern Oscillation
GBR	Great Barrier Reef
Hol	Holocene
ICP-OES	Inductively Coupled Plasma – Optical Emission Spectroscopy
ka / Ma	Thousands / Millions of years before present
kyr / Myr	Thousands / Millions of years (duration of time)
(u/l) LCDW	(upper/lower) Lower Circumpolar Deep Water
LGM	Last Glacial Maximum
MAT	Modern Analogue Technique
MIS	Marine Isotope Stage
MPT	Mid-Pleistocene Transition
NCBR	New Caledonia Barrier Reef
NCT	New Caledonia Trough
NHG	Northern Hemisphere Glaciation
(g)NPDW	(glacial) North Pacific Deep Water
ODP	Ocean Drilling Program
ODV	Ocean Data View
SEM	Standard Error on Mean
SPCZ	South Pacific Convergence Zone
SST	Sea Surface Temperature
(g)UCDW	(glacial) Upper Circumpolar Deep Water
VPDB	Vienna Pee Dee Belemnite
VSMOW	Vienna Standard Mean Ocean Water
WEP	Western Equatorial Pacific
WOA	World Ocean Atlas
WOCE	World Ocean Circulation Experiment



Blank Page

*How inappropriate to call this planet Earth,
when it is, quite clearly, Ocean.*

Arthur C Clarke



Blank Page

Chapter 1: General Introduction

1.1 Thesis overview

This thesis presents, describes and interprets a series of paleoceanographic reconstructions from the southern Coral Sea in the subtropical southwest Pacific. These reconstructions span the period of the Mid-Pleistocene Transition (1200-500ka¹) at ~5kyr resolution. The dominant modes of global climatic variability on 10-100kyr time-scales over the Pleistocene are the so-called ‘glacial/interglacial cycles’ and these are widely believed to be related to periodic variations in the Earth’s orbital parameters. The Mid-Pleistocene Transition constituted the last major shift in the dominant mode of glacial/interglacial variability and occurred in the absence of any corresponding change in the orbital forcing. Better understanding the origins of this non-linearity in the climate system response, both within the glacial/interglacial cycles on 10-100kyr time-scales, and on the >100kyr time-scale of the transition itself is the underlying motivation for this thesis.

Many of the key unresolved problems in orbital time-scale climate relate to the relative importance of high- and low-latitude processes and the connections between them. In particular, the roles played by ice-sheet dynamics, the carbon-cycle and the low-latitude ocean/atmosphere circulation system in both the origins and structure of the Mid-Pleistocene Transition remain unclear. Subtropical climate on orbital time-scales is sensitive to both high- and low-latitude processes such that single core, multi-proxy reconstructions of past variability from these latitudes have the potential to significantly advance understanding of these questions. This thesis presents the first geochemical reconstructions of subtropical southwest Pacific sea surface temperature, regional hydrological cycle variability and deep water carbon chemistry that span the Mid-Pleistocene Transition at sub-orbital resolution.

¹ The notation ‘ka’ refers to thousands of years before present, as distinct from ‘kyr’ which refers to a duration of time without a prescribed reference point. Analogous notation is used for millions of years (Ma/Myr). The aeon notation always implies the existence of some form of age-model, as discussed in §4.

The main body of this thesis is presented as a series of four papers, which are either published or in the process of being published, that use these reconstructions to address specific research questions relating to the Pleistocene paleoceanography of the subtropical southwest Pacific. These chapters may be read as self-contained units, although they have all been altered somewhat from their original forms to allow for reading as part of a continuous thesis. Preceding this material, the remainder of the current chapter provides an introduction to both the science of paleoceanography and the more specific context for the thesis. The subsequent chapter provides a detailed introduction to the region and the sediment core material that houses the geochemical proxies which are presented in the paper-style chapters. Following the paper-style chapters, a general discussion brings together the preceding material in order to address the general aim of the thesis, namely to better constrain and understand the roles played by the carbon-cycle and the low-latitude ocean/atmosphere circulation system in both the origins and structure of the Mid-Pleistocene Transition. Finally, a general conclusions chapter summarizes the key findings from the thesis.

1.3 The science of paleoceanography

Paleoceanography is the study of the past physical, chemical and biological properties of the Earth's oceans. It is, as such, a highly inter-disciplinary area of research within the wider Earth sciences and has only been generally recognized as a distinct field since the seminal work of the chemists Harold Urey and Cesare Emiliani in the 1940-1950s. Taken collectively, their work demonstrated that the chemical composition of the shells of marine microfossils can be related quantitatively to past environmental conditions [for example; *Urey, 1947; Emiliani, 1954, 1955*]. This observation expanded the temporal domain of potential study open to oceanographers from the instrumental (i.e. the past few centuries) to that of the marine sediment record (Myrs). In doing so, the science of paleoceanography was born and has been in a state of growth ever since.

The reason for this expansion can be attributed partly to the innate fascination of the oceans themselves, but also relates strongly to the intimate connection between the physical and chemical states of the oceans and those of the atmosphere on the time-scales of interest. This connection stems from the relatively rapid chemical mixing and thermal equilibration of the upper-ocean and atmosphere and the relatively large size of the oceans as a chemical reservoir when compared to the atmosphere. For example, in the important example of the carbon-cycle, there exists ~50 times more carbon dissolved in the modern oceans than there does CO₂ gas in the atmosphere. Given that most paleoceanographic reconstructions are made on temporal resolution of centuries or higher, time-scales exceeding the upper-ocean/atmosphere mixing time, it follows that these reconstructions provide an insight not only into the state of the oceans, but also into that of the atmosphere. Furthermore, the major alternative archives for atmospheric properties beyond the last few millennia are the polar ice-core records, but even the longest of these only extends to the middle Pleistocene. Therefore, paleoceanographic records have a fundamental role to play in constraining past variability throughout the coupled ocean/climate system.

The particularly intense interest in climatology as a science that exists at the time of writing this thesis stems mainly from the need of humanity to develop an adequate understanding of the likely climate response to carbon-cycle perturbations on decadal to millennial time-scales. In order to achieve this, sophisticated models of ocean/atmosphere circulation are required and to test these models, some constraints on the past variability of the system. As understanding of the dynamics of the climate system and model skill improves, it becomes increasingly evident that many of the major uncertainties in current models stem from incomplete knowledge of the feedback processes embedded in the system [*Jansen et al.*, 2007]. These feedback processes have characteristic times that are, in many cases, of significant magnitude relative to the duration of instrumental ocean/climate records and can thus only be numerically constrained through proxy reconstructions of past variability.

Paleoceanography is, therefore, a science that exists between the geological and anthropogenic time-scales. Research in the field serves to develop not only the collective scientific understanding of natural variability within the ocean/climate system but also allows better constraints to be placed on the likely response of that system to the rapid changes it is presently undergoing.

1.4 Paleooceanographic proxies and age-models

The work of Urey and Emiliani marked the establishment of the paleo-environmental ‘proxy’ concept, which has become central to almost all paleooceanographic research. A paleooceanographic proxy is a mathematical model relating a measurable property (generally derived from a sedimentary archive) to an environmental variable. The measured property is often (but not always) a chemical one - such as the isotopic ratio of a given element in a certain material. The ideal such ‘geochemical proxy’ would be one in which the chemical variable of interest depends on precisely one environmental parameter and is measurable exactly (i.e. zero measurement and reproducibility uncertainty) and for which the proxy model, or calibration, is also known exactly (i.e. zero calibration uncertainty). As the Earth is a real, rather than mathematical, system however, none of these criteria is ever fulfilled. Consequently, whilst providing an extremely powerful tool for the study of past ocean/climate variability, it must be remembered that proxy reconstructions are never equivalent to direct measurements of diagnostic climate parameters and must be interpreted with awareness of their inherent limitations.

The main proxy systems used in the present thesis are all derived from geochemical measurements made on the calcitic tests of the group of marine microfossils known as foraminifera. The foraminifera are a group of amoeboid protists which molecular phylogenies suggest form a clade within the rhizaria super-group [*Cavalier-Smith*, 2003]. Certain groups of foraminifera show both benthic and planktic ecologies and collectively they have been widely distributed throughout the global ocean over most of the Cenozoic. Their great abundance in marine sediment cores from most oceanic areas in which calcite is preserved at the sea floor make them a useful archive for paleooceanographic proxies. The three proxy systems used here are the stable isotopic compositions of oxygen and carbon, $\delta^{18}\text{O}_{\text{calcite}}$ and $\delta^{13}\text{C}_{\text{calcite}}$ respectively, and the Mg/Ca trace-metal ratio of their calcite tests. Measurements are made on both planktic and benthic taxa for the stable isotope proxies - the notation $\delta^{18}\text{O}_{\text{benthic}}$ is used to denote the $\delta^{18}\text{O}_{\text{calcite}}$ of the benthic taxa,

and analogous notation is used for the other measurements. In contrast, Mg/Ca ratios were only measured for the planktic taxa.

For the purposes of paleoceanography, it is generally assumed that foraminiferal $\delta^{18}\text{O}_{\text{calcite}}$ provides a proxy for both the calcification temperature and the isotopic composition of the seawater ($\delta^{18}\text{O}_{\text{sw}}$) from which calcification occurs [Bemis *et al.*, 1998]. The local value of $\delta^{18}\text{O}_{\text{sw}}$ is determined in turn by factors within the hydrological cycle, on both the regional and global scales. Foraminiferal $\delta^{13}\text{C}_{\text{calcite}}$, when measured for certain benthic taxa, provides a proxy for the isotopic composition of Dissolved Inorganic Carbon (DIC), $\delta^{13}\text{C}_{\text{DIC}}$, within deep ocean water masses - which relates in turn to both the organic and inorganic cycling of carbon within the oceans [Shackleton and Opdyke, 1973]. It may also be used, in certain circumstances, as a tracer for deep water mass circulation [Charles and Fairbanks, 1992]. The incorporation of trace-metals such as Mg into foraminiferal calcite is thought to relate principally to the calcification temperature and hence provides an alternative method to $\delta^{18}\text{O}$ for reconstructing paleotemperature variability [Nurnberg *et al.*, 1996]. Furthermore, combination of coupled $\delta^{18}\text{O}$ and Mg/Ca measurements allows for the potential de-convolution of the calcification temperature and hydrological cycle components of the $\delta^{18}\text{O}$ signal [Elderfield and Ganssen, 2000]. More detailed overviews of the chemical principles, systematics and limitations of these three proxy systems are given in appendix 1.

All of the various proxy records discussed in this thesis are ultimately derived from marine sediment or terrestrial ice cores. The original proxy measurements were, therefore, made as a function of depth within each core. In order to develop a reconstruction as a function of age, i.e. to translate depth-space into age-space, and allow the inter-comparison of proxy reconstructions between different cores, a core 'age-model' is required in each and every case. An age-model is simply a model relating the depth and age variables, thus quantifying the sediment accumulation rate over time. Chronostratigraphic age-model creation is based upon the correlation of certain down-core measurements to independently determined ages. In the case of late Neogene sediment core records, the principle chronostratigraphic methods used

involve the ‘known’ ages of magnetic reversal and bio-stratigraphic horizons. These tie-points are relatively sparse, however, with only two major magnetic reversals over the past one million years. This means that, unless the sedimentation rate can be assumed to be temporally invariant, which is not generally the case, then large interpolation uncertainties arise between tie-points, leading to large (of the order of 10kyr) absolute age-model uncertainties (e.g. *Huybers and Wunsch [2005]*).

Orbital cyclostratigraphy provides a complementary method for age-model development. It vastly increases the potential number of age-depth tie-points and hence, significantly reduces the age-model interpolation uncertainty. The method relies upon the assumption that a continuous down-core proxy variable, (generally $\delta^{18}\text{O}_{\text{benthic}}$, as discussed in appendix 1, §1) can be correlated, or ‘tuned’, to a global reference record for that variable, which in turn is correlated to some aspect of the theoretically computed orbital solution for the Earth. It follows that cyclostratigraphy involves the additional assumption, in relation to the chronostratigraphic methods, that an ‘orbital theory of climate’, in some form at least, is correct. If this assumption is accepted, then the method provides a very powerful tool in the reduction of age-model uncertainty, although it is still limited to resolutions of at least several millennia by the uncertainties arising from both the choice of tie-point positioning and the correlation of specific proxy records to global reference records.

Proxy reconstructions of environmental variables, as plotted on core age-models, provide the backbone to modern paleoceanographic understanding. However, regardless of both the proxy system in question and the method of age-model development used, there exist intrinsic uncertainties on both axes and these must be carefully considered in terms of their significance to each potential scientific application.

1.5 Plio-Pleistocene evolution of the climate system

On the Myr time-scale, the mean-global surface temperature of the Earth is thought to be controlled principally by the carbon-cycle balance, mediated through the abundance of CO₂ gas in the atmosphere (the partial pressure of which is denoted pCO₂), between volcanic and metamorphic degassing of carbon and the weathering of continental silicate rocks [Berner *et al.*, 1983; Raymo and Ruddiman, 1992]. Within this paradigm, the general planetary cooling trend associated with most of the Cenozoic is attributed to the uplift and subsequent erosion of the Himalayan orogen [Raymo and Ruddiman, 1992]. However, continuous down-core proxy reconstructions of paleoclimatic variables over this interval show that the patterns of change were not at all monotonic on the >100kyr time-scale, implying that a variety of other mechanisms and feedback processes must have also played significant second-order roles. In particular, the Cenozoic $\delta^{18}\text{O}_{\text{benthic}}$ compilation shown in *Figure 1.1* [Zachos *et al.*, 2001a] shows relatively rapid positive excursions associated with the development and expansion of large ice-sheets, first in the southern hemisphere from the Eocene-Oligocene boundary onwards and then more recently in the northern hemisphere, during the Pliocene and Pleistocene periods, which collectively comprise the last ~5300ka³ of Earth history.

³ This thesis follows the pre-2004 International Committee on Stratigraphy definition of placing the beginning of the Pleistocene at 1800ka, between the Calabrian and Gelasian stages. The author notes that this definition has now been moved to 2600ka (i.e. including the Gelasian within the Pleistocene) in the most recent geological time-scales (e.g. [Gradstein *et al.*, 2004]). This change does not, however, substantively impinge on the arguments developed or terminology used in this thesis as the main sediment core record discussed does not extend beyond 1800ka. Stage nomenclature is not used in the present thesis; instead the Pleistocene is divided into the three sub-series: early, middle and late [Gibbard *et al.* 2005]. The early to middle Pleistocene boundary is taken as the Brunhnes/Matuyama paleomagnetic boundary at 780ka [Cande and Kent, 1995] and the middle to late Pleistocene boundary is taken as the Blake magnetic excursion at 120ka [Gibbard *et al.* 2005], although this latter definition is not extensively used.

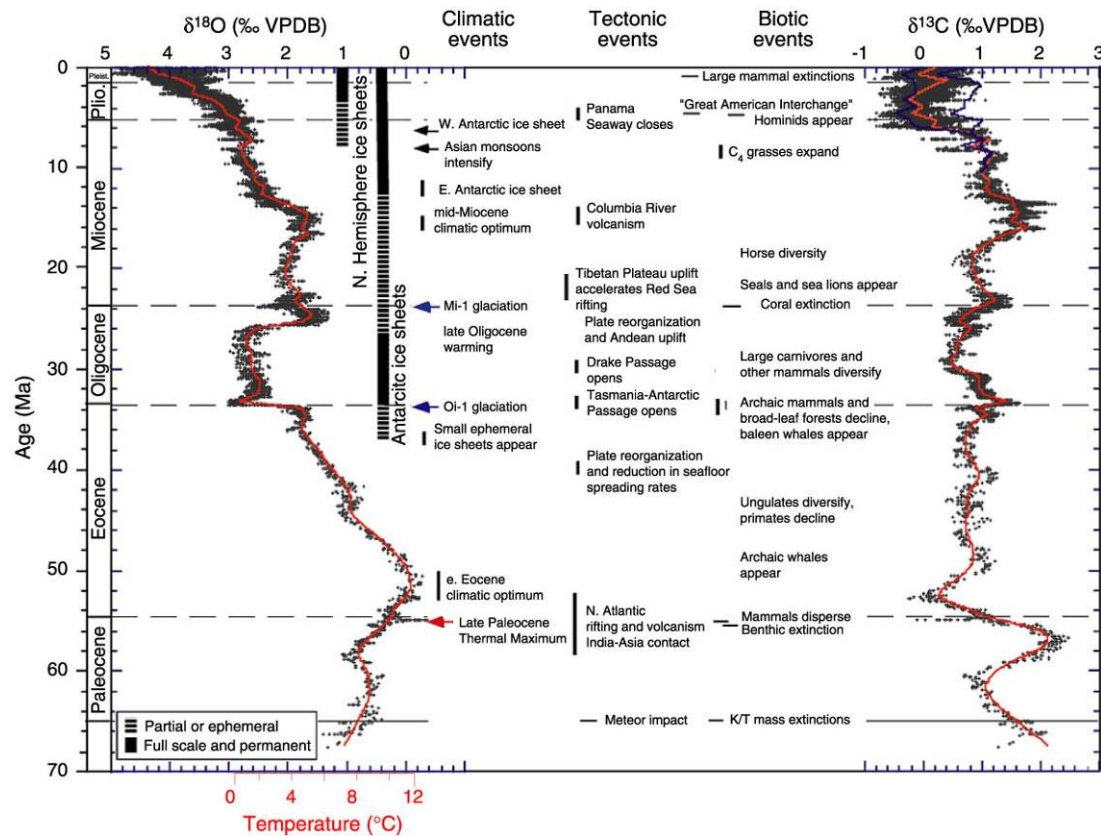


Figure 1.1 The Plio-Pleistocene as seen in a Cenozoic context, based upon compilations of globally distributed $\delta^{18}\text{O}_{\text{benthic}}$ (left panel) and $\delta^{13}\text{C}_{\text{benthic}}$ (right panel) records over the past 65Ma. Only the $\delta^{18}\text{O}_{\text{benthic}}$ record is discussed in the text. The ‘temperature’ scale refers to global average deep water temperature, based on the principles of the isotopic paleotemperature equation, as described in appendix 1, §1. This figure is reproduced directly from *Figure 2* of *Zachos et al. [2001a]*.

The onset of permanent Northern Hemisphere Glaciation (NHG) is placed at 2700-2500ka by studies based on increasing >100kyr mean $\delta^{18}\text{O}_{\text{benthic}}$ values [*Shackleton, 1984; Raymo, 1994; Bintanja and van de Wal, 2008*] and as early as 3700-3500ka by others using more complex methods of $\delta^{18}\text{O}_{\text{benthic}}$ time-series analysis [*Mudelsee and Raymo, 2005; Meyers and Hinnov, 2010*]. In any case, large ice-sheets were certainly established by 2500ka, based on the appearance of ice-rafted debris in the North Atlantic [*Shackleton et al., 1984*]. Attempts to de-convolve the ice-volume and Deep Water Temperature (DWT) components of $\delta^{18}\text{O}_{\text{benthic}}$ variability suggest that the late Pliocene and early Pleistocene then represented a period of gradual deep water cooling, but not significant ice-volume expansion

[*Sosdian and Rosenthal, 2009*]. This was followed by a period of glacial intensification during the early Pleistocene, lasting ~40kyr and centred on ~920ka [*Mudelsee and Schulz, 1997*].

The only major global tectonic event to have occurred during the Plio-Pleistocene interval was the closure of the Panama seaway during the early Pliocene (see the ‘tectonic events’ column on *Figure 1.1*). This event would certainly have had a significant impact on global ocean circulation patterns, for both surface and deep water masses, which may potentially have led to the onset of northern hemisphere cooling and NHG [*Bartoli et al., 2005*]. However, the relative causality of such changes is not at present firmly established [*Molnar, 2008*] and in any case the early Pleistocene intensification of NHG is highly unlikely to have been a direct consequence of the tectonic changes. Therefore, whilst Plio-Pleistocene climate evolution on the >100kyr time-scale is certainly influenced by both the continued effects of Himalayan orogenesis and the closure of the Panama seaway, other processes and feedback mechanisms must also have been significant, especially in the case of the changes occurring during the Pleistocene.

As well as the >100kyr time-scale patterns described above, the $\delta^{18}\text{O}_{\text{benthic}}$ record shown in *Figure 1.1* also demonstrates that significant amplitude (1-2‰) variability on the <100kyr time-scale has been present in the global climate response, at least since the onset of Antarctic glaciation. Furthermore, the amplitude of this latter variability is seen to be greater during the Plio-Pleistocene than during any other interval over the Cenozoic. The subsequent sections now consider in more detail the nature and origins of this <100kyr time-scale climate variability. However, this thesis will also present new data relevant to the >100kyr time-scale problem of what caused the early Pleistocene intensification of NHG and consequently this topic is revisited in more depth in §7.1.

1.6 The Milankovitch paradigm – orbital time-scale variability in the climate system

A more detailed view of Plio-Pleistocene $\delta^{18}\text{O}_{\text{benthic}}$ change than that seen in the *Zachos et al.* [2001a] record (*Fig 1.1*) is presented in the LR04 stack of 57 globally distributed records (*Fig 1.2*), which offers 1-5kyr resolution [*Lisiecki and Raymo, 2005*]. The LR04 stack clearly shows that some form of periodic variability on the 10-100kyr time-scale is present in the climate system throughout at least the past 5000ka. It can also be seen that the amplitude of this variability has generally increased from the early Pliocene to the middle/late Pleistocene, driven principally by increasingly positive maxima values (*Fig 1.2A*). Furthermore, two shifts in the dominant periodicity of this variability are present; firstly, the emergence of a significant ~40kyr mode at ~2700ka and then the emergence of a dominant ~100kyr mode during the early/middle Pleistocene (*Fig 1.2B*). Whilst the present study focuses exclusively on the Plio-Pleistocene, studies of various proxy systems in both Miocene [*Moore et al., 1982*] and Oligocene [*Zachos et al., 2001b; Palike et al., 2006*] age sediments have also revealed significant spectral power at similar periods, suggesting that periodic 10-100kyr time-scale variability has been a major feature of the climate system since at least the establishment of Antarctic glaciation.

The dominant mode of 10-100kyr variability in the climate system for any given period is referred to as the ‘glacial/interglacial’ mode of cyclicity, because of the associated fluctuations in (principally northern hemisphere) ice-volume, as reflected in $\delta^{18}\text{O}_{\text{benthic}}$ records such as LR04. However, glacial/interglacial variability is also present, in some form, in almost all other Plio-Pleistocene paleoceanographic and palaeoclimatic proxy records, demonstrating that these modes affect the entirety of the climate system. Understanding the origin of glacial/interglacial climatic variability has constituted a major goal of paleoceanographic research since its inception.

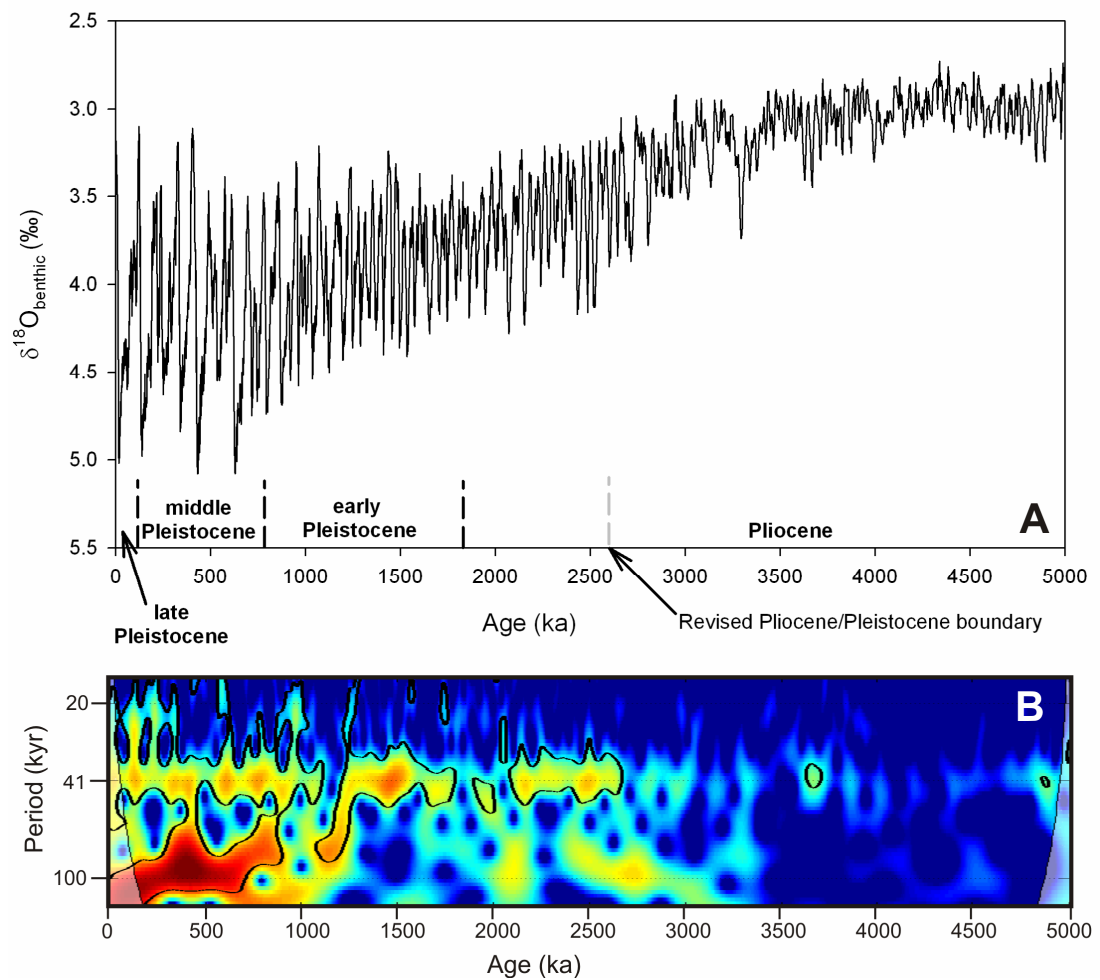


Figure 1.2 A) LR04 $\delta^{18}\text{O}_{\text{benthic}}$ stack over the past 5000ka [Lisiecki and Raymo, 2005] with sub-series divisions of the Pleistocene highlighted. B) Local wavelet power spectra of LR04 derived using a modified version of the WTC-16 code [Grinsted et al., 2004]. Warmer colours represent greater spectral power (on a logarithmic scale from 1/16 to 16 units of squared normalized variance, the same scale as shown for Figure 6.3) and black contour-lines show 5% confidence intervals above a modelled first order autoregressive red-noise process. Shaded areas show the cone-of-interference, within which edge effects become significant. The LR04 stack was smoothed to 5kyr resolution before wavelet decomposition, which limits the capacity of the method to resolved periodicities $\leq 20\text{kyr}$. More detail on the wavelet methodology used is given in chapter 6, §4.

In the late 19th Century James Croll first proposed that the form of the Earth's orbit around the sun may have influenced global climate. However, calculation of the Earth's 'orbital solution', to determine the time periods of such variability and the subsequent elaboration of an 'orbital theory of climate' was not performed until the 1940s and the work of Milutin Milankovitch. This contribution remains so seminal that the paradigm that periodic fluctuations in the Earth's climate are forced and/or paced by changes in the insolation budget arising from orbital variations bears his name. Evaluation of this hypothesis was not, however, made possible until the 1970s and the availability of suitable resolution proxy archives in, and age-models for, marine sediment cores, largely as a consequence of the Deep Sea Drilling Project (DSDP). In their seminal 1976 paper, Hays, Imbrie and Shackleton provided the first down-core validation of the fundamental Milankovitch hypothesis. This was that periodic variability exists in Neogene paleoceanographic proxy records and that the dominant periods present in these records correspond closely to the three dominant orbital cycles, namely those of precession (19kyr and 23kyr periods), obliquity (41kyr period) and eccentricity (100kyr and 400kyr periods)⁴.

Whilst the essence of the Milankovitch paradigm has remained intact over the past three decades of paleoceanographic research, a single, process-based model for the response of the Earth system to orbital forcing has remained elusive. The reasons for this relate variously to the presence of non-deterministic variability in the system, the inherent limitations arising from paleoceanographic age-models and to the form of the reconstructions themselves. In the first case, a significant component of the 10-100kyr variability in the climate system, at least as seen in $\delta^{18}\text{O}_{\text{benthic}}$ records, arises from stochastic processes rather than through deterministic forcing and/or pacing⁵ of the climate response by orbital variations [*Saltzman, 1982; Wunsch, 2004; Meyers and Hinnov; 2010*]. However, the relative importance of the deterministic,

⁴ The range of orbital periodicities, excluding the 400kyr eccentricity cycle, leads to the definition of an 'orbital time-scale', namely periodicities in the range of 10-100kyr. The term 'glacial/interglacial cycle' does not in itself refer to any defined range of periods or indeed imply any connection to the orbital cycles.

⁵ The stochastic – deterministic distinction is not always easily definable in climate systems. However, 'stochastic' phenomena lack phase coherence with their primary forcing mechanism, whereas 'deterministic' ones do display a simple phase relationship.

'Milankovitch' component has apparently increased from the more stochastic early Pliocene towards the middle/late Pleistocene [*Meyers and Hinnov*; 2010].

The study of the spectral properties of paleoceanographic proxy records, which provides one of the key methods for evaluating and exploring the Milankovitch paradigm, relies ultimately on the creation of core age-models. As discussed in §4, these age-models often involve the application of orbital tuning and hence, the pre-assumption of some form of the underlying association itself. However, the general similarity, at least on >1kyr time-scales, between strongly orbitally tuned records, such as the LR04 $\delta^{18}\text{O}_{\text{benthic}}$ stack, and un-tuned ones, such as the H07 stack, which is based on a 'depth-derived age-model' [*Huybers*, 2007] and does not pre-assume a strong orbital control of climate, suggests that most of the 10-100kyr features of the records are not a direct consequence of the tuning itself. This observation, combined with the great efficacy of the general Milankovitch paradigm in explaining much of the observed orbital time-scale climate variability, leads to the wide acceptance of a general orbital theory of climate, and hence the underlying principle of orbital tuning.⁶

A more intractable challenge to the development of a complete orbital theory of climate is that the climate response, as seen in Plio-Pleistocene proxy records, regardless of whether they are orbitally tuned or not, is far more complex than the general form of the orbital solution derived insolation curve at any given latitude and season. It follows that the Earth system response to the orbital forcing is strongly non-linear, both on the orbital time-scale itself and also on the >100kyr time-scale [*Elkibbi and Rial*, 2001; *Ruddiman*, 2003; *Maslin and Ridgwell*, 2005; *Clark et al.*, 2006], as seen in the Plio-Pleistocene transitions between dominant glacial/interglacial modes (*Fig 1.2*). The existence of this degree of non-linearity has fundamental epistemological implications for the development of any successful orbital theory of climate. It means that any model must contain either sufficiently realistic treatment of the crucial feedback processes within the Earth system or

⁶ This assumption is also adopted in the present thesis and the orbitally tuned LR04 $\delta^{18}\text{O}_{\text{benthic}}$ stack is used as the reference record in the creation of the associated core age-model.

artificially impose threshold levels to recreate the observed variability [Imbrie and Imbrie, 1980; Paillard, 1998; Gildor and Tziperman, 2000]. The development of both approaches is limited fundamentally by understanding of which processes within the climate system actually manifest the non-linearity on each time-scale. This limitation is now discussed in detail for the last example of significant >100kyr time-scale non-linearity, namely the early/middle Pleistocene transition in the dominant mode of glacial/interglacial variability, which is known as the Mid-Pleistocene Transition (MPT).

1.7 The Mid-Pleistocene Transition

During the MPT, the interval of which is defined as 1200-500ka, using the boundary dates of *Head and Gibbard* [2005], the dominant glacial/interglacial mode of the climate system evolved, in the absence of any corresponding shift in the orbital forcing itself, from the relatively low-amplitude and (near) symmetric [Ashkenazy and Tziperman, 2004] 40kyr cycles of the late Pliocene and early Pleistocene towards the more high-amplitude, non-linear and variable duration 100kyr ‘cycles’ of the middle/late Pleistocene (as shown in the LR04 stack in *Figure 1.2*). As discussed in §5, the early Pleistocene was also associated with a period of ice-volume expansion and the intensification of NHG. Hence, the term MPT, as used here, refers to two semi-independent changes within the global climate system which occurred over several 100kyrs and consequently, this thesis favours the broad temporal definition for the MPT of *Head and Gibbard* [2005]⁷. Statistical analysis of $\delta^{18}\text{O}_{\text{benthic}}$ records show that whilst the increase in >100kyr time-scale mean $\delta^{18}\text{O}_{\text{benthic}}$ value (and by inference ice-volume) was centred on 920ka, the emergence of dominant ~100kyr periodicity did not occur until ~600ka [Mudelsee and Schulz, 1997]. This temporal relationship, which is also visible on *Figure 1.2*, suggests that the intensification of NHG led to the onset of the 100kyr glacial/interglacial mode.

⁷ It should be noted that the MPT interval as taken here, 1200-500ka, *sensu Head and Gibbard* [2005], does not correspond to the middle Pleistocene sub-series and instead includes parts of both the middle and early Pleistocene sub-series. Furthermore, no suitable chronostratigraphic term exists for the ‘post-MPT’ world of the past 500ka and this is thus referred to as either the ‘100kyr world’ or as a subset of the middle/late Pleistocene. These distinctions are clearly illustrated through comparison of the wavelet decomposition plot for LR04 and the sub-series definitions given in *Fig 1.2*.

However, the potential causality of this relationship is not at present fully resolved and hence these two components of the MPT are discussed separately in the following sub-sections.

1.7.1 Potential origins of the early Pleistocene intensification of northern hemisphere glaciation

The early Pleistocene increase in the rate of expansion of northern hemisphere ice-volume has been proposed to result from >100kyr time-scale global cooling trends, driven by a secular decrease in pCO₂ [Paillard, 1998; Gildor and Tziperman, 2000]. However, geochemical reconstructions of early Pleistocene pCO₂ do not show any detectable trend of this type [Honisch *et al.*, 2009], suggesting that other processes may have been responsible. One such alternative view is that >100kyr time-scale changes in the low-latitude (taken here as being 30°N to 30°S) ocean/atmosphere circulation system led to the intensification of glaciation [McClymont and Rosell-Mele, 2005]. The basis for this idea is that the low-latitude Pacific is the ‘heat and moisture engine’ for the global atmosphere and changes in the underlying Sea Surface Temperature (SST) distribution lead to significant changes in the advection of both properties towards higher latitudes [Philander and Fedorov, 2003; Shukla *et al.*, 2009; Vizcaíno *et al.*, 2010]. This importance of the coupled low-latitude ocean/atmosphere system for global climate is clearly manifested on the inter-annual time-scale with the El-Niño Southern Oscillation (ENSO) phenomenon. If changes in this system also occurred on the >100kyr time-scale then they may indeed have significantly influenced ice-sheet development.

Plio-Pleistocene reconstructions of SST from the equatorial (taken here as being 5°N to 5°S) Pacific show that the zonal SST gradient associated with the modern circulation regime, which is closely related to the ENSO system, has been a feature of the Pleistocene and late Pliocene only [Wara *et al.*, 2005]. Therefore, during the early Pliocene, when global-mean surface temperatures were several °C warmer than at present, there also existed a zonally homogenous SST structure in the low-latitude Pacific, resembling a “permanent El-Niño” state of the climate system

on the 100kyr time-scale [*Wara et al.*, 2005; *Ravelo et al.*, 2006] (*Fig 1.3*). The onset of the upwelling of cool subsurface water masses in the Eastern Equatorial Pacific (EEP) and the weakening of the permanent El-Niño occurred over the interval 4000-3000ka, which was prior to the onset of NHG [*Vizcaíno et al.*, 2010]. The establishment of a distinct ‘warm pool’ in the Western Equatorial Pacific (WEP) also occurred over a similar interval, 4400-3600ka [*Sato et al.*, 2008].

The onset of a significant zonal equatorial SST gradient and by association, atmospheric Walker Circulation, occurred over the interval 2000-1500ka [*Wara et al.*, 2005; *Ravelo et al.*, 2004], much later than the onset of upwelling in the EEP (*Fig 1.3*). Furthermore, certain reconstructions of low-latitude SST gradients, both meridional [*Jia et al.*, 2008] and zonal [*McClymont et al.*, 2005] also show a final period of rapid change over the interval 1200-1000ka, only ~100kyr prior to the intensification of NHG at 940-900ka [*Mudelsee and Schulz*, 1997] (*Fig 1.3*). The origin of the late Neogene reorganisation of the low-latitude ocean circulation regime and SST distribution may have been ultimately related to the early Pliocene closure of the Panama seaway, but may also have been significantly influenced by southern high-latitude climatic changes through the thermocline water masses ventilated in the EEP [*Philander and Fedorov*, 2003]. In any case, the relative timing of the changes in the low-latitude Pacific SST distribution and those inferred for northern hemisphere ice-volume, as summarized in *Figure 1.3*, supports the possibility that the low-latitude ocean/atmosphere circulation system may indeed have played a key role in driving the >100kyr evolution of both global climate and NHG over the Plio-Pleistocene.

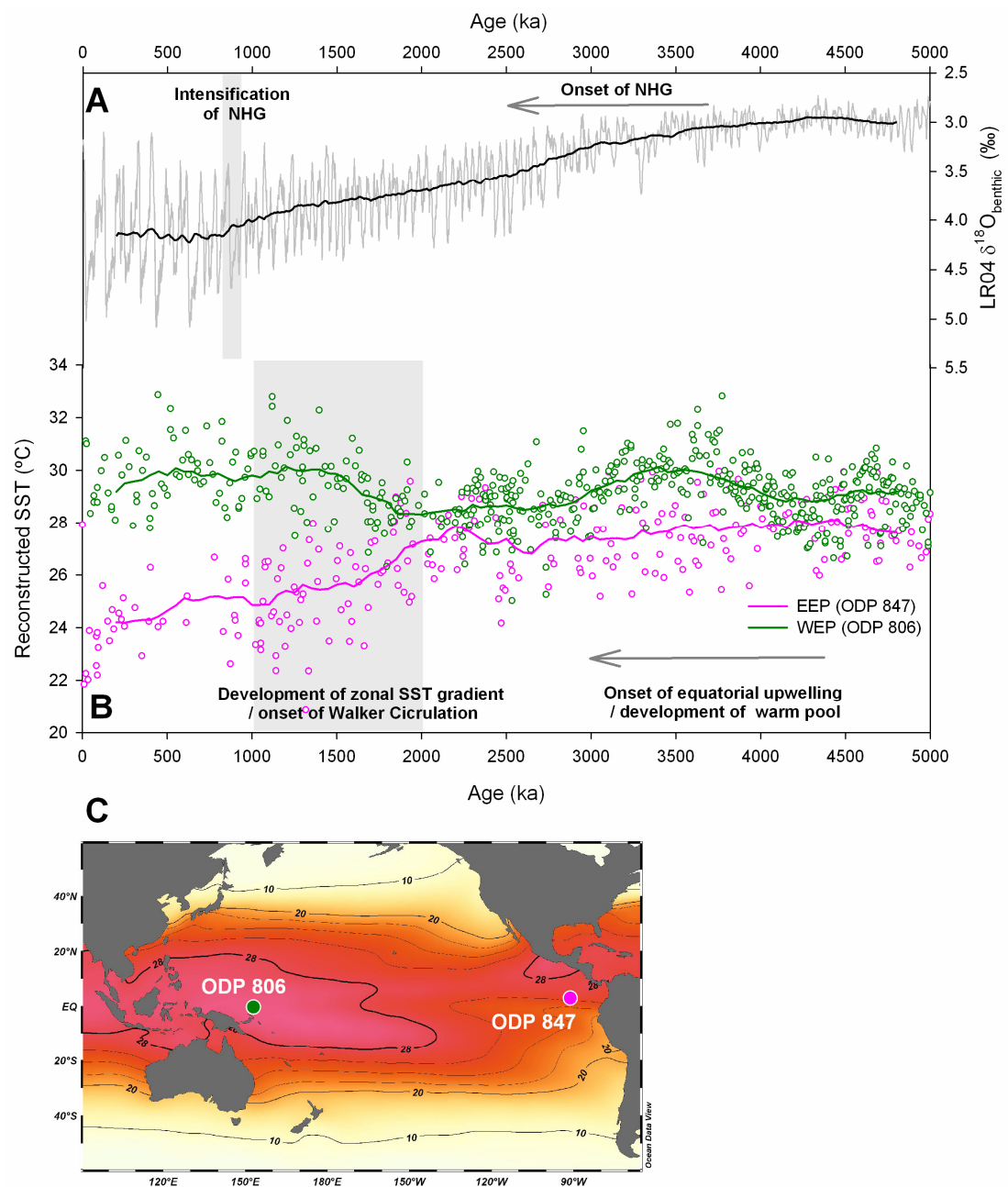


Figure 1.3 The relative timing of major events in Plio-Pleistocene climate as seen in records of **A)** stacked $\delta^{18}\text{O}_{\text{benthic}}$ [Lisiecki and Raymo, 2005] and **B)** equatorial Pacific SST [Wara *et al.*, 2005]. The grey boxes show events visible in the records shown here and the arrows show events as inferred from other sources of evidence, as discussed in the text. The bold lines represent 400kyr box-car running means for each record. The SST reconstructions are based on Mg/Ca paleothermometry in the surface dwelling planktic species *Globigerinoides sacculifer* from WEP sediment core ODP 806 (2520m water depth) and EEP sediment core ODP 847 (3360m water depth) [Wara *et al.*, 2005]. **C)** The two core locations relative to the modern mean-annual SST distribution in the Pacific based on World Ocean Atlas (WOA) 2005 data [Locarnini *et al.*, 2006], plotted using the Ocean Data View (ODV) software [Schlitzer, 2007]. Contours are in °C.

1.7.2 The ‘100kyr’ problem

Early attempts to provide a unified model for the evolving modes of Pleistocene glacial/interglacial variability followed the ideas of Milankovitch directly in suggesting that the principle sensitivity of the global system to orbital forcing at all three main orbital periods; precession, obliquity and eccentricity, arose through the direct response of northern hemisphere ice-sheets to peak summer insolation [Hays *et al.*, 1976]. The MPT represents an example not only of non-linearity in climate response to orbital forcing on the >100kyr time-scale, but is also intimately related to the so-called ‘100kyr problem’, which represents the most extreme example of non-linearity on the 10-100kyr time-scale. The ‘100kyr problem’ arises because the direct forcing of insolation at all latitudes by the orbital eccentricity cycle at that period is very weak compared to that from both the precession and obliquity cycles and even that from the 400kyr component of the eccentricity cycle. It follows that the large amplitude of the middle/late Pleistocene 100kyr mode glacial/interglacial cycles cannot be explained as any kind of direct response to the insolation forcing arising from the 100kyr eccentricity cycle [Imbrie *et al.*, 1993; Elkibbi and Rial, 2001; Maslin and Ridgwell, 2005].

Given the high ratio of ‘cycle’ period to the duration of the 100kyr mode (700-500ka, depending on the statistical method used) it is difficult to characterize the mode in a statistically robust way [Huybers and Wunsch, 2005], as can be seen from the wide ‘blur’ of significant wavelet spectral power in *Figure 1.3*. However, most authors accept that the underlying structure of these cycles is at least quasi-periodic and that they are probably phase-locked to at least one of the orbital cycles. Disagreement exists as to whether this phase-locking occurs for the obliquity [Huybers and Wunsch, 2005; Liu *et al.*, 2008], precession and its modulation by eccentricity [Raymo, 1997; Paillard, 1998; Lisiecki, 2010] cycles or to a combination of the above [Ruddiman, 2003]. Regardless of the pacing of the ~100kyr ‘cycles’, the bulk of the radiative forcing of the climate response seen within the ‘100kyr world’ (defined in this thesis as being the past 500ka⁷) must have originated from processes internal to the Earth system. The most plausible sources for such processes have

generally been considered to be either ice-sheet dynamics [*Imbrie and Imbrie*, 1980; *Paillard*, 2001] and/or the carbon-cycle [*Lea et al.*, 2000; *Shackleton*, 2000; *Toggweiler*, 2008], based on the capacity of these systems to sustain internal characteristic times of the order of 10-100kyr.

Subsequent revisions to the *Hays et al.* [1976] approach, in response to the ‘100kyr problem’, advocated a view of the MPT in which the expanded ‘large’ middle Pleistocene northern hemisphere ice-sheets exhibited an increased non-linearity of response to precession and obliquity forcing [*Imbrie et al.*, 1993], rather than a shift in sensitivity from obliquity to eccentricity forcing [*Hays et al.*, 1976]. This revised view also added a series of de-glacial feedback processes involving ocean/atmosphere teleconnections that act to communicate the northern hemisphere ice-sheet response to orbital insolation changes into the low- and southern high-latitudes, such that a carbon-cycle response, arising mainly from processes in the Southern Ocean, then acted as a positive feedback on ice-sheet melting [*Imbrie et al.*, 1992; *Imbrie et al.*, 1993]. Regardless of these differences, both of these models address the MPT as having been fundamentally a matter of northern hemisphere ice-sheet dynamics, arising from an ice-sheet size threshold associated with the early Pleistocene intensification of NHG.

Other subsequent models have ascribed this northern hemisphere ice-sheet dynamics threshold crossed during the MPT more specifically to the merger of the Laurentide and Eurasian ice-sheets [*Bintanja and van de Wal*, 2008] or to a shift in the mode of ice-sheet to bedrock interactions, rather than ice-sheet extent [*Clark and Pollard*, 1998; *Clark et al.*, 2006]. In the *Imbrie et al.* [1993] model, the 100kyr mode is viewed as being a result of the large climatic inertia associated with the middle/late Pleistocene northern hemisphere ice-sheets. Numerous subsequent refinements and/or revisions to this ice-dynamic view of the 100kyr problem have also been made, including those that advocate sea-ice as the climatic ‘switch’ [*Gildor and Tziperman*, 2000; *Tziperman and Gildor*, 2003] and those that advocate the existence of a self sustained ice-sheet and thermohaline circulation oscillator [*Denton*, 2000].

Over the past two decades new sources of proxy data for glacial/interglacial variability in both the carbon-cycle, as seen in Antarctic ice core records of air temperature and atmospheric pCO₂ variability [*Petit et al., 1999; Jouzel et al., 2007; Luthi et al., 2008*] and the low-latitude ocean/atmosphere system, as seen in proxy records of SST variability [*Lea et al., 2000; Koutavas et al., 2002; Schefuss et al., 2004*] have become available. The analysis of these records has led to the proposal of several other, very different, approaches to the MPT and to the 100kyr problem, which constitute fundamental challenges, rather than revisions or refinements to the ice-sheet dynamic view outlined above. These are; that the 100kyr mode originated principally in the carbon-cycle [*Lea et al., 2000; Shackleton, 2000; Toggweiler, 2008*] and/or the low-latitude ocean/atmosphere circulation system [*Liu et al., 2008*]. As well as questioning the fundamental importance of ice-sheet dynamics in the orbital time-scale global climate response, these new models also suggest that the two components of the MPT, namely the intensification of NHG and the subsequent emergence of the 100kyr mode, were probably not directly related. Before considering what the present thesis can contribute to the evaluation of these various hypotheses, the following section reviews the observations that have led to the development of the carbon-cycle and low-latitude ocean/atmosphere system models.

1.7.3 Orbital time-scale variability in the carbon-cycle and the low-latitude ocean/atmosphere circulation system

Proxy reconstructions show that variability in low-latitude Pacific SST and atmospheric pCO₂ have remained in-phase with one another (on millennial time-scales) across the middle/late Pleistocene glacial/interglacial cycles and that both of these variables lead changes in $\delta^{18}\text{O}_{\text{benthic}}$ (and by inference, northern hemisphere ice-volume) by several millennia during the associated glacial terminations [Lea *et al.*, 2000]. Furthermore, whilst current ice-core pCO₂ records do not extend beyond 800ka, equatorial Pacific SST reconstructions for the early Pleistocene suggest that the lead of that variable over $\delta^{18}\text{O}_{\text{benthic}}$ was also a feature of the 40kyr world [Medina-Elizalde and Lea., 2005]. These observations has been taken to mean that the northern high-latitudes are unlikely to be the primary origin of the global climatic response to orbital forcing in either the 40kyr or 100kyr worlds [Lea *et al.*, 2000; Medina-Elizalde and Lea., 2005].

An additional, independent line of reasoning that arrives at similar conclusions comes from the work of the late Sir Nicholas Shackleton, whose career has very substantially shaped the entire field of Pleistocene paleoceanography. Whereas his work on the Hays *et al.* [1976] paper, which provided the key down-core validation of the Milankovitch paradigm, marked almost the beginning of this remarkable contribution, his very important 2000 paper came sadly very close to its end. In it, the author uses an alternative method for de-convolving the various influences on the $\delta^{18}\text{O}_{\text{benthic}}$ signal and arrives at the conclusion that the 100kyr mode cycles in Antarctic air temperature, atmospheric pCO₂ and DWT are all in-phase with orbital eccentricity, but that all of these variables lead the $\delta^{18}\text{O}_{\text{benthic}}$ response at this period [Shackleton, 2000]. Taken in combination, the findings of Lea *et al.* [2000] and Shackleton [2000] suggest that the carbon-cycle may have played a key role, rather than simply acted as a feedback mechanism, in the orbital time-scale global climate response during the 100kyr world. If the 100kyr mode does indeed originate in the carbon-cycle then it follows that, rather than being a consequence of ice-sheet dynamics, the MPT must have instead represented either an increase in the

relative importance of the carbon-cycle forcing of the climate and/or a shift in the sensitivity of the carbon-cycle to orbital forcing.

The principle mechanism by which the carbon-cycle influences climate over glacial/interglacial cycles is through fluctuations in atmospheric greenhouse gas levels, principally pCO₂. Over the middle/late Pleistocene, Antarctic ice cores constrain the amplitude of this variability as being in the range 60-100ppmV [Luthi *et al.*, 2008]. The change in radiative forcing of the Earth's surface arising from these fluctuations constitutes a significant contribution to the radiative budget on these time-scales, especially at low-latitudes where the radiative effect of changes in ice-sheet extent are not directly felt [Broccoli, 2000]. It is plausible therefore, that the observed close temporal relationship between low-latitude Pacific SST and pCO₂ may have arisen from dominant greenhouse gas forcing of low-latitude SST variability on these time-scales. The modern low-latitude Pacific ocean/atmosphere system is, however, also closely coupled to the climate of the southern high-latitudes through the ventilation of upper-ocean water masses in the EEP [Liu *et al.*, 2002; Philander and Fedorov, 2003]. The onset of the upwelling of cool subsurface waters during the early Pliocene has been proposed as an alternative origin (as opposed to the onset of NHG) for the 40kyr glacial/interglacial climate mode, through amplification by the low-latitude system of the high-latitude obliquity sensitivity [Philander and Fedorov, 2003]. The low-latitude ocean/atmosphere circulation system may, therefore, also have been important, independently of the carbon-cycle, in the global climate response on orbital time-scales. Reconstructions of EEP SST show that precursor cyclicties of the middle/late Pleistocene 100kyr mode, arising through obliquity cycle bundling, emerged during the early Pleistocene, prior to the intensification of NHG [Liu *et al.*, 2008]. These observations suggest that the low-latitude ocean/atmosphere circulation system may have played a significant role not only in the origins of the intensification of northern hemisphere glaciation (on the >100kyr time-scale) but also in the evolving orbital global climate sensitivity over the MPT.

1.8 Rationale and motivation for thesis

The Milankovitch paradigm remains an extremely powerful tool for understanding orbital time-scale variability within the climate system. In spite of decades of intensive research, however, no single theory has gained general acceptance in explaining; the origins of the northern hemisphere ice-volume expansion occurring during the early part of the MPT, the causes of the observed shift in dominant glacial/interglacial periodicity over the transition and/or the 100kyr problem. For good review papers on these issues the reader is referred to *Elkibbi et al.* [2001], *Ruddiman et al.* [2003] and *Clark et al.* [2006]. Of particular interest here, the relative importance of, and relationships between, the external forcing of insolation from the orbital variations themselves and then the feedback mechanisms in ice-sheet dynamics, the carbon-cycle and the low-latitude ocean/atmosphere circulation system remain unresolved. These are the outstanding challenges to the orbital theory of climate that form the essential background and motivation for this thesis.

Identifying phase differences between proxy variables representing different aspects of the climate response within glacial/interglacial cycles, such as $\delta^{18}\text{O}_{\text{benthic}}$, pCO_2 and paleothermometry proxies, is a powerful and widely used tool in resolving the underlying causality relationships. This approach is, however, limited by both the inherent proxy and age-model uncertainties [*Ashkenazy and Tziperman, 2006*]. In particular, as discussed in §4, the uncertainties involved in age-model correlations between orbitally tuned records in different cores is of the order of at least several millennia [*Lisiecki and Raymo, 2009*], values that are comparable, in many cases, to the documented leads themselves [*Lea et al., 2000*]. Furthermore, in the specific case of the apparent lead of pCO_2 over ice-volume at glacial terminations, this has been shown to be both a function of the proxy data and analysis method used [*Alley et al., 2002*] and also to disappear when the time differential of ice-volume is used, rather than ice-volume itself, as is proposed in revised forms of the traditional Milankovitch formulation [*Roe et al., 2006*].

A complimentary approach to the study of the orbital time-scale relationships between these different components of the climate system, which forms the basis of the present work, is to expand the spatial coverage of single core multi-proxy records that span the MPT. By studying the amplitudes of glacial/interglacial variability in proxy variables that are sensitive to differing regional or global aspects of climate evolution across the MPT, inferences can be drawn regarding changes in the underlying processes themselves. This approach has the advantage of being much less constrained by age-model uncertainties as it compares features on the 10-100kyr, rather than 1kyr, time-scales. Furthermore, when variables within the same core are compared, this can be achieved in depth-space (or 'relative age-space'), reducing even further the relative chronology uncertainties. This approach does, however, remain subject to the proxy uncertainties, indeed perhaps even more so than the phase based approach, necessitating the careful consideration of these limitations in relation to each application.

The thesis introduces a subtropical southwest Pacific view on the MPT, based upon a series of single core multi-proxy reconstructions from 23°S in the southern Coral Sea. This region is important for the global climate system as it lies between the Southern Ocean and the western Pacific warm pool, which are key regions for variability in both the carbon-cycle and the low-latitude ocean/atmosphere circulation system respectively. By utilising a subtropical core site it is possible to reconstruct aspects of variability in both systems and their evolving response to orbital forcing on both the 10-100kyr and >100kyr time-scales over the period of the MPT.

The particular sensitivity of the southern Coral Sea to fluctuations in the low-latitude ocean/atmosphere circulation system arises from its positioning immediately to the south of the modern extent of the western Pacific warm pool. It should thus be sensitive to any past changes in the meridional extent of the warm pool, which is a key and yet poorly constrained diagnostic variable for the wider state of the low-latitude system [De Deckker, 1997] and in particular the atmospheric export of heat and moisture towards high-latitudes. Changes in these fluxes on the >100kyr time-

scale may have played a key role in the early Pleistocene intensification of NHG, but at present the meridional SST distribution in the low-latitude Pacific remains poorly constrained over this interval [Jia *et al.*, 2008]. The Coral Sea region is also sensitive to ENSO fluctuations in both SST and precipitation and has the potential to allow evaluation of whether any orbital time-scale fluctuations in the mean-state of the low-latitude ocean/atmosphere circulation system occurred and, if so, whether this response evolved over the period of the MPT.

The sensitivity of the subtropical southwest Pacific region to fluctuations in the carbon-cycle arises in several ways. Whilst very considerable debate remains as to the processes leading to the observed patterns of middle/late Pleistocene pCO₂ variability it is generally accepted that the deep ocean DIC reservoir must have played a key role [Archer *et al.*, 2000; Sigman and Boyle, 2000]. Mechanisms for the enhanced storage of glacial stage carbon in the deep ocean have invoked, amongst other things, changes in both whole ocean alkalinity arising from various mechanisms, including changes in neritic calcification, physical and chemical stratification of the deep oceans and changes in the efficacy of the biological pumps for both organic and inorganic carbon [Archer *et al.*, 2000; Sigman and Boyle, 2000].

Regardless of the mechanism(s) involved in moving the carbon into the deep ocean, it follows that the circulation and ventilation of waters within the deep ocean is of key importance for the residence time of this carbon and for its subsequent release to the atmosphere during glacial terminations. Deep waters originating in several distinct sectors of the Southern Ocean enter the subtropical southwest Pacific region through a series of distinct pathways, as a result of the complex regional bathymetry. Both the vertical [Hodell *et al.*, 2003] and lateral [McCave *et al.*, 2008] zonation of glacial stage deep and bottom water masses within the Southern Ocean has been documented, with important implications for deep ocean carbon storage. Reconstructions of subtropical southwest Pacific deepwater chemistry have the potential to provide ‘downstream’ constraints on the spatial patterns across the Indian and Pacific sectors of the Southern Ocean.

Radiative forcing models suggest that glacial/interglacial variability in subtropical SST should, as for the equatorial Pacific band, be dominated by pCO₂ variability [Broccoli, 2000]. Thus, reconstructions of subtropical SST can be compared to those from other latitudes to evaluate this hypothesis and potentially offer new paleoclimatic insights into climate sensitivity to pCO₂. Finally, the Coral Sea region is home to many of the planet's largest coral reef systems and, as above, neritic carbonate sedimentation may play an important role in the glacial/interglacial carbon-cycle [Opdyke and Walker, 1992; Rickaby et al., 2010]. Many of the Coral Sea reef systems are documented to have undergone a period of expansion during the middle Pleistocene [Braithwaite et al., 2004; Cabioch et al., 2008; Dubois et al., 2008]. This expansion, if extrapolated to the global scale, has the potential to have significantly altered the mode of glacial/interglacial pCO₂ variability in the 100kyr world. Reconstructions of SST from the region allow the evaluation of whether this hypothesis is plausible, through constraining the regional environmental factors may also have led to the observed reef expansion.

1.9 Aims of thesis

The over-arching aim of this thesis is the development of a sub-orbital time-scale resolution reconstruction of paleoceanographic and paleoclimatic variability in the subtropical southwest Pacific, over the period of the MPT and with a view to better understanding the interactions between orbital variations, the carbon-cycle and the low-latitude ocean/atmosphere circulation system, on both the 10-100kyr and >100kyr time-scales. In particular, it seeks to bring the subtropical perspective and an approach independent of the phase relationships at glacial terminations, to bear on the question as to in which of these systems a fundamental transition in orbital sensitivity occurred over the MPT. In order to move towards this general goal, the thesis advances through the evaluation of some more specific research questions, as summarized below.

- I. To develop an understanding on both the glacial/interglacial and >100kyr time-scales of the deep water circulation regime in the bathymetrically complex subtropical southwest Pacific, where deep water masses enter the open Pacific from the Southern Ocean via several distinct pathways. Changes in this regime over the MPT are evaluated in terms of the ventilation and chemical zonation of Southern Ocean deep waters, which have important implications for the carbon-cycle.

- II. To make a detailed assessment of the uncertainties associated with the Mg/Ca-derived SST for the southern Coral Sea, including the effect of seasonal biases on the proxy. This combined uncertainty approach will then be used to evaluate whether any significant changes in interglacial stage climate over the MPT can be detected using the Mg/Ca paleothermometer. If such changes can be identified, and shown to be of sufficient magnitude, then this would imply that regional climate change could have been the cause of the observed middle Pleistocene expansion of coral reef systems in the region.

- III. To reconstruct, on the >100kyr time-scale, the Pleistocene SST history of the southern Coral Sea region and to use this to evaluate whether the early Pleistocene contraction of the Pacific warm pool also affected its meridional extent in the southern hemisphere. This will allow better evaluation of the existing hypothesis that ocean/atmosphere circulation changes in the low-latitude Pacific limited the expansion of northern hemisphere ice-volume seen during the early part of the MPT.

- IV. To characterize the amplitude and structure of glacial/interglacial variability in both SST and the regional hydrological cycle response seen in the southern Coral Sea across the MPT. The orbital controls on these two variables and the effect on them arising from changes in carbon-cycle induced greenhouse gas forcing and the low-latitude ocean/atmosphere circulation regime will be evaluated. This will then allow constraints to be placed on the extent to which either the carbon-cycle and/or the low-latitude ocean/atmosphere circulation regime underwent a fundamental shift in orbital sensitivity over the transition.

1.10 Structure of thesis

The main body of this thesis, comprising chapter 3 through chapter 6, is presented as a series of paper-style chapters. These chapters are based closely around papers that have either been published (in the case of chapter 3 and chapter 5), are in press (in the case of chapter 6) or are awaiting submission (in the case of chapter 4). As such, these individual chapters are largely self-contained in form, although alterations have been made where appropriate to avoid repetition or inappropriate ordering of material. The main such alteration is the relocation into **chapter 2** of all the material dealing with the setting and physical properties of the giant piston core MD06-3018, which is the source of the new proxy data presented in the paper-style chapters. This chapter also includes additional material, which is not present in the published papers, relating to the sedimentology of the core and aspects of the modern oceanography and climatology of the core-site. There is no separate methodology chapter as each of the methods used is introduced as required within the relevant sections of the paper-style chapters. However, more background on the various proxy systems and the full analytical methods used are given as appendices, as described below.

The paper-style chapters are not presented in chronological order of publication, but in that which in the author's opinion best serves to develop the arguments that unify the thesis. **Chapter 3** introduces the benthic stable isotope records and the core age-model for MD06-3018 and then uses the $\delta^{13}\text{C}_{\text{benthic}}$ record to characterize and interpret the regional deep water circulation regime, addressing aim I. Chapters 4, 5 and 6 then introduce the planktic Mg/Ca trace-metal and $\delta^{18}\text{O}$ records and use these to characterize and interpret the surface ocean paleoceanography and paleoclimatology of the region. **Chapter 4** presents the MD06-3018 Mg/Ca-derived SST reconstruction and examines its uncertainties in detail. It also presents independent, foraminiferal transfer function derived estimate of seasonal SST, in order to address aim II. **Chapter 5** focuses on >100kyr time-scale variability in the SST reconstruction to address aim III whereas **chapter 6** presents the coupled $\delta^{18}\text{O}_{\text{planktic}}$ record and focuses on orbital time-scale variability in

both SST and the hydrological cycle to address aim IV. Following the paper-style chapters is **chapter 7**, a general discussion chapter which draws together the common themes present in the preceding material and uses these to address the general aim of the thesis as defined above. It also offers suggestions for both future work and directions in the specific and wider field. Finally, **chapter 8** summarises the key conclusions from the thesis as a whole.

A series of appendices contains more detailed information on the proxy systems used (**appendix 1**), the full analytical techniques used for the geochemical measurements (**appendices 2 and 3**), the full down-core data-sets used in the thesis (**appendices 4, 6 and 7**) and also a reference plot of the data-sets versus core depth, (**appendix 5**). Data sets for $\delta^{13}\text{C}_{\text{planktic}}$ and the Sr/Ca trace-metal ratio of the planktic samples are given in the data appendices for reference, although they are not discussed explicitly in the thesis. The published papers upon which chapter 3 and chapter 4 are based, the submitted manuscript upon which chapter 5 is based and an additional published paper dealing with box-modelling of the carbon-cycle response to orbital forcing, *Russon et al.* [2010b], which is referred to in chapter 7 and was published during the course of the PhD but is not part of the project itself, are also included within the electronic version of the thesis.

Chapter 2: Setting and sedimentology of giant piston core MD06-3018

2.1 Chapter overview



This chapter introduces the location and sedimentological characteristics of marine sediment core MD06-3018, from which all of the new paleoceanographic proxy measurements presented in this thesis are derived. In order to avoid repetition, the ‘setting/materials’ content that was present in each of the paper-style chapters has been removed from those sections and expanded upon here. A full description of the geographical, geological, oceanographic and climatic setting of the region is given, followed by a brief review of past deep sea drilling and paleoceanographic work. The physical sampling methods used in core processing are described as are down-core measurements of foraminiferal shell weights and bulk weight% CaCO_3 for the core. All the lab-work, data analysis and interpretation in this chapter are the work of the author.

2.2 Core location and geological setting

Deep sea sediment core MD06-3018 was recovered from 23°00'S, 166°09'E and 2470m water depth on the eastern side of the New Caledonia Trough (NCT), ~60km offshore of the island of New Caledonia (*Fig 2.1*), during cruise AUSFAIR/ZoNéCo12 (Spring 2006) on board the R.V. *Marion Dufresne* [Foucher *et al.*, 2006]. When considering the surface geography of the region, New Caledonia lies close to the boundary, not exactly defined, of the Coral Sea to the north and the Tasman Sea to the south. In the present study, when discussing surface water processes, the term 'southern Coral Sea' is used to describe the core location. At water depths below ~1500m however, the term 'NCT' is used, as the subtropical southwest Pacific region is bathymetrically extremely complex and a more detailed description is required of the position and significance of the core location.

The NCT is one of a series of broadly NW-SE trending basins in the subtropical southwest Pacific region¹, lying between the Lord Howe Rise to the west and the New Caledonia Ridge, which becomes the Norfolk Ridge as one moves southwards, to the east [Lafoy *et al.*, 2005; Pelletier, 2006]. To the west of the Lord Howe Rise is the Tasman Sea Basin and to the east of the Norfolk Ridge are the Norfolk and South Fiji Basins. Beyond the South Fiji Basin is the Kermadec Ridge, which marks the contact of the Indo-Australian and Pacific plates and the beginning of the basins of the open Pacific (*Fig 2.1*). The NCT is open to a sill depth of ~3000m into the New Hebrides Basin to the north, attains its deepest depths near to New Caledonia itself (~3600m) and shallows to the south as it approaches New Zealand [Lafoy *et al.*, 2005]. The New Hebrides Basin is connected at depths exceeding 3000m to both the Coral Sea Basin to the west and the Central Pacific Basin to the north.

¹ The term 'subtropical southwest Pacific' is defined as referring to the region 10-35°S and 150-180°E, comprising the basins of the northern Tasman Sea, the Coral Sea, the New Hebrides Basin, the NCT and the North and South Fiji Basins (*Fig 2.1*).

The tectonic origin of the basins in the subtropical southwest Pacific region is related to stretching and thinning of Indo-Australian plate continental crust from the late Cretaceous into the late Palaeocene [Lafoy *et al.*, 2005]. The central NCT (that component of the basin south of 22.5°S) experienced subsequent emplacement of oceanic crust and further subsidence which is not thought to have occurred in either the northern NCT or the adjacent Norfolk Basin. The two regimes are separated by a SW-NE trending boundary fault zone which reaches the island at ~22°S [Lafoy *et al.*, 2005]. The core-site of MD06-3018 lies just to the south of this fault zone and as such is located on thinned continental, rather than oceanic, crust.

The island of New Caledonia comprises a NW-SE trending fragment of continental crust composed principally of basic igneous rocks, with some overlying sediments [Lafoy *et al.*, 2005; Pelletier, 2006]. By the Eocene and early Oligocene, extensional tectonics had largely been replaced by convergence in the New Caledonia region which culminated in the emplacement of the ophiolitic nappe that dominates the island's geology [Pelletier, 2006]. The remainder of the Oligocene and much of the Miocene was dominated by the uplift and erosion of the New Caledonia Ridge and island system. By the late Miocene (~10Ma) east-dipping subduction had commenced on the Vanuatu trench, leading to the emplacement of the New Hebrides Arc and a general return to weak extensional tectonics in the basins westwards of the trench [Pelletier, 2006]. This regime has broadly persisted to the present, resulting in the continual accumulation of sediment in the NCT from the Miocene to the present day.

The Coral Sea region is the location of many of the world's largest coral reef systems. The MD06-3018 core site is ~60km from the New Caledonia Barrier Reef, which runs parallel to the island and separates the lagoon from the open ocean (*Fig 2.1*). The barrier reef has the effect of trapping much of the eroded terrigenous material from the island in the lagoon. The basin slope from the reef front down to the floor of the NCT is cut by several large submarine canyons, as seen on the high resolution bathymetry in *Figure 2.1*, down which eroded material from both the lagoon and the reef itself are carried into the deep basin. The MD06-3018 core-site

is, however, located on a broad bathymetric high that shelters the site from the delivery of material through any of the modern canyon systems. Evaluating the relative influences of pelagic and down-slope sedimentation at the core-site, through time, is a key aim of the current chapter and is considered in detail in §6-11.

2.3 Modern oceanography

At surface, mode and intermediate water depths, the subtropical southwest Pacific region forms an integral part of the wider South Pacific gyre system. Surface waters in the NCT are influenced both by the South Equatorial Current and the East Australian Current, which transports warm waters from the western equatorial Pacific southwards to the Tasman Front (~32°S) where they separate from the Australian coast and flow westwards (*Fig 2.2A*) [*Bostock et al.*, 2006; *Ridgway and Dunn*, 2003]. In the modern regime, the influence of the East Australian Current is restricted principally to the Australian margin and western Coral Sea, so that the dominant surface flow around New Caledonia is westwards and constitutes the most southerly branches of the South Equatorial Current.

The mean-annual thickness of the mixed layer (depth to the top of the thermocline) in the central NCT is ~75m (*Fig 2.3*). Within the coastal region this varies however from 100-150m during austral winter to 20-50m during austral summer [*Alory et al.*, 2006]. The dominant flow at both mode and intermediate water depths is also westwards, with water masses entering the region both to the north and south of the island [*Gourdeau et al.*, 2008; *Sokolov and Rintoul*, 2000]. The mode water mass present in the NCT has been called variously Tropical Lower Water [*Sokolov and Rintoul*, 2000] and South Pacific Tropical Water [*Delcroix and Lenormand*, 1997]. It is found from the mixed layer down to 400-500m depth and is characterized by a salinity maximum at ~200m (*Fig 2.3*). This water mass is formed by seasonal advection of the thermocline principally in two distinct regions; the central Southern Pacific (in the case of the solid orange arrows on *Fig2.2B*) and the southern and central Tasman Sea (in the case of the dashed green arrows on *Fig2.2B*), although in both cases the water masses undergo extensive recirculation within the South Pacific gyre before entering the Coral Sea region.

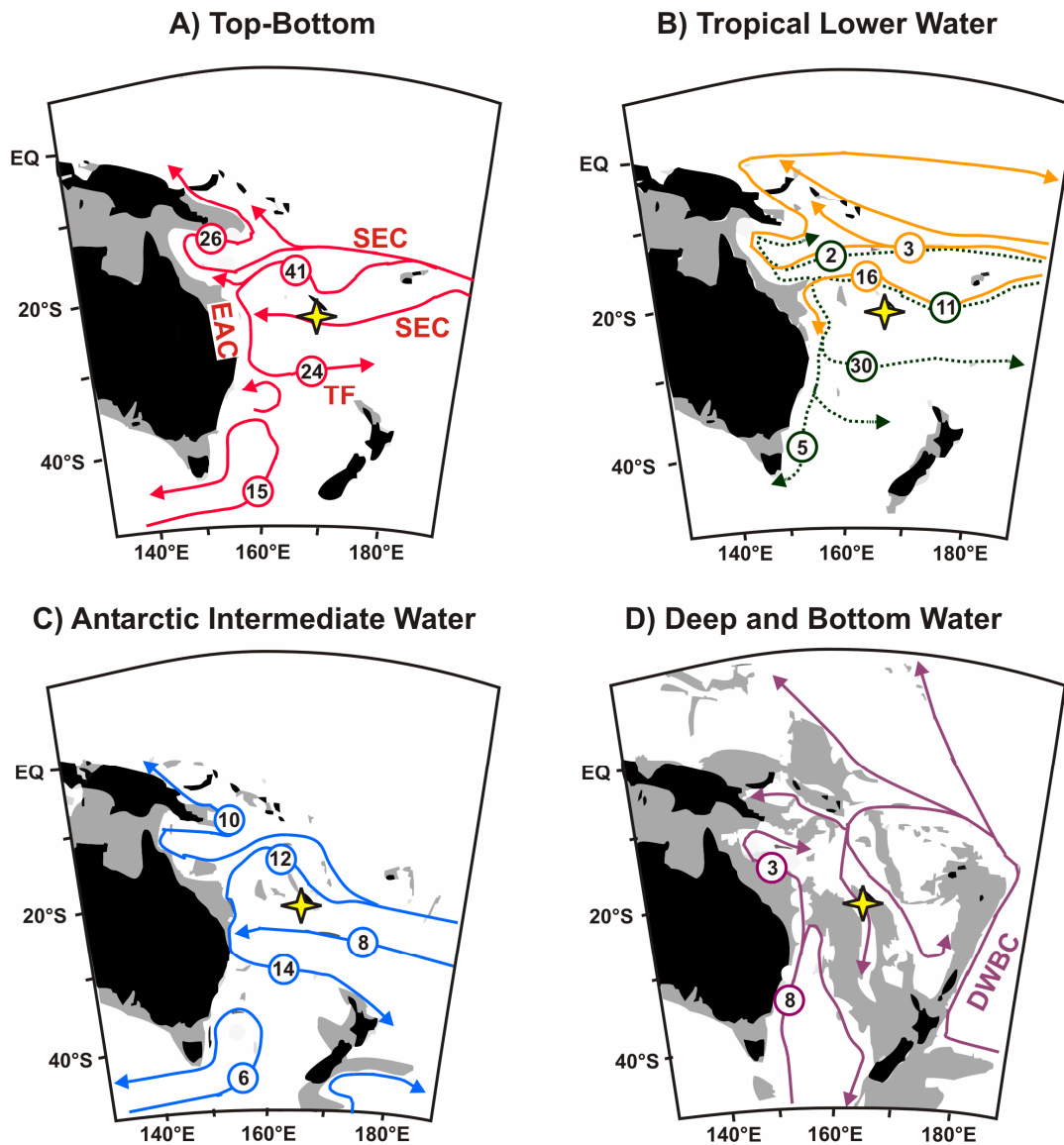


Figure 2.2 Schematic circulation regimes in the subtropical southwest Pacific for selected water-masses, as shown in *Figure 2.3*. The ‘top-bottom’ plot (A) represents the depth-integrated averaged flow, which is dominated by the surface water mass flow. The solid orange lines on (B) show mode water of open Pacific origin and the dashed green lines show mode water of ultimately southwest Pacific origin. The numbers in circles show flow in Sv, the yellow star shows the location of MD06-3018. The grey shading shows the relevant, schematic bathymetry at the depth of each water mass. Abbreviations are as follows: SEC = South Equatorial Current, EAC = East Australian Current, TF = Tasman Front. The flow values are taken and the form of the figure adapted from *Figure 16* of Sokolov and Rintoul [2000].

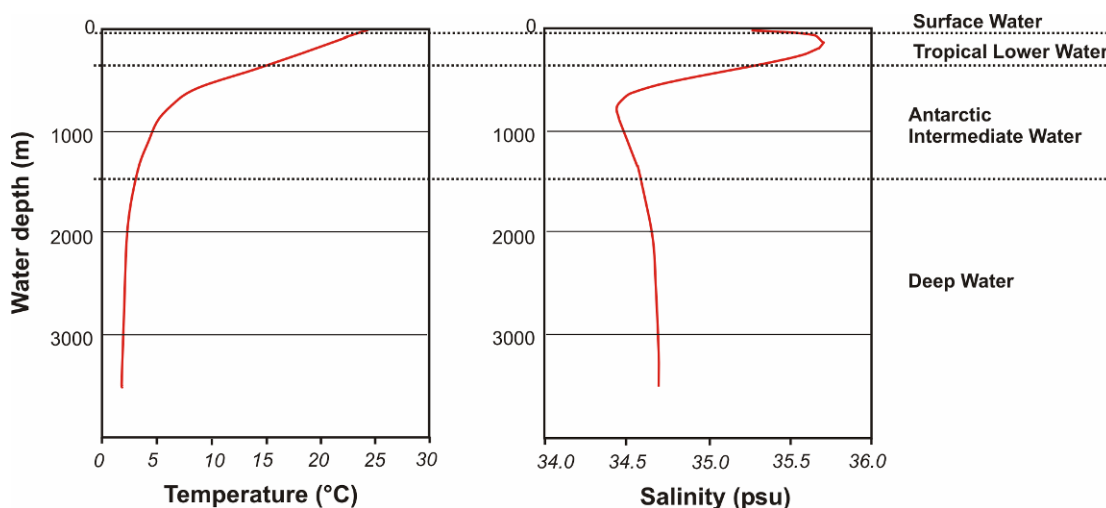


Figure 2.3 Mean-annual water column profiles for temperature and salinity from WOA2005 data for the central NCT (2° by 2° grid around the MD06-3018 core-site) [Locarnini *et al.*, 2006], plotted using ODV software [Schlitzer, 2007]. Horizontal bars show schematic positions of the water masses discussed in the text.

The intermediate water mass present throughout the subtropical southwest Pacific region is Antarctic Intermediate Water (AAIW), which is found in the depth range 500-1500m and is marked by the prominent salinity minimum at ~ 800 m (Fig 2.3). The component of AAIW that reaches New Caledonia originates mainly in the southeast Pacific and has been entrained in the south Pacific gyre (Fig 2.2C). AAIW of direct Southern Ocean origin also enters the southern Tasman Sea but the influence of this does not extend further north than $\sim 35^\circ$ S in the modern regime [Sokolov and Rintoul, 2000].

For water depths exceeding ~ 1500 m, the complex bathymetry of the region means that deep water exchange with the larger adjacent basins of the Tasman Sea and the open Pacific Ocean is restricted and a variety of water masses and circulation pathways are relevant (Fig 2.2D). The modern regional deep water circulation regime and its global context is discussed in detail in chapter 3, §3.

The subtropical southwest Pacific is not generally an area characterized by substantial upwelling of subsurface water-masses. However, the orientation of the trade south-easterly trade winds along the axis of the New Caledonia Island and the barrier reef drives a narrow band (~10km wide) of upwelling along the reef front [Alory *et al.*, 2006; Henin and Cresswell, 2005]. The upwelled water is from ~100m depth and leads to cool SST anomalies of the order of several °C and positive salinity anomalies of the order of 0.1 near to the reef front. However, the effect of the coastal upwelling is spatially limited to a few tens of kilometres from the reef front and temporally limited to time-scales of days. It does not, therefore, have a significant impact on modern seasonal or mean-annual SST values at the core-site of MD06-3018 [Alory *et al.*, 2006; Henin and Cresswell, 2005].

2.4 Modern climatology

New Caledonia lies across the Tropic of Capricorn and is as such considered to have a ‘tropical’ climate. It is affected by the Australasian Monsoon system, leading to more intense precipitation during the austral summer and experiences some typhoon activity during the later part of that season. The dominant wind system is the south-easterly trade winds with infrequent westerlies, associated with the low-pressure systems and cyclones. World Ocean Atlas (WOA) 2005 SST values, at 0m depth, for the 1° by 1° grid encompassing the MD06-3018 core-site range from winter (JAS) values of 22.2°C to summer (JFM) values of 26.0°C [Locarnini *et al.*, 2006]. The seasonally averaged SST cycle is thus ~4°C, but the maximum monthly range is ~6°C. Precipitation over New Caledonia ranges from ~50mm/month during the late winter and early spring to >140mm/month in the summer rainy season. The mean-annual open ocean surface salinity in the central NCT is 35.4 (*Fig 2.3*), with seasonal fluctuations driven by precipitation changes of the order of ~0.2 [Delcroix and Lenormand, 1997].

Both SST and the hydrological cycle in the New Caledonia region also show significant inter-annual variability, related principally to the ENSO phenomenon. In the case of the hydrological cycle, inter-annual precipitation anomalies can be 50% of the long-term mean-annual values and are highly significant against the seasonal precipitation cycle, with the El Niño (La Niña) state characterized by dry (wet) conditions [Nicet and Delcroix, 2000]. These fluctuations are driven primarily by the intensity and position of the atmospheric South Pacific Convergence Zone (SPCZ). The SPCZ is the NW-SE trending band of low-level convergence and high convection in the southern Pacific. In the modern regime it lies generally to the east of New Caledonia but during El Niño (La Niña) events migrates north-eastward (south-westward) [Gouriou and Delcroix, 2002]. Compared to the hydrological cycle fluctuations, SST variability in the southwest subtropical Pacific arising from ENSO is relatively low in amplitude compared to the seasonal variations. El Niño (La Niña) events correspond to regionally cool (warm) SST values [Gouriou and Delcroix, 2002], but these anomalies are generally $<1^{\circ}\text{C}$. The ENSO SST anomalies are, however, strengthened in the coastal zone adjacent to the New Caledonia Island, as the orientation of winds during an El Niño event becomes closer to that of the barrier reef, favouring the wind-driven upwelling of cooler subsurface waters [Henin and Cresswell, 2005].

2.5 History of ocean drilling in the region

The subtropical southwest Pacific is a relatively poorly sampled region in terms of paleoceanographic studies. DSDP Leg 90 in 1986 took several sediment cores from the Lord Howe Rise (sites 588 - 592). Four Ocean Drilling Program (ODP) legs have subsequently occurred within the region, namely Leg 133 (1993) on the northeast Australian margin, Leg 134 (1993) around the New Hebrides Arc, Leg 189 (2000) in the Tasmanian gateway and Leg 194 (2002) on the GBR. However, none of these legs has sampled the NCT and most of the scientific work has focused on the older Neogene sediments, often with a view to better understanding the history of coral reef development in the region and/or the basement structure.

A special issue of the journal *Palaeogeography, Palaeoclimatology, Palaeoecology* in 1997 presented a wide range of paleoceanographic articles on the region, many of which are based in part or entirely on the DSDP Leg 90 or ODP Leg 133/134 material and many of which are cited during this thesis. However, few of these studies comprise down-core geochemical proxy records spanning the Pleistocene and none do so at sub-orbital temporal resolution. More recently, analysis of a suite of RV *Franklin* cores from the Australian margin have allowed analysis of middle/late Pleistocene patterns of down-slope sediment transport from the Great Barrier Reef [*Dunbar and Dickens, 2003*]. These same cores, which have very high sedimentation rates, have also been used to reconstruct aspects of the surface, mode and intermediate water circulation regimes at millennial resolution over the last glacial termination [*Bostock et al., 2004; 2006*]. Several RV *Marion Dufresne* giant piston cores, retrieved as part of various programmes, have also now been collected from the central part of the region, where sedimentation rates are generally lower. These include MD97-2125, from which multi-proxy geochemical records for the NCT over the past ~360ka are presented in *Tachikawa et al. [2009]* and MD06-3018, which spans a much longer interval and is the focus of the present thesis. These giant piston cores provide the first opportunity to develop continuous, sub-orbital resolution, down-core proxy reconstructions of Pleistocene paleoceanography from the region.

2.6 Core description and sampling

Sediment core MD06-3018 is 24.5m long and composed almost entirely of foraminifera-rich calcareous ooze. The core was divided into 18 sections on board the vessel (referred to as I – XVIII), which are generally 150cm each in length, except in the cases of sections I (20cm), II (130cm) and XVIII (95cm). The trigger core from the Calypso giant piston coring device was not available for the present study. All observations and sampling were performed on the work halves of each core section; the archive sections are stored at the Institut de Recherche pour le Développement (IRD), Bondy-CEDEX, Paris. Prior to the main core sampling phase, u-channels were removed from the centre of the working sections for magnetic analysis, as described in chapter 3, §5.2.

The working sections were sampled at 1cm resolution throughout the core, with half of the available material being sampled in each case. This strategy was pursued as it yielded more than adequate numbers of foraminifera for all aspects of the work and allowed the remaining material to be left in case of the need for re-sampling from the work section. The resultant sediment samples, which were of 10-15 cm³ volume, were stored in sealed plastic bags in a cool room. Around 10% of these samples were then prepared for the selection of foraminifera and subsequent geochemical analysis. The sampling strategy used was for one sample per 10cm to be prepared in the first instance. Higher sampling resolutions were used for certain intervals, for example over the upper 400cm of the core. Additional samples were also taken adjacent to internal voids in the core, to allow evaluation of whether the isotope stratigraphies used in the development of the core age-model (chapter 3, §7) were continuous over these breaks. Much higher resolutions (every 2-5cm) were also used over three glacial terminations, as is discussed in chapter 4. In total samples from 474 depth intervals were analyzed and the full list of sampling depths is given in appendices 4 and 6. These samples were dried in an oven at 45°C overnight and wet-sieved through a 150µm sieve. The >150µm size fraction was again dried in an oven at 45°C prior to transfer into clean plastic sample vials.

2.7 Core photographs

Digital photograph images of the core sections were taken using a standard personal camera in the laboratory during the sampling process. These images, given as *Figure 2.4* and ignoring the artefacts arising from both the sampling and the photographic methods used, serve to demonstrate the relatively uniform nature of the sediment material present throughout the core.

2.8 Composite core depth scale

The original, working depth scale for the core (termed “Raw” in appendices 4 and 6) was derived from the simple addition of the total lengths of the core-section tubes. However, three sections of the core possessed internal voids. These are section VII with a 15cm void, section IX with a 10cm void and section XI with a 5cm void (*Fig 2.4*). Furthermore, sections VIII and XIII were also shorter than the 150cm core tube by 5-10cm. None of these gaps show visual evidence of erosional unconformities, such as changes in either grain size or sediment colour, and they are therefore ‘closed up’ in the creation of the ‘core composite depth’ scale, termed “CCD” in appendices 4 and 6. This approach is validated by the extremely close match up of the geochemical measurements on either side of each void, as seen when plotted on the core composite depth scale in appendix 5. Hereafter, all down-core measurements are given on the composite core depth scale.

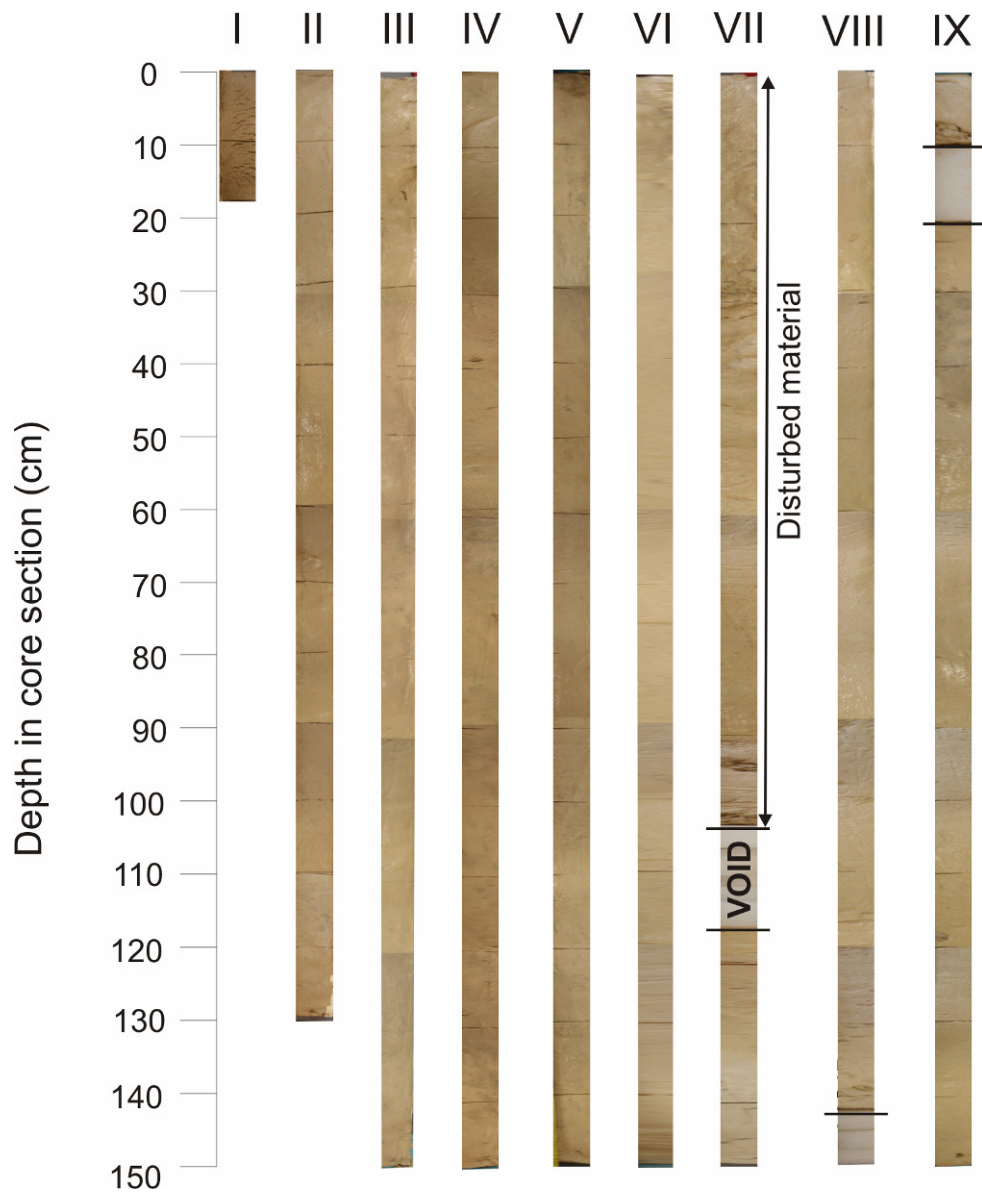


Figure 2.4 Core photographs of sections I – IX. Fine dark lines every 10cm are an artefact from core sampling. Each photograph is a composite of three images, stitched together electronically, leading to some colour artefacts. The bold black lines show the extent of the voids in the core, as labelled for the example in section VII. There are internal voids in sections VII and IX and a void at the end of section VIII. The grey colours of these sections arises from the presence of the polypropylene material that was used to infill the voids and support the sediment.

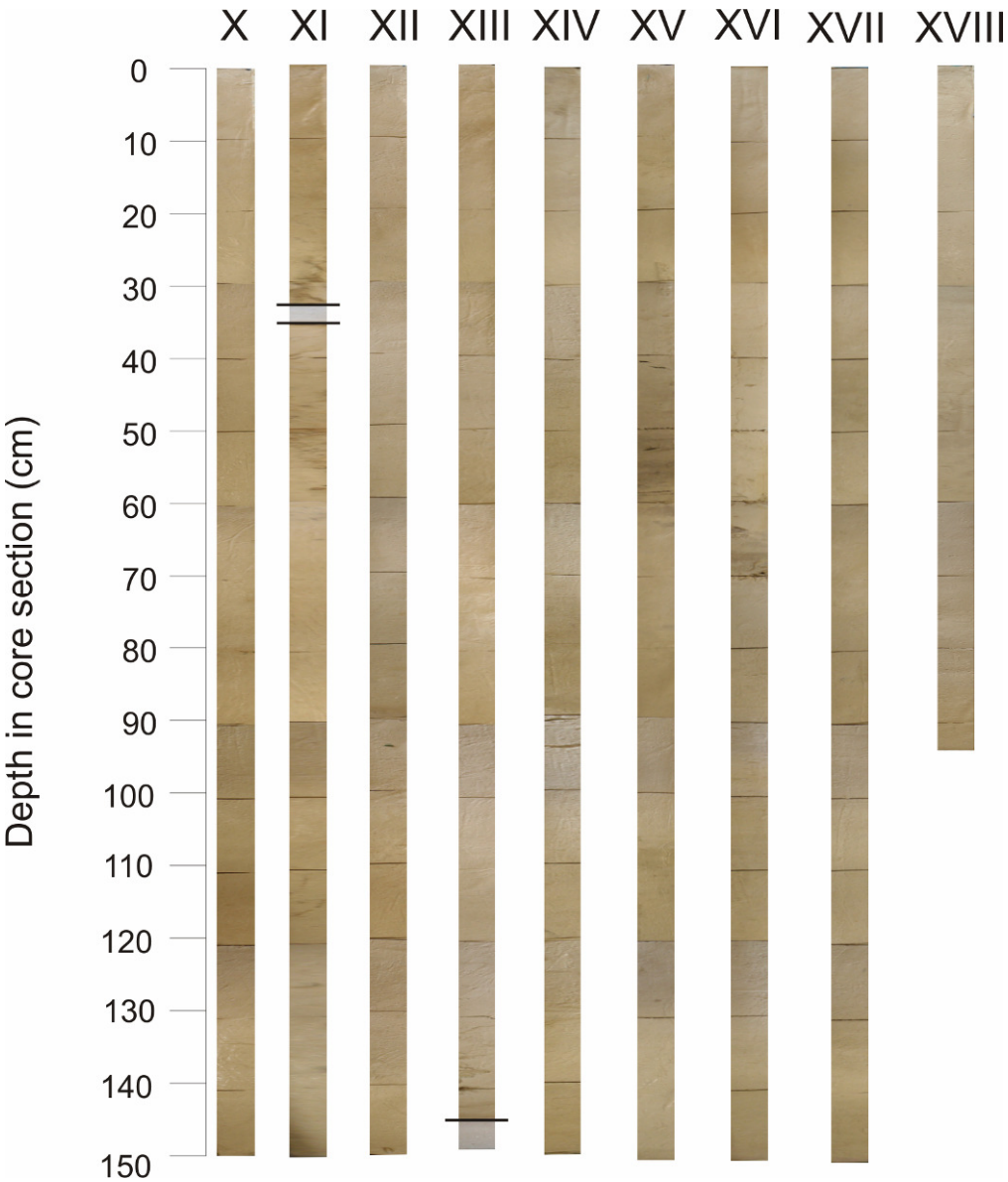


Figure 2.4 continued Core photographs of sections X – XVIII. There are internal voids in section XI and a void at the end of section XIII.

2.9 Core sedimentology

Estimates of dry and wet bulk sediment density were made at nine, evenly spaced, down-core intervals using both oven and freeze drying methods. The mean and one standard deviation range (1σ) of the wet bulk sediment densities was $1.3 \pm 1\sigma=0.2 \text{ g/cm}^3$ and for the dry bulk densities it was $0.8 \pm 1\sigma=0.2 \text{ g/cm}^3$. Neither measurement showed any systematic variation with depth in core or with drying method. The relatively large spread in values for both measurements is attributed principally to the fact that sample volumes were not measured separately for each sample and the assumption of a single volume for all samples leads to a significant volumetric uncertainty.

The material in the $>150\mu\text{m}$ fraction is dominated by planktic foraminifera of a characteristically tropical/subtropical assemblage (appendix 7 gives faunal counts at selected depth intervals). For the uppermost 350cm of the core and the interval 740-855cm composite core depth, detrital terrigenous material, principally in the form of carbonate fragments (coral/algal/bivalve material), but also as silicate mineral material (principally in the form of volcanic glass), is also present, although planktic foraminifera remain the dominate constituent. These layers also contain well preserved, characteristically shallow water, benthic foraminifera, such as *Elphidium crispum*, which are not present in the rest of the core. The layer at 740-855cm also shows pronounced visual evidence of vertical disturbance, as can be seen in section VII on *Figure 2.4*.

2.10 Indices of carbonate preservation

The modern regional lysocline depth in the NCT has been estimated to be at ~3100m water depth [Martinez, 1994]. Thus, the MD06-3018 core site at 2470m is ~700m shallower than the lysocline, which in turn lies above the sedimentary manifestation of carbonate dissolution, the Carbonate Compensation Depth. However, the position of the core site in relation to the Carbonate Compensation Depth may have varied back through time. In order to directly assess the state of carbonate preservation within the core, scanning electron microscope images of foraminifera from the core-top were examined, as were two quantitative down-core indices of carbonate preservation; namely, planktonic foraminiferal shell weights and bulk sediment weight% CaCO₃.

2.10.1 Scanning electron microscope images

Scanning electron microscope images of the planktic foraminiferal taxa *Globigerinoides ruber* (white) and the benthic taxa *Cibicides wuellerstorfi* from the MD06-3018 core-top were taken to visually examine the quality of carbonate preservation in the core. In all instances, there is no clear evidence of substantial dissolution, although un-cleaned samples of *G. ruber* show significant numbers of coccolith fragments adhering to the surface as can be seen in the higher resolution image on *Figure 2.5*.

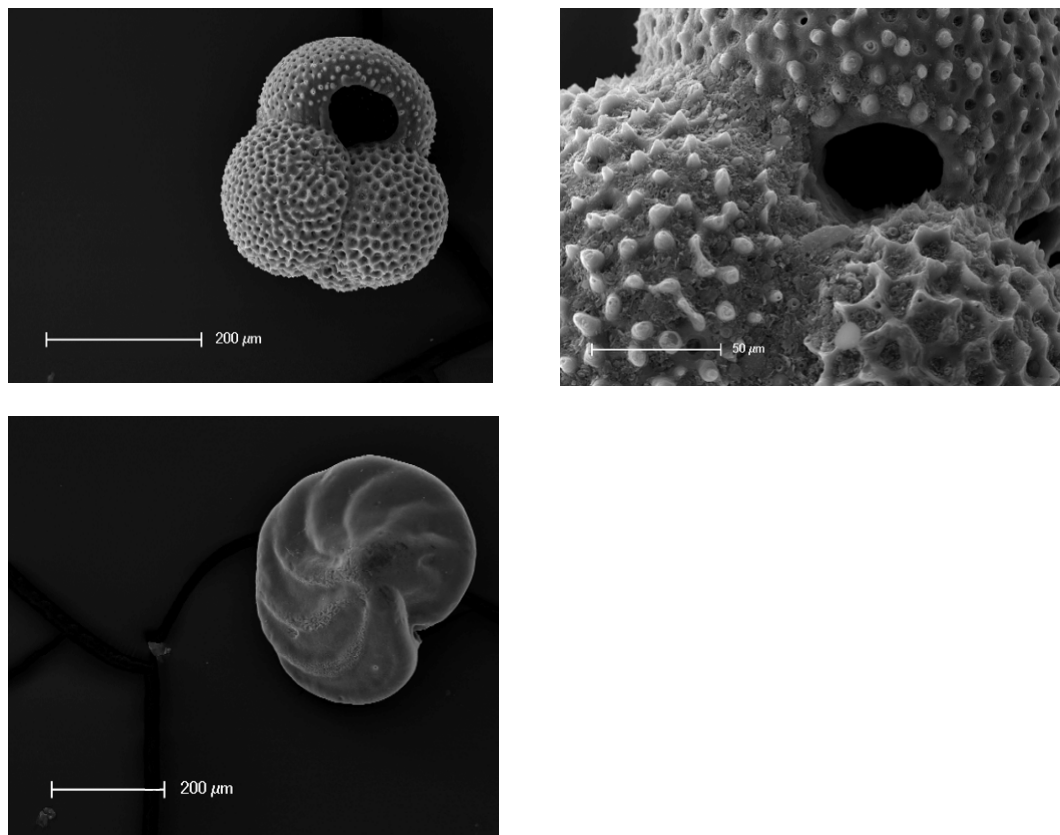


Figure 2.5 Scanning electron microscope images of specimens of *G. ruber* (upper two panels) and *C. wuellerstorfi* (lower panel) from the core-top.

2.10.2 Planktonic foraminifera shell weights

Specimens of *G. ruber* were picked from the 250-315 μ m size fraction from sixteen selected down-core depth intervals, corresponding to both glacial and interglacial stages. For each sample, $n \geq 10$ individuals were weighed and the mean and 1σ values calculated (Table 2.1). No systematic down-core trend is present in the data. Glacial stage values are slightly heavier on average than the interglacial stage ones, suggesting a slight improvement in preservation during glacial stages, but this difference lies within 1σ range of the data spread on either average.

Core depth CCD (cm)	Interglacial (I) / glacial (G) stage	Mean weight (μ g)	1σ (μ g)
20	I	11.2	2.9
80	G	12.9	3.4
485	I	9.3	1.4
575	G	9.3	2.6
740	I	10.9	3.0
760	G	12.6	3.1
985	I	10.1	1.9
1025	G	13.1	5.5
1354	I	12.7	2.8
1384	G	11.1	3.8
1664	I	15.7	3.9
1684	G	15.0	3.3
2118	I	13.5	3.6
2148	G	11.7	3.0
2368	I	11.4	3.3
2408	G	14.5	4.5
	Mean glacial	12.7	1.8
	Mean interglacial	11.8	1.9

Table 2.1 *G. ruber* shell weights for selected core, selected so as to correspond to various glacial and interglacial stages, pre-assuming the core age-model as defined in chapter 3, §7.

2.10.3 Sediment bulk weight% CaCO_3

Bulk weight% CaCO_3 was measured directly on 86 down-core samples using a UC Instruments CO_2 coulometer. Measurements of a carbonate reference material during each run indicated that the precision of the method is better than 5 weight%. Values do not show systematic down-core variability and always lie in the range 60–85 bulk weight% CaCO_3 , with the exception of one measurement at 2128cm (Fig 2.6A).

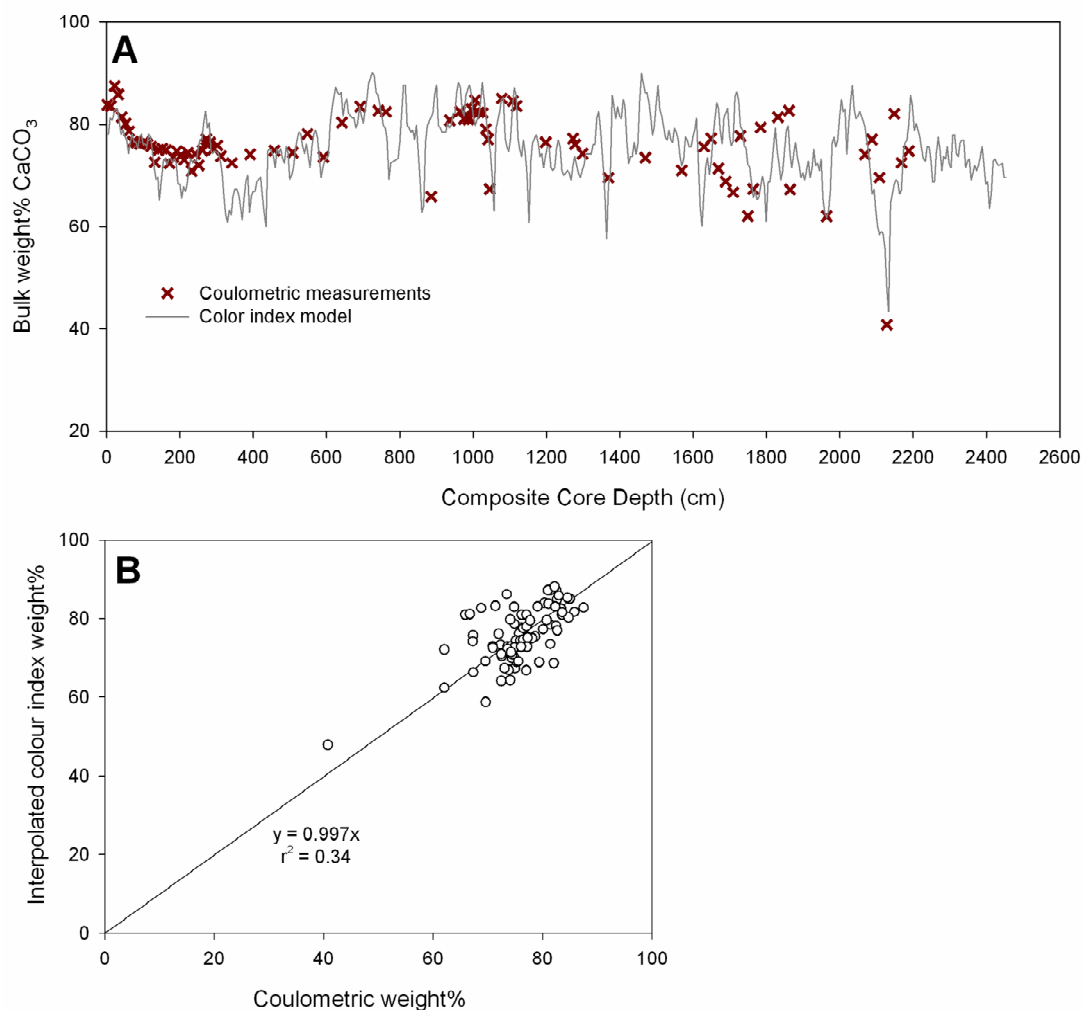


Figure 2.6 A) Down-core plot of bulk weight% CaCO_3 based on both coulometer measurements and values calculated from a colour index based model. B) Correlation plot of bulk weight% CaCO_3 values based on the two methods. Data is given at the coulometric data points and where a lightness index value was not available for that 1cm interval, a linearly interpolated value between the adjoining measurements was used. A linear regression trend-line (constrained to pass through the origin); its equation and correlation coefficient are also shown.

In order to provide a more continuous estimate of down-core bulk weight% CaCO₃ a complementary approach based on the extraction of a digital %lightness index at 5cm resolution from greyscale versions of the core photographs was also used. This lightness index was calibrated linearly to coulometric bulk weight% CaCO₃ over the upper 200cm of the core and the index was then extrapolated down-core (*Fig 2.6A*). Adjustments were made at core section boundaries to prevent discontinuities in photograph conditions (*Fig 2.4*) from affecting the index.

Whilst the lightness index method is prone to significant errors, an x-y correlation plot (*Fig 2.6B*) of the two methods at the coulometric data points (where a lightness index value was not available for that 1cm interval, a linearly interpolated value between the adjoining measurements was used) shows a reasonable correlation between the two methods (a correlation coefficient value of $r^2=0.3$ for a linear trend passing through the origin). Most importantly, the replication of the low coulometer bulk weight% CaCO₃ values at 2120-2130cm core depth in the lightness index suggests that the coulometer measurements do record the entire range of bulk weight% CaCO₃ values present in the core and that there are not any intervals with very low values that have been missed by the coulometric sampling resolution.

2.11 Discussion

MD06-3018 shows no evidence of erosional hiatuses or any significant changes in sediment colour across its 24.5m length. Even in the layers showing evidence of significant down-slope transport of material, planktonic foraminifera continue to form the main component of the >150 μ m size fraction. This suggests that pelagic sedimentation has always been the dominant source of material to the core site. However, during the intervals 0-350cm and 740-855cm composite core depth there is detectable evidence of a secondary influence from down-slope transport of material from the adjacent island and reef system. The bulk weight% CaCO₃ measurements (*Fig 2.6A*) do not show significant excursions over these intervals, presumably because much of the down-slope material is also of carbonate mineralogy. Two lines of evidence are used to justify the choice made in the subsequent age-model development (chapter 3, §7) to effectively remove the material in the section 740-855cm from the core age-model (i.e. to treat the sedimentation rate during this interval as being near infinite) but to retain the material in the section 0-350cm.

- The 740-855cm interval shows clear visual evidence of liquefaction and disturbance of the sediment, which is not seen for 0-350cm (*Fig 2.4*).
- The paleomagnetic inclination record for the core (*Fig 3.3*) shows a pronounced disturbance at the 740-855cm interval, indicating a ‘twist’ in the core and certainly an interval of interrupted sedimentation. No such variability is seen for the 0-350cm interval.

It seems likely, therefore, that the interval 740-855cm represents a down-slope slump, or possibly turbidite, deposit which led to both a much greater apparent sedimentation rate and significant vertical mixing over this interval. In contrast, the upper 350cm of the core shows a persistent, but much smaller, degree of down-slope transport, which evidently did not have the effect of compromising the isotope stratigraphy.

The foraminiferal shell weights, SEM images and bulk weight% CaCO₃ measurements all support the conclusion that carbonate preservation throughout the core is very good. The one exception may be during the interval 2120-2130cm where the core becomes darker in colour (visible ~65cm from the top of section XVI on *Fig 2.4*) and measured weight% CaCO₃ drops to ~40% (*Fig 2.6A*). This interval does not correlate with any inferred increase in down-slope transport and may represent a short carbonate dissolution event. However, neither the planktic and benthic stable isotope records, nor the trace-metal records show any perturbation in values beyond the glacial/interglacial rhythm over this interval (shown as the yellow bar on appendix 5), suggesting that if a dissolution event was indeed present, then it did not significantly affect the geochemical signatures of the foraminifera.

2.12 Conclusions

This chapter has shown that core MD06-3018 provides an excellent sedimentary archive for proxies of palaeoceanographic change at 23°S in the southern Coral Sea. The sedimentary mode at the core location, whilst not purely pelagic, is always dominated by the pelagic component. The secondary contribution from down-slope transport is temporally variable, generally decreases in importance down-core and does not compromise the core stratigraphy, except during one interval, which is interpreted as a slump deposit. Carbonate preservation within the core is also generally excellent and does not vary as a function of depth, meaning that the geochemical signatures housed within the core have the potential to provide reliable palaeoceanographic proxies. Now that the viability of the core as an archive of well preserved pelagic carbonate materials has been established, the following chapters will introduce a series of geochemical paleoceanographic reconstructions based on the foraminifera sampled from the core.

Chapter 3: Subtropical southwest Pacific deep water circulation across the Mid-Pleistocene Transition

Chapter abstract

The modern $\delta^{13}\text{C}_{\text{DIC}}$ distribution in subtropical southwest Pacific deep waters is consistent with a regional mixing regime between water masses of open Pacific Ocean and Tasman Sea origin. This mixing regime is reconstructed across the period of the Mid-Pleistocene Transition using a record of benthic foraminiferal $\delta^{13}\text{C}$ from sediment core MD06-3018 in the New Caledonia Trough. The relative influence on the mixing regime from open Pacific Ocean deep waters is seen to be significantly reduced during glacial in comparison to interglacial stages over the past 1100ka. The spatial $\delta^{13}\text{C}$ gradient in the Southern Ocean between deep waters entering the Tasman Sea and the open Pacific Ocean is shown to be consequently greater during glacial than interglacial stages but was generally reduced across the Mid-Pleistocene Transition.

3.1 Chapter overview



This chapter presents the benthic stable isotope records from MD06-3018. The $\delta^{18}\text{O}$ record is used, in conjunction with magnetic- and bio-stratigraphy, to define the core age-model which is then used throughout the remainder of the thesis. The $\delta^{13}\text{C}$ record is used to reconstruct aspects of deep water circulation in the NCT on both orbital and >100kyr time-scales. The work presented in this chapter is based closely on the following paper, which was published in 2009 with *Paleoceanography* and is included in its published form within the electronic version of thesis.

Russon, T., M. Elliot, C. Kissel, G. Cabioch, P. De Deckker, and T. Corrège (2009), Middle-Late Pleistocene Deep Water Circulation in the Southwest Subtropical Pacific, *Paleoceanography*, 24, PA4205. Copyright (2009) - American Geophysical Union.

All the lab-work, data analysis, interpretation and paper writing were the work of the author, except for the majority of the paleomagnetic lab-work and post-processing which were undertaken by paper co-author Kissel at the LSCE, France.

3.2 Introduction

The majority of the inorganic carbon in the ocean/atmosphere system resides in the deep waters of the global ocean. The modern residency time for these waters is of the order of 100-1000yrs, meaning that changes in deep water circulation have the potential to play a key role in driving and propagating climatic change on centennial, millennial [Elliot *et al.*, 2002; Pahnke and Zahn, 2005] and orbital timescales [Charles and Fairbanks, 1992; Archer *et al.*, 2000; Piotrowski *et al.*, 2005]. On the >100kyr timescale, changes in the mean state of regional and global deep water circulation regimes both contribute to and are diagnostic of different states in the evolution of Plio-Pleistocene climate [Raymo *et al.*, 1997].

Past deep water circulation patterns may be reconstructed using proxy measurements of chemical properties characteristic of certain water masses. One such proxy is measurements of $\delta^{13}\text{C}_{\text{benthic}}$ which, in certain taxa at least, reflects the isotopic composition of Dissolved Inorganic Carbon ($\delta^{13}\text{C}_{\text{DIC}}$) in the overlying water mass. The $\delta^{13}\text{C}_{\text{DIC}}$ of deep water depends on the chemistry of the source region for that water mass and $\delta^{13}\text{C}_{\text{benthic}}$ measurements can therefore potentially be used to reconstruct past water mass distributions. However, deep water $\delta^{13}\text{C}_{\text{DIC}}$ is also affected by whole ocean chemistry changes on a range of timescales. On Pleistocene glacial/interglacial timescales, fluctuations in the terrestrial biomass lead to mean ocean $\delta^{13}\text{C}_{\text{DIC}}$ changes [Shackleton, 1977; Crowley, 1995]. During the MPT, global mean ocean $\delta^{13}\text{C}_{\text{DIC}}$ shows a ~500kyr perturbation on the >100kyr time-scale towards more negative values [Raymo *et al.*, 1997].

The deep open Pacific Ocean is the largest reservoir of DIC on the planet and Pleistocene records of deep equatorial Pacific $\delta^{13}\text{C}_{\text{benthic}}$ show the lowest amplitude of glacial/interglacial variability of any major ocean basin [Raymo *et al.*, 1997], with values close to estimates of the mean ocean glacial/interglacial $\delta^{13}\text{C}_{\text{DIC}}$ change [Crowley, 1995]. In the modern open Pacific circulation regime, all deep water masses originate from the Southern Ocean, as there is no ventilation of deep waters anywhere in the Pacific itself. However, reconstructions of Pacific-wide $\delta^{13}\text{C}_{\text{DIC}}$

distributions at the Last Glacial Maximum (LGM) suggest that a very different circulation regime may have been active, possibly involving the ventilation of deep waters in the North Pacific [Curry *et al.*, 1988; Keigwin, 1998] and/or radical changes in Southern Ocean deep water formation and circulation [Michel *et al.*, 1995; Ninnemann and Charles, 2002; Hodell *et al.*, 2003]. In the modern Southern Ocean, the Antarctic Circumpolar Current effectively homogenizes deep waters down to the sea floor, but at the LGM reconstructions suggest that enhanced vertical $\delta^{13}\text{C}_{\text{DIC}}$ gradients existed in the region [Hodell *et al.*, 2003]. Such an increase in the stratification of the deep Southern Ocean is potentially an important mechanism in lowering glacial stage pCO_2 [Toggweiler, 1999; Sigman and Boyle, 2000; Hodell *et al.*, 2003].

The subtropical southwest Pacific is a bathymetrically complex region, bounded to the north and east by the basins of the open Pacific and to the south and west by that of the Tasman Sea, which opens in turn into the Southern Ocean. In the modern deep water circulation regime, water masses from the Central Pacific Basin, Tasman Sea and Southwest Pacific Basin all enter the subtropical southwest Pacific region (*Fig 3.1*) leading to a deep water mixing regime sensitive to the chemistry of both open Pacific Ocean and Tasman Sea deep waters [Wyrski, 1961; Warren *et al.*, 1994; Tsimplis *et al.*, 1998]. This chapter evaluates how the subtropical southwest Pacific deep water mixing regime has evolved across much of the Pleistocene, specifically whether it is variable between glacial and interglacial stages and whether it persists across the shift in dominant glacial/interglacial climatic mode that occurred during the MPT. In order to do this, it is first demonstrated that the modern $\delta^{13}\text{C}_{\text{DIC}}$ chemistry of regional deep waters is consistent with the modern mixing regime. The $\delta^{13}\text{C}_{\text{benthic}}$ record from MD06-3018, at 2470m depth in the NCT, in comparison with other regional records, is then used to reconstruct the relative influences of open Pacific Ocean and Tasman Sea deep waters on the mixing regime. Finally, reconstruction of the mixing regime allows constraints to be placed on past deep water chemical gradients between the different regions of the Southern Ocean from which the Tasman Sea and open Pacific Ocean deep waters originate.

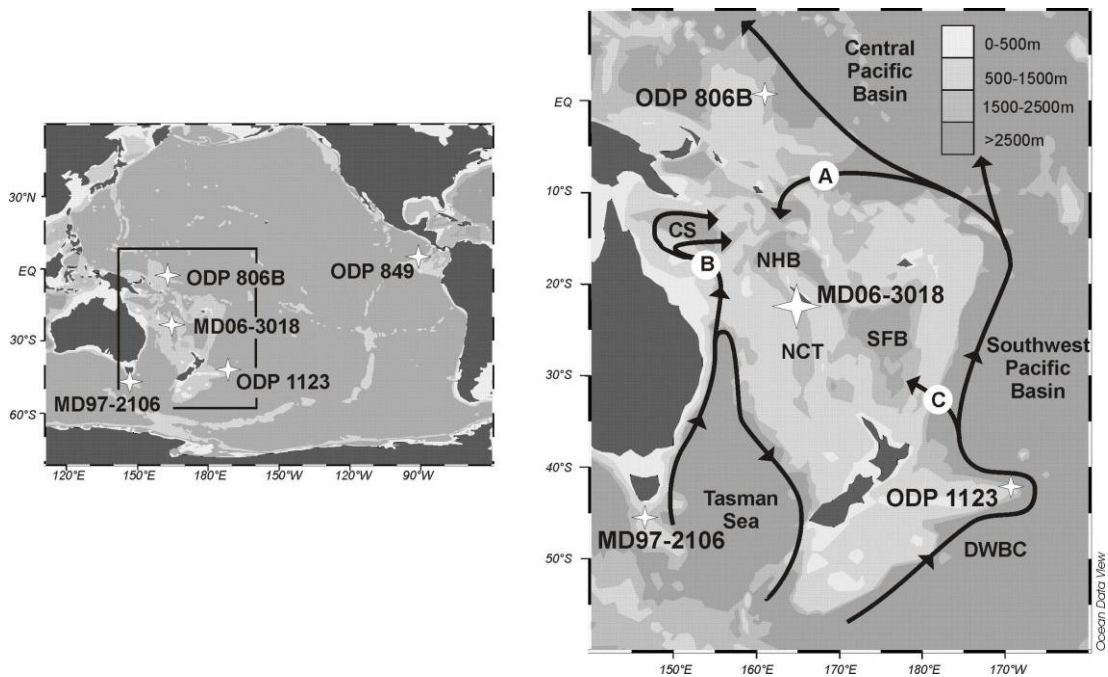


Figure 3.1 **Left panel:** Map of the Pacific Ocean region with core locations mentioned in text. Details of core locations are given in *Table 3.2*. **Right panel:** Simplified bathymetric map of the subtropical southwest Pacific region with the location of cores MD06-3018, ODP 1123 and ODP 806B. Bathymetry from WOCE Ocean Atlas [WOCE, 2002; Talley, 2007] viewed in ODV software [Schlitzer, 2007]. Arrows indicate dominant directions of bottom water flow, adapted from [Sokolov and Rintoul, 2000]. Lettered arrows refer to flow paths described in text. Abbreviations not given in *Figure 2.1* are as follows: SFB = South Fiji Basin, CS= Coral Sea Basin, DWBC = Deep Western Boundary Current.

3.3 Modern deep water circulation and mixing in the subtropical southwest Pacific

The Southern Ocean is the ultimate source of all modern deep waters in both the open Pacific Ocean and the Tasman Sea. These deep waters enter the basins of the open Pacific principally via the Deep Western Boundary Current (DWBC) in the Southwest Pacific Basin [Whitworth *et al.*, 1999] (*Fig 3.1*). The deep water entering both the Pacific DWBC and the southern Tasman Sea consists of Lower Circumpolar Deep water (LCDW) overlain by Upper Circumpolar Deep Water (UCDW). LCDW is characterized by salinities of 34.71–34.73 and dissolved oxygen concentrations of $\sim 200\mu\text{mol/kg}$. It may be subdivided into upper LCDW (*uLCDW*), characterized by a salinity maximum related to the presence of relict North Atlantic Deep Water [Gordon, 1975; Warren, 1981; Wijffels *et al.*, 2001] and lower LCDW (*lLCDW*) which consists of Southern Ocean origin deep and bottom-waters [Rintoul, 1998]. The northward flow of LCDW is kept balanced on a Pacific-wide scale by the net southward return flow at depths of 1500-3000m of chemically aged North Pacific Deep Water (NPDW), which is characterized by salinities of 34.65-34.66 and much lower dissolved oxygen concentrations of $<150\mu\text{mol/kg}$ [Reid, 1997]. UCDW has similar properties to NPDW as it consists of re-circulated NPDW and Indian Ocean deep waters that have been entrained into the DWBC [Gordon, 1975; McCave *et al.*, 2008].

Deep waters below $\sim 2000\text{m}$ in the NCT are net-southward flowing and enter from the New Hebrides Basin [Wyrki, 1961; Reid, 1997; Tsimplis *et al.*, 1998] (*Fig 3.1*). They are characterized at 2500m depth by salinities of ~ 34.68 and dissolved oxygen concentrations of $\sim 160\mu\text{mol/kg}$ (as represented by station P06-215 on *Fig 3.2C*). The dominant modern deep water inflow to the New Hebrides Basin is from the Central Pacific Basin (arrow A, *Fig 3.1*) to which it is open down to depths of 3000m [Sokolov and Rintoul, 2000; Wijffels *et al.*, 2001]. Central Pacific Basin Deep Water (CPBDW) in the depth range 2000-3000m is characterized by salinities of 34.65-34.66 and dissolved oxygen concentrations of 130-140 $\mu\text{mol/kg}$, consistent with a UCDW/NPDW origin (*Fig 3.2C*). The NCT deep water properties are,

however, too chemically ‘young’ (i.e. relatively enriched in dissolved oxygen) and too saline to be explained purely from an open Pacific Ocean source. Instead, NCT deep waters represent the product of a mixing regime between deep waters from the open Pacific Ocean and those from the Tasman Sea (arrow B, *Fig 3.1*), as first described by *Wyrcki* [1961].

The Tasman Sea inflow to the subtropical southwest Pacific occurs over a sill depth at 2850m into the Coral Sea [*Wijffels et al.*, 2001] and is poorly constrained volumetrically, having been estimated as both 0.05Sv [*Wyrcki*, 1961] and 3.0Sv [*Sokolov and Rintoul*, 2000]. The contact between UCDW/NPDW and *u*LCDW is substantially shallower in the Tasman Sea than in the DWBC region (*Fig 3.2C*). This means that the deep waters entering the subtropical southwest Pacific from the Tasman Sea at ~2500m depth lie close to the core of the Tasman Sea *u*LCDW, with salinities of ~34.72 dissolved oxygen concentrations of ~180 μ mol/kg (as seen at station P06-234 on *Fig 3.2C*). The influence of the chemically younger and more saline Tasman Sea deep water is seen to decline eastwards across the subtropical southwest Pacific region but remains detectable in the New Hebrides Basin and the NCT [*Wyrcki*, 1961]. Following this early work by *Wyrcki*, subsequent conservative tracer measurements, taken as part of the SCORPIO and WOCE projects [*Warren*, 1973; *Tsimplis et al.*, 1998; *Sokolov and Rintoul*, 2000; *Wijffels et al.*, 2001], have not changed this basic picture although the South Fiji Basin has been shown to receive a small (~0.2Sv) inflow (arrow C on *Fig 3.1*) of DWBC water directly from the Southwest Pacific Basin over a sill depth of less than 2500m [*Warren et al.*, 1994].

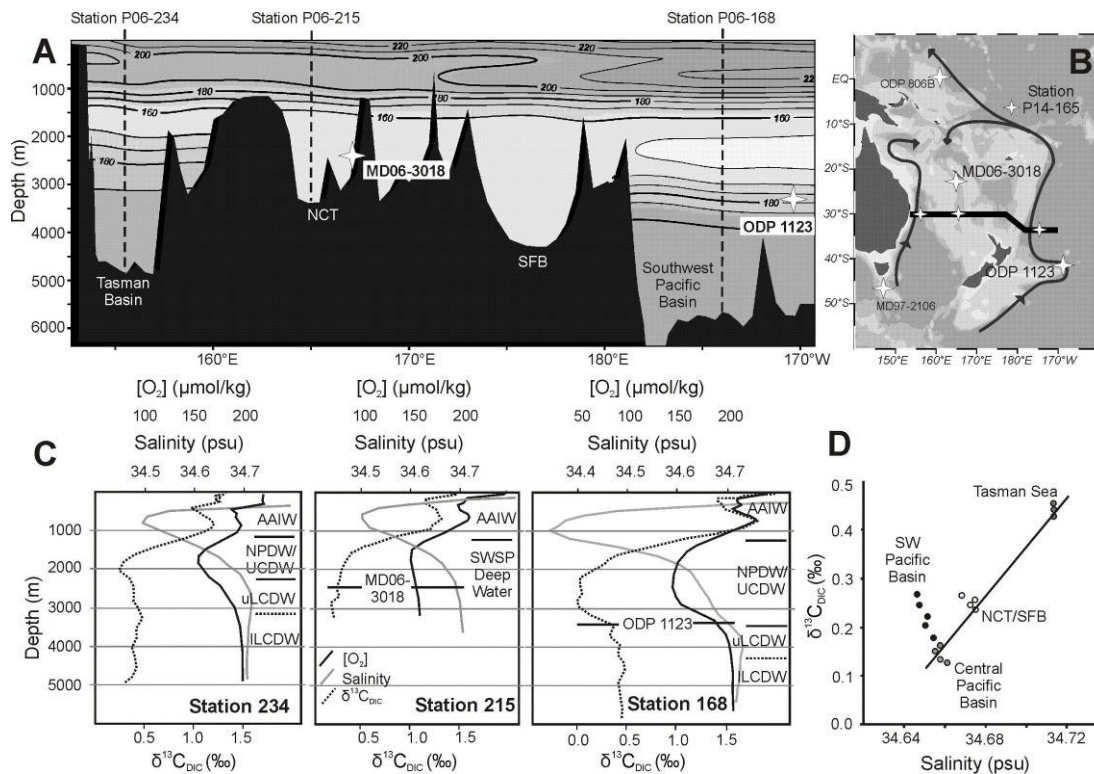


Figure 3.2 A) Dissolved $[O_2]$ section across the subtropical southwest Pacific region along WOCE P06W section line. The longitudinal positions and water depths of MD06-3018 and ODP 1123 are shown although both core sites are off the section line. B) Location of WOCE P06W section line (bold line) and WOCE stations (white stars) referred to in the text in relation to the dominant deep water pathways. C) Dissolved $[O_2]$ (solid black lines), salinity (solid grey lines) and $\delta^{13}C_{DIC}$ (dotted lines) profiles from the Tasman Sea (Station P06-234), NCT (station P06-215) and the Southwest Pacific Basin (station P06-168). The main intermediate and deep water masses as seen in $[O_2]$ and salinity are highlighted. D) Scatter plot and mixing line plot of salinity against $\delta^{13}C_{DIC}$ at $2500 \pm 100\text{m}$ depth for WOCE P06W, P14S and P15S stations with available $\delta^{13}C_{DIC}$ measurements. The line represents a two end-member mixing regime of Central Pacific Basin and Tasman Sea water. CTD and bottle data from the WOCE Pacific Ocean Atlas [McTaggart *et al.*, 1994; McTaggart and Johnson, 1997; Tsimplis *et al.*, 1998; Johnson *et al.*, 2001; Wijffels *et al.*, 2001; WOCE, 2002; Key *et al.*, 2004; Talley, 2007] viewed in ODV software [Schlitzer, 2007].

3.4 Modern deep water mass $\delta^{13}\text{C}_{\text{DIC}}$ in the subtropical southwest Pacific

Deep water masses may potentially be characterized by their $\delta^{13}\text{C}_{\text{DIC}}$ signatures due to variations in the isotopic composition of the source regions for the deep waters and the general inverse relationship between $\delta^{13}\text{C}_{\text{DIC}}$ and nutrient concentrations [Kroopnick, 1985; Duplessy *et al.*, 1988; Charles and Fairbanks, 1992]. Comparison of modern $\delta^{13}\text{C}_{\text{DIC}}$, dissolved oxygen and salinity measurements from WOCE stations in the subtropical southwest Pacific region demonstrates that the same deep water masses definable on the basis of the conservative tracers are also visible in the corresponding $\delta^{13}\text{C}_{\text{DIC}}$ profiles (Fig 3.2C).

Modern $\delta^{13}\text{C}_{\text{DIC}}$ values at 2500m depth in the NCT (represented by station P06-215) are 0.25‰, with an analytical uncertainty of ± 0.03 ‰. These are similar to the values of 0.23‰ seen at the same depth and latitude in the Southwest Pacific Basin (station P06-168). The direct deep water inflow from the Southwest Pacific Basin into the subtropical southwest Pacific (arrow C, Fig 3.1) cannot account for this similarity as it occurs over a sill depth shallower than 2500m [Warren *et al.*, 1994]. Instead, the dominant inflow from the open Pacific occurs through the Central Pacific Basin (arrow A, Fig 3.1). Deep water at 2500m depth in the Southwest Pacific and Central Pacific Basins becomes progressively lighter in $\delta^{13}\text{C}_{\text{DIC}}$ towards the equator due principally to the increasing relative influence of NPDW over UCDW (Fig 3.2D). The values of 0.12‰ seen in CPBDW (station P14-165) are significantly lighter than those seen in the NCT. Thus, as with the conservative tracers, the NCT $\delta^{13}\text{C}_{\text{DIC}}$ values cannot be explained from a purely open Pacific deep water source. The positive NCT deep water $\delta^{13}\text{C}_{\text{DIC}}$ values do not arise from vertical mixing with AAIW ($\delta^{13}\text{C}_{\text{DIC}} \sim 1$ ‰) as there is no evidence for downward penetration of the AAIW salinity minima to depths of 2500m at Station P06-215. However, modern $\delta^{13}\text{C}_{\text{DIC}}$ values in northern Tasman Sea deep waters at 2500m (*u*LCDW) are 0.42‰ (station P06-234), sufficiently positive to provide a viable second end-member to the deep water mixing regime.

The regional mixing relationship derived from the $\delta^{13}\text{C}_{\text{DIC}}$ values along the isopycnal corresponding to water at 2500m depth in the NCT is consistent with that seen for the corresponding salinities (*Fig 3.2D*). This suggests that proxy records of past deep water $\delta^{13}\text{C}_{\text{DIC}}$ may be used as a pseudo-conservative tracer to reconstruct the regional mixing regime. Using this simple linear model, modern NCT deep waters are seen to be a roughly 2:1 admixture of Central Pacific Basin UCDW/NPDW and Tasman Sea *u*LCDW.

3.5 Methods

3.5.1 Benthic foraminiferal stable isotope measurements

Mono-specific samples of the epibenthic foraminifera *Cibicides wuellerstorfi* (3-6 individuals from the >315 μm size fraction) were picked under the microscope and subsequently cleaned for 10s in an ultrasonic bath with methanol. Samples were analyzed with a Thermo Electron Delta+ Mass Spectrometer with Kiel Preparation Device in the School of GeoSciences, University of Edinburgh for $\delta^{18}\text{O}$ and $\delta^{13}\text{C}$. Long term accuracy (two standard deviations of standard measurements made against an internal standard calibrated to NBS19) of the device over May 2006 to October 2008 was $2\sigma_{\text{a}} = 0.18\text{‰}$ for $\delta^{18}\text{O}$ and 0.16‰ for $\delta^{13}\text{C}$. The term $2\sigma_{\text{a}}$ provides a measure of the analytical uncertainty. Replicate analyses ($3 < n < 6$) were performed at six intervals down-core, and the short-term measurement reproducibility was always better than $2\sigma_{\text{r}} = 0.26\text{‰}$ for $\delta^{18}\text{O}$ and $2\sigma_{\text{r}} = 0.32\text{‰}$ for $\delta^{13}\text{C}$. The term $2\sigma_{\text{r}}$ provides a measure of the sample reproducibility uncertainty. *C. wuellerstorfi* $\delta^{18}\text{O}$ values are corrected by the standard $+0.64\text{‰}$ to account for disequilibrium with the surrounding seawater [*Shackleton and Opdyke, 1973*]. The underlying principles and limitations of the $\delta^{18}\text{O}$ and $\delta^{13}\text{C}$ proxy systems are discussed in appendix 1, §1 and §2 respectively. Full details of the stable isotope sample preparation and analysis methodology may be found in appendix 3. The full down-core data-sets used in this chapter are tabulated in appendix 4.

3.5.2 Magnetic measurements

Measurements of natural remnant magnetization were made on u-channel samples taken in the central part of the half core. The measurements were performed in the shielded room at the Laboratoire des Sciences du Climat et de l'Environnement using the 2G-pass-through cryogenic magnetometer equipped with high resolution coils. Measurements were taken every 2cm with a resolution of 4cm inducing a slight smoothing of the signal. The data from the extreme 3cm at the ends of each core section are not presented due to edge-effects. The natural remnant magnetization was stepwise demagnetized at 5, 10, 15, 20, 25, 30, 35, 40, 45, 50, 60 and 80 mT. The Characteristic Remnant Magnetization (ChRM) was then determined using principal component analysis [Mazaud, 2005]. Nine steps out of thirteen have been taken into account to define the ChRM with mean angular deviations ranging between 5° and 10° (a few horizons reach 20°).

3.6 Results

3.6.1 Benthic foraminiferal stable isotopes measurements

The $\delta^{18}\text{O}_{\text{benthic}}$ record (*Fig 3.3A*) shows a succession of well-defined cycles on the 50-250cm scale with average amplitude of 1.2‰ in the section 0-1100cm and amplitudes in the range 0.5-0.7‰ below 1100cm. The running mean value (250cm linear smoothing using a box-car method) of $\delta^{18}\text{O}_{\text{benthic}}$ is in the range $4.15 \pm 0.15\text{‰}$ across the length of the record. The $\delta^{13}\text{C}_{\text{benthic}}$ record (*Fig 3.3B*) shows variability on the 50-250cm scale with average amplitude of 0.8‰ in the section 0-1250cm and average amplitude of 0.5‰ below 1250cm. The running mean value (250cm linear smoothing using a box-car method) of $\delta^{13}\text{C}_{\text{benthic}}$ is in the range $0.25 \pm 0.15\text{‰}$ across the sections 0-1250cm and 1800-2450cm but undergoes a negative perturbation towards a minimum value of 0.0‰ during the intervening section.

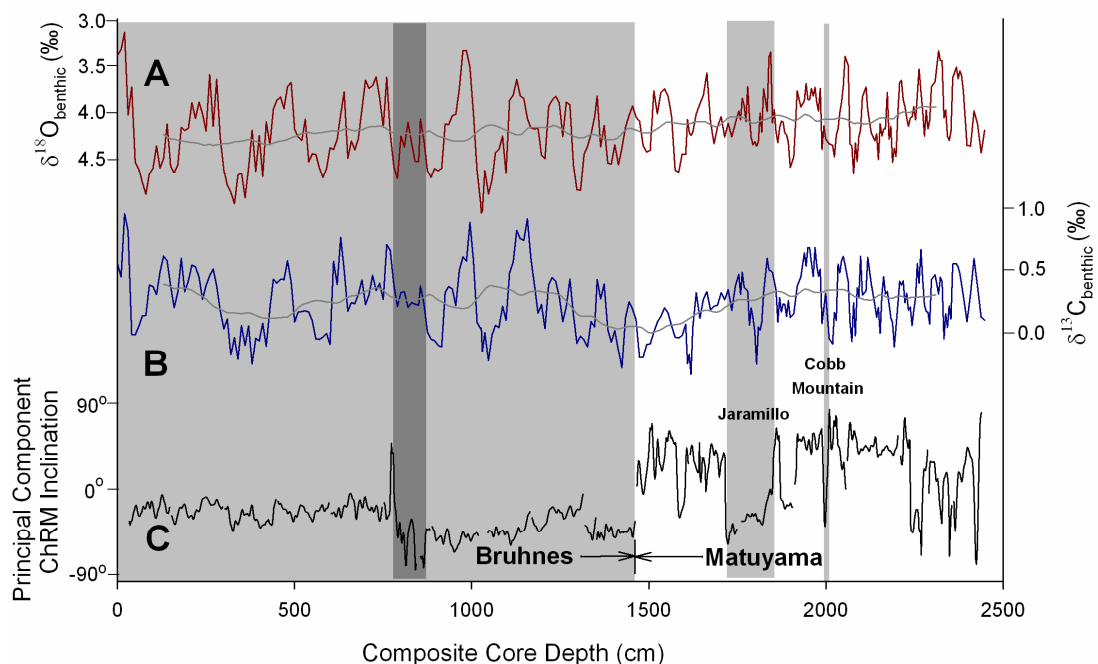


Figure 3.3 Plot of **A**) $\delta^{18}\text{O}_{\text{benthic}}$, (grey line is 250cm linear smoothed mean value), **B**) $\delta^{13}\text{C}_{\text{benthic}}$ (grey line is 250cm linear smoothed mean value) and **C**) Principal Component of ChRM Inclination from MD06-3018 against depth. The position of identified magnetic reversals and events are highlighted with light grey boxes representing periods of normal polarity. The dark grey box at 755-840cm depth highlights a period of disturbed sedimentation.

3.6.2 Magnetic measurements

The ChRM Inclination record (*Fig 3.3C*) shows a series of reversals between positive (reversed polarity) and negative (normal polarity) inclination. The section between the core-top and 1500cm has consistently negative inclination and corresponds to the Bruhnes Chron followed by a period of overall positive inclination corresponding to the Matuyama Chron. Within the Matuyama Chron, the beginning and end of the Jaramillo reversal and the mid-point of the shorter Cobb Mountain reversal are identified.¹

¹ The magnetic chronology used is that of *Cande and Kent* [1995], as based upon the ODP Site 677 and DSDP Site 607 records of *Shackleton et al.* [1990]. Other events in the MD06-3018 record may be related to events shown in the ODP 980-984 stratigraphies [*Laj and Channell*, 2007].

3.7 MD06-3018 age-model

An age-model for MD06-3018 was developed based on both the magnetic stratigraphy (*Fig 3.3C*) and tuning of the $\delta^{18}\text{O}_{\text{benthic}}$ record to the LR04 stack [*Lisiecki and Raymo, 2005*] (*Fig 3.4A*) using the Analyseries software package [*Paillard et al., 1996*]. The consistently greater amplitude of glacial/interglacial $\delta^{18}\text{O}_{\text{benthic}}$ variability seen in the LR04 record, relative to MD06-3018, is attributable to the different temporal resolutions of the two records. The orbital age-model yields average sedimentation rates of 25mm/ka in the upper 750cm of the core and 15mm/ka in the section below this. Comparison of the orbital age-model with the magnetic tie-points shows consistency to within $\pm 10\text{kyr}$, which is less than one quarter of an obliquity cycle, at the depth of each magnetic reversal (*Fig 3.4B, Table 3.1*). An additional tie-point at 280cm based on the disappearance of *Globigerinoides ruber* (pink) from the Pacific at 120ka [*Thompson et al., 1979*] is also in close agreement with the orbital model.

As discussed in chapter 2, the interval 740-855cm shows signs of enhanced vertical mixing in the physical properties of the core, the presence of shallow-water benthic foraminifera taxa, perturbations to the ChRM Inclination record and a lack of reproducibility in the $\delta^{18}\text{O}_{\text{benthic}}$ measurements (*Fig 3.3*). The data from this interval is likely to be significantly contaminated with down-slope signals and is excluded from the development of the core age-model as shown in *Figure 3.4*. The core section below 2230cm also shows high variability in the ChRM Inclination record not associable with any known magnetic event but without additional accompanying evidence of sediment disturbance, leading to a reduction in age-model confidence below 2230cm (1360ka). The benthic stable isotope sampling resolution based on the core age-model is $\sim 5\text{kyr}$ and each 1cm sample thickness represents time-averaging of 450-600yrs. When plotted against the core age-model the $\delta^{18}\text{O}_{\text{benthic}}$ data (*Fig 3.5A*) allows the identification of Marine Isotope Stages (MIS)² as far back as MIS 51, with the core bottom being at 1550ka.

² The term Marine Isotope Stage refers to the maxima (glacial stages, denoted by even MIS numbers) and minima (interglacial stages, denoted by odd MIS numbers) in the $\delta^{18}\text{O}$ stratigraphy. The numbering convention used here follows that of *Lisiecki and Raymo, 2005*.

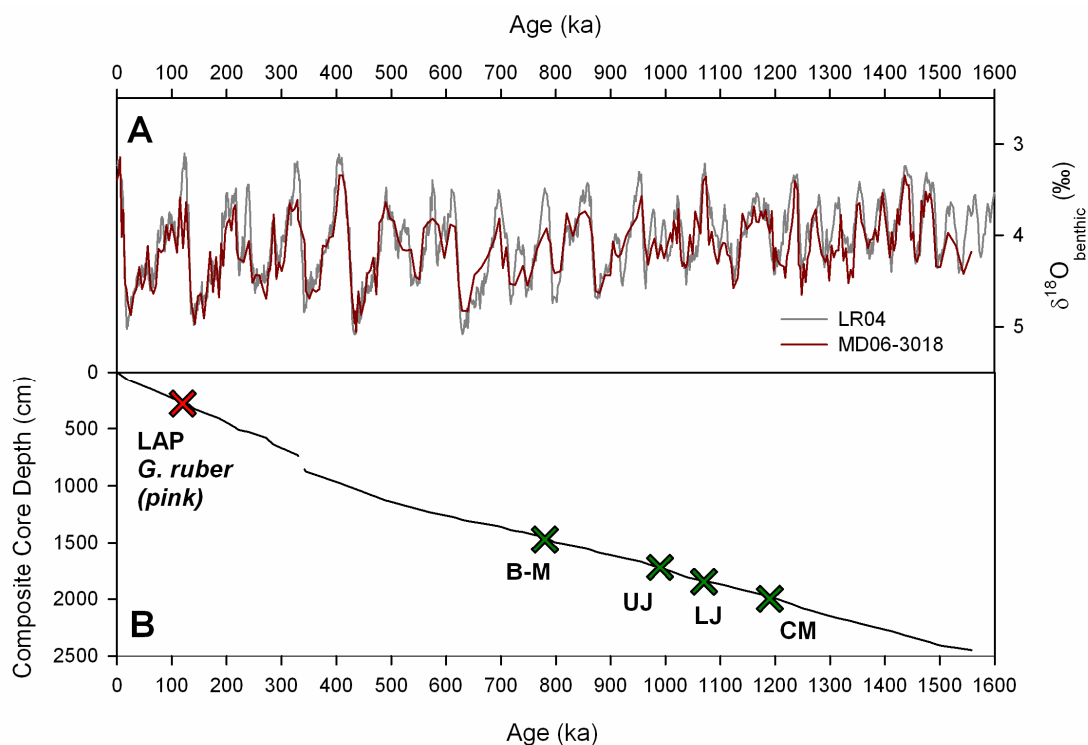


Figure 3.4 A) Comparison of $\delta^{18}\text{O}_{\text{benthic}}$ from LR04 and MD06-3018 used in development of tuned age-model. B) Line shows the LR04-derived age-model. Crosses represent the four identified magnetic tie-points (B-M = Bruhnes-Matuyama, UJ = Upper Jaramillo, LJ = Lower Jaramillo, CM = mid-point of the Cobb Mountain event) and the Last Appearance (LAP) of *G. ruber* (pink). Gap in the age-model arises from the interval of disturbed sedimentation at 740-855cm.

Magnetic event	Depth in core (cm CCD)	Age based on orbital age model (ka)	Age from <i>Cande and Kent</i> [1995] stratigraphy (ka)
B-M	1469	789	780
UJ	1717	988	990
LJ	1848	1078	1070
CM	1994	1200	1190

Table 3.1 Comparison of the ages predicted by the MD06-3018 orbital age-model with those of the magnetic reversal intervals identified in *Figure 3.3*. Acronyms in the first column are as given in *Figure 3.4*.

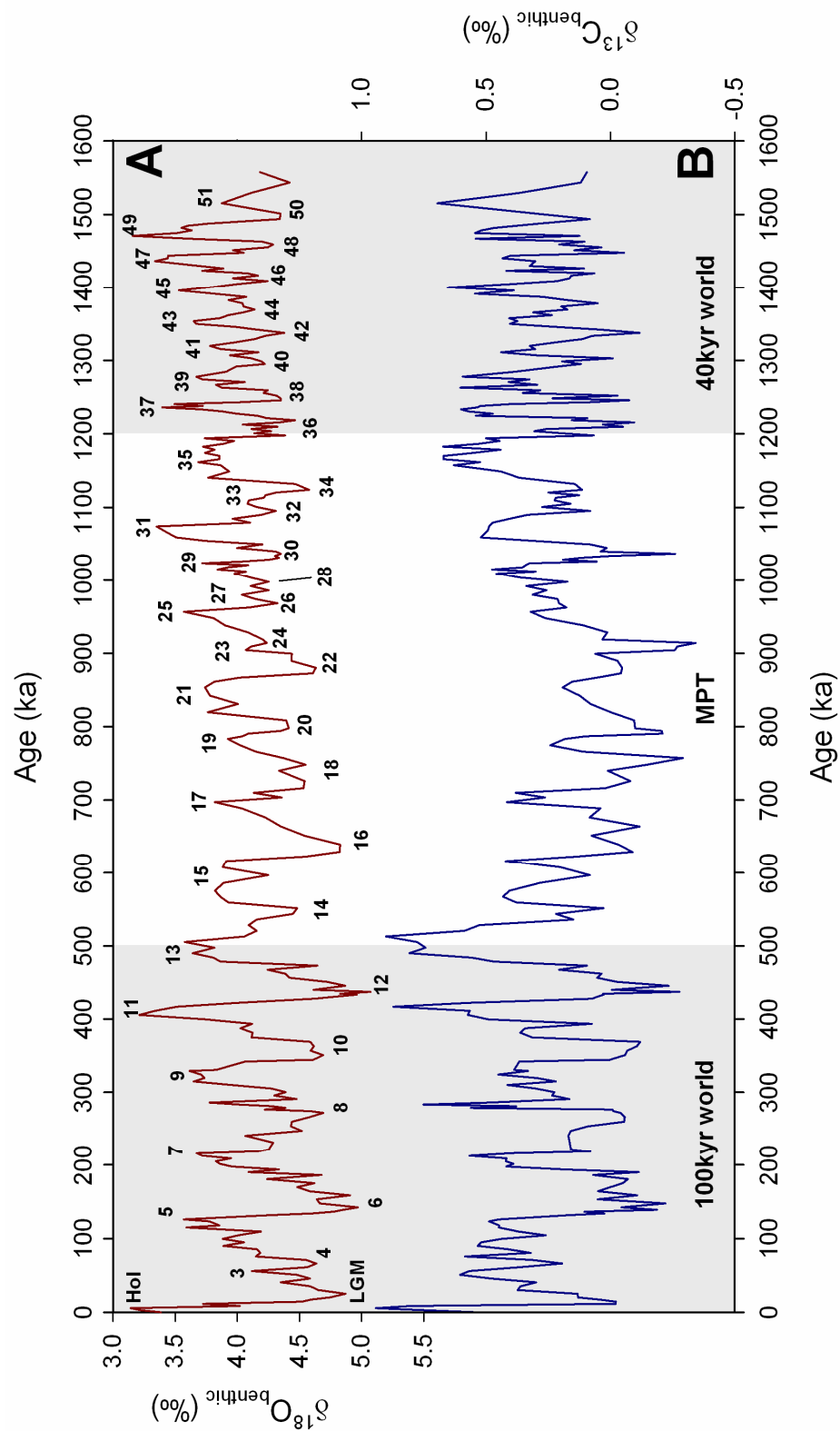


Figure 3.5 MD06-3018 *C. wuellerstorfi* stable isotope plots against the core age-model. **A)** $\delta^{18}\text{O}_{\text{benthic}}$, with numbers showing MIS. Hol = Holocene, equivalent to MIS 1, LGM is equivalent to MIS 2. **B)** $\delta^{13}\text{C}_{\text{benthic}}$. The MPT interval, *sensu* Head and Gibbard [2005], is shown by background shading.

3.8 Discussion

3.8.1 Does $\delta^{13}\text{C}_{\text{benthic}}$ at site MD06-3018 record $\delta^{13}\text{C}_{\text{DIC}}$?

The $\delta^{13}\text{C}_{\text{benthic}}$ value of *C. wuellerstorfi* tests is widely held to be a reliable direct recorder of bottom-water $\delta^{13}\text{C}_{\text{DIC}}$ [Shackleton and Opdyke, 1973; Curry and Lohmann, 1982; Duplessy et al., 1984; McCorkle and Keigwin, 1994]. The absence of an absolute age for the core-top in MD06-3018 means that direct verification of this relationship at the core site is not possible. An average of four $\delta^{13}\text{C}_{\text{benthic}}$ measurements with age-model values in the range 5-0ka yields a late Holocene value of $0.56 \pm \sigma_{\text{SEM}}=0.08\text{‰}$ (Standard Error on the Mean, $\sigma_{\text{SEM}}=\sigma_r/\sqrt{n}$) an offset of $+0.31 \pm \sigma_{\text{diff}}=0.09\text{‰}$ (standard error on difference, $\sigma_{\text{diff}}=\sqrt{(\sigma_1^2+\sigma_2^2)}$, $\sigma_{1,2}$ is taken as σ_r for single proxy measurements and σ_{SEM} for averaged proxy measurements, unless stated otherwise) from the nearest $\delta^{13}\text{C}_{\text{DIC}}$ measurement at WOCE Station P06-215. Apparent offsets of similar magnitude have been described in other southwest Pacific cores [McCave et al., 2008]. However, in all these cases, in the absence of both core-top material and more local $\delta^{13}\text{C}_{\text{DIC}}$ measurements, there is no clear basis for the application of a down-core offset.

Two effects that have been documented to lead to a break-down in the $\delta^{13}\text{C}_{\text{DIC}}$ to $\delta^{13}\text{C}_{\text{benthic}}$ relationship are carbonate dissolution and productivity overprints [Mackensen et al., 1993; McCorkle and Keigwin, 1994]. The core-site of MD06-3018 is not affected significantly by dissolution as it is situated ~600m above the modern lysocline depth in the NCT [Martinez, 1994]. Measurements of $\delta^{13}\text{C}_{\text{benthic}}$ made in *C. wuellerstorfi* from modern or past environments with high overlying productivity have been shown to yield considerable negative excursions from $\delta^{13}\text{C}_{\text{DIC}}$ [Mackensen et al., 1993]. Whilst the subtropical southwest Pacific is a fairly oligotrophic region there is an upwelling zone along the axis of the western New Caledonia barrier reef which stimulates significant variations in seasonal productivity [Henin and Cresswell, 2005; Alory et al., 2006]. However, the core location of MD06-3018 is 60km seaward of the reef and therefore unlikely to experience strong upwelling fluxes. The reproducibility of the $\delta^{13}\text{C}_{\text{benthic}}$ data is similar to that for

$\delta^{18}\text{O}_{\text{benthic}}$, thus there is no empirical evidence for local phytodetrital effects [Mackensen *et al.*, 1993]. The MD06-3018 $\delta^{13}\text{C}_{\text{benthic}}$ record is considered to provide a reliable record of past deep water $\delta^{13}\text{C}_{\text{DIC}}$ variability at 2500m depth in the NCT. However, the term $\delta^{13}\text{C}$ is used to distinguish inferences made about past $\delta^{13}\text{C}_{\text{DIC}}$ based on $\delta^{13}\text{C}_{\text{benthic}}$ measurements from direct measurements of $\delta^{13}\text{C}_{\text{DIC}}$.

3.8.2 Glacial/interglacial variability in the regional deep water mixing regime

In the modern circulation regime, UCDW/NPDW from the Central Pacific Basin provides the dominant influence on the subtropical southwest Pacific deep water mixing regime. The ultimate source of the majority of both the UCDW and NPDW in the open Pacific is the Pacific DWBC. All DWBC sourced deep water should, therefore, be isotopically ‘younger’ than those found in the DWBC itself, because the longer a deep water mass remains out of contact with the surface ocean and atmosphere, the more isotopically-depleted its $\delta^{13}\text{C}_{\text{DIC}}$ signature becomes due to the “aging effect”. This effect arises through the progressive addition of remineralized organic carbon from the overlying water column and will vary in strength according to variations in both deep water flow rate and productivity regime.

One constraint on the subtropical southwest Pacific mixing regime independent of past changes in deep water flow rates is that when the difference in $\delta^{13}\text{C}$ values at ~2500m depth between the deep waters of the NCT and the DWBC ($\Delta\delta^{13}\text{C}_{\text{NCT-DWBC}}$) exceeds 0‰, then the NCT $\delta^{13}\text{C}$ signal cannot be explained entirely from a DWBC origin. In the modern regime, where both the aging effect and the relative influence of DWBC origin water can be quantified, the value of $\Delta\delta^{13}\text{C}_{\text{NCT-DWBC}}$ from $\delta^{13}\text{C}_{\text{DIC}}$ measurements is $+0.02 \pm \sigma_{\text{diff}}=0.04\text{‰}$ (Table 3.2). The positive value reflects the known Tasman Sea deep water influence, but is within one standard deviation of zero, consistent with the known dominance of DWBC waters. To test whether this dominance persisted in the past, the MD06-3018 $\delta^{13}\text{C}_{\text{benthic}}$ record is compared to another record of similar age range from a core site located within the DWBC.

ODP Site 1123 is located on the North Chatham Drift in the Southwest Pacific Basin at 3290m depth (*Figs 3.1 and 3.2, Table 3.2*). Before using the ODP 1123 $\delta^{13}\text{C}_{\text{benthic}}$ record [*Hall et al., 2001*] to evaluate $\Delta\delta^{13}\text{C}_{\text{NCT-DWBC}}$ over the past 1100ka it is first necessary to evaluate the assumptions involved in the comparison of the two records. The original age-model for ODP 1123 is based on the SPECMAP timescale [*Imbrie and Imbrie, 1980*] and has been adjusted to that of MD06-3018, which is based on LR04, using the $\delta^{18}\text{O}_{\text{benthic}}$ records over the past 1100ka (*Fig 3.6A*). The sedimentation rate seen at the site of ODP 1123 is approximately twice that seen at MD06-3018, leading to a higher temporal sampling resolution and a reduced relative effect of bioturbation on the glacial/interglacial amplitudes in $\delta^{18}\text{O}_{\text{benthic}}$ and $\delta^{13}\text{C}_{\text{benthic}}$ at ODP 1123. In order to directly compare the stable isotope records, all records are smoothed to a common time-step resolution of 5kyr using linear interpolation. The uncertainty in the age-model correlation is dominated by this smoothing timescale.

Core	Latitude	Longitude	Water Depth	Taxa used for $\delta^{13}\text{C}_{\text{benthic}}$ measurements	References
MD06-3018	23°00'S	166°09'E	2470m	<i>Cibicides wuellerstorfi</i>	Present Study
ODP 1123	41°47'S	171°20'W	3290m	<i>Uvigerina</i> spp	<i>Hall et al., 2001</i> <i>Harris, 2002</i>
ODP 806B	0°19'N	159°22'E	2520m	<i>Cibicides wuellerstorfi</i>	<i>Bickert et al., 1993</i>
ODP 849	0°11'N	110°31'W	3840m	<i>Cibicides wuellerstorfi</i> and <i>Uvigerina</i> spp	<i>Mix et al., 1995</i>
MD97-2106	45°09'S	146°17'E	3310m	<i>Cibicides</i> spp	<i>Moy et al., 2006</i>

Table 3.2 Locations and details of the sediment core records used in the current chapter.

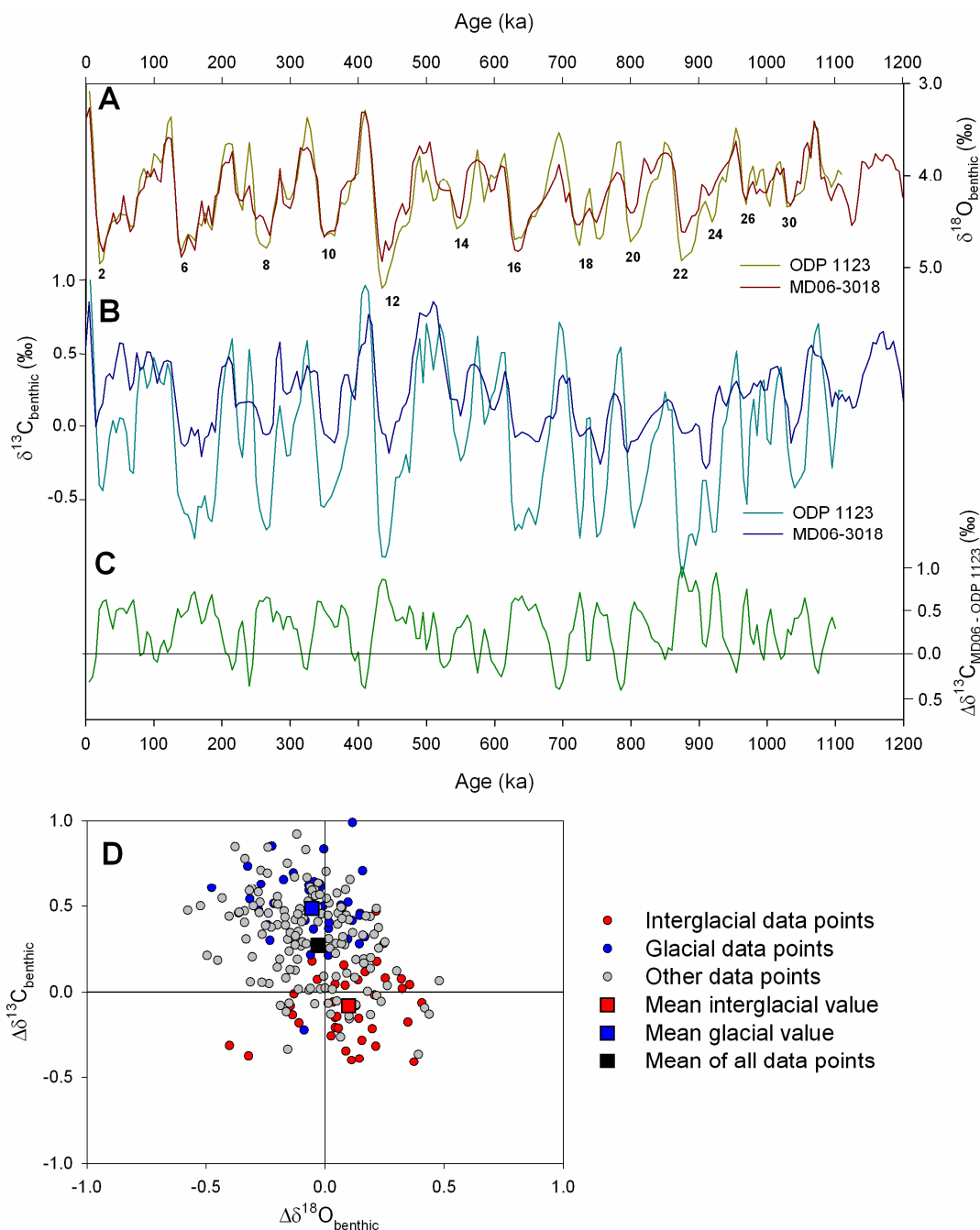


Figure 3.6 A) Comparison of MD06-3018 $\delta^{18}\text{O}_{\text{benthic}}$ data with that from ODP 1123 to demonstrate adjustment of the age-model to that of MD06-3018. The period from 1100ka to the end of the record for ODP 1123 is not shown due to the difficulties in matching the age-models in this interval. Numbers refer to selected glacial Marine Isotope Stages. B) Comparison of MD06-3018 $\delta^{13}\text{C}_{\text{benthic}}$ data with that from ODP 1123. C) $\Delta\delta^{13}\text{C}_{\text{MD06-ODP1123}}$. D) $\Delta\delta^{13}\text{C}_{\text{benthic}}$ and $\Delta\delta^{18}\text{O}_{\text{benthic}}$ data for the MD06-3018 – ODP 1123 comparison. Data points are grouped by interglacial, glacial or other stage (see text for definition used) and the average values for the interglacial, glacial and complete data sets are shown.

The ODP 1123 $\delta^{13}\text{C}_{\text{benthic}}$ measurements were made on infaunal *Uvigerina* taxa rather than the epibenthic *C. wuellerstorfi*. Due to their differing habitats the two groups may respond differently to changes in overlying productivity and organic carbon accumulation [Zahn *et al.*, 1986]. Furthermore, frontal movement on the glacial/interglacial timescale in the overlying waters of the Southwest Pacific Basin have been shown to lead to significant variability in productivity at the site of ODP 1123 [Crundwell *et al.*, 2008]. Thus, we follow a transfer function method based on *Uvigerina* $\delta^{18}\text{O}_{\text{benthic}}$ to convert *Uvigerina* $\delta^{13}\text{C}_{\text{benthic}}$ measurements to *Cibicides*-equivalent, rather than simply applying a constant offset, as proposed in McCave *et al.* [2008]. The transfer function is derived from coupled *Uvigerina* and *Cibicides* measurements from another core at similar latitude to ODP 1123 in the Southwest Pacific Basin [McCave *et al.*, 2008]. This approach generates more positive interglacial than glacial offsets between the two groups in response to the regional productivity changes. The late Holocene (5-0ka) average *Cibicides*-equivalent $\delta^{13}\text{C}_{\text{benthic}}$ value (n=5) using the transfer function is $0.76 \pm \sigma_{\text{SEM}}=0.07\text{‰}$, an apparent offset of $+0.34 \pm \sigma_{\text{diff}}=0.08\text{‰}$ from $\delta^{13}\text{C}_{\text{DIC}}$ at 3300m at WOCE Station P06-168. The errors calculated here assume the same reproducibility error on individual $\delta^{13}\text{C}_{\text{benthic}}$ measurements as in MD06-3018 ($2\sigma_r=0.32\text{‰}$). The late Holocene offset from modern $\delta^{13}\text{C}_{\text{DIC}}$ is similar to that found for MD06-3018, suggesting that variability in the $\delta^{13}\text{C}_{\text{DIC}}$ gradient between the two sites may be reconstructed with greater confidence than the absolute value at either site alone.

The core-site of ODP 1123 is situated at ~800m greater water depth than MD06-3018 (Fig 3.2A/C). Although this means that ODP 1123 is closer to the modern regional lysocline depth than MD06-3018, shoaling of the lysocline to the depth of the ODP 1123 core site does not seem to have occurred over the past 1200ka and glacial/interglacial differences in carbonate dissolution are very small [Crundwell *et al.*, 2008]. The depth difference between the two cores does mean that the difference in $\delta^{13}\text{C}_{\text{benthic}}$ values ($\Delta\delta^{13}\text{C}_{\text{MD06-ODP1123}}$) cannot be used as a direct proxy for past $\Delta\delta^{13}\text{C}_{\text{NCT-DWBC}}$, unless the vertical gradient of $\delta^{13}\text{C}$ in the DWBC region is also known. Depth-transect studies in the region have shown that the $\delta^{13}\text{C}$ values at 2500m remain more negative than those at 3300m over the past two glacial

cycles [McCave *et al.*, 2008]. If it is assumed that this relationship holds across the past 1100ka then the value of $\Delta\delta^{13}\text{C}_{\text{MD06-ODP1123}}$ provides an estimate of the minimum value of $\Delta\delta^{13}\text{C}_{\text{NCT-DWBC}}$ (Table 3.3). The criterion $\Delta\delta^{13}\text{C}_{\text{MD06-ODP1123}} > 0\text{‰}$ therefore provides an even more conservative estimate of when the influence of non-DWBC origin deep water on the mixing regime is required.

Term	Definition	Modern $\Delta\delta^{13}\text{C}_{\text{DIC}}$ (‰)	Late Holocene (0-5ka) value (‰)	Average interglacial stage value n=39 (‰)	Average glacial stage value n=35 (‰)	Difference in average interglacial-glacial values (‰)	Student t-test two-tailed p value for interglacial-glacial difference
$\Delta\delta^{13}\text{C}_{\text{MD06-ODP1123}}$	Difference in $\delta^{13}\text{C}$ between core-sites of MD06-3018 and ODP 1123.	-0.17 $\pm\sigma_{\text{diff}}=0.04$	-0.20 $\pm\sigma_{\text{diff}}=0.11$	-0.08 $\pm\sigma_{\text{SEM}}=0.04$ $\sigma=0.20$	+0.48 $\pm\sigma_{\text{SEM}}=0.04$ $\sigma=0.24$	-0.56 $\pm\sigma_{\text{diff}}=0.05$	p < 0.0001
$\Delta\delta^{13}\text{C}_{\text{NCT-DWBC}}$	Difference in $\delta^{13}\text{C}$ between 2500m in the NCT and the DWBC.	+0.02 $\pm\sigma_{\text{diff}}=0.04$	> -0.20 $\pm\sigma_{\text{diff}}=0.11$	> -0.08 $\pm\sigma_{\text{SEM}}=0.04$ $\sigma=0.20$	> +0.48 $\pm\sigma_{\text{SEM}}=0.04$ $\sigma=0.24$	> -0.56 $\pm\sigma_{\text{diff}}=0.05$	p < 0.0001
$\Delta\delta^{13}\text{C}_{\text{MD06-ODP849}}$	Difference in $\delta^{13}\text{C}$ between core-sites of MD06-3018 and ODP 849.	+0.25 $\pm\sigma_{\text{diff}}=0.04$	+0.40 $\pm\sigma_{\text{diff}}=0.12$	+0.37 $\pm\sigma_{\text{SEM}}=0.04$ $\sigma=0.11$	+0.33 $\pm\sigma_{\text{SEM}}=0.04$ $\sigma=0.15$	+0.04 $\pm\sigma_{\text{diff}}=0.03$	p = 0.16
$\Delta\delta^{13}\text{C}_{\text{NCT-CPBDW}}$	Difference in $\delta^{13}\text{C}$ between 2500m in the NCT and the Central Pacific Basin.	+0.13 $\pm\sigma_{\text{diff}}=0.04$	> -0.20 $\pm\sigma_{\text{diff}}=0.11$	> -0.09 $\pm\sigma_{\text{SEM}}=0.04$ $\sigma=0.19$	> +0.29 $\pm\sigma_{\text{SEM}}=0.04$ $\sigma=0.14$	> -0.38 $\pm\sigma_{\text{diff}}=0.04$	p < 0.0001

Table 3.3 Terms used in the comparison of regional $\delta^{13}\text{C}$ records. The WOCE Stations used for calculating $\Delta\delta^{13}\text{C}_{\text{DIC}}$ values are P06-215 (for MD06-3018 and NCT), P06-168 (for ODP 1123 and DWBC), P18-163 (for ODP 849) and P14-165 (for CPBDW). The late Holocene $\Delta\delta^{13}\text{C}_{\text{benthic}}$ terms are calculated from the difference of the averages of all available, unsmoothed data in the 5-0ka age range. Where > symbols are used, this indicates the use of $\Delta\delta^{13}\text{C}_{\text{benthic}}$ as an estimate of the minimum value of $\Delta\delta^{13}\text{C}$. The ‘n’ values for the average interglacial and glacial columns refer to the number of data points used in each case. The error terms are defined in the text.

Over the past 1100ka the $\Delta\delta^{13}\text{C}_{\text{MD06-ODP1123}}$ record shows 10-100kyr variability with amplitude of $\sim 1\text{‰}$ around a long-term mean value of 0.27‰ (Fig 3.6C). Given the errors arising from the alignment of the core age-models and subsequent data smoothing, any given $\Delta\delta^{13}\text{C}_{\text{MD06-ODP1123}}$ value cannot be deemed diagnostic of conditions in that 5kyr interval. However, the more positive excursions are seen to generally correspond with glacial stages and the more negative excursions with interglacial stages (Fig 3.6B). The average value of all the “interglacial” data points over the past 1100ka, defined as those for which the corresponding MD06-3018 $\delta^{18}\text{O}_{\text{benthic}}$ data point lies within $\pm 5\text{kyr}$ of an interglacial $\delta^{18}\text{O}_{\text{benthic}}$ minimum and excluding those falling during a glacial termination, is $-0.08 \pm \sigma_{\text{SEM}}=0.04\text{‰}$ with

a 1σ spread on the data of 0.20‰ (Fig 3.6D, Table 3.3). The average value of the “glacial” points is $+0.48 \pm \sigma_{\text{SEM}}=0.04\text{‰}$ with $1\sigma=0.24\text{‰}$. The $\Delta\delta^{13}\text{C}_{\text{MD06-ODP1123}}$ data points constitute a broadly normally distributed population and thus, whilst the values of individual data points cannot be robustly compared, an unpaired student t -test may be used to statistically determine whether the averaged interglacial and glacial stage values differ at a given confidence level. At the 95% confidence level, the p value for such a test is <0.0001 , demonstrating that there is significant statistical difference in the average interglacial and glacial stage $\Delta\delta^{13}\text{C}_{\text{MD06-ODP1123}}$ gradients.

The same exercise performed for the $\Delta\delta^{18}\text{O}_{\text{MD06-ODP1123}}$ values demonstrates an average interglacial value of $+0.10 \pm \sigma_{\text{SEM}}=0.03\text{‰}$ with $1\sigma=0.18\text{‰}$ and an average glacial value of $-0.05 \pm \sigma_{\text{SEM}}=0.03\text{‰}$ with $1\sigma=0.16\text{‰}$ (Fig 3.6D). The offset between, and non-zero value of, the interglacial and glacial stage averages arises principally from the differential effects bioturbation in the two cores. The slower sedimentation rate at MD06-3018 leads to an average glacial/interglacial $\delta^{18}\text{O}_{\text{benthic}}$ amplitude which is $\sim 90\%$ of that at ODP 1123. This effect, whilst statistically significant ($p=0.002$ at the 95% confidence interval) in itself, cannot account for the significance of the $\Delta\delta^{13}\text{C}_{\text{MD06-ODP1123}}$ offset. The interglacial to glacial $\Delta\delta^{18}\text{O}_{\text{MD06-ODP1123}}$ offset as a proportion of the glacial/interglacial variability in the ODP 1123 record is only $\sim 10\%$ whereas for $\Delta\delta^{13}\text{C}_{\text{MD06-ODP1123}}$ it is $\sim 50\%$.

The late Holocene value of $\Delta\delta^{13}\text{C}_{\text{MD06-ODP1123}}$ does not significantly differ (at the 1σ level) from the average interglacial stage value (Table 3.3). If it is assumed that the vertical $\delta^{13}\text{C}$ profile, deep water flow rate and overlying productivity regime in the DWBC and subtropical southwest Pacific were similar to the modern during past interglacial stages then it follows that the modern mixing regime, in which DWBC origin deep waters dominate but a small influence from Tasman Sea deep waters also exists, is representative of average interglacial conditions over the past 1100ka. If these assumptions are not made, then at the minimum estimate, under average interglacial stage conditions, NCT $\delta^{13}\text{C}$ can be explained entirely from a DWBC origin. The same assumptions are definitely not justified under glacial stage

conditions. However, even at the minimum estimate, the average glacial stage $\Delta\delta^{13}\text{C}_{\text{MD06-ODP1123}}$ value is significantly more positive than not only the average interglacial stage value but also the modern $\Delta\delta^{13}\text{C}_{\text{NCT-DWBC}}$ value. Thus, during glacial stage conditions the influence on the subtropical southwest Pacific mixing regime required from a water mass chemically younger than that found at 2500m in the DWBC was significantly enhanced compared to both the modern regime and likely past interglacial stage conditions. This could arise from the enhanced relative influence of glacial Tasman Sea deep waters (affecting arrow B, *Fig 3.1*) and/or the presence of an additional chemically younger water mass in the glacial Central Pacific Basin (affecting arrow A, *Fig 3.1*).

3.8.3 Glacial decoupling of Deep Western Boundary Current to Central Pacific Basin deep waters

The $\delta^{13}\text{C}_{\text{benthic}}$ gradient between ODP 1123 and ODP 849 [*Mix et al.*, 1995] from 3840m water depth on the East Pacific Rise (*Fig 3.1*, *Table 3.3*) decreases significantly (and even reverses in certain stages) during past glacials [*Hall et al.*, 2001]. This means that the $\delta^{13}\text{C}$ of glacial deep waters in the equatorial Pacific can no longer be readily explained simply as more chemically aged DWBC waters [*McCave et al.*, 2008]. One hypothesis to explain this change is the presence of a chemically younger water mass resulting from deep ventilation of the glacial North Pacific, termed here gNPDW³ [*Keigwin*, 1998; *Matsumoto et al.*, 2001]. If the chemical signature of gNPDW penetrated far enough south to influence the southern Central Pacific Basin and enter the subtropical southwest Pacific, it could potentially account for the very positive glacial stage $\Delta\delta^{13}\text{C}_{\text{NCT-DWBC}}$ values without any need for changes in the relative influence from Tasman Sea deep waters.

³ Unlike NPDW in the Holocene deep water regime, gNPDW is proposed to result from the ventilation of the North Pacific water column from the surface to depths of over 2500m.

To constrain the potential effect of such open Pacific ventilation and circulation changes on the subtropical southwest Pacific mixing regime it is assumed that the $\delta^{13}\text{C}$ values of deep waters at 2500m depth in the southern Central Pacific Basin ($\delta^{13}\text{C}_{\text{CPBDW}}$) can always be explained from an admixture of DWBC and equatorial Pacific deep waters at that depth. The minimum relative contribution to the observed NCT $\delta^{13}\text{C}$ values required from non-open Pacific deep waters can then be evaluated from $\Delta\delta^{13}\text{C}_{\text{NCT-CPBDW}}$ rather than $\Delta\delta^{13}\text{C}_{\text{NCT-DWBC}}$. Considering the aging effect, it follows that the chemistry of open Pacific Ocean deep waters cannot account for all NCT $\delta^{13}\text{C}$ variability in the case that $\Delta\delta^{13}\text{C}_{\text{NCT-CPBDW}} > 0\text{‰}$.

ODP Site 806B provides a record of $\delta^{13}\text{C}_{\text{benthic}}$ over the past $\sim 750\text{ka}$ [Bickert *et al.*, 1993; Berger *et al.*, 1996] from the western equatorial Pacific at 2520m depth (Figs 3.1 and 3.2, Table 3.2). In the modern regime, the site of ODP 806B is bathed by NPDW and should record the signature of any gNPDW that could possibly reach further south into the subtropical southwest Pacific. At equatorial latitudes in the modern Pacific, the mixing of NPDW and U/LCDW is zonally homogenous [Reid, 1997] such that the longer ODP 849 record from the deep eastern equatorial Pacific allows the comparison to be extended back to 1500ka. Throughout the duration of the ODP 806B record the two equatorial $\delta^{13}\text{C}_{\text{benthic}}$ records are seen to be strongly correlated (Fig 3.7B), suggesting that the depth difference between the sites does not lead to a significant difference in isotopic composition. The ODP 806B $\delta^{13}\text{C}_{\text{benthic}}$ measurements are made entirely on *C. wuellerstorfi* and the ODP 849 ones predominantly so, with some *Uvigerina* measurements that have been corrected to *Cibicides*-equivalent using a constant offset. Both records are compared directly to the MD06-3018 $\delta^{13}\text{C}_{\text{benthic}}$ (Fig 3.7B) values after correlation of the age-models through the $\delta^{18}\text{O}_{\text{benthic}}$ records (Fig 3.7A). Sedimentation rates at both equatorial sites are closer to that seen at MD06-3018 than was the case for ODP 1123. Thus, the degree of glacial/interglacial smoothing of $\delta^{18}\text{O}_{\text{benthic}}$ and $\delta^{13}\text{C}_{\text{benthic}}$ values is similar and the difference between the average interglacial and glacial stage $\Delta\delta^{18}\text{O}_{\text{MD06-ODP849}}$ values is less than 0.05‰ (Fig 3.7D).

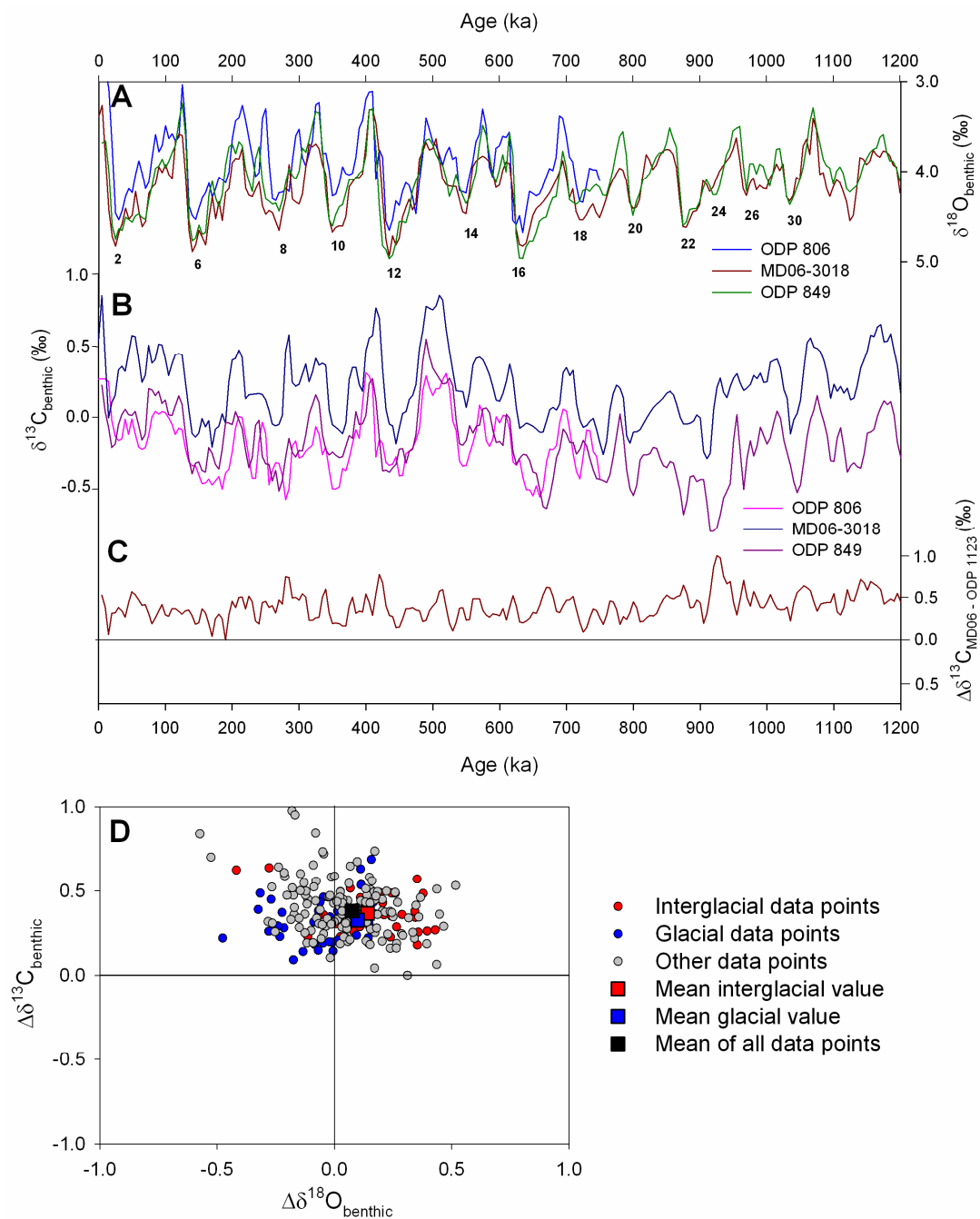


Figure 3.7 A) Comparison of MD06-3018 $\delta^{18}\text{O}_{\text{benthic}}$ data with that from ODP 806B and ODP 849 to demonstrate adjustment of the age-model to that of MD06-3018 B) Comparison of MD06-3018 $\delta^{13}\text{C}_{\text{benthic}}$ data with that from ODP 806B and ODP 849. C) $\Delta\delta^{13}\text{C}_{\text{MD06-ODP849}}$, note that the vertical scale is the same as in *Figure 3.6C*. D) $\Delta\delta^{13}\text{C}_{\text{benthic}}$ and $\Delta\delta^{18}\text{O}_{\text{benthic}}$ data for the MD06-3018 – ODP 849 comparison. Data points are grouped by interglacial, glacial or other stage (see text for definition used) and the average values for the interglacial, glacial and complete data sets are shown.

Across the past 1100ka, the $\Delta\delta^{13}\text{C}_{\text{MD06-ODP849}}$ record shows a long-term mean value of 0.38‰ and generally lower amplitude 10-100kyr variability than that seen in $\Delta\delta^{13}\text{C}_{\text{MD06-ODP1123}}$ (*Fig 3.7C* as compared to *Fig 3.6C*). The average interglacial value over the past 1100ka for $\Delta\delta^{13}\text{C}_{\text{MD06-ODP849}}$ is $+0.37 \pm \sigma_{\text{SEM}}=0.04\text{‰}$ with $1\sigma=0.11\text{‰}$ and the average glacial value is $+0.33 \pm \sigma_{\text{SEM}}=0.04\text{‰}$ with $1\sigma=0.15\text{‰}$ (*Fig 3.7D, Table 3.3*). These populations show no significant statistical difference at the 95% level ($p=0.16$) using the student t -test method. Thus, whereas the $\Delta\delta^{13}\text{C}_{\text{MD06-ODP1123}}$ record shows significant glacial/interglacial variability caused by changes in deep water chemistry and/or circulation, the uniformity of offset seen in the $\Delta\delta^{13}\text{C}_{\text{MD06-ODP849}}$ record suggests that the amplitude of glacial/interglacial $\delta^{13}\text{C}$ variability at both sites is dominated by global mean-ocean chemistry changes.

The value of $\Delta\delta^{13}\text{C}_{\text{NCT-CPBDW}}$ must lie between those of $\Delta\delta^{13}\text{C}_{\text{MD06-ODP849}}$ and $\Delta\delta^{13}\text{C}_{\text{MD06-ODP1123}}$. The least positive possible estimate of $\Delta\delta^{13}\text{C}_{\text{NCT-CPBDW}}$ over the past 1100ka may thus be derived from a composite of the two records, as shown in *Figure 3.8*. The average interglacial stage value over the past 1100ka for this minimum estimate to $\Delta\delta^{13}\text{C}_{\text{NCT-CPBDW}}$ is $-0.09 \pm \sigma_{\text{SEM}}=0.04\text{‰}$ with $1\sigma =0.19\text{‰}$ and the average glacial value is $+0.29 \pm \sigma_{\text{SEM}}=0.04\text{‰}$ with $1\sigma=0.14\text{‰}$ (*Table 3.3*). At the 95% confidence level, the p value for a student t -test of these two populations is 0.006. Even when the potential ventilation of gNPDW is considered, it remains the case that open Pacific deep waters can potentially explain NCT $\delta^{13}\text{C}$ values under interglacial stage conditions but cannot do so under glacial stage conditions. The most plausible explanation is that the relative influence on the mixing regime from Tasman Sea deep waters was significantly enhanced during glacial in comparison to interglacial stages.

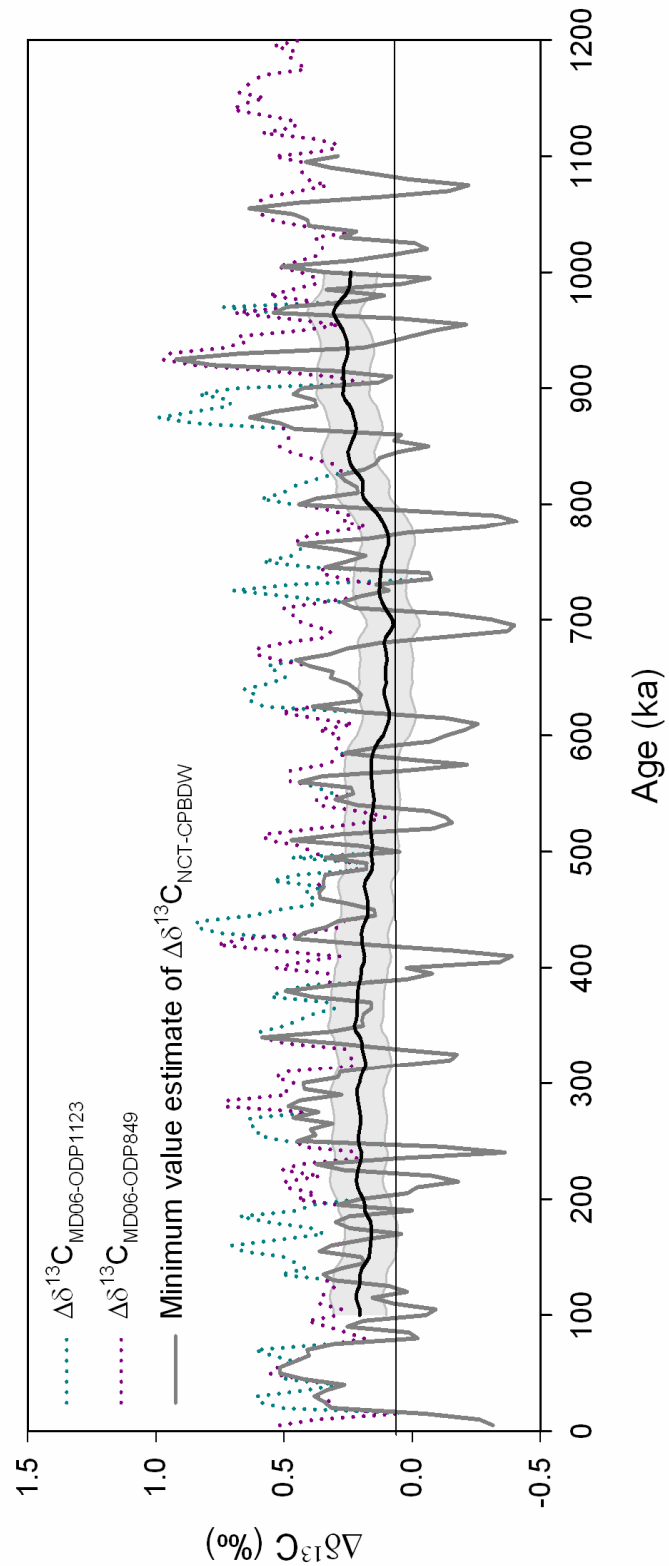


Figure 3.8 $\Delta\delta^{13}\text{C}_{\text{MD06-ODP1123}}$ and $\Delta\delta^{13}\text{C}_{\text{MD06-ODP849}}$ plotted together to show the development of the composite minimum value estimate to $\Delta\delta^{13}\text{C}_{\text{NCT-CPBDW}}$. The 200kyr running mean of the composite estimate is shown by the bold black line with $\pm 2\sigma_{\text{SEM}}$ confidence intervals shown by the grey envelope.

3.8.4 Glacial stage deep water chemistry gradients in the southwest Pacific

Changes in either the relative fluxes or $\delta^{13}\text{C}_{\text{DIC}}$ values associated with the Tasman Sea and open Pacific Ocean inflows to the subtropical southwest Pacific region could account for the observed glacial/interglacial variability in the mixing regime. Pleistocene reconstructions of DWBC flow strength at site ODP 1123 have shown generally increased fluxes during glacial stages [Hall *et al.*, 2001]. This suggests that the relatively reduced DWBC influence seen in the glacial subtropical southwest Pacific cannot be explained by flow rate changes in the DWBC. In the absence of reconstructions for the past inflow rates from the Tasman Sea it remains impossible to quantitatively reconstruct the mixing regime. However, given the assumption that NCT $\delta^{13}\text{C}$ values arise from a mixture of only open Pacific Ocean and Tasman Sea deep waters, the MD06-3018 $\delta^{13}\text{C}_{\text{benthic}}$ record may be used to place an indirect constraint on the $\delta^{13}\text{C}$ values of northern Tasman Sea deep water at ~2500m depth. In periods where some influence from Tasman Sea deep water is required (those during which the minimum value of $\Delta\delta^{13}\text{C}_{\text{NCT-CPBDW}}$ is $>0\text{‰}$, Fig 3.8) the $\delta^{13}\text{C}$ value of this water mass must have been more positive than the corresponding MD06-3018 $\delta^{13}\text{C}_{\text{benthic}}$ value.

During the last two glacial stages (the LGM and MIS 6) in the DWBC region, isotopically-depleted ($\delta^{13}\text{C}$ values of $<-0.5\text{‰}$) Southern Ocean sourced glacial Upper Circumpolar Deep Water (gUCDW) replaced NPDW/UCDW as the dominant water mass in the “mid-depth” range 2000–3500m [McCave *et al.*, 2008]. In contrast, the MD06-3018 constraint on $\delta^{13}\text{C}$ at ~2500m depth in the northern Tasman Sea predicts average glacial stage $\delta^{13}\text{C}$ values of $>0.2\text{‰}$. This suggests that the gUCDW present in the DWBC region [McCave *et al.*, 2008] was not present as the dominant mid-depth water mass in the glacial Tasman Sea. The modern $\delta^{13}\text{C}$ –depth gradient across the range 2500–3500m in the Tasman Sea is close to zero (as seen at station P06-234, Fig 3.2C). The MD97-2106 $\delta^{13}\text{C}_{\text{benthic}}$ record from 3310m water depth on the South Tasman Rise, near to where most deep water enters the Tasman Sea from the Southern Ocean (Figs 3.1 and 3.2, Table 3.2), shows average values of -0.25‰

during the LGM and -0.40‰ during MIS 6 [Moy *et al.*, 2006]. These values are slightly more positive than those seen in the glacial DWBC, but still significantly more negative than those predicted for 2500m in the average glacial stage northern Tasman Sea. Therefore, during at least the past two glacial stages, the $\delta^{13}\text{C}$ -depth gradient in the Tasman Sea is predicted to have been significantly negative, consistent with the presence of a glacial stage chemocline at 2500-3000m depth. In contrast, the glacial DWBC $\delta^{13}\text{C}$ -depth gradient retained the modern positive value over the same depth range [McCave *et al.*, 2008]. The future study of a Pleistocene $\delta^{13}\text{C}$ record from \sim 2500m depth in the northern Tasman Sea will allow direct evaluation of this hypothesis.

At depths below \sim 3500m several deep hydrographic zones with different characteristic $\delta^{13}\text{C}$ signatures have been proposed for glacial Southern Ocean bottom waters [Ninnemann and Charles, 2002; McCave *et al.*, 2008]. In one such scenario the bottom waters flowing into the southern Atlantic sector are formed in the Weddell Sea, those entering the open Pacific in the Ross Sea and those entering the Tasman Sea along the Adélie Coast [McCave *et al.*, 2008]. The subtropical southwest Pacific mixing constraint additionally demonstrates that the $\delta^{13}\text{C}$ gradient between Tasman Sea and DWBC waters at \sim 2500m was significantly enhanced during glacial, relative to interglacial stages. The enhanced glacial stage spatial $\delta^{13}\text{C}$ gradient could be explained if the isotopically-enriched water of North Atlantic origin which lies at or above the observed glacial stage chemocline at 2100-2700m in the southern Atlantic sector of the Southern Ocean [Ninnemann and Charles, 2002; Venz and Hodell, 2002; Hodell *et al.*, 2003] was able to pass round the glacial Circumpolar Current and enter the Tasman Sea but not the Pacific DWBC. Alternatively, the mid-depth glacial Tasman Sea could be filled with Southern Ocean sourced deep water, but this water mass would be required to be isotopically-enriched in relation to the gUCDW seen in the DWBC. Therefore, in addition to the previously described threefold zonation of glacial Southern Ocean bottom waters [McCave *et al.*, 2008]; a strong spatial chemical gradient existed between the overlying mid-depth waters associated with the Adélie Coast and Ross Sea bottom

water domains, but apparently not between those of the Weddell Sea and Adélie Coast domains.

3.8.5 Pleistocene evolution of deep water circulation and mixing

The shift in dominant glacial/interglacial periodicity from 40kyr to 100kyr modes during the MPT is evident in both the $\delta^{18}\text{O}_{\text{benthic}}$ and $\delta^{13}\text{C}_{\text{benthic}}$ records (*Fig 3.5*). As well as this orbital time-scale variability, all of the Pacific $\delta^{13}\text{C}_{\text{benthic}}$ records discussed here show a perturbation on the >100kyr time-scale towards more negative mean values during the period of the MPT (*Figs 3.5B, 3.6B, 3.7B*). This perturbation is also recorded in all other major ocean basins and has thus been interpreted as a global shift in mean ocean $\delta^{13}\text{C}$ [*Raymo et al., 1997*]. In this global average, the perturbation constitutes a decrease in mean ocean $\delta^{13}\text{C}$ of $\sim 0.3\text{‰}$ during the period 1000-900ka followed by a more gradual return to pre-1000ka values by 400ka [*Raymo et al., 1997*].

To study the behaviour of the subtropical southwest Pacific deep water mixing regime on the >100kyr time-scale the effect of glacial/interglacial variability is removed by considering the 200kyr running mean value (calculated through linear smoothing using a box-car method) of $\Delta\delta^{13}\text{C}_{\text{NCT-CPBDW}}$ (*Fig 3.8*). The running mean value is seen to have remained above zero across the duration of the record, demonstrating that on this time-scale there is always a component of variability in subtropical southwest Pacific deep water $\delta^{13}\text{C}$ that cannot be explained by the influence of open Pacific Ocean deep waters alone. However, the running mean also shows significant variations in magnitude across the past 1100ka, indicating that >100kyr time-scale shifts have occurred in the mode of the deep water circulation regime. Over the period 500-0ka the average value for the estimate of the minimum value of $\Delta\delta^{13}\text{C}_{\text{NCT-CPBDW}}$ was 0.20‰ , whereas during the period 1100-900ka it was 0.24‰ (*Fig 3.8*). In the intervening period, the running mean value decreased to $\sim 0\text{‰}$ during the interval 900-750ka before then increasing more gradually across the interval 750-500ka. The spatial gradient between deep waters entering the Pacific DWBC and Tasman Sea from the Southern Ocean was, therefore, generally

decreased during the period 900-500ka, coincident with the main part of the global mean ocean $\delta^{13}\text{C}$ perturbation across the MPT.

The MPT is associated with generally weaker global deep water exchange [Schmieder *et al.*, 2000]. Reconstructions of the flow strength associated with water masses in the Pacific DWBC suggest reduced flow during the period 900-400ka [Hall *et al.*, 2001; Venuti *et al.*, 2007]. Because the majority of northward flow in the DWBC is of Southern Ocean origin deep and bottom waters, this may represent reduced ventilation of the Southern Ocean over this period. Furthermore, the ventilation of North Atlantic deep waters is also thought to be reduced across the MPT [Raymo *et al.*, 1997]. The MD06-3018 $\delta^{13}\text{C}_{\text{benthic}}$ record is more sensitive to changes in the ventilation rates of North Atlantic deep waters than the ODP 1123 and ODP 849 $\delta^{13}\text{C}_{\text{benthic}}$ records. This arises because the subtropical southwest Pacific deep water mixing regime means that NCT deep water is sensitive to both DWBC and Tasman Sea deep water chemistry whereas open Pacific Ocean deep water is sensitive mainly to the former. Mid-depth deep waters in the Tasman Sea show more influence from relict North Atlantic deep waters than those of the DWBC and this difference is shown to be enhanced during past glacial stages. Therefore, a reduction in the ventilation of both North Atlantic and Southern Ocean deep waters could lead to the observed reduction in the $\delta^{13}\text{C}$ gradient between the mid-depth waters of the Tasman Sea and DWBC during the MPT.

3.9 Conclusions

The modern deep water $\delta^{13}\text{C}_{\text{DIC}}$ distribution in the subtropical southwest Pacific region has been shown to be consistent to the first order with conservative water mass properties and the modern deep water mixing regime between open Pacific Ocean and Tasman Sea sourced deep waters [Wyrki, 1961]. Using this principle, the MD06-3018 reconstruction of deep water $\delta^{13}\text{C}$ in the NCT, in comparison with other regional records, has allowed constraints to be placed on aspects of the mixing regime across the past 1600ka.

This chapter has shown that on the glacial/interglacial timescale the difference in $\delta^{13}\text{C}_{\text{benthic}}$ values between the NCT record and a core from the Pacific DWBC was significantly more positive during glacial than interglacial stages. The effect of potential ventilation of deep waters in the North Pacific on this offset was examined using the comparison of the NCT $\delta^{13}\text{C}_{\text{benthic}}$ record with ones from the deep equatorial Pacific. Even with these possible circulation changes, glacial stage NCT $\delta^{13}\text{C}$ values cannot be explained entirely from a purely open Pacific Ocean source. Instead, a significantly enhanced relative influence from glacial Tasman Sea deep waters compared to those from the open Pacific is shown to be required, in comparison to the interglacial regime. The enhanced relative influence of Tasman Sea over open Pacific deep waters during glacial stages reflects a steepening of the spatial gradient between the $\delta^{13}\text{C}$ of deep waters found at ~2500m depth in the Tasman Sea and the Pacific DWBC. This arose from the relatively greater glacial stage influence of isotopically-depleted mid-depth waters of Southern Ocean origin in the DWBC compared to the Tasman Sea. The glacial stage Southern Ocean is shown to contain significant spatial chemical gradients at depths well above the sea floor topography.

On the >100kyr timescale the influence of the chemically younger Tasman Sea deep waters on the mixing regime is shown to have been a persistent feature of the past 1100ka. The spatial $\delta^{13}\text{C}$ gradient between the mid-depth deep waters of the Tasman Sea and the Pacific DWBC was generally reduced, on the >100kyr timescale, during the period of the MPT, consistent with this being a period of reduced deep water ventilation in both hemispheres.

The conclusions presented in this chapter based on the $\delta^{13}\text{C}_{\text{benthic}}$ record are largely self contained and are not revisited again until chapter 7, §3, when the implications of the enhanced glacial stage spatial chemical gradients within the Southern Ocean are considered in terms of glacial/interglacial variability in the global carbon-cycle. The potential origins of the >100kyr time-scale perturbation in deep water ventilation are also discussed in that same section. The core age-model is now used to provide a framework for the planktic proxy records that form the focus of the next three chapters. The $\delta^{18}\text{O}_{\text{benthic}}$ record is also reconsidered directly in chapters 4 and 6, as a first-order proxy for global ice-volume changes that can be compared in an age-model independent manner to the planktic records.

Blank Page

Chapter 4: Sources of uncertainty in the Mg/Ca paleothermometer: did climate change limit the middle Pleistocene expansion of reefs in the southern Coral Sea?

Chapter abstract

A reconstruction of Sea Surface Temperature (SST) in the southern Coral Sea over the past 1600ka is derived from MD06-3018 planktic foraminiferal Mg/Ca measurements. No significant >100kyr time-scale trend is present in reconstructed SST, but glacial/interglacial variability of 2-3°C exists across the record. Comparison of the geochemical SST reconstruction with foraminiferal transfer function estimates of seasonal sea surface temperature, across selected glacial terminations, is consistent with the former representing mean-annual SST. An estimate of the ‘combined uncertainty’ associated with the SST reconstruction is introduced, based on proposed corrections to the Mg/Ca proxy for the effects of past variability in salinity and ocean trace metal chemistry. The MD06-3018 core-site lies close to the modern climatic southern limit to tropical coral reef growth. However, when the combined proxy uncertainties are considered, the Mg/Ca paleothermometry method does not show any significant change in the mean-annual SST values associated with interglacial stages over the Mid-Pleistocene Transition interval. Whilst it is unlikely that regional climate change could have constituted a significant control on the observed middle Pleistocene reef expansion, paleothermometry proxy limitations mean that the question cannot be unequivocally addressed at present.

4.2 Introduction

The Coral Sea in the tropical and subtropical southwest Pacific is home to many of the world's largest coral reef systems, including the Great Barrier Reef (GBR) and the New Caledonia Barrier Reef (NCBR) (*Fig 4.1*). Geological studies have shown that both of these major reef systems underwent a pronounced period of expansion during the middle Pleistocene. In particular, borehole studies at 22°S on the NCBR have shown that whilst carbonate platforms were initiated as early as 1400ka and developed by 780ka, widespread barrier reef development only commenced during MIS 11 at ~400ka [*Cabioch et al., 2008*]. Geochemical dating of the oldest reef material present in boreholes on the outer part of the central GBR at 16°S has yielded ages of 600±280ka [*Alexander et al., 2001*], consistent with the significant increases in down-slope carbonate transport and inferred GBR extent documented at both ~400ka [*Isern et al., 1996; Braithwaite et al., 2004*] and 670-560ka [*Dubois et al., 2008*]. This middle Pleistocene expansion of reef systems was not limited to the Coral Sea region, with reefs elsewhere in the Pacific and Atlantic Oceans also undergoing expansion during the interval 800-400ka [*Kievman, 1998; Alexander et al., 2001; Braithwaite et al., 2004; Yamamoto et al., 2006; Cabioch et al., 2008; Dubois et al., 2008*].

The distribution of modern tropical/subtropical coral reefs is limited by a range of geological and environmental factors, including the availability of suitable substrate at water depths shallow enough to permit photo-symbiosis and to regions with a suitable climatic regime [*Achituv and Dubinsky, 1990; Falkowski et al., 1990; Kleypas et al., 1999*]. One of the key climatic parameters limiting reef development is SST, namely that this should not drop below 18°C for more than a few weeks of each year [*Kleypas et al., 1999*]. At the latitude of the MD06-3018 core-site in the southern Coral Sea (23°S), the modern open-ocean seasonal SST range based on WOA5005 values is 22.2-26.0°C, with a mean-annual value of 24.4°C [*Locarnini et al., 2006*]. Open-ocean SST variability in the NCT over the past 25 years has been shown to be well correlated with SST changes within the New Caledonia lagoon [*Quinn and Sampson, 2002*]. Thus, any past changes in open-ocean SST of the order

of several °C at 23°S may have provided a regional climatic limit to reef development.

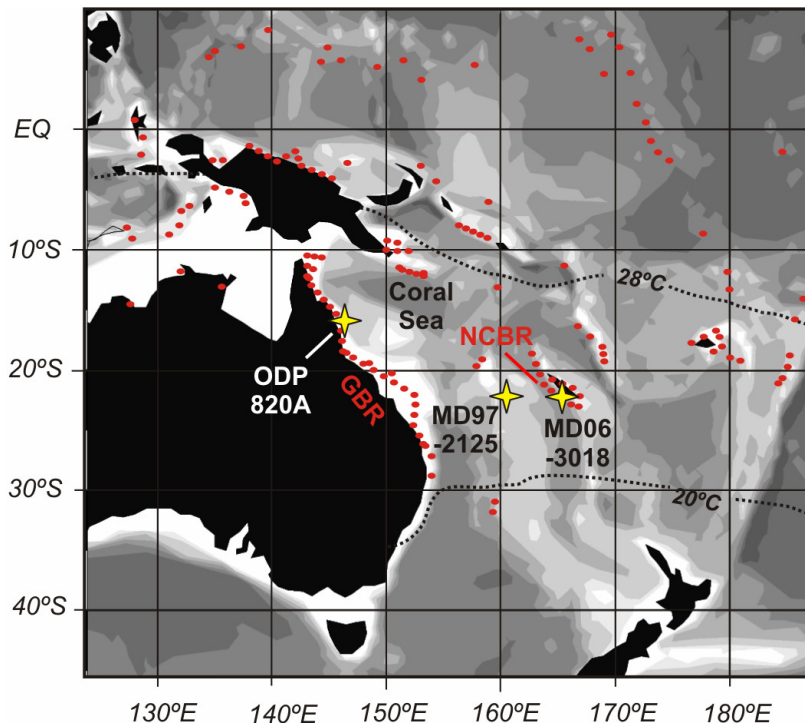


Figure 4.1 Map of the subtropical southwest Pacific region with major modern coral reef systems highlighted by red dots. Yellow stars show the location of the sediment core records discussed in this chapter, the details of which are given in *Table 4.1*. Dashed lines show position of selected modern mean-annual SST isotherms using WOA2005 data for 0m depth [*Locarnini et al., 2006*]. Bathymetry is from the ODV software [*Schlitzer, 2007*]. A higher resolution map showing the location of the MD06-3018 core-site in relation to the NCBR is given as part of *Figure 2.1*.

The reconstruction of past regional SST variability therefore provides a method to evaluate whether the middle Pleistocene phase of Coral Sea reef expansion can plausibly have been limited by regional climatic changes. The $\delta^{18}\text{O}_{\text{planktic}}$ record from ODP 820A at 280m water depth on the central GBR (*Fig 4.1, Table 4.1*) shows a pronounced trend towards lighter values from 700-300ka [*Peerdeman et al., 1993*]. This trend was initially interpreted as representing a significant SST warming (4-6°C) that would very plausibly have limited widespread barrier reef development prior to the middle Pleistocene [*Isern et al., 1996*].

However, subsequent studies have shown that the shallow water material used from that core-site was substantially diagenetically altered, rendering the $\delta^{18}\text{O}_{\text{planktic}}$ record of little use as a paleothermometer [Lawrence and Herbert, 2005]. Indeed, the application of the alkenone saturation index (U^k_{37}) paleothermometer to material from the same core site shows no significant trends in $>100\text{kyr}$ time-scale SST over the past 800ka [Lawrence and Herbert, 2005]. It therefore seems unlikely, unless very large changes in long-term SST seasonality are invoked, that long-term trends in regional climate can account for the middle Pleistocene reef expansion.

Core	Latitude	Longitude	Water Depth	Temporal resolution and (range)	SST proxy	References
MD06-3018	23°00'S	166°09'E	2470m	~5kyr (1600ka)	Mg/Ca	Present Study
MD97-2125	22°34'S	161°44'E	1680m	<2kyr (360ka)	Mg/Ca U^k_{37}	Tachikawa et al. [2009]
ODP 820A	16°38'S	146°18'E	280m	<10kyr (800ka) <20kyr (800ka)	$\delta^{18}\text{O}_{\text{planktic}}$ U^k_{37}	Peerdeman et al. [1993] Lawrence and Herbert [2005]

Table 4.1 Core locations, sampling resolutions, record lengths and paleothermometry methods used for the SST reconstructions discussed in this chapter.

The interval of middle Pleistocene reef expansion overlaps with the latter stages of the MPT, suggesting that the change in the dominant mode of glacial/interglacial SST variability over the transition may have played a role, even in the absence of any change in the $>100\text{kyr}$ time-scale mean values. The ODP 820A U^k_{37} derived SST reconstruction shows glacial/interglacial variability of $<1^\circ\text{C}$, suggesting that, as for the $>100\text{kyr}$ time-scale, it is very unlikely that orbital time-scale SST variability could have played any role in limiting reef expansion, at least at 16°S [Lawrence and Herbert, 2005]. However, higher temporal resolution reconstructions of SST variability, derived from both the U^k_{37} and Mg/Ca paleothermometry methods for MD97-2125 at 22°S (Fig 4.1, Table 4.1), show glacial/interglacial SST variability over the past three climatic cycles of $2\text{-}3^\circ\text{C}$

[Tachikawa *et al.*, 2009]. Glacial/interglacial and potentially also interglacial by interglacial stage changes in SST of $>1^{\circ}\text{C}$ have, therefore, apparently occurred in the southern Coral Sea over the MPT interval. Resolving whether these changes could have been significant in limiting reef development is, however, dependent on first demonstrating that these changes are in fact statistically significant against the paleothermometry proxy uncertainties.

This chapter presents the MD06-3018 *G. ruber* Mg/Ca derived SST reconstruction for the southern Coral Sea. All current paleothermometry proxies, including the Mg/Ca method which will be considered in detail in this chapter, using the MD06-3018 record as a case study, generally remain subject to sample reproducibility uncertainties equivalent to at least 1°C . Furthermore, there exist additional certainties, relating to the calibration relationships themselves, which are often poorly constrained but potentially both very large in relation to the reproducibility uncertainty and temporally variable. In the case of the Mg/Ca proxy system, this would include known ‘non-SST’ controls on the incorporation of Mg into foraminiferal calcite, such as the effects of changes in salinity and the Mg/Ca ratio of seawater. Furthermore, the relationship between the reconstructed proxy SST values and the seasonal SST range is not always well constrained. All of these factors may have varied systematically down-core (i.e. with age), leading to the sample reproducibility uncertainty potentially being a significant underestimation of the ‘real’ uncertainty in reconstructed SST.

Before evaluating what changes in southern Coral Sea SST on orbital time-scales can be significantly resolved using the MD06-3018 SST reconstruction it is therefore necessary to constrain the amplitude of both the down-core seasonal biases and proxy calibration uncertainties. To address the former, the MD06-3018 Mg/Ca-derived SST reconstruction is compared, across selected glacial terminations, to transfer function estimates of seasonal SST in order to evaluate the extent of any climatically induced seasonality biases in the geochemical reconstruction. To address the calibration uncertainty, this chapter then introduces one strategy for the quantitative estimation method of the ‘combined proxy uncertainty’ associated with

the Mg/Ca paleothermometer, based upon the application of proposed corrections for the effects of past variability in seawater chemistry. It is then possible to evaluate whether the MD06-3018 SST reconstruction, the first such regional record to extend at sub-orbital resolution across the entire MPT, is capable of resolving potential regional changes in southern Coral Sea SST of the order of several °C, such as could have played a role in limiting the expansion of reef systems during the climatic transition.

4.3 Methods

4.3.1 Planktic foraminiferal Mg/Ca measurements and Mg/Ca paleothermometry

Thirty-five to forty individuals of the surface-dwelling planktic foraminifera *Globigerinoides ruber* (white) were picked from the 250-315µm size fraction. Different morphotypes of *G. ruber* are known to have different environmental preferences [Lowemark *et al.*, 2005; Steinke *et al.*, 2005; Sadekov *et al.*, 2008; Wang *et al.* 2000] and thus only the *G. ruber ruber* morphotype¹ was selected. The cleaning methodology used for foraminiferal Mg/Ca analysis has been shown to have a significant bearing on the measured trace-metal ratios [Barker *et al.*, 2003; Rosenthal *et al.*, 2004]. The present study follows closely the “Mg/Ca cleaning method” as described in Barker *et al.* [2003]. The only significant alterations are the use of three, rather than five, water rinse steps and the addition of a final centrifuge stage (10min at 6000rpm) after sample dissolution [Greaves *et al.*, 2005]. Samples were diluted to a target calcium concentration of 60ppm and analyzed following the intensity-ratio calibration method as described in de Villiers *et al.* [2002] using the Varian VISTA Pro ICP-OES (Axial) in the School of Geosciences, University of Edinburgh.

¹ *G. ruber ruber*, in the terminology of Sadekov *et al.* [2008] is taken here as being identical to *G. ruber sensu stricto* from Wang *et al.* [2000] and Steinke *et al.* [2005] and *G. ruber* morphotype I from Lowemark *et al.* [2005]. This morphotype is hereafter referred to in this thesis simply as *G. ruber*.

To monitor residual inorganic contamination of samples, the intensities of Al, Fe, Mn were measured in addition to those of Ca and Mg. Samples with a Fe/Mg ratio exceeding 1mol/mol [Barker *et al.*, 2003], or Al or Mn intensities significantly ($>3\sigma$) above the background level were rejected (seven samples out of 395 analyzed were rejected on these criteria). Long-term reproducibility was assessed through repeat measurements of carbonate reference material ECRM-521, which was centrifuged prior to dilution to 60ppm calcium. Over the period of analysis the measured value for ECRM-521 Mg/Ca was $3.762 \pm 2\sigma_a=0.0352$ mmol/mol ($n=162$), highly consistent with previous characterization and inter-laboratory studies [Greaves *et al.*, 2005; Greaves *et al.*, 2008]. Short-term (sample) reproducibility was assessed by four down-core repeated ($n \geq 5$, including full replication of picking and cleaning stages) foraminiferal measurements and was always better than $2\sigma_r=0.52$ mmol/mol. Full details of the trace-metal analytical methods, standards, reference materials and sample rejection criteria are presented in appendix 2. The full down-core Mg/Ca data set is tabulated in appendix 4 and plotted against composite core depth in appendix 5.

The exponential relationship observed between the amounts of Mg incorporated into foraminiferal calcite and the surrounding water temperature has been validated in many studies [Elderfield and Ganssen, 2000; Anand *et al.*, 2003; McConnell and Thunell, 2005; Kisakurek *et al.*, 2008]. The principles of this system are outlined in appendix 1, §3. The constants that define the Mg/Ca – SST calibration function (the terms a and b in equation A1.4, appendix 1, §3) have, however, been shown to vary between taxa, size fraction and with other environmental factors. The MD06-3018 Mg/Ca record is calibrated to mean-annual SST using a sediment-trap based *G. ruber* calibration for the 250-350 μ m size fraction, without a pre-assumed partition coefficient ($a = 0.34$ mmol/mol, $b = 0.102(^{\circ}\text{C})^{-1}$) [Anand *et al.*, 2003]. This calibration function is preferred as it is based on a similar size fraction and cleaning method as those used in the present study. No correction for dissolution is applied as the core location lies well above the modern regional lysocline [Martinez, 1994].

In general, the uncertainty in absolute SST value associated with the calibration function constants is relatively large ($\pm 4.9^\circ\text{C}$ for $\text{Mg}/\text{Ca}=4\text{mmol}/\text{mol}$ using the above calibration) compared to that arising from sample reproducibility ($2\sigma_r=1.0^\circ\text{C}$ in this study) or analytical precision ($2\sigma_a=0.1^\circ\text{C}$ in this study). Consequently, individual reconstructed SST values are subject to considerably greater uncertainty than down-core variability in SST. However, the calibration uncertainty may be constrained by evaluating whether the core-top reconstructed SST value corresponds to the known late Holocene conditions.

The MD06-3018 core-top Mg/Ca value, based on seven repeated measurements, is $4.60 \pm 2\sigma_r=0.52\text{mmol}/\text{mol}$. This yields a calibrated SST value of $25.5 \pm 2\sigma_r=1.0^\circ\text{C}$. The modern mean-annual SST at 0m depth from WOA2005 data for the core-site is 24.4°C [Locarnini *et al.*, 2006]. Therefore, the reconstructed core-top SST is warmer than the measured mean-annual value by 1.1°C . The instrumental value lies nearly within the $2\sigma_r$ error of the data, but there are also several known calibration factors that may also explain such an offset. The foraminifera used in the present study represent a smaller subset of the size fraction and a more particular morphotype selection than those used in the Anand *et al.* [2003] calibration. They are also from a generally fresher part of the global ocean, leading to a potential salinity bias. All of these effects are likely to have acted in the sense of biasing the reconstructed SST towards higher values [Sadekov *et al.*, 2008].

In the absence of absolute dates for the core-top sample and given the known time-averaging of at least several centuries per sample (chapter 3, §7), it is likely that the core-top sample reflects an average of late Holocene, rather than strictly modern, SST conditions. Given, furthermore, that reconstructed mean-annual SST in the WEP at only $\sim 1\text{ka}$ has been shown to be $\sim 0.5^\circ\text{C}$ warmer than modern [Linsley *et al.*, 2010], the entirety of the core-top Mg/Ca -derived SST to modern mean-annual SST offset can be explained by this effect and the sample reproducibility alone. There is, therefore, no need to invoke the statistical calibration uncertainty to explain the core-top offset. The approach taken in this chapter towards constraining the down-core proxy uncertainty is, therefore, to neglect the error arising from the calibration

constants themselves and to focus on both the reproducibility uncertainty and environmental factors that may have systematically compromised the validity of the down-core application of the core-top calibration.

4.3.2 Transfer function estimates of SST

A seasonal bias towards summer conditions may exist in the *G. ruber* Mg/Ca-derived reconstructed SST values, due to preferential growth (and hence flux to the sediment) of *G. ruber* individuals during warmer conditions [Kawahata *et al.*, 2002]. Whilst *G. ruber* has been shown to calcify at water temperatures as low as 14°C, it declines in abundance below ~21°C [Bijma *et al.*, 1990]. In the case of the southern Coral Sea, past periods with lower than modern mean-annual SST, for example glacial stages, may well have had cold season temperatures dropping below 21°C, potentially introducing enhanced seasonal bias away from the mean-annual SST in the Mg/Ca-derived estimates than that recorded at the core-top. The present study constrains the effect of this seasonal bias by comparing the geochemical SST estimates to independent estimates of down-core seasonal SST variability derived from foraminiferal transfer function analysis.

Transfer function techniques provide an independent, non-geochemical proxy for quantifying past environmental conditions, such as SST. The essence of the technique is to assume that the modern spatial relationship between different faunal groups (species of planktic foraminifera in this case) relates to the modern spatial distribution of environmental parameters, such as seasonal or mean-annual SST. By comparing down-core fossil assemblages with a range of core-top assemblages, for which the modern environmental parameters of interest are known, statistical analysis (using a variety of methods) allows the same parameters to be estimated for the fossil assemblage. The sources of error in the transfer function technique arise principally from the statistical methods used, which may be quantified, and in assuming temporally invariant relationships between ecology and environment, which cannot be so easily quantified but are likely to increase with age, due to ecological turnover. Furthermore, the faunal assemblage is a function of multiple

environmental variables, rather than SST alone, introducing the same potential auto-correlation problems as for geochemical paleothermometry.

Transfer function estimates of winter season SST (winSST) and summer season SST (sumSST) were made for the MD06-3018 fauna across the LGM/Hol, MIS12/11 and MIS38/37 glacial terminations, using the Modern Analogue Technique (MAT) [Prell, 1985] and a global training data set ($n = 61$) [Imbrie and Kipp, 1971]. These three terminations were chosen as the LGM/Hol interval has a wide variety of existing data for comparison, within the definition of the ‘100kyr world’ used in this thesis (see chapter 1, §7.2), MIS 12/11 is the first termination of that regime, whereas MIS 38/37 is ‘typical’ of the early Pleistocene, 40kyr world regime, as seen in the Mg/Ca-derived SST record. Additional 1-2kyr resolution Mg/Ca data is also presented for these three glacial terminations and this high-resolution data is tabulated in appendix 6. Whilst numerous other transfer function methods and much more extensive and/or regionalized training databases exist, the present approach is designed only to provide a first order control on past seasonality and hence a global training set is considered appropriate. For each sample, $n > 240$ foraminifera ($n > 300$ for all but two samples) were identified from the $> 150\mu\text{m}$ size fraction following the Imbrie and Kipp [1971] taxonomy and MAT analysis was carried out using the C2 software program [Juggins, 2007]. The average statistical error on the winSST reconstructions was $\pm 1.8^\circ\text{C}$ and for the sumSST reconstructions it was $\pm 1.2^\circ\text{C}$. The faunal counts themselves are tabulated in appendix 7.

4.3.3 Proposed down-core corrections to the Mg/Ca paleothermometer

Salinity is increasingly understood to exert a secondary control on foraminiferal Mg/Ca ratios [Kisakurek *et al.*, 2008; Sadekov *et al.*, 2008]. The application of a Mg/Ca - SST calibration that does not account for the salinity effect, such as the one used for MD06-3018, potentially leads to a differential bias in reconstructed SST across glacial/interglacial cycles, whereby glacial stages are likely to experience more saline conditions, thus systematically biasing reconstructed SST towards warmer values [Mathien-Blard and Bassinot, 2009]. This effect would act in the same sense (warm biased SST values during more saline periods, such as glacial stages) as the potential seasonality effect described in the preceding section and would thus also lead to the underestimation of glacial/interglacial SST amplitudes.

A specific correction for this salinity effect when using Mg/Ca - SST calibrations, based on coupled $\delta^{18}\text{O}_{\text{planktic}}$ - Mg/Ca measurements, knowledge of the global component of $\delta^{18}\text{O}_{\text{sw}}$ change and an assumed invariant regional $\delta^{18}\text{O}_{\text{sw}}$ - salinity relationship, has been proposed by Mathien-Blard and Bassinot [2009], the form of which is given in equations 4.1 and 4.2. In the present study a record of the global component of $\delta^{18}\text{O}_{\text{sw}}$ change, relative to the modern ($\Delta\delta^{18}\text{O}_{\text{global}}$), as derived from benthic foraminiferal $\delta^{18}\text{O}$ -Mg/Ca measurements [Sosdian and Rosenthal, 2009] is used, as is the modern $\delta^{18}\text{O}_{\text{sw}}$ - salinity relationship for the tropical Pacific [LeGrande and Schmidt, 2006]. In order to make the salinity correction, the MD06-3018 SST reconstruction and $\delta^{18}\text{O}_{\text{planktic}}$ record, as well as the global $\Delta\delta^{18}\text{O}_{\text{sw}}$ record [Sosdian and Rosenthal, 2009] were smoothed (through linear-interpolation) to a common time-step of 5kyr resolution.

Equation 4.1

$$T^* = 16.9 - 4.38 \times (\delta^{18}O_{planktic} - \delta^{18}O_{sw}^*) + 0.1 \times (\delta^{18}O_{planktic} - \delta^{18}O_{sw}^*)^2$$

(T^* is the corrected value of the calcification temperature and $\delta^{18}O_{sw}^*$ is the corrected value of $\delta^{18}O_{sw}$, calculated using equation 4.2. The isotopic paleotemperature equation constants used in the correction are those of *Shackleton* [1974]. The difference in T^* values arising from the use of these constants, rather than those of *Bemis et al.* [1998], as is used in equation 6.1 to calculate MD06-3018 $\delta^{18}O_{sw}$ for later interpretation in chapter 6, is less than 0.2°C for SST values in the range 20-30°C.)

Equation 4.2

$$\delta^{18}O_{sw}^* = \delta^{18}O_{planktic} - 71.0 + 5 \times \sqrt{(196.8 + 0.4 \times T_{Mg/Ca} + 3.3 \times \Delta\delta^{18}O_{global} - 4.0 \times \delta^{18}O_{planktic})}$$

($T_{Mg/Ca}$ is the original, uncorrected Mg/Ca-derived SST value.)

Traditional Mg/Ca - SST calibrations also rely on the assumption that the Mg/Ca ratio of seawater ($Mg/Ca_{(sw)}$) has remained constant through time. Modelling studies question the validity of this assumption, especially for reconstructions extending beyond the middle Pleistocene [*Fantle and DePaolo*, 2005; 2006]. It has been proposed that the effect of varying $Mg/Ca_{(sw)}$ may be corrected for through adjustment of the pre-exponential constant in the Mg/Ca – SST calibration equation (the term a in equation A1.4, appendix 1, §3) by an amount proportional to the change, relative to the modern, in $Mg/Ca_{(sw)}$ [*Medina-Elizalde et al.*, 2008]. A second component to the correction arises from a proposed exponential decrease in the partition coefficient (the term b in equation A1.4) for the incorporation of Mg into foraminiferal calcite with increasing $Mg/Ca_{(sw)}$. The theoretical basis for the partition coefficient correction parameterization is much less certain than that for the pre-exponential one [*Medina-Elizalde et al.*, 2008]. However, the partition coefficient component of the correction never accounts for more than 30% of the total change in reconstructed SST. Both components of the proposed correction are applied here, in the forms proposed by *Medina-Elizalde et al.* [2008] and as given in equation 4.3.

The ‘varying $\delta^{44}\text{Ca}$ ’ form of the modelled $\text{Mg}/\text{Ca}_{(\text{sw})}$ reconstruction from *Fantle and DePaolo* [2006] is used for the correction, although the choice of weathering rate assumption has little effect on the correction over the Pleistocene [*Medina-Elizalde et al.*, 2008]. In order to make the $\text{Mg}/\text{Ca}_{(\text{sw})}$ correction, the MD06-3018 SST reconstruction and the modelled reconstruction of $\text{Mg}/\text{Ca}_{(\text{sw})}$ [*Fantle and DePaolo*, 2006] were smoothed (through linear-interpolation) to an equal time-step of 5kyr resolution.

Equation 4.3

$$T^* = \frac{0.102 \times T_{\text{Mg/Ca}} - \ln\left(\frac{\text{Mg/Ca}_{(\text{sw})}}{4.9623}\right)}{0.102 \times 1.12^{\left(\frac{4.9623 - \text{Mg/Ca}_{(\text{sw})}}{4.9623}\right)}}$$

(The Mg/Ca – SST calibration constants are those of *Anand et al.*, 2003. The term 4.9623 is the zero-age value (in mol/mol) for $\text{Mg}/\text{Ca}_{(\text{sw})}$ in the *Fantle and DePaolo* [2006] model. The numerator contains the pre-exponential correction and the denominator contains the partition coefficient correction, such that as $\text{Mg}/\text{Ca}_{(\text{sw})} \rightarrow 4.9623$, $T^* \rightarrow T_{\text{Mg/Ca}}$.)

4.4 Results

4.4.1 The MD06-3018 Mg/Ca-derived reconstruction of southern Coral Sea SST

The MD06-3018 *G. ruber* Mg/Ca-derived SST reconstruction shows glacial/interglacial variability across the Pleistocene in the range 2-3°C (Fig 4.2A). Over the past five interglacial stages, those of the 100kyr world, reconstructed SST values range from 25.3°C to 25.9°C with an average value of $25.6 \pm 2\sigma=0.6^\circ\text{C}$ (where σ is the standard deviation of the individual stage values). Glacial stage SST minima values over the same interval show an average of $22.6^\circ\text{C} \pm 2\sigma=0.6^\circ\text{C}$, such that the average amplitude of reconstructed glacial/interglacial SST variability over these cycles was $3.0 \pm 2\sigma=0.4^\circ\text{C}$ (where σ is the standard deviation of the individual peak glacial to peak interglacial SST amplitudes within each glacial/interglacial cycle). Prior to MIS 11, the average reconstructed interglacial stage SST value was $24.6 \pm 2\sigma=1.0^\circ\text{C}$, $\sim 1^\circ\text{C}$ cooler on average than those in the 100kyr world. In contrast, the average reconstructed glacial stage SST minima prior to MIS 12 was $23.0 \pm 2\sigma=1.0^\circ\text{C}$, not significantly different, on average, than those in the 100kyr world. Whilst individual cycles prior to the MIS 12/11 transition do show more variability in glacial/interglacial SST amplitude than those after it, the average was significantly lower at $1.7 \pm 2\sigma=1.0^\circ\text{C}$. This change was driven from the interglacial stage values, with only three interglacial stages prior to MIS 11, namely MIS 15, 21 and 31, showing SST values greater than 25 °C. The ‘long-term mean’ is defined here as the 200kyr running box-car average, so as to remove all of the glacial/interglacial variability. This term is seen to vary by less than $\pm 0.5^\circ\text{C}$ around an average value of 23.9°C (with an SEM value of $2\sigma_{\text{SEM}}=0.3^\circ\text{C}$) over the past 1500ka (Fig 4.2A).

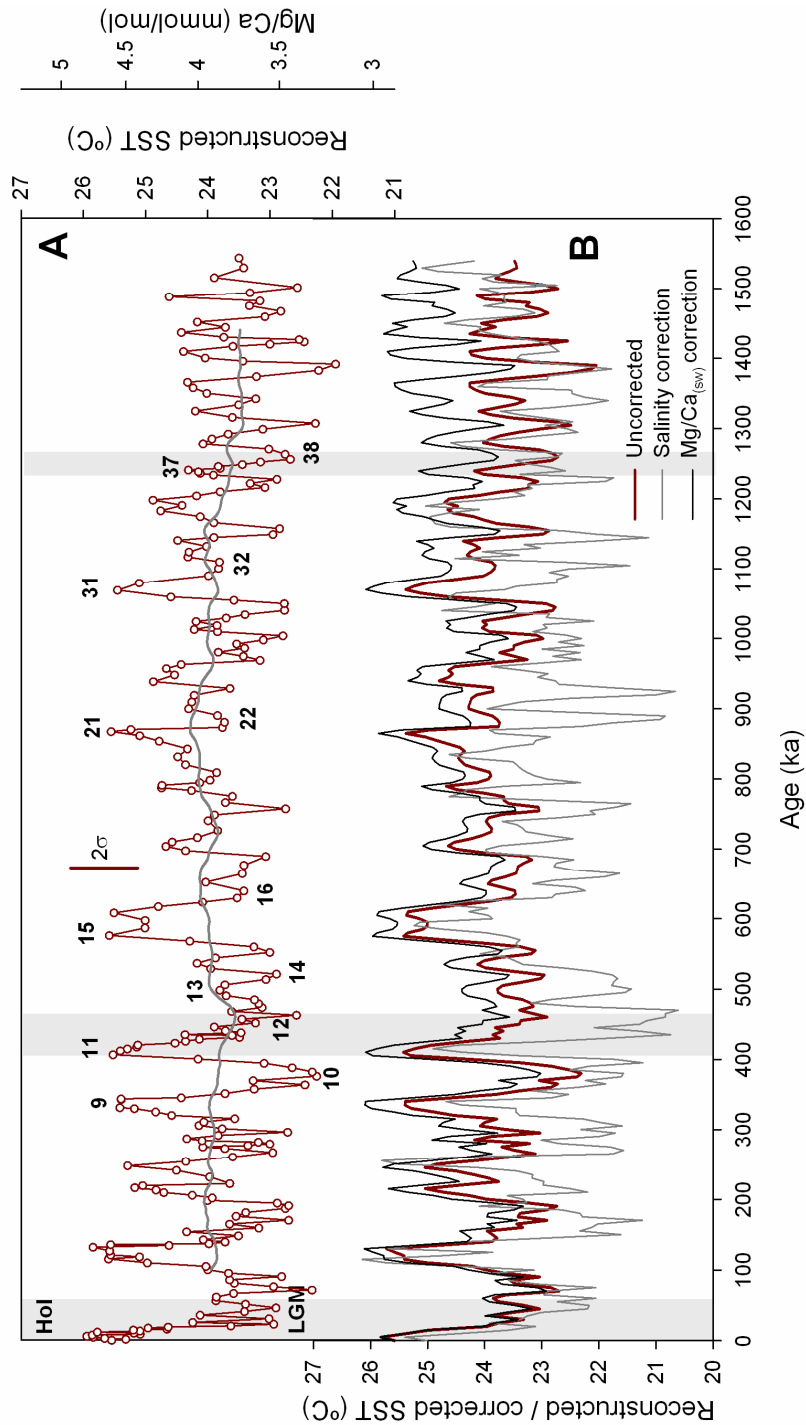


Figure 4.2 A) The MD06-3018 Mg/Ca-derived SST reconstruction. Vertical bar shows the $2\sigma_r$ sample reproducibility error, as defined in §3.1. The dark grey line shows the 200kyr running mean. B) Plots of the SST reconstruction, uncorrected and using the proposed salinity [Mathien-Blard and Bassinot, 2009] and Mg/Ca_(sw) [Medina-Elizalde et al., 2008] corrections. All records are at 5kyr resolution following smoothing through linear interpolation. Glacial terminations shown in greater detail in Figure 4.3 are highlighted with grey boxes and numbers on upper plot refer to selected MIS.

4.4.2 The down-core effects of the salinity and Mg/Ca_(sw) corrections

The salinity and Mg/Ca_(sw) corrected MD06-3018 SST reconstructions are presented and compared to the uncorrected one at 5kyr resolution in *Figure 4.2*. Application of the *Mathien-Blard and Bassinot* [2009] salinity correction does not change the reconstructed interglacial stage SST values by more than ~1°C, but does lead to more substantial shifts in the glacial stage values, especially over the past ~1000ka (*Fig 4.2B*). These offsets are almost always in the sense of colder values and are as large as 4°C during the interval 900-400ka, coincident with the latter part of the MPT. This has the effect increasing the average glacial/interglacial SST amplitudes during the 100kyr world to $4.1 \pm 2\sigma = 1.4^\circ\text{C}$ and to $2.2 \pm 2\sigma = 1.4^\circ\text{C}$ during the MPT and 40kyr worlds combined. Thus, whilst the salinity corrected reconstruction shows higher glacial/interglacial amplitudes than the uncorrected reconstruction, the proportional increase in glacial/interglacial SST amplitude across the MPT is only slightly increased, from ~40% to ~50%.

Application of the *Medina-Elizalde et al.* [2008] Mg/Ca_(sw) correction does not significantly change the glacial/interglacial SST amplitude at any point in the record, but does lead to warmer reconstructed SST values for all past MIS. This effect becomes more pronounced with age, as a consequence of the form of the modelled Mg/Ca_(sw) curve [*Fantle and DePaolo*, 2006], with offsets exceeding 1°C arising prior to ~1200ka. The correction has the effect, therefore, of also changing the >100kyr time-scale trends present in the SST reconstruction. In particular it removes the very slight warming trend seen in the uncorrected data prior to ~1000ka (*Fig 4.2B*) and replaces it instead with a more pronounced cooling trend, which persists over the duration of the record. This, in turn, means that the statistically significant increase in average interglacial MIS SST values seen in the uncorrected reconstruction between the past five climatic cycles and those during the MPT and the 40kyr world is not maintained under the Mg/Ca_(sw) correction.

4.4.3 Transfer function estimates of seasonal SST compared to high-resolution Mg/Ca paleothermometry across glacial terminations

The 1-2kyr resolution Mg/Ca-derived SST data is compared with the MAT-derived winSST and sumSST estimates for the LGM/Hol, MIS 12/11 and MIS 38/37 glacial terminations in *Figure 4.3*. In the case of the core-top transfer function estimates of seasonal SST, these are seen to be well within statistical error of the WOA2005 (0m depth) seasonal SST values for the core-site [*Locarnini et al.*, 2006]. In all three studied glacial stages the estimated seasonality (calculated as sumSST – winSST, with an error calculated by propagation of the statistical uncertainties on the two seasonal terms) is seen to have increased, relative to the corresponding interglacial, for example, from $3.5 \pm 2.2^\circ\text{C}$ for the late Holocene to $6.0 \pm 2.2^\circ\text{C}$ for the LGM. Whilst the propagated statistical uncertainties associated with these seasonality estimates are seen to be relatively large, the replication of the same general pattern across all of the three glacial stages considered here suggests that the increase in seasonality is a real effect, arising from greater winter season cooling during glacial stage conditions.

For all the studied terminations the MAT-derived mean-annual SST estimates (calculated as the mean of sumSST and winSST) are seen to always lie within the $\pm 2\sigma_r$ envelope for the uncorrected Mg/Ca-derived values (*Fig 4.3*). During the LGM/Hol transition there is no systematic difference between the Mg/Ca-derived values and the mean-annual MAT values. For MIS 12/11 the former are generally slightly warmer and for MIS 38/37 they are cooler by $\sim 1^\circ\text{C}$. During the LGM/Hol transition both the corrected and uncorrected Mg/Ca-derived SST estimates plot within the reproducibility error of the uncorrected values and are thus not distinguishable (at the $2\sigma_r$ level) from either each other, or the MAT-derived values. For MIS 12/11 the MAT-derived mean-annual SST values are closer to the uncorrected Mg/Ca values than to either of the corrected set of values. The salinity corrected Mg/Ca values plot between the cold season and MAT-derived mean-annual SST values, whereas the $\text{Mg/Ca}_{(\text{sw})}$ corrected values plot between the warm season and mean-annual MAT-derived values. For MIS 38/37 the mean-annual MAT-

derived values are closest to the $Mg/Ca_{(sw)}$ corrected values and consistently warmer than both the uncorrected and salinity corrected values.

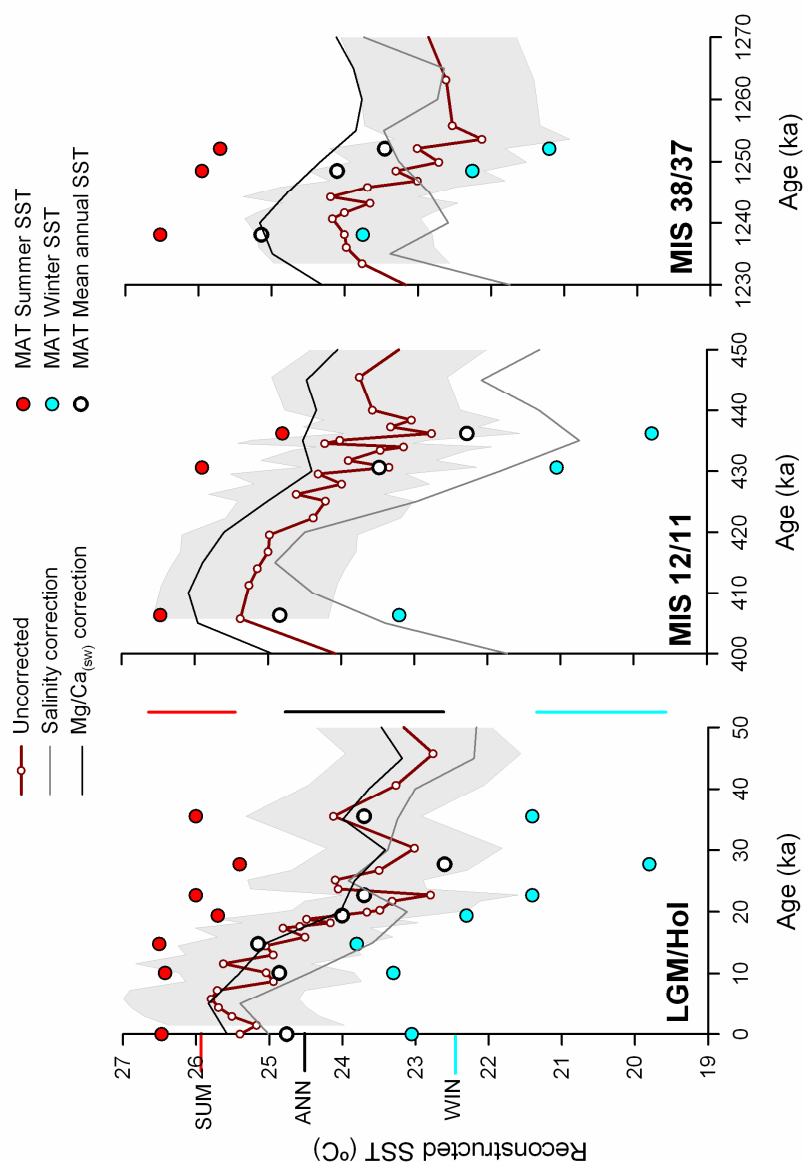


Figure 4.3 Comparison of Mg/Ca -derived and MAT-derived SST estimates across the LGM/Hol, MIS 12/11 and MIS 38/37 terminations. Lines show uncorrected Mg/Ca SST data (bold red line, at 1-2kyr resolution), salinity corrected data (grey line, at 5kyr resolution) and $Mg/Ca_{(sw)}$ corrected data (black line, at 5kyr resolution). Grey shaded area shows $\pm 2\sigma_r$ reproducibility error envelope for the uncorrected Mg/Ca -derived SST reconstruction. On the LGM/Hol plot, horizontal bars at the axis show WOA2005 SST values for 0m depth at the core-site [Locarnini *et al.*, 2006]. Vertical bars show statistical uncertainties on the MAT-derived SST estimates; the statistical uncertainty for the mean-annual SST estimate was calculated using standard error propagation formulae.

4.5 Discussion

4.5.1 Does the MD06-3018 Mg/Ca-derived SST reconstruction record mean-annual SST?

The observation that the MAT-derived mean-annual SST estimates across the LGM/Hol transition remain within the $\pm 2\sigma_r$ reproducibility error of the down-core Mg/Ca-derived SST reconstruction (*Fig 4.3*) suggests that the geochemical values do not contain a significant seasonal bias. Were this to have been the case, a warm bias in the Mg/Ca-derived reconstruction should have been persistent across the Holocene and enhanced during the LGM part of the record, as this shows enhanced seasonality in the MAT-derived seasonality estimates. Furthermore, the MD06-3018 Mg/Ca- and MAT-derived estimates of LGM/Hol mean-annual SST change compare well, both with each other and with previous estimates in the New Caledonia region using a range of transfer function methods (1-3°C) [*Barrows and Juggins, 2005*] and the organic geochemical U^{k}_{37} paleothermometer ($\sim 2^\circ\text{C}$) [*Tachikawa et al., 2009*]. If it were the case that the *G. ruber* based Mg/Ca paleothermometer was more sensitive to seasonality biases than these other methods, then it should have recorded smaller amplitudes of SST change. What is instead seen is a Mg/Ca-derived reconstructed LGM/Hol SST amplitude that is slightly greater, but well within the various proxy reproducibility errors of the other methods. It also follows that a seasonal bias is probably not the cause of the offset between the core-top Mg/Ca-derived SST and modern mean-annual SST, as described in §3.1.

Past variations in seasonality, such as those inferred for the three glacial stages for which MAT-derived SST seasonality estimates are presented in *Figure 4.3*, may have arisen as a consequence of changes to the annual insolation cycle as a consequence of orbital variations, or through regional climatic factors such as changes in ocean circulation. The former may be quantified using the difference between mid-summer and mid-winter insolation at 23°S from a computed orbital solution [*Laskar et al., 2004*], and this record is seen to be dominated by the precession cycle and its modulation by eccentricity (*Fig 4.4B*). However, no

systematic correlation between the seasonal insolation difference and MAT-derived SST seasonality is present either within or between any of the three studied terminations (*Fig 4.4*). This suggests that regional climatic factors tied to the glacial/interglacial cycles, rather than orbitally derived insolation changes, led to the increases in glacial stage seasonality. However, regardless of the origin of the seasonality changes, the data presented here shows that they did not compromise the capacity of the down-core MD06-3018 Mg/Ca-derived SST reconstruction to provide a reliable guide to variability in mean-annual SST.

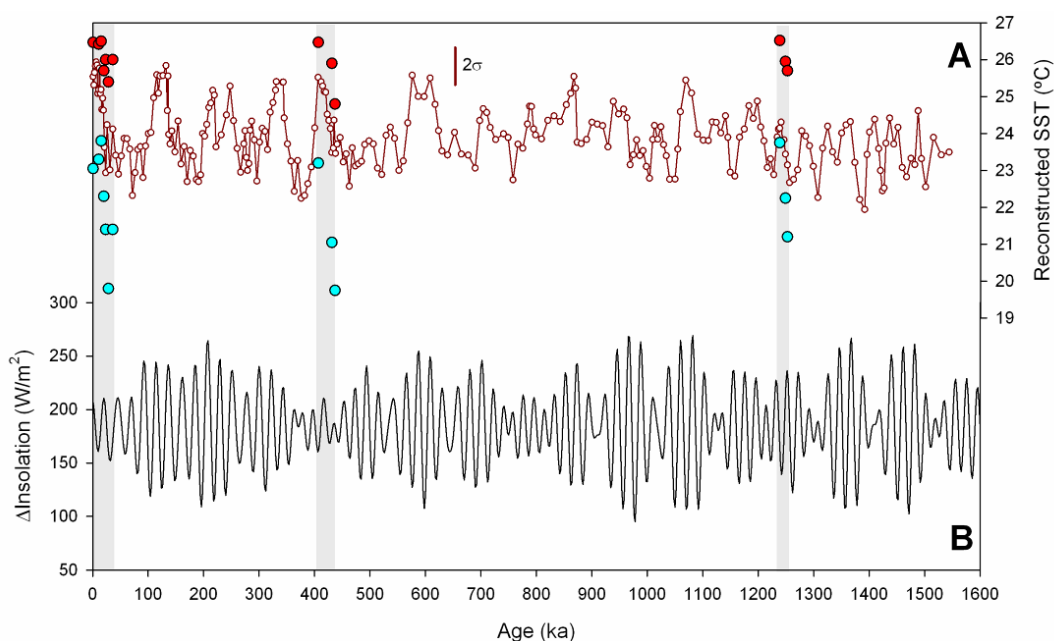


Figure 4.4 A) The MD06-3018 Mg/Ca-derived SST reconstruction and MAT-derived seasonal SST estimates for the three glacial terminations (grey boxes) shown in *Figure 4.3*. B) Difference in insolation between Jan21 and Jul21 for 23°S, from the La03 orbital solution [*Laskar et al.*, 2004].

4.5.2 Assessing the validity of the proposed Mg/Ca corrections

The independent MAT-derived estimates of mean-annual SST provide a set of comparison points with which to evaluate the relative down-core ‘skill’ of the corrected and uncorrected Mg/Ca-derived mean-annual SST records. The proposed salinity correction [Mathien-Blard and Bassinot, 2009] leads to generally enhanced glacial/interglacial amplitudes of SST variability across the duration of the MD06-3018 record (*Fig 4.2B*). During both the LGM/Hol and MIS 38/37 transitions this does not lead to a significant change, relative to the uncorrected record, in either the interglacial or glacial stage SST values (*Fig 4.3*). However, during the MIS 12/11 transition significantly colder glacial values are predicted and these then plot well below the MAT-derived mean-annual SST value for MIS 12 and closer to the winSST value. This suggests that either there is a flaw in the salinity correction methodology, as employed here, possibly arising from the assumption of a constant $\delta^{18}\text{O}_{\text{sw}} - \text{salinity}$ relationship or from the correlation of age-models involved in the $\Delta\delta^{18}\text{O}_{\text{sw}}$ subtraction, or alternatively that the transfer function method is not performing well this far back in time. The latter explanation is considered less likely, as no significant faunal turnover in the planktic foraminifera has occurred between MIS 12 and the Holocene. Furthermore, in the case of the core-top, the salinity correction, whilst shifting the reconstructed SST values towards the WOA2005 mean-annual value, only removes ~30% of the offset (*Fig 4.3*). This suggests that any systematic salinity bias within the calibration function, as discussed in §3.1, is not the dominant source of the core-top to modern mean-annual SST offset.

The main effect of the proposed $\text{Mg}/\text{Ca}_{(\text{sw})}$ correction [Medina-Elizalde *et al.*, 2008] is to shift progressively older reconstructed SST values towards progressively higher values (*Fig 4.2B*). This effect is negligible at the LGM/Hol transition and falls within the reproducibility error envelope of the uncorrected values at the MIS 12/11 transition (*Fig 4.3*). For the MIS 38/37 transition, the correction leads to significantly improved agreement with the MAT-derived mean-annual SST values and this provides tentative empirical support for the proposed form and amplitude of the $\text{Mg}/\text{Ca}_{(\text{sw})}$ correction [Medina-Elizalde *et al.*, 2008].

4.5.3 The ‘combined uncertainty’ associated with the down-core Mg/Ca-derived SST reconstruction

The Mg/Ca paleothermometer, as applied to the MD06-3018 core-site, was shown in §5.1 to have not been prone to significant and/or temporally variable seasonality biases. This does not, however, mean that temporal variability in seawater chemistry factors, namely salinity and Mg/Ca_(sw), might not have compromised the down-core applicability of the core-top to modern SST calibration, leading to the sample reproducibility uncertainty representing a significant underestimation of the real proxy uncertainty.

To develop a method for better estimating the ‘true’ proxy uncertainty, it is now assumed that both the salinity and Mg/Ca_(sw) corrections provide equally skilful estimates of mean-annual SST to the uncorrected Mg/Ca-derived reconstruction. The data comparison exercise in §5.2 suggests that there are some reasons to suspect this is not, in fact, the case. However, the underlying theory behind both corrections is accepted here as being valid and given the large uncertainties also associated with the MAT-derived SST estimates, the present study cannot provide any firm (and non-circular) conclusions regarding the validity of either correction method. Thus, a conservative approach is favoured, not as offering a precise quantification of the true ‘combined proxy uncertainty’, but as providing a better lower bound to it. Given that the uncorrected Mg/Ca-derived SST reconstruction generally plots between the two corrected ones (*Fig 4.2B*), and that all three reconstructions are based ultimately on the same underlying Mg/Ca data, the revised estimate of mean-annual SST, to which the combined uncertainty concept applies, is defined as the mean of the maximum and minimum SST values derived from the three methods. This reconstruction is referred to as the ‘revised Mg/Ca reconstruction’.

The combined uncertainty, denoted as σ_c , arises from a combination of the reproducibility uncertainty and that arising from down-core variation in the non-SST controlling factors. The ‘correction’ approach described in §3.4 provides a method to quantify this latter uncertainty. The magnitude of the correction uncertainty is defined here as half the difference in SST values between the maximum and minimum estimates. The combined uncertainty at any given time-step is then defined as being whichever is greater of the correction uncertainty and the sample reproducibility uncertainty at that point. It is seen that the combined uncertainty exceeds the reproducibility uncertainty by nearly a factor of two ($2\sigma_c \sim 2^\circ\text{C}$) during the intervals of high correction uncertainty, which coincide in turn with intervals of the greatest interglacial to interglacial stage variability in SST, notably 1200-800ka and 500-300ka (*Fig 4.5A/B*). Furthermore, the peaks in combined uncertainty are seen to generally coincide with glacial stages, as can be seen by comparing *Figure 4.5B* with the MD06-3018 $\delta^{18}\text{O}_{\text{benthic}}$ record in *Figure 4.5C*, principally due to the large SST differences arising between the salinity correction and the other two reconstructions at these times. In contrast, the combined uncertainty for all interglacial stages, excepting MIS 7, 13, 31 and 43, is seen to not exceed 130% of the reproducibility uncertainty ($2\sigma_c < 1.3^\circ\text{C}$).

The combined uncertainty approach, as defined here, yields a lower-bound estimate to the true combined proxy uncertainty as it does not account for the propagation of the reproducibility uncertainty onto the correction uncertainty when the latter is larger in magnitude. Other factors both known, but neglected here, such as preferential carbonate dissolution and the effect of carbonate ion concentrations (as discussed in appendix 1, §3), and those as yet unknown, will also lead to further underestimation of the true proxy uncertainty. However, the combined uncertainty estimates, as plotted in *Figure 4.5D*, provide a more realistic lower-bound than use of the reproducibility uncertainty alone. These combined uncertainty estimates are now used to consider the context problem for this chapter, namely whether the revised MD06-3018 Mg/Ca-derived SST reconstruction can resolve significant changes in SST, such as might have limited middle Pleistocene reef expansion.

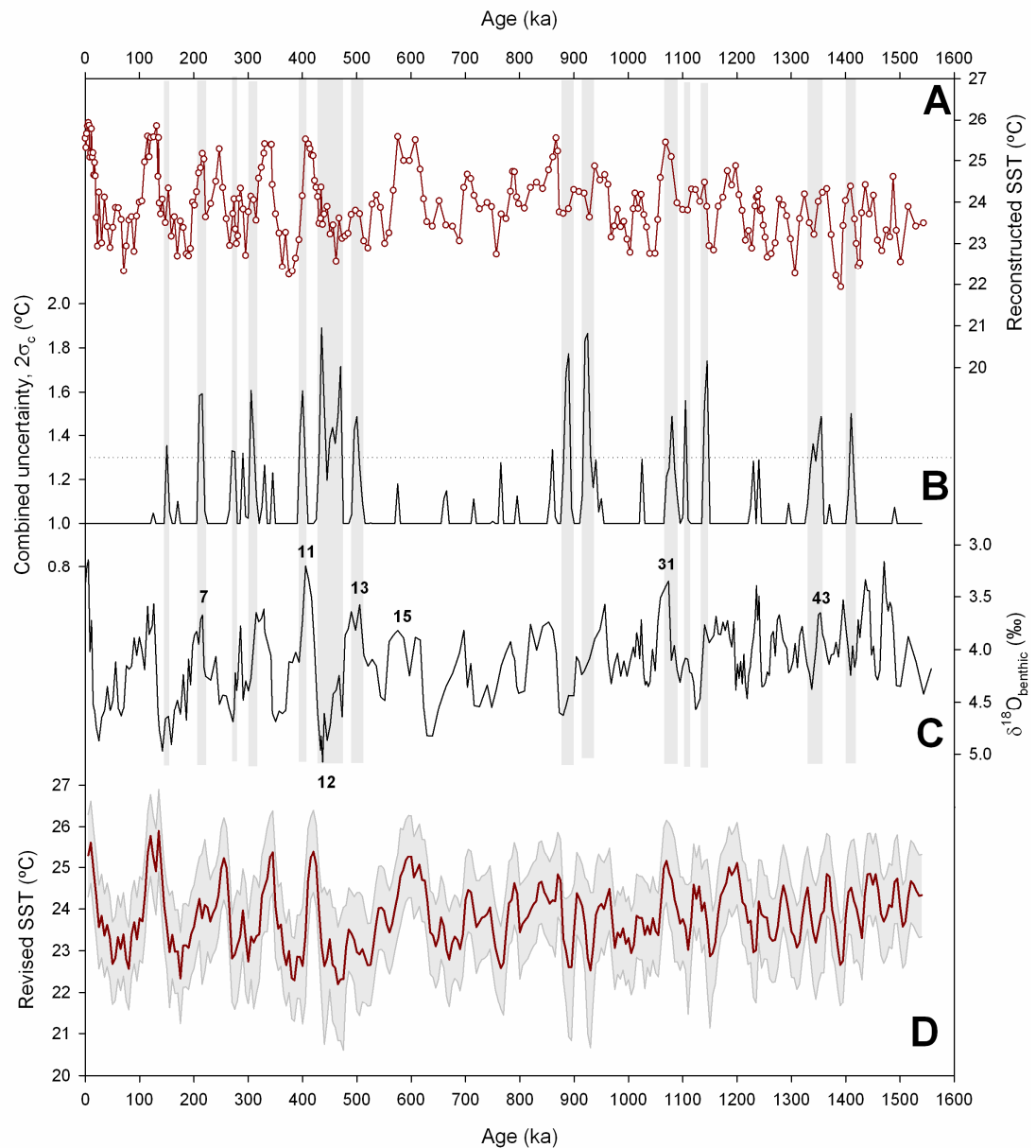


Figure 4.5 **A)** The uncorrected MD06-3018 Mg/Ca-derived SST reconstruction. **B)** The calculated combined uncertainty ($2\sigma_c$) in the SST reconstruction. **C)** The MD06-3018 $\delta^{18}\text{O}_{\text{benthic}}$ record, shown to highlight the relative timing of the variability in σ_c in relation to the MIS chronology. Numbers show selected MIS mentioned in the text. The grey boxes on plots A-C highlight intervals for which σ_c , as shown in B, exceeds the reproducibility uncertainty by $>30\%$. **D)** The revised MD06-3018 SST reconstruction with the $\pm 2\sigma_c$ uncertainty envelope.

4.5.4 Did regional climate change limit middle Pleistocene reef expansion in the Coral Sea?

The revised MD06-3018 Mg/Ca-derived SST reconstruction shows a generally stable southern Coral Sea climate with mean-annual SST values that did not drop below 20°C during any MIS over the past 1600ka, even when the combined proxy uncertainty is considered (*Fig 4.5D*). This implies that mean-annual SST is unlikely to have provided a first order control on reef growth at 23°S on the >100kyr time-scale, in agreement with the previous U^{k}_{37} based SST reconstruction from 15°S on the GBR [*Lawrence and Herbert, 2005*]. During glacial stages however, if ‘at least modern’ seasonality is assumed, as is supported by analogy to the three glacial stage MAT-derived estimates, then winter season SST may well have dropped below 18°C. This suggests that glacial stage reef growth in the southern Coral Sea may have been partly limited by seasonal SST, as well as by sea-level and substrate availability.

Given that only interglacial stage aged NCBR material is preserved in drill cores [*Cabioch et al., 2008*], robust evaluation of potential changes in interglacial stage SST across the MPT period is required to robustly address whether climatic changes could plausibly have played a role in the middle Pleistocene reef expansion. When considering the differences between the average SST values associated with groups of values, such as interglacial stages during and after the MPT, the combined uncertainty for each average group value is defined as whichever is larger out of the average amplitude of the correction uncertainty envelope for the interval within which the values lie and the standard error on the mean arising from the sample reproducibility uncertainties. The emergence of higher amplitude 100kyr mode cycles in southern Coral Sea SST at ~500ka, as described in §4.1, meant that interglacial values from MIS 11 onwards were, on average, ~1°C warmer than those prior to this in the uncorrected MD06-3018 Mg/Ca-derived SST reconstruction. This difference is seen to be significant at the 95% confidence level (using a student-*t* test) when using the standard error on the mean arising from the reproducibility error.

When the revised SST reconstruction and combined proxy uncertainty are considered, the effect of the $\text{Mg}/\text{Ca}_{(\text{sw})}$ correction envelope is to make the interglacial stages prior to $\sim 1000\text{ka}$ as warm as those of the past 500ka (*Fig 4.5D*), removing any statistical significance from the difference between the 40kyr and 100kyr world interglacial SST values. If the 100kyr world interglacials are compared to those of the MPT interval (1200-500ka) alone, during which the effect of the $\text{Mg}/\text{Ca}_{(\text{sw})}$ correction was less pronounced, then no statistically significant difference at the 95% confidence level is seen against the combined uncertainty, even though this is now given by the standard error on the mean of the reproducibility error. Therefore, when a more realistic estimate of the true proxy uncertainty is used, no statistically significant shift in interglacial stage climate can be described between any relevant groupings of interglacial MIS over the MPT interval.

The interval 600-400ka, preceding MIS 11 and the proposed timing of NCBR expansion [*Cabioch et al., 2008*] is, however, marked by the largest inter-MIS variability in reconstructed interglacial SST values seen anywhere in the uncorrected MD06-3018 reconstruction. In particular, the coolest interglacial value of $23.8 \pm 2\sigma_{\text{r}}=1.0^{\circ}\text{C}$ is seen at MIS 13, immediately preceding the first true 100kyr mode interglacial value of $25.6 \pm 2\sigma_{\text{r}}=1.0^{\circ}\text{C}$ seen at MIS 11 (*Fig 4.5A*). The difference in SST between these two stages is 1.8°C , with a propagated uncertainty of $\pm 2\sigma_{\text{diff}}=1.4^{\circ}\text{C}$. However, this interval is also seen to coincide with one of the intervals of high correction uncertainty (*Fig 4.5B*), and hence high combined uncertainty (*Fig 4.5D*). When the revised SST reconstruction and combined proxy uncertainty are considered, the MIS 13 value becomes $23.5 \pm 2\sigma_{\text{c}}=1.5^{\circ}\text{C}$ and the MIS 11 value becomes $25.4 \pm 2\sigma_{\text{c}}=1.0^{\circ}\text{C}$, leading to a difference of 1.9°C , with an enhanced propagated uncertainty of $2\sigma_{\text{diff}}=1.8^{\circ}\text{C}$. Whilst this difference remains significant at the 95% confidence level, implying that a climatic change in interglacial climate did occur over between MIS 13 and MIS 11, the magnitude of the climatic shift cannot be robustly constrained to exceed even 0.1°C .

In summary, no significant SST variability in the Mg/Ca-derived southern Coral Sea reconstruction can be detected on either the >100kyr or interglacial to interglacial time-scales over the MPT interval when using the revised form of the SST reconstruction and the combined uncertainty, as shown in *Figure 4.5D*. Assuming that changes in mean-annual SST of at least several °C would have been required to exert a first-order control on reef development at 23°S, then it follows that regional change in mean-annual SST is unlikely to have played a first-order role in limiting reef expansion prior to the middle Pleistocene. However, in the absence of better constraints on past seasonality, and given the comparable values of the combined uncertainty term ($2\sigma_c \sim 1\text{-}2\text{ }^\circ\text{C}$) in relation to the environmental changes of interest, it is possible that seasonal SST changes may have played some role in the expansion, even though these are not resolvable in the MD06-3018 reconstruction. Future, higher temporal resolution SST reconstructions over the MIS 15 – MIS 11 interval, especially those including estimates of seasonality, are required to better characterize the pattern of climate evolution over this interval and hence, its potential role in limiting reef development.

4.6 Conclusions

The MD06-3018 *G. ruber* Mg/Ca-derived reconstruction of southern Coral Sea SST over the past 1600ka shows no significant >100kyr time-scale trends, but glacial/interglacial variability of 2-3°C across the record. The comparison of these estimates of reconstructed SST with other, independent estimates based on planktic foraminiferal transfer functions, shows that there is no evidence for a persistent seasonal SST bias away from mean-annual conditions in the geochemical record. The effect on the MD06-3018 Mg/Ca-derived SST reconstruction of proposed corrections for the effects of variations in past salinity and Mg/Ca_(sw) was also considered. The salinity correction has the effect of significantly lowering the reconstructed glacial stage SST values and thus increasing the amplitudes of glacial/interglacial SST variability. However, this correction is less consistent than the uncorrected values with the transfer function estimates for glacial stage mean-annual SST. The Mg/Ca_(sw) correction has no significant effect on glacial/interglacial variability but does change the >100kyr time-scale trends present in the data, especially prior to ~1000ka. The Mg/Ca_(sw) corrected SST values are more consistent than the uncorrected ones with the transfer function estimates in the early Pleistocene, suggesting that such a correction may be merited on this time-scale. Taken together with the method reproducibility error, the spread of SST values associated with the two corrections methods allows for a more realistic lower-bound estimate of the real combined proxy uncertainty to be made. This ‘combined uncertainty’ term is seen to be generally greater for the glacial than interglacial stage values and to vary in amplitude with age, the greatest combined uncertainties being during the early (1200-800ka) and later (500-300ka) parts of the MPT.

This chapter has shown that when the combined uncertainty is considered, no statistically significant change in mean-annual SST can be resolved, either on the >100kyr time-scale or between individual (or grouped) interglacial stages over the MPT. Whilst it is unlikely that changes in regional climate provided a first-order limitation to middle Pleistocene reef expansion in the Coral Sea, the uncertainties associated with the Mg/Ca paleothermometry method mean that this question cannot

be unequivocally addressed at present. The potential implications for the global carbon-cycle of the absence of a regional climatic control on reef expansion are, however, considered further in chapter 7, §4. The potential regional climatic mechanisms by which the observed increases in glacial stage SST seasonality, as described in §5.1, could have occurred are also considered in chapter 7, §2.

The following two chapters now take the MD06-3018 Mg/Ca-derived SST reconstruction and characterise the >100kyr (chapter 5) and 10-100kyr (chapter 6) time-scale variability present in the record and the significance of these patterns for the evolution of global climate over the MPT. In both chapters, the uncorrected form of the SST reconstruction is used (i.e. that in *Fig 4.2A*), in order to allow consistent comparison with other published reconstructions. However, the sensitivity of the conclusions drawn in these chapters to the revised SST reconstruction and combined uncertainty approach (as presented in *Fig 4.5D*) is also considered in both cases.

Chapter 5: Inter-hemispheric asymmetry in the early Pleistocene Pacific warm pool

Chapter abstract

The position of the southern boundary of the Pacific warm pool is shown to have been stable, on the >100kyr time-scale, over at least the past 1500ka, based upon the planktic foraminiferal MD06-3018 Mg/Ca-derived reconstruction of sea surface temperature in the southern Coral Sea. This contrasts with previous reconstructions showing warm pool contraction from the north and east and consequently means that the early Pleistocene warm pool was more hemispherically asymmetric than its present configuration. The latter was not established until ~1000ka, supporting a strengthening of the northern Hadley Cell, which was not replicated in its southern counterpart, prior to the early Pleistocene intensification of northern hemisphere glaciation.

5.2 Introduction

As the largest body of warm water on the planet, the Indo-Pacific warm pool is a key source of both heat and moisture to the atmosphere, which acts to transport those properties polewards. Temporal variability in these fluxes plays an important role in global climate on time-scales ranging from the seasonal to the geological [Koutavas *et al.*, 2002; Ravelo *et al.*, 2004]. The modern extent of the warm pool, defined here as the region for which mean-annual SST exceeds 28°C, is limited to the western Pacific and eastern Indian Ocean. Within the Pacific it is hemispherically asymmetric, extending between ~20°N and ~15°S (Fig 5.1). Variability in the meridional extent of the past warm pool implies changes not only to meridional ocean/atmosphere heat and moisture fluxes but also to the wider low-latitude system, as the subtropics are a significant source for the cool upper-ocean water masses that upwell in the modern Eastern Equatorial Pacific (EEP) [Brierley *et al.*, 2009]. The extent of past inter-hemispheric warm pool asymmetry is also important as the relative strength of the two branches of the meridional atmospheric Hadley circulation is a function of the latitudinal position of maximum atmospheric convergence in the tropics, which is sensitive to the extent of extra-tropical SST asymmetry [Broccoli *et al.*, 2006].

Reconstructions of Pliocene SST distributions in the Pacific show substantially reduced zonal equatorial [Wara *et al.*, 2005] and meridional equatorial-subtropical [Brierley *et al.*, 2009] gradients, implying a significantly expanded warm pool and a permanent ‘El-Niño like’ state (on the >100kyr time-scale) at that time [Wara *et al.*, 2005; Fedorov *et al.*, 2006]. Since ~3000ka the planet has experienced a general global cooling, the onset and intensification of Northern Hemisphere Glaciation (NHG) and warm pool contraction [Ravelo *et al.*, 2004; Wara *et al.*, 2005; Jia *et al.*, 2008]. The timing of these various climatic changes was not, however, synchronous, as described in chapter 1, §7.1. Continuous down-core reconstructions of Plio-Pleistocene SST from the equatorial Pacific show that, by ~1000ka, the modern tropical SST distribution was broadly established with an equatorial gradient of 4-5°C between the Western Equatorial Pacific (WEP) and the cooler, upwelled

waters of the EEP (Fig 5.1) [Wara *et al.*, 2005; Lawrence *et al.*, 2006; Dekens *et al.*, 2008]. The associated onset of significant zonal atmospheric Walker Circulation is thought to have occurred over the interval 2000-1500ka [Ravelo *et al.*, 2004]. In contrast, the last significant period of northern high-latitude deep-water cooling and ice-volume expansion occurred at 1200-850ka [Sosdian and Rosenthal, 2009] and 940-900ka [Mudelsee and Schulz, 1997] respectively. The relative timing of these changes has led to the suggestion that the early Pleistocene reorganization of the low-latitude ocean/atmosphere circulation system may have played an important role in the intensification of NHG and the origins of the MPT [McClymont and Rosell-Mele, 2005; Jia *et al.*, 2008].

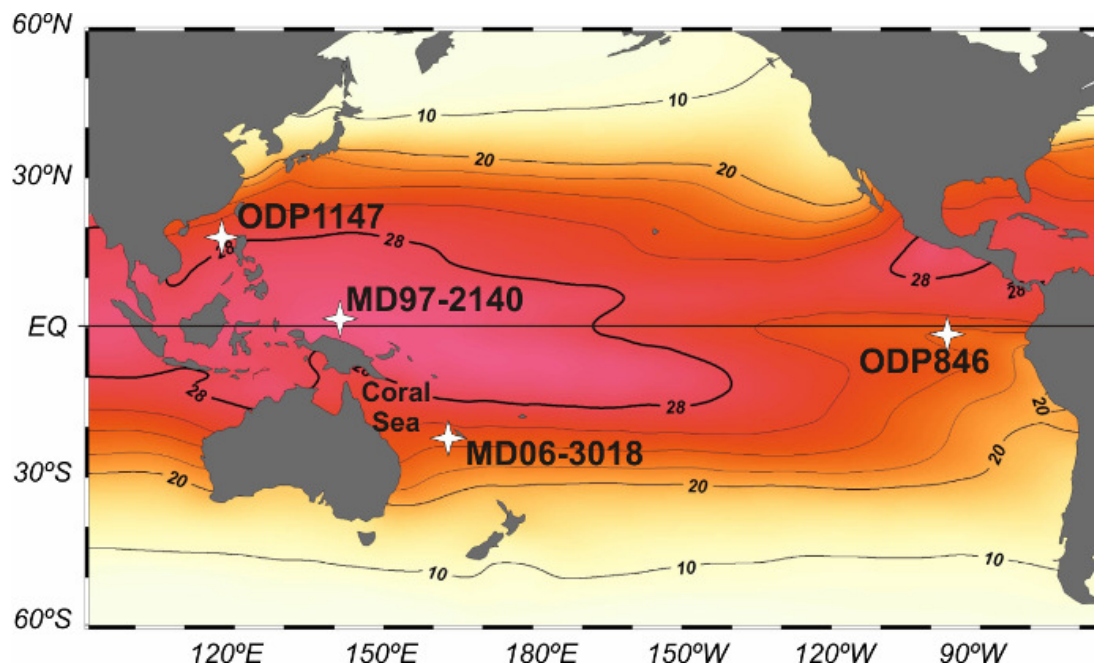


Figure 5.1 Map of the modern Pacific mean-annual SST distribution from WOA2005 data [Locarnini *et al.*, 2006], plotted using the ODV software [Schlitzer, 2007]. The unlabeled contour interval is 2°C. Full details of the core locations are given in Table 5.1.

The evaluation of this hypothesis relies upon reconstruction of meridional as well as zonal low-latitude SST gradients. The evolution of the SST gradient between the equator and the northern subtropics in the western Pacific has been shown to closely resemble that of the zonal equatorial gradient, including a rapid increase prior to ~1000ka [Jia *et al.*, 2008]. As modelling studies suggest that increasing equatorial-subtropical SST gradients lead to reductions in air temperature and increases in precipitation over North America [Brierley and Fedorov, 2010], this supports a potential low-latitude control on the intensification of NHG. The mechanism for such a connection potentially relates to the positive correlation between underlying meridional SST gradients and Hadley Cell strength [Rind and Perlwitz, 2004; Brierley *et al.*, 2009].

This chapter seeks to establish whether the early Pleistocene phase of warm pool contraction was hemispherically symmetric and what impact any such changes may have had on poleward heat and moisture transport prior to the intensification of NHG and the MPT. In order to achieve this, the >100kyr trends in the MD06-3018 reconstruction of subtropical southwest Pacific SST are evaluated over the middle/late Pleistocene and compared to those present in existing reconstructions both the equatorial band and the subtropical northwest Pacific. The MD06-3018 core site lies to the south of the modern warm pool, such as to be sensitive to past fluctuations in the southern extent of warm pool influence.

5.3 Comparison of the MD06-3018 SST reconstruction to others from the low-latitude Pacific

The long-term mean of the MD06-3018 Mg/Ca derived reconstruction of mean-annual SST was defined in the previous chapter as the 200kyr running box-car average, so as to remove all of the glacial/interglacial variability. This term is seen to vary by less than $\pm 0.5^{\circ}\text{C}$ around an average value of 23.9°C (with an SEM value of $2\sigma_{\text{SEM}}=0.3^{\circ}\text{C}$) over the past 1500ka (*Fig 4.2A*). Both the average long-term SST value and the absence of any long-term trends exceeding $\pm 0.5^{\circ}\text{C}$ over the duration of the record are seen to be insensitive to the combined uncertainty concept, namely allowing for uncertainties arising from past fluctuations in salinity and $\text{Mg}/\text{Ca}_{(\text{sw})}$, and hence to remain unchanged in the revised form of the SST reconstruction (*Fig 4.5D*). To place the MD06-3018 reconstruction of southern Coral Sea SST in a Pacific context it is compared in *Figure 5.2* to existing SST reconstructions from the WEP (MD97-2140 [*de Garidel-Thoron et al., 2005*]), South China Sea (ODP 1147 [*Jia et al., 2008*]) and EEP (ODP 846 [*Lawrence et al., 2006*]) (locations are given in *Fig 5.1* and *Table 5.1*).

Core	Latitude	Longitude	Water depth	Temporal resolution	SST proxy	References
MD06-3018	23°00'S	166°09'E	2470m	~5kyr	Mg/Ca	Present study
MD97-2140	2°02'N	141°46'E	2550m	~5kyr	Mg/Ca	<i>de Garidel-Thoron et al. [2005]</i>
ODP 846	3°06'S	90°49'W	3300m	~3kyr	U^{k}_{37}	<i>Lawrence et al. [2006]</i>
ODP 1147	18°50'N	116°33'E	3250m	~20kyr	U^{k}_{37}	<i>Jia et al. [2008]</i>

Table 5.1 Locations of the sediment core records used in both this chapter and chapter 6.

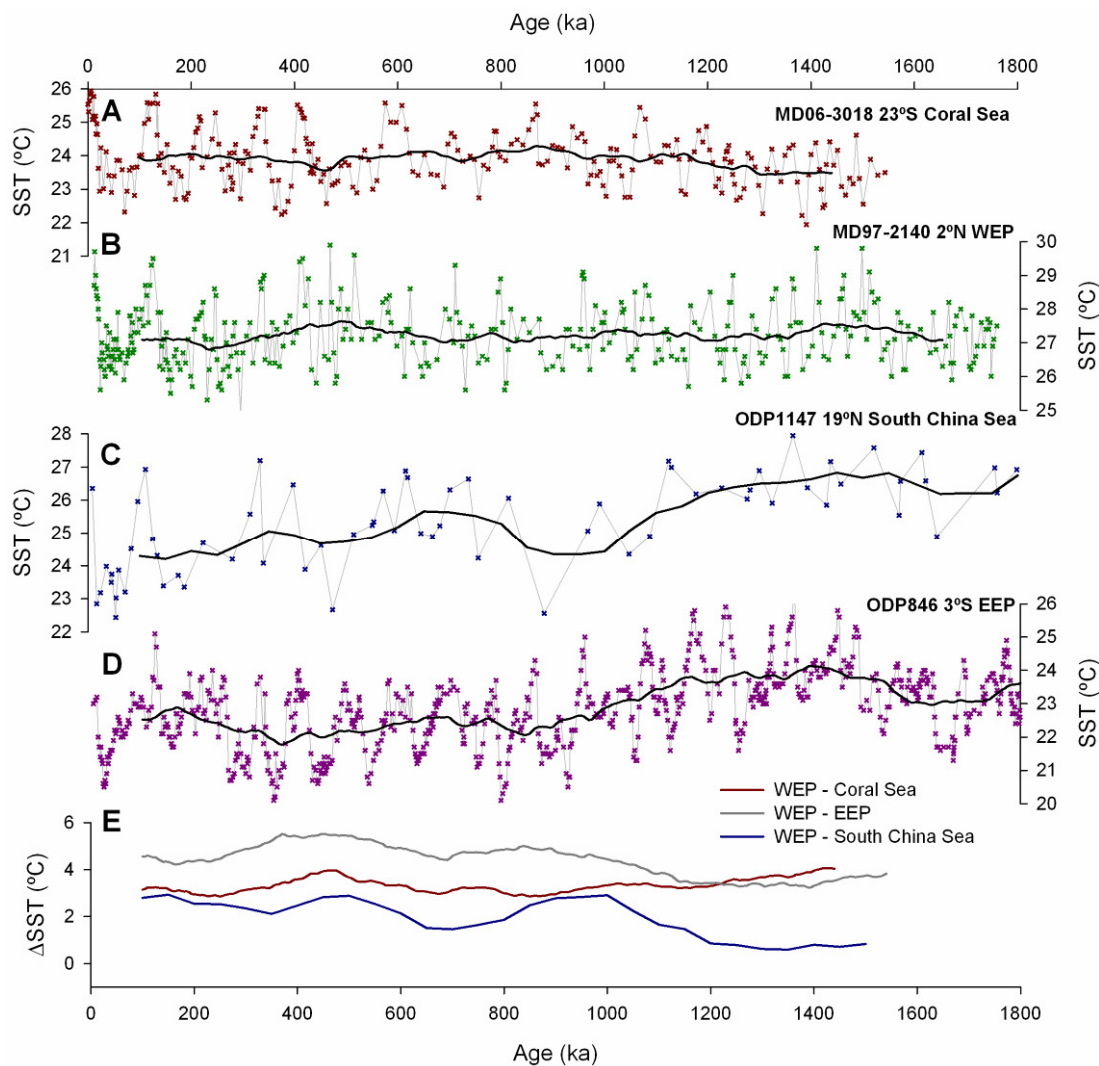


Figure 5.2 Pleistocene SST reconstructions from the core locations shown in *Figure 5.1*, *Table 5.1*. **A)** Southern Coral Sea core MD06-3018 (present study), **B)** WEP core MD97-2140 [*de Garidel-Thoron et al.*, 2005], **C)** South China Sea core ODP1147 [*Jia et al.*, 2008] and **D)** EEP core ODP846 [*Lawrence et al.*, 2006]. Bold black lines show 200kyr running means, calculated after 5kyr re-sampling (through linear interpolation) of all records except ODP1147, which was re-sampled to 50kyr resolution. All records are presented on published core age models. **E)** Calculated SST gradients between the running means.

Whereas the Coral Sea and WEP SST reconstructions are based on Mg/Ca paleothermometry, the South China Sea and EEP reconstructions are based on alkenone saturation indices. Whilst the two proxy systems possess differing sensitivities to potential seasonal biases, diagenetic effects and other, non-SST, controlling factors, they have been shown to be in agreement regarding first-order trends in EEP SST over the past 5000ka [Dekens *et al.*, 2008]. In the case of the South China Sea record, there is no available Mg/Ca record for comparison, but transfer function studies [Wang, 1994] show similar patterns of variability to those seen in the alkenone reconstructions [Jia *et al.*, 2008]. All records are presented on their original published age-models as the >100kyr trends considered here should be insensitive to uncertainties in age-model comparison on the shorter, orbital time-scales.

The WEP record shows a similar lack of variability in the long-term mean to that from the southern Coral Sea, but with an average value across the past 1500ka of 27.4°C (Fig 5.2A/B). The reconstructed SST gradient between the WEP and the southern Coral Sea, a measure of the equatorial-southern subtropical gradient, thus remains within $\pm 2\sigma_{SEM}=0.4^\circ\text{C}$ (the MD06-3018 reproducibility error is assumed for all reconstructions) of 3.5°C, consistent with modern conditions (Fig 5.1), across the past 1500ka (Fig 5.2E). In contrast to the southern Coral Sea and WEP, both the EEP and South China Sea records show significant cooling trends during the early Pleistocene (Fig 5.2C and 5.2D). The reconstructed zonal equatorial SST gradient consequently increased by ~1.5°C over the interval 1200-900ka before remaining near to its modern value of ~4.5°C over the past 900ka (Fig 5.2E). The reconstructed WEP-South China Sea SST gradient, a measure of the equatorial-northern subtropical gradient, increased by ~2.0°C over the interval 1200-1000ka before remaining near to its modern value of ~2.5°C over the past 1000ka (Fig 5.2E). Identification of the start/end ages for given intervals of SST gradient change depends on the choice of window length used for the calculation of the running averages, especially in the case of calculations based on the relatively low-resolution ODP1147 record. This uncertainty should not, however, exceed $\pm 100\text{kyr}$ (twice the ODP1147 re-sampling resolution).

The difference between the WEP-South China Sea and WEP-Coral Sea SST gradient reconstructions provides a first-order proxy for the extent of inter-hemispheric SST asymmetry between the northern and southern subtropics in the western Pacific. Over the past ~1000ka, the two gradients remain within ~1°C of each other, with the latter always the more positive (*Fig 5.2E*), consistent with the existing inter-hemispheric SST asymmetry in the western Pacific (*Fig 5.1*). Prior to ~1000ka, however, they are seen to diverge with age, with a value of ~3°C difference attained by ~1200ka, indicating a significantly increased degree of asymmetry, relative to the modern, during much of the early Pleistocene.

5.4 Discussion

Reconstructed southern Coral Sea SST shows no significant long-term variability (on the >100kyr time-scale) over the past 1500ka. This climatic stability requires the corresponding stability of the southern boundary of the warm pool on this time-scale. Whilst the MD06-3018 record does not extend beyond the Pleistocene, the middle Pliocene (~3000ka) PRISM project SST reconstructions show subtropical southwest Pacific values similar to the modern [*Dowsett and Robinson, 2009*], suggesting that the climatic stability of the region probably has extended across at least the past 3000ka.

From the middle Pliocene to ~1000ka both the eastern [*Wara et al., 2005; Lawrence et al., 2006*] and northern [*Jia et al., 2008*] boundaries of the warm pool were generally contracting. This contraction is thought to be driven by the upwelling of cooler thermocline waters in the former case [*Philander and Fedorov, 2003*] and may have been related to inferred changes in the vigour of the Kuroshio Current system [*Dowsett et al., 1996*] in the latter. The present study demonstrates that the southern boundary of the warm pool did not follow this pattern and instead remained stable, at least during the early Pleistocene. Consequently, the early Pleistocene warm pool, whilst expanded relative to its modern configuration, was also more hemispherically asymmetric. Recent ocean/atmosphere models for the Pliocene have assumed a meridionally symmetric configuration for the expanded Pacific warm pool

[*Barreiro et al.*, 2006; *Brierley et al.*, 2009]. However, if the early Pleistocene trends documented here can indeed be extrapolated to the Pliocene then the present reconstruction questions this choice of boundary conditions and is instead more consistent with those outlined in the PRISM reconstructions [*Dowsett et al.*, 1996; *Dowsett and Robinson*, 2009].

The latitudinal position of atmospheric inter-tropical convergence and hence the relative strength of the northern and southern branches of the Hadley circulation is partly controlled by the extent of inter-hemispheric extra-tropical SST asymmetry [*Broccoli et al.*, 2006]. This principle is supported on the glacial/interglacial time-scale by proxy reconstructions showing a southward shift of the Pacific inter-tropical convergence during periods of northern hemisphere cooling [*Koutavas and Lynch-Stieglitz*, 2004]. On the longer, >100kyr time-scales of interest here, a reduction in inter-hemispheric low-latitude western Pacific SST asymmetry (by at least a factor of two) over the interval from 1200-1000ka (with an uncertainty not exceeding ± 100 kyr on both the start and end age values) implies southward migration of maximal atmospheric convergence and the relative strengthening of the northern Hadley Cell. Whilst it also implies a corresponding weakening of the southern Hadley Cell, the relative stability of the equatorial-southern subtropical SST gradient constrains these latter changes as being very limited.

An increase in the strength of the northern Hadley Cell during the early Pleistocene is consistent in both sense and timing with previously proposed changes based on the equatorial-northern subtropical SST gradient alone [*Jia et al.*, 2008]. Existing modelling studies suggest that such an increase in the equatorial-northern subtropical SST gradient may have led to significant long-term reductions in air temperature and increased precipitation over North America [*Brierley and Fedorov*, 2010], both of which effects may have contributed significantly to the early Pleistocene intensification of NHG. The new data presented here, whilst supporting the general viability of such a scenario, places two important constraints on these approaches. Firstly, meridional SST gradient reconstructions in one hemisphere alone may have overestimated changes in Hadley Cell strength as they do not allow

for migration of the ascending limb between the two core locations over the period of the reconstruction. Secondly, future modelling studies including enhanced, rather than reduced, inter-hemispheric asymmetry in the low-latitude western Pacific are needed to better evaluate the physical mechanisms underlying any low-latitude control on the intensification of NHG.

The processes driving the observed decrease in inter-hemispheric subtropical Pacific SST asymmetry during the early Pleistocene may have ultimately been tropical or high-latitude in origin. In the former case, the tectonic arrangement of the western Pacific region and corresponding changes in the Indonesian through-flow were largely completed during the Pliocene [Jochum *et al.*, 2009] and are unlikely to have influenced the early Pleistocene changes. However, upstream changes in the north and south equatorial current systems, potentially arising as a long-term consequence of the closing of the Panamanian isthmus, could have affected the relative strength of oceanic heat transport to the northern and southern subtropics. Such variability could be closely linked to the enhanced warm pool asymmetry as the southern subtropics were probably more important, relative to their northern counterpart, as a source of thermocline waters to the EEP under such conditions. Alternatively, the decrease in inter-hemispheric subtropical Pacific SST asymmetry could have resulted from the differential cooling of the northern and southern high-latitudes across the Plio-Pleistocene. Within this scenario, the probable Hadley Cell response discussed above would have acted as a positive feedback, rather than a driving mechanism, for the intensification of NHG. The Hadley Cell response may have also acted to reinforce the East Asian Winter Monsoon system at the expense of the Summer Monsoon [Jia *et al.*, 2008], consistent with Plio-Pleistocene continental records of monsoon variability and acting as a further positive feedback on glaciation [Xiong *et al.*, 2003].

5.5 Conclusions

This chapter has shown that the climate of the southern Coral Sea, on >100kyr time-scales, has been extremely stable over at least the past 1500ka. This means that the SST gradient across the southern boundary of the Pacific warm pool has also remained stable and hence that no significant meridional fluctuations in the southern extent of the warm pool have occurred over this interval. This is in contrast to both the northern and eastern warm pool boundaries, which underwent contraction during the early Pleistocene. The early Pleistocene warm pool was, therefore, more meridionally asymmetric than its modern configuration. If it is assumed that the position of maximal atmospheric convergence in the western Pacific followed the centre of the warm pool, then this would have migrated southwards over the interval 1200-1000ka (with an uncertainty not exceeding ± 100 kyr on both the start and end age values), consistent with a strengthening of the northern Hadley Cell prior to the intensification of NHG during the early part of the MPT. It is, therefore, at least plausible that the low-latitude Pacific climate system may have played an important role, on the >100kyr time-scale, in the early Pleistocene intensification of NHG. The mechanisms by which this may have occurred are considered in chapter 7, §6. More fundamentally however, the present study demonstrates that the meridional SST gradients in both hemispheres are important in understanding past variability in poleward heat and moisture fluxes and that greater than modern inter-hemispheric symmetry in the extent of the paleo-warm pool cannot be safely assumed.

The present chapter has focused on the >100kyr time-scale variability, or lack thereof, in the MD06-3018 SST reconstruction. It is also evident from *Figure 4.2A*, however, that significant glacial/interglacial variability is present in the reconstruction and furthermore that the dominant mode of this variability has changed over the course of the record. The next chapter turns its focus towards this orbital time-scale variability in subtropical southwest Pacific climate, using both the Mg/Ca-derived SST reconstruction and also the complementary planktic stable oxygen isotope record.

Chapter 6: The Mid-Pleistocene Transition in subtropical southwest Pacific climate

Chapter abstract

Reconstructions of orbital time-scale subtropical southwest Pacific climate variability over the Pleistocene were derived from MD06-3018 coupled planktic foraminiferal $\delta^{18}\text{O}$ -Mg/Ca measurements. A clear shift from ~40kyr to ~100kyr modes of reconstructed glacial/interglacial SST variability is seen over the Mid-Pleistocene Transition and these fluctuations are shown to have remained coherent with the orbital obliquity cycle across the transition. The likely origin of this strong obliquity signal in subtropical southwest Pacific SST is shown to be the southern high-latitudes and comparison with existing SST reconstructions from the equatorial Pacific is consistent with the communication of the signal occurring principally by greenhouse gas forcing. In contrast to the SST reconstruction, regional hydrological cycle variability (based on the calculated local component of $\delta^{18}\text{O}_{\text{sw}}$ change) shows only very limited coherence with the obliquity cycle and a stronger relationship with the precession cycle. The decoupling of the SST and hydrological cycle responses over the Mid-Pleistocene Transition allows constraints to be placed on the evolution and extent of orbitally paced fluctuations within the coupled low-latitude ocean/atmosphere system.

6.2 Introduction

The MPT represented the last major change in the observed mode of glacial/interglacial ice-volume variability, namely that from the “40kyr world” of the late Pliocene and early Pleistocene to the more asymmetric and higher amplitude cycles of the ‘100kyr world’ of the middle and late Pleistocene [*Head and Gibbard, 2005; Imbrie et al., 1993; Mudelsee and Stattegger, 1997*]. The transition occurred without any shift in the mode of orbital forcing, demonstrating that the climate response to orbital variations is non-linear on the >100kyr time-scale and that threshold levels exist within one or more of the key processes within the Earth system that have acted to change the mode of response. Evaluating whether the additional source of non-linearity that led to the emergence of the ~100kyr mode resided in ice-sheet dynamics [*Bintanja and van de Wal, 2008; Clark and Pollard, 1998*], the carbon cycle [*Shackleton, 2000*], or other processes, remains a key objective in paleoceanographic research.

Proxy records of SST from all latitudes and ocean basins also show a transition in the amplitude and dominant period of glacial/interglacial variability across the MPT period [e.g. *Crundwell et al., 2008; Liu et al., 2008; Marlow et al., 2000; Medina-Elizalde and Lea, 2005; Ruddiman et al., 1989*]. However, SST reconstructions show much more spatial variability in the amplitude, timing and structure of glacial/interglacial variability than those of $\delta^{18}\text{O}_{\text{benthic}}$. This is a consequence of both the spatial variation in the radiative forcing and feedback factors that control SST and also of the advective effect of ocean circulation patterns. It also means that reconstructions of SST from different parts of the world have the potential to yield useful information about the relative importance of different orbital time-scale climate feedback systems.

In the case of the low-latitude (taken here as being 30°N to 30°S) Pacific, where ice-sheet fluctuations do not directly affect the radiation budget, it has been proposed that greenhouse gas forcing has exerted the dominant control on glacial/interglacial SST variability across the MPT [*Medina-Elizalde and Lea, 2005*] and as far back as the late Pliocene [*Medina-Elizalde and Lea, 2010*]. If this hypothesis is correct then it would follow that reconstructed low-latitude SST variability may provide an indirect guide to the carbon cycle response to orbital forcing during the middle and early Pleistocene. Even within the low-latitudes the observed amplitude of middle/late Pleistocene glacial/interglacial SST variability is not, however, spatially uniform as would result from forcing by greenhouse gas variability alone. This heterogeneity arises principally from ocean circulation patterns and their effect on meridional heat transport. In particular, the low-latitude ventilation of upper-ocean (taken here as being thermocline and intermediate depth) waters of primarily southern hemisphere origin contributes around half of the total LGM SST cooling seen in the low-latitude Pacific in coupled ocean-atmosphere model studies [*Liu et al., 2002*].

Both theoretical studies [*Philander and Fedorov, 2003*] and proxy reconstructions [*Beaufort et al., 2001*] have suggested that, during at least the middle/late Pleistocene, the Pacific thermocline was generally shallower during glacial (as opposed to interglacial) periods, implying systematic orbital time-scale changes in upper-ocean ventilation and hence, the direct advection of the high-latitude climate response into the low-latitude Pacific. Changes in the tilt of the low-latitude Pacific thermocline are closely related on inter-annual time-scales to the coupled ocean/atmosphere El-Niño Southern Oscillation (ENSO) phenomenon, which has a significant effect on both the mean-annual SST distribution and the hydrological cycle across the low-latitude Pacific [*Sarachik and Cane, 2010*].

Modelling studies suggest that the dominant orbital influence on the dynamics of the ENSO system *sensu stricto* is the orbital precession cycle, through its effect on seasonal low-latitude insolation budgets [Clement *et al.*, 1999]. However, it has also been proposed that both millennial [Stott *et al.*, 2002] and orbital [Koutavas *et al.*, 2002; Philander and Fedorov, 2003] time-scale responses of the low-latitude ocean/climate system can be characterized as resembling so-called “super-ENSO” states¹. In these scenarios, it is possible that the low-latitude ocean/atmosphere system may, through meridional heat/moisture fluxes, have played a substantial role in modulating global climate on glacial/interglacial time-scales.

The MPT may have represented either an increase in the non-linearity of the climate system response to obliquity forcing [Huybers, 2007; Liu *et al.*, 2008] or an enhanced sensitivity to precession and/or eccentricity [Imbrie *et al.*, 1993; Raymo, 1997]. It is therefore also possible that the amplitude and character of any orbital time-scale super-ENSO fluctuations may have changed over the MPT. Any such changes would at least challenge the reliability of the middle/late Pleistocene orbital time-scale low-latitude SST to carbon cycle variability relationship as a guide to conditions in the 40kyr world.

This chapter presents reconstructions of SST (as proxied by planktic foraminiferal Mg/Ca) and hydrological cycle variability (as proxied by the extraction of the ‘local’ component of $\delta^{18}\text{O}_{\text{sw}}$ variability, calculated in turn from coupled measurements of planktic foraminiferal $\delta^{18}\text{O}$ -Mg/Ca) at sub-orbital temporal resolution and spanning the past 1500ka, from sediment core MD06-3018 in the southern Coral Sea, subtropical southwest Pacific. The Coral Sea is significantly affected by ENSO related fluctuations in both SST (*Fig 6.1*) and precipitation on the inter-annual time-scale [Delcroix and Lenormand, 1997] and coupled reconstructions of SST and hydrological cycle variability from the region therefore provide a method

¹ The term ‘super-ENSO’, as used here, is distinct from more general changes in the ‘low-latitude ocean/atmosphere circulation system’ as it refers to systematic oscillations, on a given time-scale, between ocean/atmosphere states that specifically resemble the El-Niño and La-Niña of the ENSO system *sensu stricto*. This does not imply that the ENSO cycle *sensu stricto* did not itself also operate at these times, but that systematic oscillations in the skew state of the system occurred, on the super-ENSO time-scale, between the two modes.

for evaluating the existence and importance of orbital time-scale super-ENSO variability. The simplest formulation of such an approach is that strong covariance in the response seen in the SST and hydrological cycle proxies would suggest a dominant super-ENSO control on both variables, whereas strong decoupling would imply different forcing mechanisms. The Mg/Ca-derived MD06-3018 SST reconstruction has already been presented in chapter 4 and used in chapter 5 to demonstrate the long-term (>100kyr time-scale) stability of SST in the southern Coral Sea over the past 1600ka. The record is now re-assessed, in comparison with the coupled $\delta^{18}\text{O}_{\text{planktic}}$ record, in terms of 10-100kyr time-scale variability in order to constrain the forcing mechanisms of orbital time-scale variability in subtropical southwest Pacific climate across the MPT.

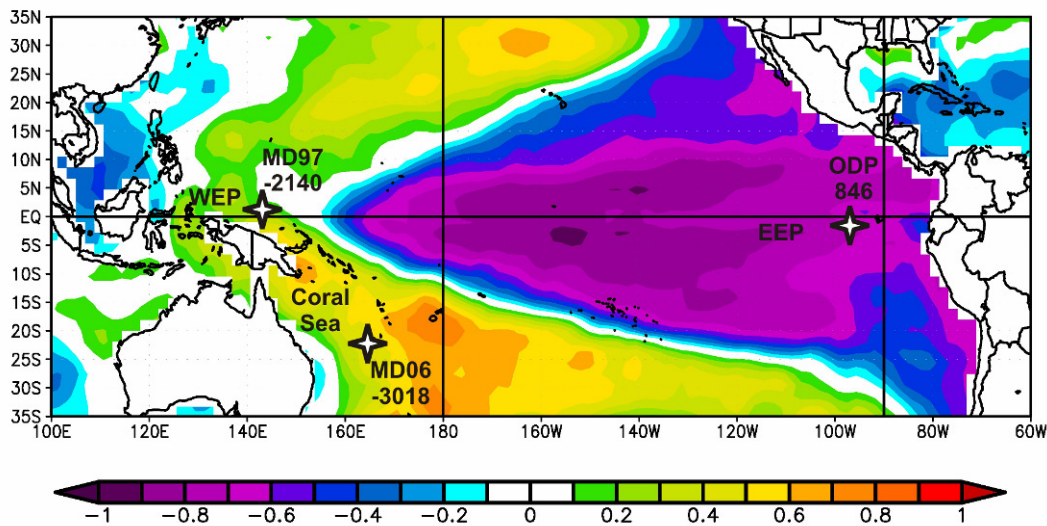


Figure 6.1 Contour map of the correlation index between mean-annual SST and the Southern Ocean Index within the low-latitude Pacific over the interval 1948-2000, with the location of the core-sites discussed in the text shown. The core locations are given in *Table 5.1*. Similar index values at any two locations imply that SST responds in an in-phase manner on the inter-annual time-scale to ENSO fluctuations. The plot was generated using data and the on-line reanalysis tool provided by the NOAA-ESRL (<http://www.esrl.noaa.gov/psd/data/correlation/>).

6.3 Methods

6.3.1 Planktic foraminiferal stable isotope measurements

Specimens of *G. ruber* (white) were picked from the 250-315 μ m size fraction. The same morphotype selection criteria discussed in chapter 4, §3.1 was used to ensure full comparability of the trace-metal and stable isotope measurements. Twelve to fifteen individuals were used for each isotopic analysis. Samples were rinsed, with tests unbroken, for 10s in an ultrasonic bath with methanol and then rinsed in de-ionized water. Samples were analyzed in the Thermo Delta+ mass spectrometer at the School of GeoSciences, University of Edinburgh. Long-term analytical reproducibility was $2\sigma_a=0.18\%$ for $\delta^{18}\text{O}$, based on standards correlated to NBS19. Short-term (sample) reproducibility based on four down-core (n=10) repeat measurements was $2\sigma_r=0.30\%$. The principles of the $\delta^{18}\text{O}$ proxy system are reviewed in appendix 1, §1, full details of the analytical methods used are given in appendix 3 and the full data-set is tabulated in appendix 4 and plotted in against core depth in appendix 5.

6.3.2 Calculation of $\delta^{18}\text{O}_{\text{sw}}$

As $\delta^{18}\text{O}_{\text{planktic}}$ depends principally on the ambient seawater temperature (taken as SST in the case of *G. ruber*) and the isotopic composition of the seawater ($\delta^{18}\text{O}_{\text{sw}}$), it follows that if $\delta^{18}\text{O}_{\text{planktic}}$ is measured and SST reconstructed (from Mg/Ca paleothermometry, as discussed in chapter 4, in the present case) then $\delta^{18}\text{O}_{\text{sw}}$ may be directly calculated [Elderfield and Ganssen, 2000]. This is achieved here using the paleotemperature equation for *Orbulina universa* (low-light), as given in equation 6.1, which has also been show to also apply well to *G. ruber* [Bemis et al., 1998]. The uncertainty in $\delta^{18}\text{O}_{\text{sw}}$ is calculated from the sample reproducibility uncertainties in $\delta^{18}\text{O}_{\text{planktic}}$ and Mg/Ca-derived SST using standard error propagation formulae. The calculated core-top $\delta^{18}\text{O}_{\text{sw}}$ value is $0.69 \pm 2\sigma_{\text{diff}}=0.34\%$, which compares well with the gridded modern value [LeGrande and Schmidt, 2006].

Equation 6.1
$$T_{Mg/Ca} = 16.5 - 4.8 \times (\delta^{18}O_{planktic} - \delta^{18}O_{sw})$$

The MD06-3018 Mg/Ca-derived SST reconstruction analysed in this chapter and used for the calculation of $\delta^{18}O_{sw}$, comprises the original, ‘uncorrected’, values (i.e. as given in *Figure 4.2A*) with the sample reproducibility error alone, rather than the revised reconstruction and combined uncertainty concept introduced in chapter 4, §5.3. The rationale for this approach is twofold; firstly, to allow comparability with other published SST reconstructions, for which no equivalent uncertainty analysis exists and secondly, because the main interest of the present study is the spectral properties of the various reconstructions, which are insensitive to both the correction methodologies considered in chapter 4 and the uncertainty in the amplitudes of the signals. However, the uncertainty in reconstructed SST arising from Mg/Ca sample reproducibility is probably an underestimate of the true proxy uncertainty, as discussed in chapter 4, and this necessarily implies that the uncertainty estimates for $\delta^{18}O_{sw}$ must also be viewed as lower-bound values.

A proxy for past changes in the regional hydrological cycle (namely the precipitation/evaporation balance), relative to the modern, may be derived from the regional component of past $\delta^{18}O_{sw}$ variability, normalized to the modern. This term, $\Delta\delta^{18}O_{local}$, is calculated by subtracting the component of global $\delta^{18}O_{sw}$ variability from the MD06-3018 $\delta^{18}O_{sw}$ reconstruction. This is achieved in the present study by using an estimate of Plio-Pleistocene global $\delta^{18}O_{sw}$ variability derived from coupled $\delta^{18}O_{benthic}$ and benthic Mg/Ca measurements from DSDP Site 607 and piston core Chain 82-24-23PC in the deep North Atlantic [*Sosdian and Rosenthal, 2009*]. The *Sosdian and Rosenthal* [2009] reconstruction has the significant advantage for the present study of spanning the entire Pleistocene. However, the capacity of such an approach to isolate the global component of $\delta^{18}O_{sw}$ variability relies upon the extent to which benthic Mg/Ca paleothermometry can accurately remove the deep water temperature component from the $\delta^{18}O_{benthic}$ signal. This is at present a contentious issue and doubts have been raised regarding this issue in specific relation to the *Sosdian and Rosenthal* [2009] reconstruction [*Yu and Broecker, 2010*]. Comparison

of the *Sosdian and Rosenthal* [2009] global ice-volume reconstruction over the past 450ka with other, independent, methods shows that whilst the absolute values of inferred relative sea-level found in the *Sosdian and Rosenthal* [2009] reconstruction differ significantly from the other methods for some intervals, the amplitudes and periodicities of variability do not differ by more than $\pm 10\%$, with the exception of the MIS12/11 termination [*Sosdian and Rosenthal*, 2009]. The main use of the *Sosdian and Rosenthal* [2009] reconstruction in the present study is therefore considered appropriate as its application is limited to the identification of significant periodic signals in the down-core calculated residual $\Delta\delta^{18}\text{O}_{\text{local}}$ record, rather than the precise quantification of their amplitudes.

To reduce age-model artifacts in the calculation of $\Delta\delta^{18}\text{O}_{\text{local}}$, the MD06-3018 $\delta^{18}\text{O}_{\text{sw}}$ record was re-tuned (using maxima and minima points in both records) to the *Sosdian and Rosenthal* [2009] time-scale². The justification for this approach is that if the *Sosdian and Rosenthal* [2009] $\delta^{18}\text{O}_{\text{sw}}$ reconstruction dominantly reflects ice-volume induced changes, then these should be globally synchronous on 10-100kyr time-scales. Therefore, the preferred method to extract the global signal from the MD06-3018 $\delta^{18}\text{O}_{\text{sw}}$ record is to assume that the major transitions in the MD06-3018 record arise from ice-volume changes and should, therefore, be aligned to those in the *Sosdian and Rosenthal* [2009] reconstruction. This approach does, however, preclude the study of phase differences between the MD06-3018 and *Sosdian and Rosenthal* [2009] $\delta^{18}\text{O}_{\text{sw}}$ reconstruction. To evaluate the sensitivity of the calculated $\Delta\delta^{18}\text{O}_{\text{local}}$ record to the tuning method, the calculation was also performed on the un-tuned $\delta^{18}\text{O}_{\text{sw}}$ records and the resultant, alternative $\Delta\delta^{18}\text{O}_{\text{local}}$ record compared to the tuned case. In both cases, to allow the direct comparison of the MD06-3018 and the *Sosdian and Rosenthal* [2009] $\delta^{18}\text{O}_{\text{sw}}$ records, both records were then re-sampled, via linear interpolation, to a common 5kyr time-step, meaning that the $\Delta\delta^{18}\text{O}_{\text{local}}$ record is presented at that resolution. The combined error on $\Delta\delta^{18}\text{O}_{\text{local}}$ is based on the assumption of the MD06-3018 $\delta^{18}\text{O}_{\text{sw}}$ reproducibility error for both reconstructions.

² Alignment of the two age-models was only undertaken over the past 1510ka due to the difficulty of correlating events over the final 30kyr of the MD06-3018 record. This means that the calculated $\Delta\delta^{18}\text{O}_{\text{local}}$ record spans a slightly shorter interval than the MD06-3018 SST or $\delta^{18}\text{O}_{\text{sw}}$ reconstructions.

6.4 Results

The MD06-3018 $\delta^{18}\text{O}_{\text{planktic}}$, Mg/Ca-derived SST and calculated $\delta^{18}\text{O}_{\text{sw}}$ records all show a clear change in the mode of glacial/interglacial variability across the period 1000-500ka, corresponding to that of the MPT (*Figs 6.2A-C*). In particular, all of these records show a transition from a regime of lower amplitude, ~40kyr period cycles prior to ~1000ka to a regime of higher amplitude, ~100kyr period cycles over the past ~500ka. In contrast, the calculated $\Delta\delta^{18}\text{O}_{\text{local}}$ record does not show such an evident transition (*Fig 6.2D*).

Analysis of the records in age-period-spectral power space using a wavelet decomposition method [*Grinsted et al., 2004*] allows the evolving periodicities in the records to be studied in more detail and this is shown in *Figure 6.3*. The wavelet transform method employed here includes auto-regressive evaluation of spectral power significance against a modelled red-noise process. This approach does not account for the effect on spectral significance of uncertainties in the proxy values themselves, but does nonetheless allow for the more objective identification of the timing of changes in the spectral properties of a given time-series. The MD06-3018 records were all re-sampled, via linear interpolation, to 5kyr spacing (the average sample spacing on the core age-model), prior to the wavelet decomposition, leading to a Nyquist period of 10kyr. This means that the range of periodicities associated with the orbital precession cycle (18-21kyr) lie within, but at the limit of, what can be resolved using the present data and method.

The $\delta^{18}\text{O}_{\text{planktic}}$ record shows significant spectral power at ~100kyr over the past 950ka (*Fig 6.3A*). Spectral power at ~40kyr is present, but of intermittent significance across the record. The average amplitude of $\delta^{18}\text{O}_{\text{planktic}}$ variability prior to 950ka was 0.7‰ (*Fig 6.2A*). After the onset of significant ~100kyr periodicity, the glacial/interglacial amplitude increased to a maximum of 1.7‰ at the MIS 12 to 11 transition. Over the last four 100kyr cycles the amplitude declined to 1.0‰ at the LGM-Holocene transition.

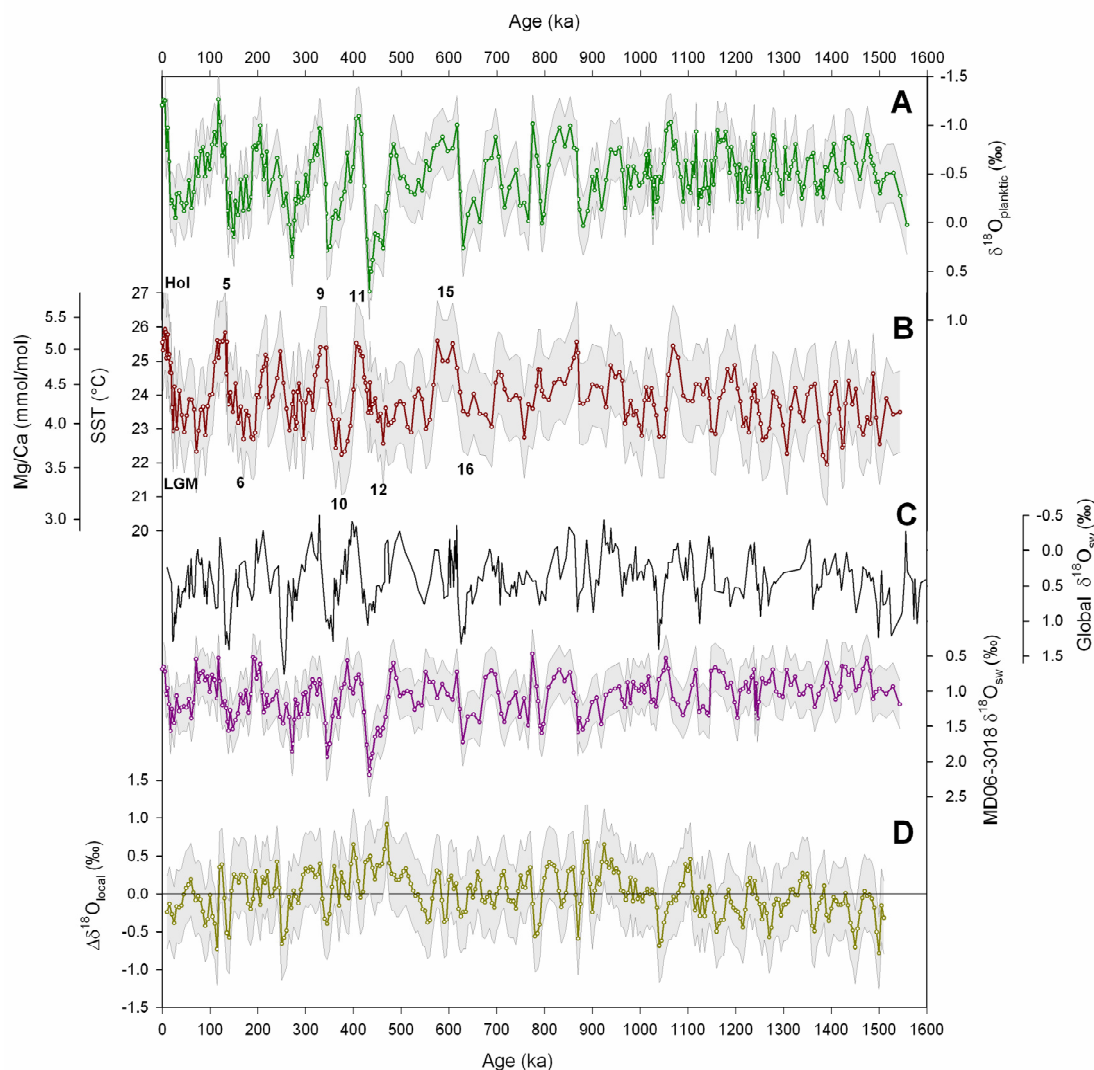


Figure 6.2 MD06-3018 *G. ruber* measurements of **A)** $\delta^{18}\text{O}_{\text{planktic}}$ and **B)** Mg/Ca-derived SST plotted against core age-model. Annotations on Mg/Ca plot show positions of selected MIS referred to in the text. Shaded areas on A/B represent $\pm 2\sigma_r$ sample reproducibility error envelopes. **C)** Purple line is calculated MD06-3018 $\delta^{18}\text{O}_{\text{sw}}$ plotted against MD06-3018 core age-model. Shaded area is the propagated error ($\pm 2\sigma_{\text{diff}}$) arising from the $2\sigma_r$ sample reproducibility error envelopes on the $\delta^{18}\text{O}_{\text{planktic}}$ and Mg/Ca-derived SST records. Black line is the *Sosdian and Rosenthal* [2009] ‘global’ $\delta^{18}\text{O}_{\text{sw}}$ reconstruction, on its published age-model. The two $\delta^{18}\text{O}_{\text{sw}}$ reconstruction axes are at the same scale, but offset by 1‰ to allow visual comparison. **D)** Calculated $\Delta\delta^{18}\text{O}_{\text{local}}$ at 5kyr resolution following tuning of the MD06-3018 $\delta^{18}\text{O}_{\text{sw}}$ record to the *Sosdian and Rosenthal* [2009] $\delta^{18}\text{O}_{\text{sw}}$ record. Shaded area is the propagated error ($\pm 2\sigma_{\text{diff}}$) arising from the assumption of the MD06-3018 $\delta^{18}\text{O}_{\text{sw}}$ sample reproducibility uncertainty for the *Sosdian and Rosenthal* [2009] $\delta^{18}\text{O}_{\text{sw}}$ record.

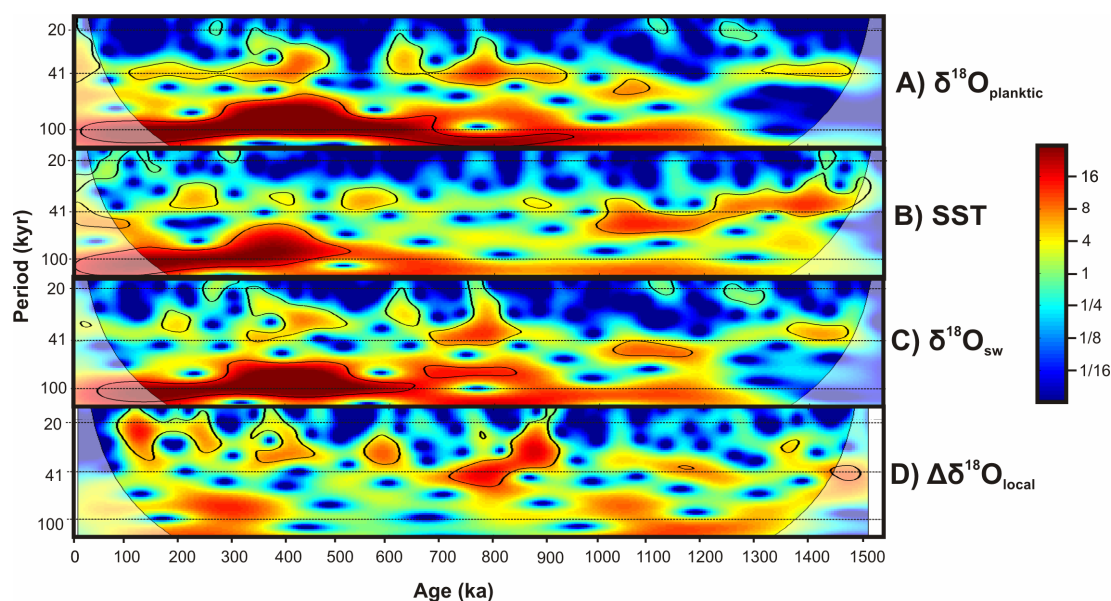


Figure 6.3 Local wavelet power spectra of MD06-3018 **A)** *G. ruber* $\delta^{18}\text{O}_{\text{planktic}}$, **B)** *G. ruber* Mg/Ca-derived SST, **C)** calculated $\delta^{18}\text{O}_{\text{sw}}$ and **D)** calculated $\Delta\delta^{18}\text{O}_{\text{local}}$ records. The $\delta^{18}\text{O}_{\text{sw}}$ record was returned to the *Sosdian and Rosenthal* [2009] age scale and all records were re-sampled (via linear interpolation) to 5kyr resolution, detrended and normalized to unit-variance prior to analysis. Wavelet decomposition was performed using the WTC-16 code [Grinsted *et al.*, 2004]. Colour bar shows spectral power in normalized units of variance. Black contour-lines show 5% confidence intervals above a modelled first order autoregressive red-noise process. Shaded areas show the cone-of-interference, within which edge effects become significant.

The Mg/Ca-derived SST record shows significant spectral power at $\sim 100\text{kyr}$ over the past 550ka (*Fig 6.3B*). Prior to this, spectral power in the 120-145kyr band is present from the beginning of the record to the emergence of the significant $\sim 100\text{kyr}$ power, but is seen to have not been statistically significant. Spectral power at $\sim 40\text{kyr}$ is noticeable throughout the record but was persistently significant and of higher spectral power prior to $\sim 1000\text{ka}$. The average amplitude of glacial/interglacial SST variability over the past 550ka was $3.0 \pm 2\sigma = 0.4^\circ\text{C}$ (where σ is the standard deviation of the individual peak glacial to peak interglacial SST amplitudes within each glacial/interglacial cycle) whereas prior to 550ka it was $1.7 \pm 2\sigma = 0.8^\circ\text{C}$ (*Fig 6.2B*). Application of the combined uncertainty concept does little to change these values, as was discussed in chapter 4, §4.2. Even in the case where the *Mathien-*

Blard and Bassinot [2009] salinity correction is applied alone (which has the largest effect on the reconstructed glacial/interglacial SST variability), this has the effect of increasing the average glacial/interglacial SST amplitudes over the past 500ka to $4.1 \pm 2\sigma = 1.4^\circ\text{C}$ and to $2.2 \pm 2\sigma = 1.4^\circ\text{C}$ prior to that. Therefore, the conclusion that the SST amplitude increased by 40-50% with the emergence of the ~100kyr mode is robust to all known and plausible uncertainties in the SST reconstruction method.

The calculated $\delta^{18}\text{O}_{\text{sw}}$ record generally resembles the $\delta^{18}\text{O}_{\text{planktic}}$ record more closely than the Mg/Ca-derived SST record, both in age space (*Fig 6.2C*) and in the wavelet decomposition (*Fig 6.3C*). The retuned $\delta^{18}\text{O}_{\text{sw}}$ record shows significant spectral power at ~100kyr over the past 900ka. Spectral power at ~40kyr is present, but of intermittent significance across the record. The average amplitude of $\delta^{18}\text{O}_{\text{sw}}$ variability prior to 900ka was 0.5‰. After the onset of significant ~100kyr periodicity, the amplitude of $\delta^{18}\text{O}_{\text{sw}}$ glacial/interglacial fluctuations declines from ~1.5‰ at the MIS 12/11 transition to 0.6‰ at the LGM-Holocene transition.

The MD06-3018 $\delta^{18}\text{O}_{\text{sw}}$ record shows amplitudes of ~100kyr middle/late Pleistocene and ~40kyr early Pleistocene glacial/interglacial variability generally within the propagated $\delta^{18}\text{O}_{\text{sw}}$ reproducibility error of the global component of $\delta^{18}\text{O}_{\text{sw}}$ variability attributable to ice-volume fluctuations [*Sosdian and Rosenthal, 2009*] as can be seen by comparing the two lines on *Figure 6.2C*. This has the consequence of removing most significant orbital time-scale variability from the $\Delta\delta^{18}\text{O}_{\text{local}}$ signal calculated after the tuning of the two records and, indeed, no significant spectral power at ~100kyr is seen across the duration of the record (*Fig 6.3D*). The calculated $\Delta\delta^{18}\text{O}_{\text{local}}$ record does show patchy intervals of significant spectral power at ~40kyr up to ~700ka and then in the 20-40kyr range over the past ~700ka.

To investigate the sensitivity of the spectral analysis presented above to the tuning assumptions involved in the generation of the $\Delta\delta^{18}\text{O}_{\text{local}}$ record, the same analysis was also undertaken with the alternative $\Delta\delta^{18}\text{O}_{\text{local}}$ record (not shown) based on the untuned $\delta^{18}\text{O}_{\text{sw}}$ records. In this case, the alternative $\Delta\delta^{18}\text{O}_{\text{local}}$ record shows patchy intervals of significant spectral power at ~40kyr up to ~600ka and then in the

20-40kyr range over the past ~600ka. A significant period of spectral power in the 40-80kyr range is also seen at 1200-1000ka. Therefore, the absence of significant 100kyr spectral power and the drift towards higher frequency variability over the middle/late Pleistocene are both apparently robust to the tuning assumptions used in the derivation of the $\Delta\delta^{18}\text{O}_{\text{local}}$ record.

The long-term mean, defined as the 200kyr running average, of the $\Delta\delta^{18}\text{O}_{\text{local}}$ record remains within error of zero throughout the duration of the record. The amplitude of the 20-40kyr period $\Delta\delta^{18}\text{O}_{\text{local}}$ variability lies in the 0.5-1.0‰ range across the duration of the record (*Fig 6.2D*) and thus exceeds the propagated sample reproducibility error arising from the subtraction of the two $\delta^{18}\text{O}_{\text{sw}}$ records ($2\sigma_{\text{diff}} = 0.48\text{‰}$). This propagated error value remains, however, a lower-bound estimate, due to both the conservative estimate of error used on the MD06-3018 Mg/Ca-derived SST reconstruction and the likely underestimate of error on the *Sosdian and Rosenthal* [2009] $\delta^{18}\text{O}_{\text{sw}}$ reconstruction involved in assuming the MD06-3018 value. It follows that at least some of the variability seen in the $\Delta\delta^{18}\text{O}_{\text{local}}$ reconstruction is likely to be noise, arising from the uncertainties inherent in both the two $\delta^{18}\text{O}_{\text{sw}}$ reconstructions and in their correlation prior to subtraction. However, the higher amplitude variability is plausibly distinct from noise and may account for the intervals of significant spectral power seen in *Figure 6.3D*. Although exact values cannot be meaningfully given, application of the slope of the modern $\delta^{18}\text{O}_{\text{sw}}$ -salinity relationship for the South Pacific [*LeGrande and Schmidt*, 2006] would imply corresponding regional salinity fluctuations of the order 0.1-1.0.

6.5 Discussion

6.5.1 Orbital influences on subtropical southwest Pacific SST variability

The MD06-3018 Mg/Ca-derived SST reconstruction shows a clear MPT from a regime of $\sim 2^{\circ}\text{C}$ amplitude, $\sim 40\text{kyr}$ cycles prior to $\sim 1000\text{ka}$ to a regime of $\sim 3^{\circ}\text{C}$ amplitude, $\sim 100\text{kyr}$ cycles over the past $\sim 500\text{ka}$ (*Fig 6.2B and Fig 6.3B*). To investigate the relative importance of different orbital influences on this evolving pattern of reconstructed SST variability, cross-spectral analysis of the SST record with those of both obliquity angle and the precession index from the *Laskar et al.* [2004] orbital solution (La04) was undertaken using a wavelet transform coherence method [*Grinsted et al.*, 2004] (*Fig 6.4A/B*). The SST reconstruction is seen to display significant coherence with the obliquity cycle (at the 95% confidence level against red noise, based on Monte Carlo analysis) and to be almost in-phase with it across almost the entire duration of the record (*Fig 6.4A*). In contrast, the SST reconstruction only shows significant coherence with the precession index during patchy intervals throughout the record and a much more variable phase relationship (*Fig 6.4B*). It appears, therefore, that the obliquity cycle has exerted the dominant orbital influence on subtropical southwest Pacific SST variability, both before, during and after the MPT.

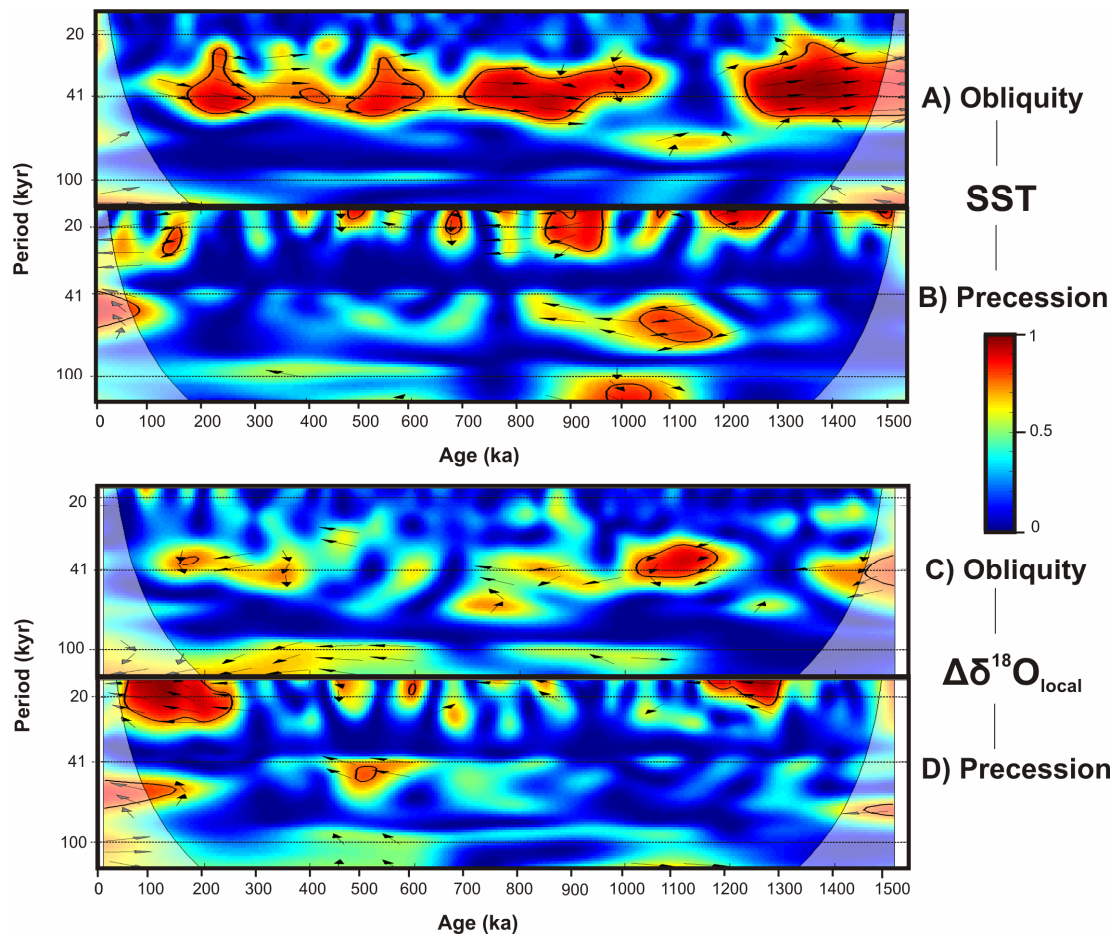


Figure 6.4 Wavelet transform coherence analysis of the MD06-3018 *G. ruber* Mg/Ca-derived SST (A/B) and calculated $\Delta\delta^{18}\text{O}_{\text{local}}$ (C/D) records with orbital obliquity and precession index records from the La04 orbital solution [Laskar *et al.*, 2004]. Analysis was performed using the WTC-16 code [Grinsted *et al.*, 2004]. Colour bar shows squared coherence (C_{xy}^2) level. Black contour-lines show 5% confidence intervals relative to red noise, determined using a Monte Carlo method. For areas of age-period space with significant coherence, the phase relationship between the two variables is shown by black arrows. Right (left) pointing horizontal arrows denote an in-phase (anti-phase) relationship. All records were re-sampled (via linear interpolation) to 5kyr resolution, de-trended and normalized to unit-variance prior to analysis. Shaded areas show the cone-of-interference, within which edge effects become significant.

The origins of the ~100kyr middle/late Pleistocene mode of glacial/interglacial variability continues to be debated. Whilst ~100kyr spectral power is the dominant characteristic of the past ~500ka in the subtropical southwest Pacific SST reconstruction (*Fig 6.3B*), significant coherence with the obliquity cycle, but not the precession index, is seen to be maintained across most of this interval (*Fig 6.4A*). Closer examination of the structure of the middle/late Pleistocene SST cycles demonstrate that these are in fact more symmetric than the classic “saw-tooth” ~100kyr pattern seen in the LR04 $\delta^{18}\text{O}_{\text{benthic}}$ stack and taken here as a crude first-order proxy for both global ice-volume fluctuations and the northern high-latitude climate response (*Fig 6.5A*). Instead, periods of relatively rapid cooling in the subtropical SST reconstruction follow the interglacial SST maxima and are followed by longer periods of relatively stable low SST. These differences are not an artifact of age model comparisons as the MD06-3018 $\delta^{18}\text{O}_{\text{benthic}}$ record, which was tuned to LR04, but is derived from the same depth-space as the MD06-3018 SST record, also shows the same differences from the SST record (*Fig 6.5A*).

The ‘interglacial’ parts of each 100kyr subtropical SST cycle, defined here as when SST exceeds 24°C (the long-term mean value of the reconstruction over the past 800ka), are seen to be coincident with individual obliquity cycles, such that maximum SST corresponds to maximum obliquity (*Fig 6.5A*). The apparent exceptions at 200-250ka (around MIS 7) and 560-630ka (around MIS 15) are related to dual SST maxima separated by weak SST minima, but these are still seen to remain in phase with the obliquity variations. Therefore, the 100kyr glacial/interglacial mode in subtropical southwest Pacific SST seems to be closely paced by the obliquity cycle, consistent with the persistent coherence relationship seen in *Figure 6.4A*.

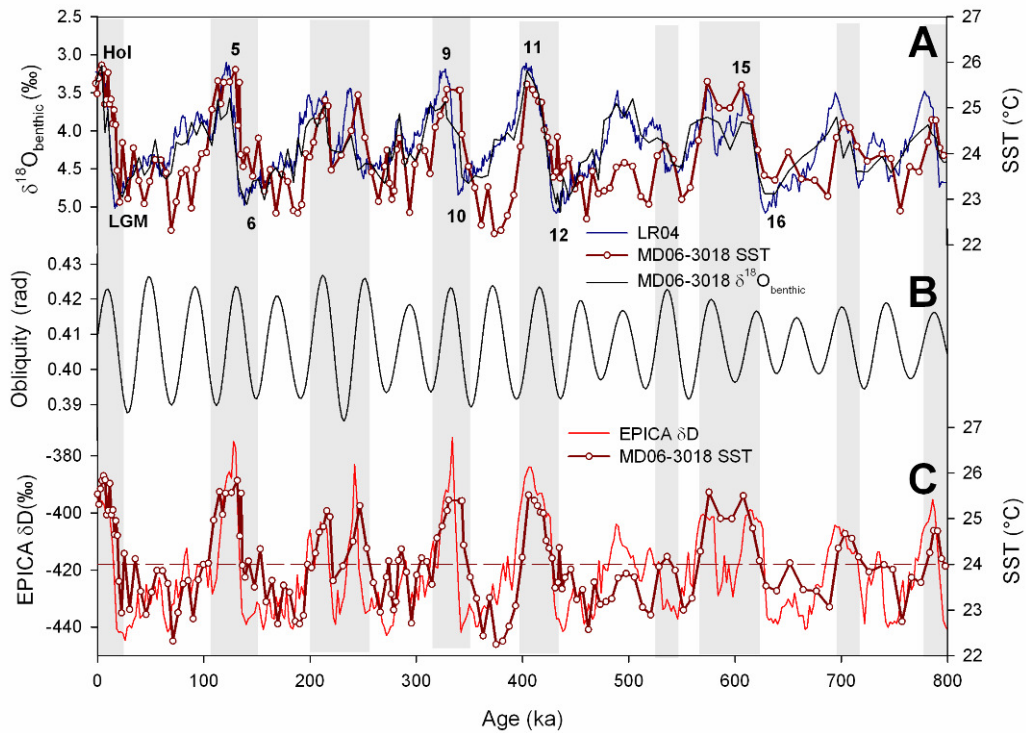


Figure 6.5 Plots over the past 800ka of **A)** MD06-3018 *G. ruber* Mg/Ca-derived SST, MD06-3018 *Cibicides wuellerstorfi* $\delta^{18}\text{O}_{\text{benthic}}$ and the LR04 $\delta^{18}\text{O}_{\text{benthic}}$ stack [Lisiecki and Raymo, 2005]. Numbers refer to same selected MIS shown in Figure 2. **B)** Orbital obliquity from the La03 solution [Laskar et al., 2004]. **C)** MD06-3018 *G. ruber* Mg/Ca-derived SST versus EPICA composite δD record, re-sampled (via linear interpolation) to 2kyr resolution [Jouzel et al., 2007]. Dashed line shows 24°C reference level (the long-term average of the SST reconstruction over the past 800ka) and grey shading shows periods when SST exceeds this.

The combined effect of the various orbital cycles on mean-annual insolation at 23°S is dominated by the effect of obliquity cycle. However, as has been previously documented for the equatorial Pacific [Liu and Herbert, 2004], this variability in local insolation forcing is almost exactly out of phase with the reconstructed subtropical southwest Pacific SST variability, even during the early Pleistocene where a dominant ~40kyr period is seen in both records. This means that the apparently obliquity paced variations in SST almost certainly cannot be a direct consequence of the effect of the orbital variations on local, low-latitude insolation. However, because changes in mean-annual insolation arising from obliquity fluctuations are out of phase between the low- and high-latitudes (but in phase between the two hemispheres), it also follows that the phase of the reconstructed SST

response would be consistent with the effect of the obliquity cycle on either the northern or southern high-latitudes.

The observation that equatorial Pacific SST reconstructions are coherent with, but lead records of $\delta^{18}\text{O}_{\text{benthic}}$ across the Pleistocene glacial/interglacial cycles suggests that the origin of the high-latitude sensitivity in wider low-latitude SST is unlikely to be in the northern hemisphere [Liu and Herbert, 2004; Medina-Elizalde and Lea, 2005]. However, this lead/lag relationship has been shown to also be potentially explicable by other factors [Ashkenazy and Tziperman, 2006]. The structure of the middle/late Pleistocene $\sim 100\text{kyr}$ SST cycles seen in the MD06-3018 reconstruction now provides an alternative approach to the problem, at least in the case of the subtropical southwest Pacific.

The pattern of long periods of low SST separated by $\sim 40\text{kyr}$ intervals of near symmetric warming and then cooling is similar to that seen in δD records from Antarctic ice cores [Jouzel *et al.*, 2007] (Fig 6.5C), taken here as a first-order proxy for high-latitude southern hemisphere climate. The interval of greatest discrepancy between the two records at 550-600ka may be partly accounted for uncertainties in the MD06-3018 age model over that interval. The SST to δD similarity is in contrast to the differences observed between the SST reconstruction and the LR04 $\delta^{18}\text{O}_{\text{benthic}}$ stack (Fig 6.5A) and supports the supposition that, during the middle/late Pleistocene at least, the origin of the strong obliquity signal within the subtropical southwest Pacific SST reconstruction was located in the southern, rather than northern, high-latitudes. The question of what processes may have acted to communicate this signal into the low-latitude climate response is considered in §5.4.

6.5.2 Orbital influences on subtropical southwest Pacific hydrological cycle variability

The MD06-3018 $\Delta\delta^{18}\text{O}_{\text{local}}$ reconstruction of regional hydrological cycle variability is subject to larger amplitude and phase uncertainties than the SST reconstruction as it depends upon both the uncertainties in the SST record itself and also the additional uncertainties arising from the correlation of two separate core age-models. Even bearing this in mind, however, it is immediately evident that the spectral properties of the $\Delta\delta^{18}\text{O}_{\text{local}}$ and SST records show significant differences over the past 1500ka (*Figs 6.3B/D*). Determining the orbital affinities of the significant 20-40kyr periodicities present in the $\Delta\delta^{18}\text{O}_{\text{local}}$ reconstruction is not, however, possible from *Figure 6.3D* alone. The wavelet transform coherence method, as described in the previous section, provides a method for evaluating these dominant orbital influences on the $\Delta\delta^{18}\text{O}_{\text{local}}$ record and hence, those acting on the regional hydrological cycle.

The $\Delta\delta^{18}\text{O}_{\text{local}}$ reconstruction shows generally lower coherence values with obliquity than was seen for SST and these values also generally decline over time such that no significant coherence is present after ~1000ka (*Fig 6.4C*). During the period prior to this, when significant coherence is present, the phase relationship between $\Delta\delta^{18}\text{O}_{\text{local}}$ and obliquity is seen to be in near anti-phase (the opposite of what was observed for SST). This implies that tilt maxima coincided with minima in $\Delta\delta^{18}\text{O}_{\text{local}}$. Like SST, $\Delta\delta^{18}\text{O}_{\text{local}}$ shows patchy coherence with the La04 precession index across the duration of the record, but in the case of $\Delta\delta^{18}\text{O}_{\text{local}}$ this is seen to become both persistent and highly significant over the past ~300ka (*Fig 6.4D*). Over this interval the $\Delta\delta^{18}\text{O}_{\text{local}}$ record and the precession index are also seen to be in near anti-phase, again meaning that maxima in the La04 precession index coincided with minima in $\Delta\delta^{18}\text{O}_{\text{local}}$.

To investigate the sensitivity of the coherence analysis presented above to the tuning assumptions involved in the generation of the $\Delta\delta^{18}\text{O}_{\text{local}}$ record, the same analysis was also undertaken with the alternative $\Delta\delta^{18}\text{O}_{\text{local}}$ record based on the untuned $\delta^{18}\text{O}_{\text{sw}}$ records, analogously to what was done for the wavelet decomposition itself in §4. In this case, coherence with obliquity is reduced to a non-significant level prior to ~1000ka, leaving only very patchy intervals of significant coherence across the record (not shown). Patchy intervals of significant coherence with the La04 precession index are retained across the duration of the record but the interval of enhanced persistence is now limited to the past ~200ka. Therefore, the absence of significant coherence between $\Delta\delta^{18}\text{O}_{\text{local}}$ and obliquity after ~1000ka and the increase in the coherence between $\Delta\delta^{18}\text{O}_{\text{local}}$ and precession over the latter part of the 100kyr world are both apparently robust to the tuning assumptions used in the derivation of the $\Delta\delta^{18}\text{O}_{\text{local}}$ record. However, both the presence of significant coherence between $\Delta\delta^{18}\text{O}_{\text{local}}$ and obliquity prior to ~1000ka and the timing/duration of the increase in precession coherence are seen to be dependent to a significant degree on the tuning assumptions and must therefore be viewed with a greater degree of caution.

6.5.3 Constraints on 'super-ENSO' over the MPT

Prior to ~1000ka, the MD06-3018 reconstructions of subtropical southwest Pacific SST and hydrological cycle variability both show significant coherence with the obliquity cycle (*Fig 6.4B/D*), although the latter observation is known to be sensitive to the assumptions involved in the generation of the $\Delta\delta^{18}\text{O}_{\text{local}}$ record. If accepted at face value, these observations could, however, potentially be indicative of the influence of an obliquity paced super-ENSO mode on the climate of the southern Coral Sea during the 40kyr world. The relative phase of the two reconstructions at the obliquity period is consistent with such a model, with SST maxima (minima) coinciding with $\Delta\delta^{18}\text{O}_{\text{local}}$ minima (maxima), which is consistent with warm, wet La-Niña (cool, dry El-Niño) -like conditions. However, the specific hypothesis of *Philander and Fedorov* [2003] that the amplification of the obliquity cycle by the low-latitude ocean/climate system should favor an El-Niño (La-Niña) state when tilt is large (small) is in the opposite sense to what is observed in the MD06-3018 reconstructions. This does not preclude the existence of such a phenomenon, but does mean that it cannot have exerted the dominant control on either SST or hydrological cycle variability in the subtropical southwest Pacific.

The definite absence of a persistently significant coherence relationship between the hydrological cycle reconstruction and obliquity after ~1000ka suggests that any obliquity paced super-ENSO mechanism that was present in the 40kyr world weakened over the MPT, with the dominant forcing mechanisms of SST and hydrological cycle variability becoming largely decoupled over the middle/late Pleistocene. In particular, whereas SST continues to exhibit significant coherence with obliquity across that time, the hydrological cycle reconstruction shows little persistent coherence with either obliquity or precession until 300-200ka. The apparent increase in the persistence of significant coherence with the precession index at that time must necessarily be interpreted with caution, given the uncertainties associated with the derivation of the $\Delta\delta^{18}\text{O}_{\text{local}}$ record and its temporal resolution. If, however, accepted at face value then the relationship may be

indicative of a precession paced super-ENSO mode becoming more significant over the latter part of the 100kyr world.

The strength of the ENSO system *sensu stricto* on the multi-annual time-scale is thought to be related to the effect of precession forcing on seasonal insolation budgets within the low-latitude Pacific [Clement *et al.*, 1999]. Furthermore, the same ENSO models also predict associated changes in the mean-state of the low-latitude Pacific on the time-scale of the precession cycle, with La-Niña like conditions being associated with high values of the La04 precession index. This scenario is consistent with the observed pattern of $\Delta\delta^{18}\text{O}_{\text{local}}$ variability over the past ~300ka, with high precession index values nearly coincident with negative $\Delta\delta^{18}\text{O}_{\text{local}}$ values (regionally wetter conditions, as associated with the La-Niña state in the regional ENSO cycle *sensu stricto*). In the modern climate regime, New Caledonia is more highly sensitive to ENSO fluctuations in precipitation than SST, mainly as a consequence of shifts in the position and intensity of the South Pacific Convergence Zone [Gouriou and Delcroix, 2002], with the El-Niño (La-Niña) mode characterized by dry (wet) conditions with inter-annual precipitation anomalies, relative to mean-annual values, of as much as 50% observed [Nicet and Delcroix, 2000]. Thus, the absence of a corresponding pattern of precession coherence in the SST reconstruction (Fig 6.4B) may be attributable to the relative weakness of the SST variations (in comparison to precipitation) associated with the ENSO cycle *sensu stricto* at the site.

The interpretation of the precession cycle relationships, in relation to those at the obliquity, is necessarily very tentative at the present, but does at least suggest that the low-latitude coupled ocean/atmosphere system may potentially have contributed to a proposed increase in the sensitivity of the global climate system precession forcing within the 100kyr world [Imbrie *et al.*, 1993; Raymo, 1997]. The future study of other sub-orbitally resolved reconstructions of low-latitude Pacific climate variability will allow the direct testing of whether the climatic pattern observed here is part of a wider, post-MPT, precession-paced, super-ENSO response.

6.5.4 Low-latitude Pacific SST forcing mechanisms over the MPT

It has been proposed that radiative forcing arising from greenhouse gas variability dominates the low-latitude glacial/interglacial SST response, at least in the western Pacific, across the MPT [Medina-Elizalde and Lea, 2005]. Both model calculation of radiative forcing across the low-latitudes for the last glacial cycle [Broccoli, 2000] and the observation that low-latitude SST variability is close to being in-phase with atmospheric pCO₂ variability over the past ~800ka [Jouzel *et al.*, 2007; Lea, 2004] support this interpretation. However, the MD06-3018 reconstructions of subtropical southwest Pacific SST and hydrological cycle variability also provide evidence that obliquity paced super-ENSO fluctuations may also have significantly influenced low-latitude western Pacific climate prior to ~1000ka.

In order to better constrain the relative influences of these two mechanisms on both subtropical southwest Pacific SST in particular and SST in the wider low-latitude system in general, the MD06-3018 SST reconstruction is now compared to others from the WEP (MD97-2140) [de Garidel-Thoron *et al.*, 2005] and the EEP (ODP site 846) [Lawrence *et al.*, 2006]. The core locations in relation to the modern Pacific mean-annual SST distribution are shown on *Figure 5.1* and given in *Table 5.1*. SST anomalies associated with the ENSO cycle *sensu stricto* are of the same sign (but different magnitude and phase) in the WEP and the southern Coral Sea, whereas the EEP is a region of extensive upper-ocean ventilation and hence ENSO SST anomalies here are anti-correlated to those in the western low-latitude Pacific (*Fig 6.1*). Unlike the Mg/Ca-derived western Pacific SST reconstructions, the ODP 846 reconstruction is based on alkenone saturation indices. Whilst the two proxy systems involve different assumptions, they have been shown to be in agreement regarding first-order trends in EEP SST over the past 5000ka [Dekens *et al.*, 2008]. The MD97-2140 and ODP 846 reconstruction are presented on the published core age models (*Fig 6.6A*). In order to analyze the long-term (i.e. super glacial/interglacial) trends in glacial/interglacial SST variance, all records were re-sampled (via linear interpolation) at 5kyr resolution and linearly de-trended prior to

the calculation of a 400kyr moving box car standard deviation SST value (σ_{SST} , Fig 6.6B).

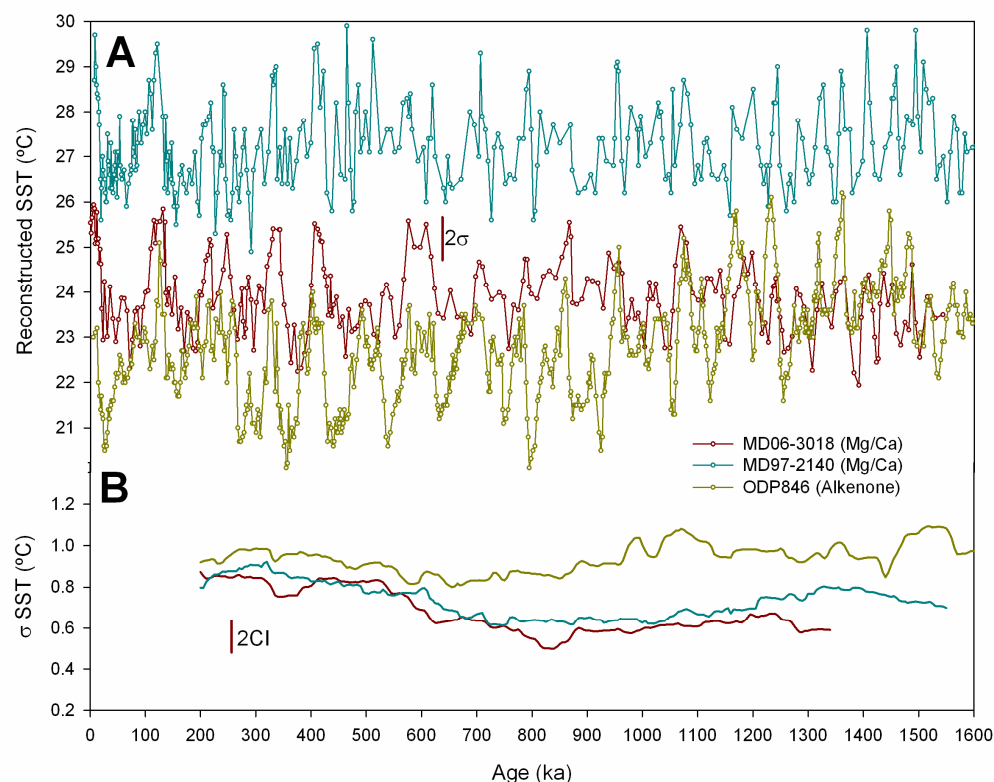


Figure 6.6 **A)** SST reconstructions from MD06-3018 in the subtropical southwest Pacific, MD97-2140 in the WEP [*de Garidel-Thoron et al.*, 2005] and ODP 846 in the EEP [*Lawrence et al.*, 2006]. The MD06-3018 and MD97-2140 reconstructions are based on Mg/Ca and the ODP 846 reconstruction on alkenone saturation index paleothermometry methods. All records are presented on published age models. Vertical bar shows MD06-3018 sample reproducibility uncertainty, as defined in chapter 4, §3.1. **B)** 400kyr running box-car σ_{SST} records after linear de-trending. Vertical bar shows 95% Confidence Interval (CI) for the σ_{SST} values.

The two western Pacific SST reconstructions (MD06-3018 and MD97-2140) are seen to be within the 95% confidence interval on σ_{SST} of $\pm 0.15^\circ\text{C}$ of one another throughout the past 1500ka (Fig 6.6B). There has, therefore, been no significant difference in glacial/interglacial SST variance between 2°N and 23°S in the western Pacific over this period. Furthermore, the first-order spectral properties of the two records are very similar (Fig 6.7A/B), suggesting that the timing of the MPT was also similar at both latitudes. These observations are most consistent with a dominant

greenhouse gas (i.e. spatially uniform) forcing of the reconstructed SST variability. A contribution from super-ENSO related circulation changes cannot be ruled out, but would be required to have been both uniform in SST amplitude between the two sites, regardless of the overall strength of any orbitally paced super-ENSO modes.

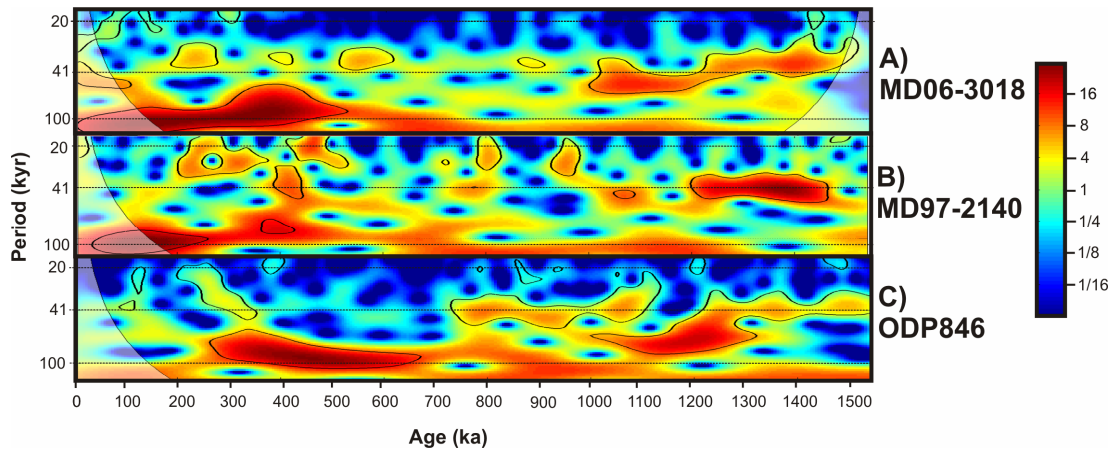


Figure 6.7 Local wavelet power spectra of the SST reconstructions from **A)** MD06-3018, **B)** MD97-2140 and **C)** ODP 846. All records were re-sampled (via linear-interpolation) to 5kyr resolution, de-trended and normalized to unit-variance prior to analysis. Wavelet decomposition was performed using the WTC-16 code [Grinsted *et al.*, 2004]. Colour bar shows spectral power in normalized units of variance. Black contour-lines show 5% confidence intervals above a modelled first order autoregressive red-noise process. Shaded areas show the cone-of-interference, within which edge effects become significant.

An additional line of evidence in support of a greenhouse gas dominated SST response is that the timing (~500ka) and increase in glacial/interglacial amplitude of ~30% associated with the emergence of the ~100kyr SST cycles in the MD06-3018 record are both consistent with the shift in glacial/interglacial pCO₂ variability between the interval 800-500ka and the past five cycles seen in ice-core records [Luthi *et al.*, 2008]. If it is assumed that the early Pleistocene glacial/interglacial pCO₂ cycles were at a ~40kyr period and of similar amplitude to those of the 800-500ka interval, as is supported by geochemical proxy reconstructions [Honisch *et al.*, 2009], then this would also be consistent with the dominant influence of greenhouse gas forcing on subtropical southwest Pacific SST having persisted across at least the

past 1500ka. The data presented here is most consistent with the contention that greenhouse gas forcing has dominated western low-latitude Pacific glacial/interglacial SST variability across the MPT and hence that the carbon-cycle acts as the main communicating mechanism for the high-latitude obliquity sensitivity described in §5.1. Whilst the influence of super-ENSO modes on the southern Coral Sea may be detectable during the early Pleistocene, they seem unlikely to have contributed significantly to the glacial/interglacial SST amplitude.

Over the past 600ka, the EEP σ_{SST} record is seen to have been slightly higher in value, but within the 95% confidence interval, of those for the two western Pacific records (*Fig 6.6B*). However, in contrast to the western Pacific records, no significant increase in EEP σ_{SST} is seen over the MPT interval. The resultant difference in σ_{SST} during the early Pleistocene between the eastern and western low-latitude Pacific reconstructions exceeds the 95% confidence interval and is not a consequence of record de-trending, as the same exercise performed on the original un-trended records leads to an even greater calculated difference.

The observed divergence of EEP and western low-latitude Pacific SST variance at 800-600ka is seen to have coincided with the decline in significant ~40kyr spectral power (~700ka) seen in the ODP 846 record (*Fig 6.7C*). This, therefore, supports a significantly enhanced relative contribution from upper-ocean ventilation changes to EEP glacial/interglacial SST variability during the ~40kyr world [*Philander and Fedorov, 2003; Liu and Herbert, 2004*]. Thus, whilst greenhouse gas forcing has apparently dominated glacial/interglacial SST variability in the low-latitude western Pacific across the entire Pleistocene, the combined effect of the changes occurring during the MPT was to also increase its relative importance in areas of upwelling, such that by the end of the transition and the advent of the 100kyr world, glacial/interglacial SST amplitudes do not significantly differ zonally across the low-latitude Pacific.

6.6 Conclusions

The MD06-3018 Mg/Ca-derived reconstruction of subtropical southwest Pacific SST shows orbital time-scale variability in the range 2-3°C and a clear MPT from dominant 40kyr to 100kyr modes, with the latter periodicity becoming more significant at ~500ka. In contrast, reconstructed regional hydrological cycle variability (based on the extraction of the local component of calculated $\delta^{18}\text{O}_{\text{sw}}$ variability, derived in turn from coupled $\delta^{18}\text{O}$ -Mg/Ca measurements) does not show significant spectral power at the ~100kyr period over the past 1600ka, but patchy intervals of significant spectral power are present in the 20-40kyr band across the duration of the record.

The MD06-3018 SST reconstruction shows a strong relationship to the orbital obliquity cycle across the past 1500ka which must arise from a high-latitude, rather than local, sensitivity to the orbital variations. The close correspondence within the 100kyr world of the structure of reconstructed subtropical southwest Pacific SST variability with proxy records of Antarctic climate suggests that the origin of this sensitivity was located in the southern rather than northern high-latitudes. In contrast to the SST response, reconstructed hydrological cycle variability in the subtropical southwest Pacific shows only limited coherence with the obliquity cycle (with no significant coherence seen after ~1000ka) and a stronger relationship with the orbital precession index.

The decoupling of the reconstructed SST and hydrological cycle responses indicate that obliquity paced super-ENSO fluctuations in the wider low-latitude ocean/atmosphere system could only have significantly affected the climate of the southern Coral Sea prior to ~1000ka. The amplitude of any such fluctuations is likely to have been relatively small, even during the 40kyr world, as comparison of the MD06-3018 SST reconstruction with others from the equatorial Pacific supports the view that greenhouse gas forcing has dominated glacial/interglacial SST variability in the low-latitude western Pacific across the entire Pleistocene.

More fundamentally, the present study has clearly demonstrated that reconstructions of different aspects of the low-latitude climate system show differing responses to orbital forcing across the MPT. This reflects the complexity of the low-latitude system on these time-scales and highlights the importance of wide spatial coverage of multi-proxy reconstructions in understanding the evolving modes of climate response to orbital forcing. This chapter has, however, developed constraints on the structure and amplitude of orbital time-scale variability in both the low-latitude ocean/atmosphere circulation system and the carbon-cycle over the MPT. The implications of these for the potential roles played by both systems in the change in global climate sensitivity to orbital forcing that occurred over the transition are discussed further in chapter 7, §2. The implications of the close relationship between reconstructed subtropical SST and ice-core pCO₂ variability over the past 800ka, as described in §5.4, are also explored further in chapter 7, §5, this time in the context of paleoclimatic constraints on climate sensitivity to pCO₂.

Blank Page

7.2 Orbital time-scale variability in the low-latitude ocean/atmosphere system: constraints from the meridional extent of the Pacific warm pool

The advective fluxes of both heat and moisture within the upper-ocean and atmosphere, in both zonal and meridional senses, constitute important processes within the modern climate system, but are difficult to directly reconstruct in the past. However, as both temperature and salinity are conservative properties of seawater, spatial comparison of reconstructed SST and potentially also $\delta^{18}\text{O}_{\text{sw}}$ (although this approach then relies upon assuming an invariant salinity - $\delta^{18}\text{O}_{\text{sw}}$ relationship) patterns allows some inferences to be made regarding past ocean circulation patterns. One of the unifying themes of this thesis has been the application of this approach to the MD06-3018 Mg/Ca-derived reconstruction of southern Coral Sea SST, in comparison to others from the low-latitude Pacific, with a specific focus on better constraining the meridional components of heat transport from the Pacific warm pool on >100kyr and orbital time-scales.

In chapter 5 it was demonstrated that no significant (in the sense of causing significant changes in reconstructed SST at 23°S) fluctuations in the southern extent of warm pool influence have occurred on the >100kyr time-scale, at least over the past 1500ka. On orbital time-scales, chapter 6 showed that the patterns of reconstructed subtropical southwest Pacific SST and hydrological cycle variability are not consistent with either a dominant control from the obliquity paced super-ENSO mechanism of *Philander and Fedorov* [2003] or the presence of any significant super-ENSO response at the ~100kyr period. These observations do not in themselves entirely preclude the existence of significant fluctuations in the southern extent of warm pool influence on 10-100kyr time-scales, as these may have occurred at other periods, for example that of the precession cycle. Any such fluctuations in the southern extent of warm pool influence could have arisen through either super-ENSO type changes in the extent of the warm pool itself, or through changes in the subtropical surface ocean circulation regime.

To constrain the extent of changes in the southern extent of warm pool influence across the entire 10-100kyr periodicity range, the MD06-3018 SST reconstruction is re-compared with the MD97-2140 Mg/Ca-derived SST reconstruction from the WEP [*de Garidel-Thoron et al., 2005*], the location of which is shown in *Figure 5.1* and given in *Table 5.1*. If it is assumed, as in chapters 5 and 6, that the MD97-2140 core-site has always remained within the heart of the warm pool, then the SST gradient between the two sites, Δ SST (analogous to the ‘WEP-Coral Sea’ gradient on *Figure 5.2E*) provides a proxy for the past southern extent of warm pool influence. If systematic changes in warm pool extent occurred sufficient to affect 23°S then the wavelet decomposition of the Δ SST record should show significant spectral power at that period. The MD97-2140 record is presented on its published core age model, but in order to allow calculation of Δ SST both records were re-sampled via linear interpolation to a common 5kyr resolution time-step prior to subtraction.¹

The calculated Δ SST record shows fluctuations of 1-3°C around a mean value of 3.5°C over the past 1600ka (*Fig 7.1B*). This mean value is consistent with the modern value of Δ SST based on WOA2005 values (*Fig 5.1*). Some significant (at the 5% confidence limit against red-noise) spectral power is seen in the wavelet decomposition of the Δ SST record in the 20-40kyr band over the past ~1000ka, and especially the past ~500ka (*Fig 7.1C*). This variability is seen to display no significant coherence with the orbital obliquity cycle (*Fig 7.2A*) and patchy coherence with the orbital precession index (*Fig 7.2B*).

¹ The age-models for the two cores are not tuned directly to one another due to the absence of a $\delta^{18}\text{O}_{\text{benthic}}$ record from MD97-2140. Direct tuning of the SST reconstructions would introduce significant circularity into the subsequent spectral analysis of the SST gradient record.

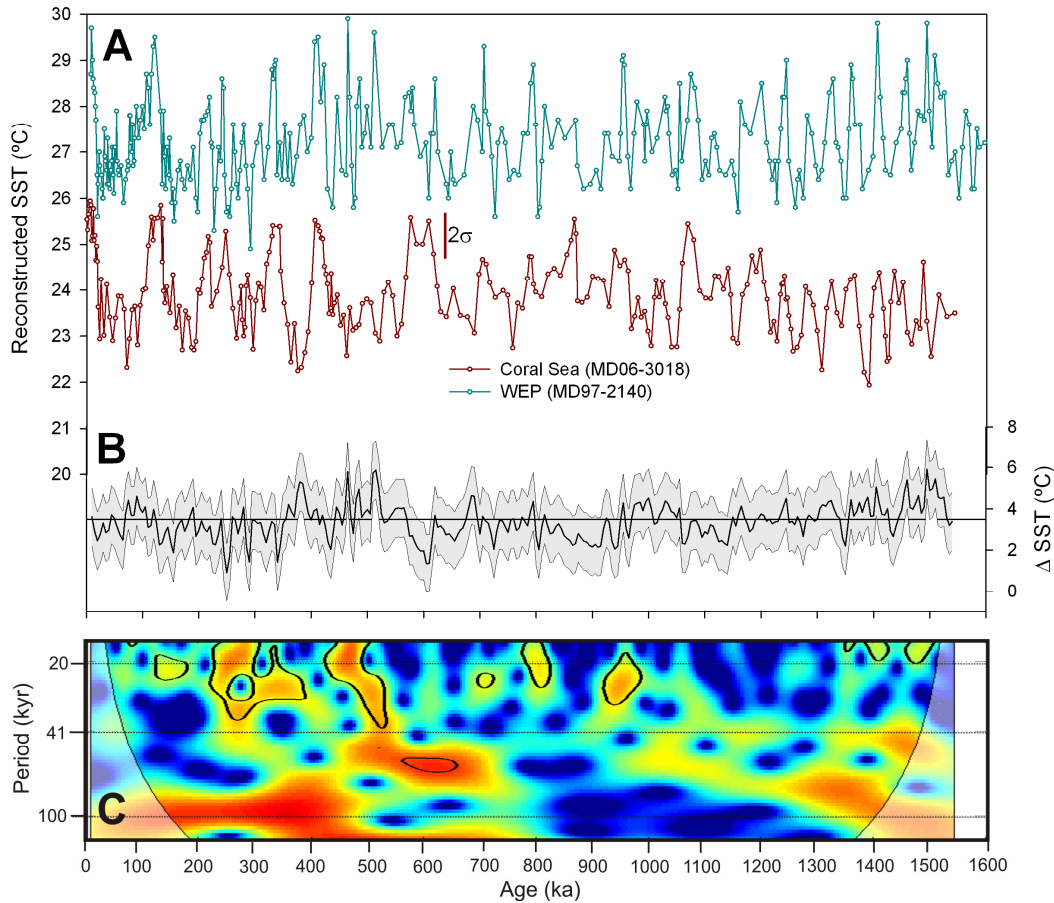


Figure 7.1 **A)** Mg/Ca-derived SST reconstructions from MD06-3018 for the southern Coral Sea and MD97-2140 for the WEP [*de Garidel-Thoron et al., 2005*]. Both records are presented on the published age models. Vertical bar shows MD06-3018 $2\sigma_r$ uncertainty. **B)** Reconstructed SST gradient (Δ SST) between the two sites. Grey shading shows $\pm 2\sigma_{diff}$ error envelope, assuming the MD06-3018 reproducibility error for both reconstructions. **C)** Local wavelet power spectra of Δ SST. Warmer colours represent greater spectral power (on a logarithmic scale from 1/16 to 16 units of squared normalized variance, the same as shown for *Figure 6.3*). Black contour-lines show 5% confidence intervals relative to a first order auto-regressive red noise process. Shaded areas show the cone-of-interference, within which edge effects become significant.

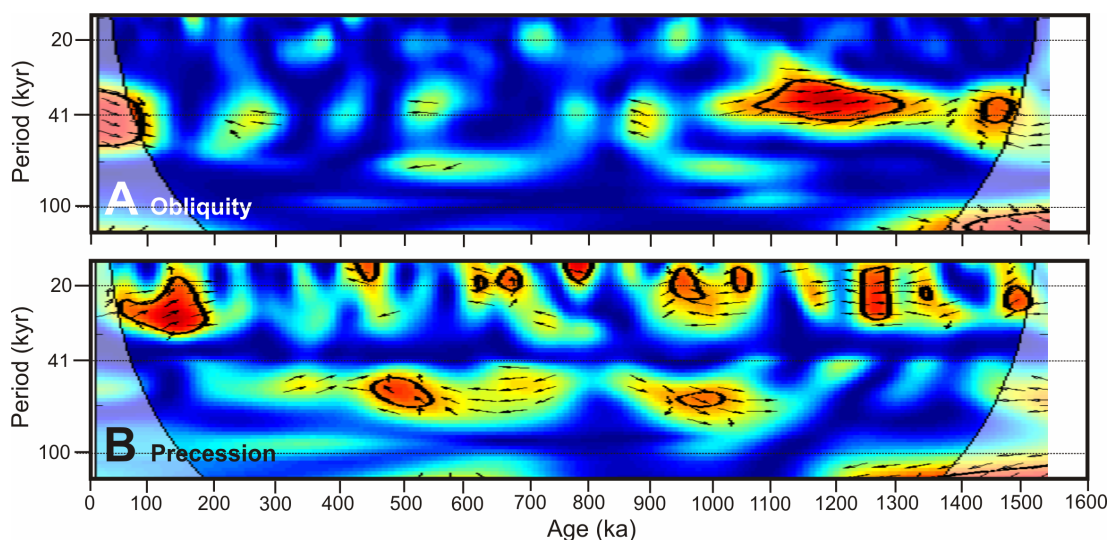


Figure 7.2 Wavelet transform coherence analysis of Δ SST with **A)** orbital obliquity and **B)** precession index records from the La04 orbital solution [Laskar *et al.*, 2004]. Warmer colours represent greater coherence (on a linear scale from 0 to 1, the same as shown in Figure 6.4). Wavelet analysis was performed using the WTC-16 code [Grinsted *et al.*, 2004]. Black contour-lines show 5% confidence intervals relative to red noise, determined using a Monte Carlo method. Shaded areas show the cone-of-interference, within which edge effects become significant. For areas of age-period space with significant coherence, the phase relationship between the two variables is shown by black arrows. Right (left) pointing horizontal arrows denote an in-phase (anti-phase) relationship.

The pattern observed in the Δ SST record of increasingly significant spectral power in the 20-40kyr band over the past ~500ka, coupled to significant coherence with the precession index, but not with the obliquity cycle is similar to that previously noted for the MD06-3018 reconstruction of regional hydrological cycle variability (Fig 6.3D and Figs 6.4C/D). This suggests that coherent precession related fluctuations in the southern extent of warm pool influence, as well as in regional precipitation patterns, may have been a feature of the 100kyr world. Although it is not significant against the red-noise test, spectral power above the background level is also present at the ~100kyr period over the past ~500ka, suggesting that the proposed enhanced sensitivity of the post-MPT warm pool to precession variability was also coupled to an enhanced ~100kyr response in the

extent of warm pool influence, probably as a consequence of the eccentricity modulation of the precession cycle.

Although it is not significant at the 5% confidence limit, spectral power above the background level at the ~40kyr period is also present in the Δ SST record prior to ~1000ka (*Fig 7.1C*) and this variability is seen to be significantly coherent with the orbital obliquity cycle over the same interval (*Fig 7.2A*). This suggests that obliquity paced fluctuations in the southern extent of warm pool influence may have had a detectable, if small, influence on the southern Coral Sea during the 40kyr world. However, as was discussed in chapter 6, §5.4, the effect of any such fluctuations in forcing SST variability at both western low-latitude Pacific core locations, is very small compared to the contribution from greenhouse gas variability.

The observed 1-3°C amplitude of the observed 20-40kyr period Δ SST variability over the past 1600ka (*Fig 7.1B*) may be partly explained by super-ENSO oscillations in the size of the warm pool itself. The propagated sample reproducibility uncertainty on Δ SST (assuming MD06-3018 reproducibility error for both reconstructions) is $2\sigma_{\text{diff}}=1.4^\circ\text{C}$. The amplitude of modern ENSO seasonal SST anomalies in the southern Coral Sea are in the range 0.1-1.0°C [*Gouriou and Delcroix, 2002*], consistent in order with the variance in Δ SST that cannot be accounted for by noise arising from the propagated sample reproducibility uncertainty. However, another possibility is that changes in the subtropical surface ocean circulation regime, rather than warm pool extent itself, led to the observed Δ SST variability and this is considered below.

Within the modern circulation regime, the influence of warm pool waters is carried southwards in the western Coral Sea by the East Australian Current, which separates from the Australian coast and flows eastwards at the Tasman Front (~32°S) [*Bostock et al., 2006*] (*Fig 2.2A*). The Tasman Front represents a diffuse SST front separating warmer tropical and subtropical waters to the north from generally cooler (<20°C) waters to the south. The front is also associated with a significant change in the planktic foraminiferal fauna, from a tropical/subtropical assemblage (with %

abundance *G. ruber* > 20% and *Globorotalia inflata* < 10%) to the north into a transitional assemblage (with % abundance *G. ruber* < 20% and *G. inflata* > 10%) at the front itself [Thiede *et al.*, 1997]. Northward migration of the Tasman Front to ~25°S during the LGM has been proposed [Martinez, 1994; Kawagata, 2001; Bostock *et al.*, 2006], possibly as a consequence of changing surface wind fields [Bostock *et al.*, 2006]. Such a meridional change in front position could potentially have accounted for some or all of the increase in LGM seasonality seen in the MD06-3018 MAT-derived SST estimates (chapter 4, §4.3) as it would have acted to increase the meridional SST gradient at 23°S.

The MD06-3018 SST reconstruction shows mean-annual SST values of >20°C for all MIS across the past 1600ka, regardless of whether a proxy correction methodology is applied or not (Fig 4.2B). This observation alone strongly suggests that the core-site has never been north of the Tasman Front, but relies on the reliability of the ability of the MD06-3018 Mg/Ca paleothermometer to record mean-annual SST values. The planktic foraminiferal faunal assemblages presented in chapter 4 provide an alternative method to reconstruct front position in relation to the MD06-3018 core-site. Decreases (increases) in the relative abundances of *G. ruber* (*G. inflata*) are observed during selected glacial stages, relative to the corresponding interglacials, throughout the past 1600ka (Table 7.1). These changes are significant, but never large enough to have constituted a full shift from a tropical/subtropical to a transitional assemblage [Thiede *et al.*, 1997].

Both the geochemical SST reconstruction and the faunal counts argue against the Tasman Front having reached as far north as 23°S during the LGM, or indeed during any MIS, over the past 1600ka. This approach places constraints on past Tasman Front migration, but does not preclude it having exerted a significant control on the observed glacial/interglacial variations in both seasonality and/or mean-annual SST. Therefore, the present MD06-3018 reconstructions cannot firmly resolve whether the origin of the 20-40kyr period variability observed in the reconstructed southern extent of warm pool influence was through super-ENSO modulation of

warm pool extent itself, or as a consequence of circulation changes within the subtropical Pacific itself.

Age-model (ka)	MIS	% <i>G. ruber</i>	% <i>G. inflata</i>
0	Late Hol	34.9	4.0
10.1	Early Hol	45.5	4.1
14.8	LGM/Hol	37.3	4.3
22.7	LGM	28.8	7.1
406.3	11	36.9	2.0
430.6	12/11	29.1	6.6
436.2	12	25.3	9.5
1238.1	37	25.2	1.1
1248.5	38/37	24.2	5.5
1252.1	38	23.8	5.9

Table 7.1 Percentage abundance data for *G. ruber* and *G. inflata* for selected MIS, as used in the high-resolution glacial termination data sets presented in chapter 4. Full planktic faunal counts for these intervals are given in appendix 7.

That the low-latitude ocean/atmosphere circulation regime exerts a significant influence on the global climate on the multi-annual time-scale is beyond dispute [Sarachik and Cane, 2010]. Millennial time-scale super-ENSO fluctuations have also been documented in warm pool SST patterns during both glacial stages [Stott *et al.*, 2002] and deglaciations [Visser *et al.*, 2003]. This thesis supports the existence of significant >100kyr time-scale reorganizations of the low-latitude ocean/atmosphere circulation system, which may have played a key role in ice-sheet evolution and climate, although these changes were not manifested in the southern extent of warm pool influence. On the intervening, orbital time-scale, the nature of the low-latitude ocean/atmosphere circulation system response is shown to have been temporally and spatially variable as well as varying between the different orbital cycles themselves.

The absence of ~100kyr spectral power from the middle/late Pleistocene reconstructions of both subtropical hydrological cycle variability (100kyr power completely absent in *Figure 6.3D*) and the southern extent of warm pool influence (100kyr power not significant in *Figure 7.1C*) shows that no coherent fluctuations in the low-latitude ocean/atmosphere circulation system occurred at that period.

Although obliquity related fluctuations in upper-ocean ventilation and the wider low-latitude ocean/atmosphere system have exerted a significant influence on EEP SST during the 40kyr world, they are only very weakly detectable in the subtropical southwest Pacific, as discussed in the case of the regional hydrological cycle reconstruction in chapter 6 and as seen in the absence of significant 40kyr power prior to ~500ka in the Δ SST proxy record for the southern extent of warm pool influence in *Figure 7.1C*. Thus, whilst the relative importance of obliquity paced fluctuations in the low-latitude ocean/atmospheres system did apparently decline over the MPT, this change is unlikely to have significantly impacted high-latitude orbital time-scale climate variability.

These constraints on the global influence of low-latitude ocean/atmosphere circulation system variability at both the 100kyr and 40kyr periods means that it is highly unlikely that the shift in orbital sensitivity seen in global climate over the MPT can be explained as a consequence of threshold changes in that system. However, there is tentative evidence from the reconstructions of both subtropical hydrological cycle variability and the southern extent of warm pool influence that the emergence of the dominant 100kyr climatic mode did act to increase the sensitivity of the low-latitude ocean/atmosphere system to forcing from the precession cycle, which may have then have significant influenced global climate at the ~20kyr period, possibly via a super-ENSO response at that period.

7.3 Orbital and >100kyr time-scale variability in the carbon-cycle: constraints from subtropical southwest Pacific deep water circulation

Just as the low-latitude ENSO system is unquestionably important for global climate on inter-annual time-scales, the global carbon-cycle exerts a significant influence on climate on time-scales ranging from centuries to Myrs. On both the orbital and >100kyr time-scales, the key dynamic processes within the carbon-cycle remain poorly understood however, especially as regards the origin of the observed glacial/interglacial fluctuations in pCO₂ [Archer *et al.*, 2000; Sigman and Boyle, 2000]. The close correspondence between Antarctic ice-core reconstructions of southern high-latitude air temperature and global pCO₂ over the past 800ka [Jouzel *et al.*, 2007], strongly suggests a close connection between southern high-latitude climate and the carbon-cycle fluctuations. This is consistent with process-based models advocating coupling between southern high-latitude climate, Southern Ocean deep water ventilation and the enhanced storage of DIC in the glacial stage deep ocean [Toggweiler *et al.*, 2006]. Understanding the origin and structure of deep water circulation in the southern hemisphere is therefore important in evaluating such models. The MD06-3018 reconstructions of subtropical southwest Pacific deep water paleoceanography, as presented in chapter 3, allow for some new constraints to be placed on both the orbital and >100kyr time-scale distribution of southern hemisphere deep water masses.

The deep water mixing regime in the subtropical southwest Pacific, as reconstructed from MD06-3018 $\delta^{13}\text{C}_{\text{benthic}}$ measurements, shows significant glacial/interglacial variability in the relative importance of different Southern Ocean source regions. This in turn implies the existence of significant spatial chemical gradients within the glacial stage Southern Ocean and in particular between the Pacific and Indian/Atlantic sectors, as described in chapter 3, §8.4. Reconstructions of the vertical deep water $\delta^{13}\text{C}$ gradient in the southern Atlantic sector of the Southern Ocean resemble the variability seen in the Vostok atmospheric pCO₂ record [Hodell *et al.*, 2003]. This provides empirical support to modelling studies

suggesting that an enhanced stratification of the glacial deep ocean can significantly contribute to lowering atmospheric $p\text{CO}_2$ [Toggweiler, 1999]. However, the present study suggests that whilst this pattern probably extended across the Indian sector (the Adélie Coast bottom water domain in the terminology of *McCave et al.* [2008]) it probably did not extend into the Pacific sector (the Ross Sea bottom water domain). This interpretation is consistent with the presence of highly depleted glacial $\delta^{13}\text{C}_{\text{benthic}}$ values seen in cores below ~2500m depth being restricted to the southern Atlantic and Indian Ocean sectors [Hodell et al., 2003].

The deep open Pacific, by far the largest reservoir of DIC on the planet, was therefore potentially not available as a sink for enhanced glacial carbon storage, or at least not to the same extent as the southern Atlantic and Indian Oceans. Many more deep sea $\delta^{13}\text{C}_{\text{benthic}}$ records, especially from the southern Pacific and Ross Sea are required to better constrain this spatial pattern, but enhanced glacial stage spatial variability in the pathways of southern hemisphere deep water circulation may provide an important limiting factor for models invoking physical and chemical stratification of the Southern Ocean as a mechanism for enhanced deep ocean carbon storage.

The dominant source of deep water to the NCT over the past 1600ka remained the Southern Ocean, based on the use in chapter 3, §8.3 of equatorial Pacific $\delta^{13}\text{C}_{\text{benthic}}$ records to place limits on the potential contribution from North Pacific deep water ventilation. The $\delta^{13}\text{C}$ approach alone cannot resolve flow-rate changes, but the pattern of variability observed across the MPT is difficult to explain without a general reduction in southern hemisphere deep water ventilation over the transition, as described in chapter 3, §8.5. This is consistent with previous studies on the Pacific DWBC [Hall et al., 2001; Crundwell et al., 2008], suggesting that it was a general trend associated with at least the Adélie Coast and Ross Sea deep water domains. Given that the MPT is also thought to have represented an interval of reduced northern hemisphere deep water formation [Raymo et al., 1997], it follows that the transition represented a relatively sluggish period of global deep water formation on the >100kyr time-scale. This contrasts with the glacial/interglacial

time-scale, on which northern and southern source deep waters show broadly opposing patterns of ventilation intensity [Charles and Fairbanks, 1992; Hall et al., 2001]. The reasons for such a perturbation in deep water formation on the >100kyr time-scale are probably related to high-latitude climatic changes occurring during the MPT. One possible mechanism to explain the hemispherically symmetric nature of the changes is meridional shifts in the mid-latitude ocean/atmosphere front systems. Within the southern hemisphere for example, a weakened Antarctic Circumpolar Current during the MPT [Crundwell et al., 2008] may have interacted with the overlying atmospheric circulation to reduce the overturning of deep waters [Toggweiler et al., 2006].

7.4 Orbital and >100kyr time-scale variability in the carbon-cycle: the role of neritic calcification

The chronology and potential causes of the middle Pleistocene expansion of coral reef systems, as reviewed in chapter 4, §2, have important implications for the Pleistocene evolution of the global carbon-cycle. Changes in net reef calcification and hence the storage of alkalinity in the shallow (as opposed to deep) ocean, may have been sufficiently large on a global scale to have constituted a significant contributing mechanism for the observed glacial/interglacial variability in middle/late Pleistocene atmospheric pCO₂, an idea that is known as the ‘coral reef hypothesis’ [Opdyke and Walker, 1992; Ridgwell et al., 2003; Vecsei and Berger, 2004]. Ocean chemistry constraints suggest, however, that the coral reef hypothesis cannot plausibly have accounted for the entirety of the observed glacial/interglacial pCO₂ variability [Archer et al., 2000; Sigman and Boyle, 2000].

An alternative version of the hypothesis states that the shift between the 60-90ppmV amplitude cycles prior to MIS 11 and the subsequent 90-100ppmV ones, as seen in Antarctic ice-core pCO₂ records [Luthi et al., 2008] (Fig 7.3A), may have arisen from an increased contribution from neritic calcification during the last five interglacial stages [Rickaby et al., 2010]. This latter hypothesis requires that middle Pleistocene reef expansion was centred on MIS 11 and controlled by a global process

(i.e. sea-level change), rather than being a more diffuse period of expansion which could have been controlled, at least in part, by regional climatic factors.

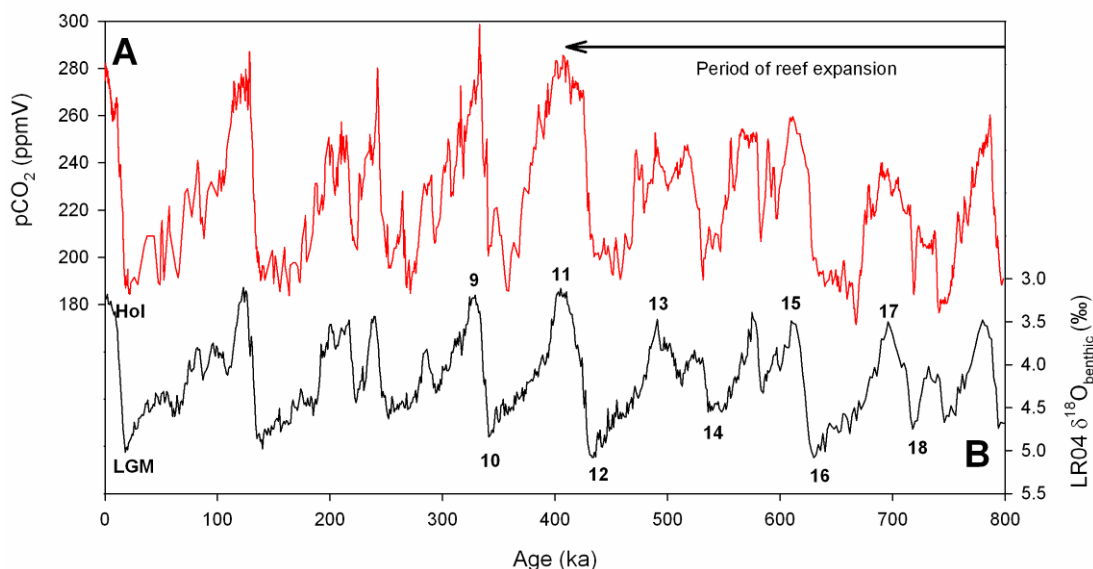


Figure 7.3 Plots of **A)** EPICA composite $p\text{CO}_2$ [Luthi *et al.*, 2008] and **B)** LR04 stacked $\delta^{18}\text{O}_{\text{benthic}}$ [Lisiecki and Raymo, 2005] over the past 800ka. Numbers show selected MIS. Arrow shows generalized period of global reef expansion, as discussed in chapter 4.

The general >100kyr time-scale Plio-Pleistocene trends of global cooling and increasing global ice volume (falling sea-level) [Zachos *et al.*, 2001; Lisiecki and Raymo, 2005] are both in the wrong sense to have plausibly limited reef development on the global scale prior to the middle Pleistocene. Furthermore, the Mg/Ca-derived SST reconstruction in the present thesis has shown that no significant trends are present in southern Coral Sea SST on the >100kyr time-scale over the past 1600ka. On the 10-100kyr time-scale, chapter 4 demonstrated that the combined proxy uncertainty associated with the MD06-3018 Mg/Ca-derived mean-annual SST reconstruction is such that no significant changes in interglacial climate can be identified. This does not, however, preclude a role for regional changes in seasonal SST in having limited reef development. However, the similar MAT-derived SST seasonality values associated with the Holocene, MIS 11 and MIS 37 reconstructions (chapter 4, §5.1) suggest that this is unlikely to have been the case. Although the data presented in this thesis cannot prove the point, it therefore seems reasonable to

assume that regional SST change did not provide a first-order limit to reef development on the glacial/interglacial time-scale. The MD06-3018 reconstruction of hydrological cycle variability does not show any significant shifts in either >100kyr time-scale or glacial/interglacial patterns of variability over the MPT interval (chapter 6, §5.2), suggesting that sea surface salinity was also unlikely to have exerted even a secondary control on reef expansion.

If it is accepted that regional climate change in the southern Coral Sea is unlikely to have led to middle Pleistocene reef expansion then, by process of elimination, it follows that the most plausible explanation was the onset of the higher amplitude middle/late Pleistocene ~100kyr glacial/interglacial cycles in sea-level [Alexander *et al.*, 2001; Yamamoto *et al.*, 2006]. A dominant control from sea-level fluctuations would be consistent with, or at least not preclude, a globally synchronous reef expansion centred on MIS 11 and hence the revised form of the coral reef hypothesis [Rickaby *et al.*, 2010]. Thus, whilst the coral reef hypothesis cannot plausibly explain the entirety of the middle/late Pleistocene pCO₂ change, neritic calcification changes may have been an important factor in restructuring of the glacial/interglacial carbon-cycle response over the MPT and into the 100kyr world.

7.5 Climate sensitivity to pCO₂ on orbital time-scales

The quantification of the relationship between changes in atmospheric pCO₂ and the Earth's surface temperature constitutes a key goal of modern climate science. However, the value of the 'climate sensitivity', defined as the equilibrium surface temperature change in response to a doubling of pCO₂, is a function of both the starting conditions and the time-scale over which the climatic change occurs. Model studies of both the LGM and a 2 x CO₂ world (relative to the pre-industrial) suggest that the amplitude of temperature change, at least as seen in low-latitude SST, is similar in both cases, suggesting that similar feedback processes are involved for pCO₂ levels in the range 150-300ppmV [Broccoli, 2000]. This, in turn, suggests that paleoclimate reconstructions, at least over the middle/late Pleistocene, during which pCO₂ is known to have remained within that same range (*Fig 7.3A*), can potentially provide an empirical alternative to a purely model based approach to the estimation of climate sensitivity.

Paleoclimatic methods tend, however, to overestimate the true equilibrium climate sensitivity, as a consequence of the known importance of climatic feedback processes which are external to the carbon-cycle itself. These relatively rapid and generally positive feedback mechanisms, such as the greenhouse gas effect of water vapour and the ice/water albedo effect, may not have a significant radiative forcing effect on the centennial time-scale, but will be inseparably linked with the direct effect of pCO₂ forcing in surface temperature change on millennial to orbital time-scales. Hence, paleoclimatic approaches to climate sensitivity must generally be viewed as upper-bound estimates to the true value. The use of low-latitude western Pacific SST reconstructions, which yield lower amplitude of glacial/interglacial temperature variability than their high-latitude counterparts, has been suggested to provide the 'best' such estimates [Lea, 2004]. However, even in this case, both the amplitude and linearity of the feedback contribution (and hence over-estimation of true sensitivity to pCO₂) remains effectively unknown [Toggweiler and Lea, 2010].

This thesis presents new data which suggests that there are good empirical reasons to suppose that the feedback/forcing relationship, at least as seen in low-latitude SST (whether this extrapolates to global average surface temperature is not considered here) remains linear on orbital time-scales. This evidence comes from the observed similarity in the patterns of glacial/interglacial amplitude in reconstructed MD06-3018 SST and Antarctic ice-core pCO₂ over the past 800ka (*Fig 7.4A/B*). To quantify this relationship, both of these records are normalized to unit standard deviation and zero mean, using equation 7.1 and plotted against each other in *Figure 7.4C*.

Equation 7.1
$$x' = (x - \bar{x}) / \sigma$$

(\bar{x} and σ are the mean and standard deviation respectively of the variable x over the duration of their respective records)

A linear trend-line fitted through a correlation plot of the glacial/interglacial amplitudes of the two normalized records over the past 800ka yields a slope of 0.9 (trend-line constrained to pass through origin) and a correlation coefficient value of $r^2 = 0.7$ (*Fig 7.4D*). A strong positive correlation therefore exists between the variables at glacial terminations and crucially the normalized SST and ice-core pCO₂ records both show an increase in amplitude between the glacial/interglacial cycles of the 100kyr world and those before MIS 12 (*Fig 7.4C*). This observation is robust to the combined uncertainty concept for the Mg/Ca paleothermometer (as defined in chapter 4, §5.3) as the value of this term is ~1°C for all interglacial MIS except MIS 13 over the past 800ka. The absence of ice-core pCO₂ records extending further back than 800ka means that the same methodology cannot be directly extrapolated into the 40kyr world. However, geochemical reconstructions of early Pleistocene pCO₂ variability [*Honisch et al., 2009*] (purple crosses on *Fig 7.4A*) are consistent with the ~40% increase in glacial/interglacial SST amplitude seen across the MPT in the MD06-3018 reconstruction (chapter 4, §4.1). Contrary to the suggestion of certain models [*Kohler and Bintanja, 2008*] there is, therefore, no clear empirical basis to suppose that either the linearity or magnitude of the climate sensitivity changed across the MPT.

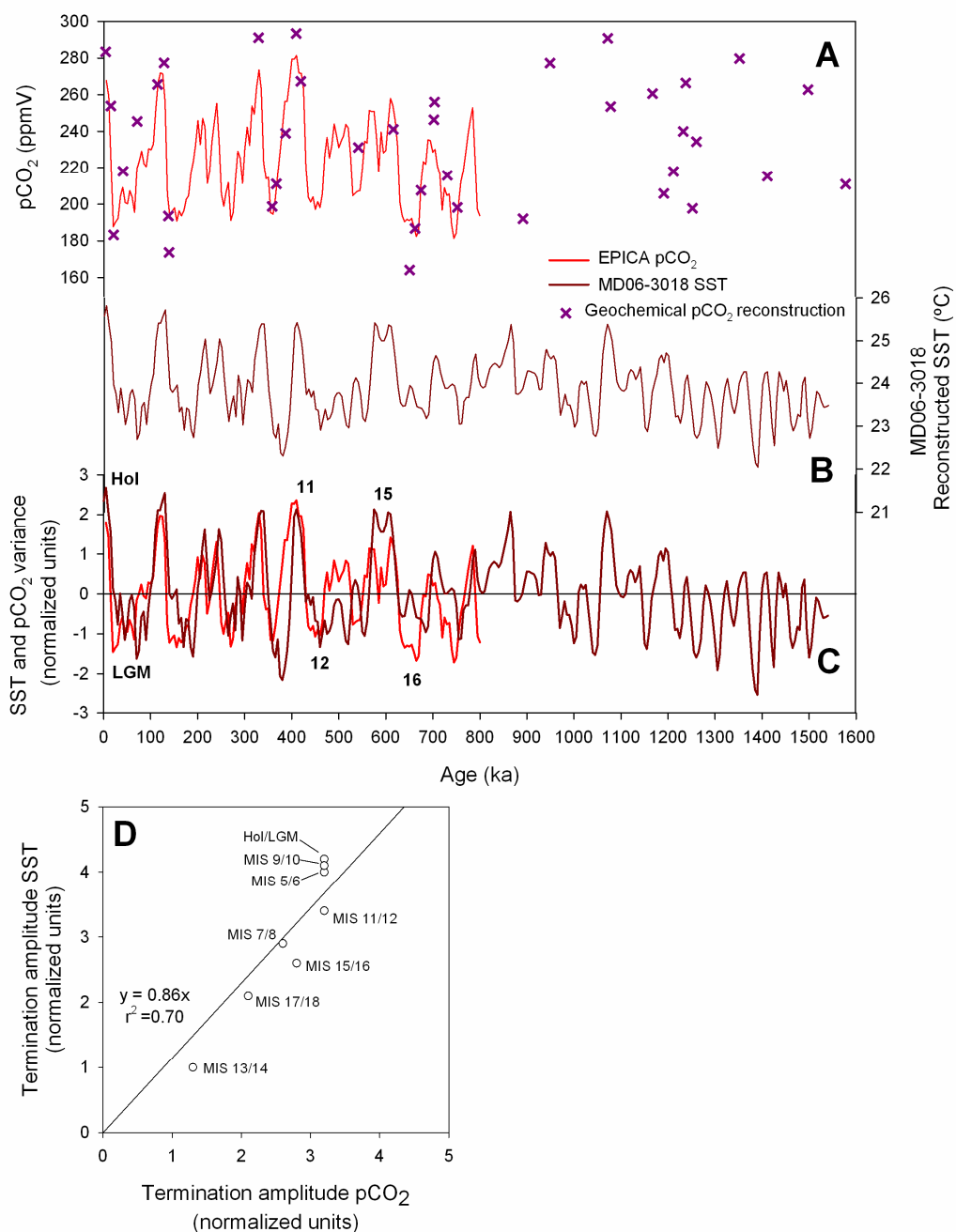


Figure 7.4 Plots of 5kyr smoothed (linear interpolation) **A)** EPICA composite pCO₂ [Luthi *et al.*, 2008] (solid red line) and geochemical reconstruction of pCO₂ based on boron isotopes from ODP 668B [Honisch *et al.*, 2009] (purple crosses) and **B)** MD06-3018 Mg/Ca-derived SST. **C)** Plots of the SST and ice-core pCO₂ records after normalization to unit standard deviation and zero mean (using equation 7.1), numbers show selected MIS. **D)** Correlation plot of normalized SST and ice-core pCO₂ glacial/interglacial termination amplitudes, defined as maximum interglacial – minimum glacial normalized variance across the transition. Data is given for the eight full terminations included in both data-sets. A linear regression trend-line (constrained to pass through the origin); its equation and correlation coefficient are also shown.

The apparent first-order linearity of the low-latitude SST to pCO₂ relationship on orbital time-scales, as seen in *Figure 7.4D*, suggests that the key feedback processes acting on these time-scales are both near-linear and temporally invariant. Using SST records from the western low-latitude Pacific, such as MD06-3018, to estimate the upper-bound climate sensitivity provides an average value of ~2°C/100ppmV (equivalent to 5.6°C/280ppmV), based on the glacial/interglacial cycles of the past 800ka. Comparison with anthropogenic time-scale climate sensitivity estimates arising from the 2 x CO₂ ocean/atmosphere global circulation models (2-6°C/280ppmV) shows that the paleoclimatic value is indeed at the upper end of, but not outside, the model estimates [*Jansen et al.*, 2007]. Thus, whilst the paleoclimate approach cannot necessarily help refine model estimates of climate sensitivity within the 2-6°C/280ppmV range, they do provide independent confirmation that this range is indeed appropriate and in particular that any higher values are unlikely to be reasonable.

7.6 The origins of the early Pleistocene intensification of northern hemisphere glaciation

Statistical analysis of $\delta^{18}\text{O}_{\text{benthic}}$ records has shown that the expansion of ice-volume associated with the intensification of NHG during the early Pleistocene occurred over a ~40kyr interval centred on ~920ka, significantly prior to the emergence of dominant ~100kyr periodicity at ~600ka (*Fig 1.3*) [*Mudelsee and Schulz, 1997; Clark et al., 2006*], a conclusion that is also supported by more recent attempts to de-convolve the global $\delta^{18}\text{O}_{\text{sw}}$ (ice-volume) component from the $\delta^{18}\text{O}_{\text{benthic}}$ records [*Sosdian and Rosenthal, 2009*]. This suggests, although does not necessarily imply, that the origin of the 100kyr glacial/interglacial mode of the middle/late Pleistocene was a consequence of the expanded ice-sheets themselves and this forms the basis of many of the proposed solutions to the ‘100kyr problem’, as discussed in chapter 1, §7.3. Therefore, analogously to the introductory chapter, it now makes sense to consider first what the MD06-3018 reconstructions can inform us about the >100kyr time-scale processes that might have caused the early Pleistocene expansion of northern hemisphere ice-volume, before reconsidering them in relation to the ‘100kyr problem’ in the following section.

The main hypotheses for processes that may have caused the intensification of NHG invoke either long-term cooling, driven by a >100kyr time-scale decline in $p\text{CO}_2$ [*Raymo, 1997; Paillard, 1998*], or changes in meridional ocean/atmosphere heat and/or moisture fluxes arising from the low-latitude ocean/atmosphere system [*McClymont and Rosell-Mele, 2005; Jia et al., 2008*]. The long-term cooling hypothesis is not supported by geochemical reconstructions of early Pleistocene $p\text{CO}_2$, which show no significant >100kyr time-scale trends [*Honisch et al., 2009*] (*Fig 7.4A*). In contrast, the relative timing of reconstructed early Pleistocene changes in low-latitude meridional SST gradients (~1200-1000ka, as discussed in chapter 5) and ice-volume expansion (940-900ka, [*Mudelsee and Schulz, 1997*]) suggests that the low-latitude SST gradient changes preceded the high-latitude ice-volume changes by periods similar to the assumed characteristic times of large ice-sheets themselves

(i.e. 10-100kyr) [Imbrie *et al.*, 1993]. Thus, the potential mechanisms underlying such a ‘low-latitude scenario’ deserve further investigation.

The magnitudes of reconstructed changes in the equatorial to subtropical and zonal equatorial Pacific SST gradients are relatively small over the Pleistocene (of the order of 0.1 - 1.0°C/Myr, *Fig 5.2E*), certainly when compared to those occurring at high-latitudes. However, even very small changes in the low-latitude ocean circulation regime and SST distribution can have extremely important implications for the overlying atmospheric circulation [Rind and Perlwitz, 2004; Otto-Bliesner and Clement, 2005; Brierley *et al.*, 2009], principally because the majority of deep atmospheric convection occurs over the warm waters of the low-latitude ocean, especially those of the Pacific warm pool. Given that the atmosphere is responsible for at least half of the meridional heat transport between the low- and high-latitudes in the modern climate system [Trenberth and Solomon, 1994], it is probable that SST induced changes in the atmospheric fluxes, rather than ocean circulation changes themselves, played the dominant role in communicating any low-latitude signal into the high-latitudes on the >100kyr time-scale [McClymont and Rosell-Mele, 2005; Brierley *et al.*, 2009; Brierley and Fedorov, 2010].

Modelling studies show that meridional SST changes are more important than zonal ones for both global cooling and the increase in moisture supply to the northern high-latitudes [Brierley and Fedorov, 2010]. In particular, model simulations based on an increasing meridional low-latitude SST gradient indicate simultaneous reductions (increases) in heat (moisture) transport to the northern high-latitudes [Brierley and Fedorov, 2010]. Chapter 5 has shown that warm pool contraction during the early Pleistocene was hemispherically asymmetric, consistent with such a pattern of SST evolution in the northern (but not southern) subtropical Pacific. Therefore, whilst the general sense of the McClymont *et al.* [2005] hypothesis may well be correct, namely that reorganisation of the low-latitude ocean/atmosphere circulation system dictated the timing of ice-volume expansion in the northern hemisphere, it is now proposed that meridional, rather than zonal, SST gradient

changes constituted the key influence on the overlying atmospheric circulation patterns.

The observed >100kyr time-scale changes in the low-latitude SST distribution are likely to have ultimately originated in the structure of the thermocline and the thermal characteristics of the water masses found at those depths, thus providing an ultimate connection back to the climate of the high-latitudes. It has been proposed that the progressive shoaling of the EEP thermocline has been a general feature of the late Neogene, with the onset of upwelling of cool waters and hence the establishment of a pseudo-modern low-latitude ocean/atmosphere circulation system at ~3000ka [*Philander and Fedorov, 2003*]. The ultimate onset of this process may have been related to the closing of the Panamanian isthmus, although the relative chronology of these events remains poorly resolved. It is now proposed that the continued >100kyr time-scale evolution of the equatorial upwelling system potentially led to a further contraction of the warm pool during the late Pliocene and early Pleistocene which, through the mechanisms discussed above, may have significantly influenced meridional heat and moisture fluxes to the northern high-latitudes prior to the MPT. The arguments in this thesis cannot refute the long-term cooling hypothesis for the origins of the early Pleistocene intensification of NHG, but they do provide further empirical support for the viability of the alternative 'low-latitude' hypothesis.

7.7 The '100kyr problem' revisited

The dominant ~100kyr periodicity seen in reconstructions of middle/late Pleistocene climate variability is unlikely to represent a direct response of the climate system to the orbital eccentricity cycle, as suggested in *Hays et al.* [1976], because insolation changes at that period are extremely small (at all latitudes), both in an absolute sense and in relation to the insolation changes occurring at the precession and obliquity periods [*Imbrie et al.*, 1993; *Elkibbi and Rial*, 2001; *Maslin and Ridgwell*, 2005]. This implies that the bulk of the insolation forcing at the ~100kyr period arises from processes internal to the Earth system, as suggested by *Imbrie et al.* [1993]. That study, in common with most other early approaches to the problem suggested that long characteristic times associated with 'large' ice-sheets was the principal origin of this forcing, although subsequent studies have now challenged this view [*Ruddiman*, 2003; *Shackleton*, 2000; *Liu et al.*, 2008; *Toggweiler*, 2008]. In particular, it has been proposed that the ~100kyr period may have originated principally in the carbon-cycle [*Shackleton*, 2000; *Toggweiler*, 2008] and hence that the MPT represented a fundamental shift in the mode of carbon-cycle, rather than ice-sheet dynamics, response to orbital forcing. Alternatively, reconstructions of low-latitude SST variability showing that the 100kyr mode may have appeared earlier there than in ice-volume, suggest that changes in the low-latitude ocean/atmosphere circulation system may have played a role in the evolving orbital sensitivity [*Liu et al.*, 2008]. This section considers what the subtropical view on the MPT derived in this thesis can contribute to the '100kyr problem' debate.

As was discussed in §2, the reconstructions of subtropical climate variability over the MPT presented here are not consistent with the low-latitude ocean/atmosphere circulation system having played a key role in the origin of the 100kyr mode. However, whereas the 'internal-modes' within the ocean/atmosphere circulation system are generally limited to sub-kyr periods by the relatively short characteristic times for the advective processes in those systems, the carbon cycle has the potential for 10-1000kyr internal-modes, as a consequence of the much longer characteristic times associated with aspects of the inorganic carbon-cycle, notably

rock weathering and carbonate sedimentation [Toggweiler, 2008; Russon *et al.*, 2010b; Toggweiler and Lea, 2010]. This means that the carbon-cycle response to orbital forcing can vary from orbital cycle to cycle, with the potential to amplify climatic signals at some periods and buffer others, as seems to be the case for the ~400kyr eccentricity cycle [Russon *et al.*, 2010b]. Within the ‘carbon-cycle view’ of the 100kyr problem, the ~100kyr mode may have originated either as a consequence of such internal amplification at the eccentricity period [Shackleton, 2000] or as a purely internal mode of the system [Toggweiler, 2008].

The present thesis supports the view of a strong coupling of southern high-latitude climate, the carbon-cycle and, through greenhouse gas forcing, low-latitude Pacific SST variability on orbital time-scales. However, this relationship appears to be strongly connected to the orbital obliquity cycle and is apparently maintained into the 100kyr world, as demonstrated by the in-phase early glacial stage cooling relationships seen in *Figure 6.5* and discussed in chapter 6, §5.1. Furthermore, the higher pCO₂ values associated with the last five interglacial MIS, relative to their counterparts during the MPT, may potentially be explicable by the revised form of the coral reef hypothesis, as discussed in §4. On the balance of the evidence considered here, therefore, the structure of the 100kyr mode in middle/late Pleistocene pCO₂ is more consistent with a modified form of the inferred early Pleistocene 40kyr mode than either an internal mode of the carbon-cycle or an enhanced response to the eccentricity cycle. Within this interpretation, the MPT probably did not represent a fundamental shift in the sensitivity of the carbon-cycle to orbital forcing.

In contrast, several lines of evidence support the ‘traditional’ view that the origin of the 100kyr mode lay in some aspect of northern hemisphere ice-sheet dynamics. Within the data presented here, the onset of statistically significant, rather than simply ‘above-background’, ~100kyr variability in the wavelet decomposition of both the LR04 $\delta^{18}\text{O}_{\text{benthic}}$ (*Fig 1.2B*) and MD06-3018 $\delta^{18}\text{O}_{\text{sw}}$ (*Fig 6.3C*) records occurred relatively early (900-700ka) compared to all of the low-latitude SST reconstructions, which show it at 650-500ka (*Fig 6.7*). Further, additional lines of

evidence, not based on the new data presented here, are provided by the increasing variety of relatively sophisticated models that can simulate an MPT using ice-sheet processes [Clark *et al.*, 2006; Bintanja and van de Wal, 2008], demonstrating an increasing well understood physical basis for this approach. More generally, but of great fundamental importance, statistical studies show that the deterministic component of 10-100kyr time-scale climate variability increased during both the onset of NHG and its intensification during the early Pleistocene [Meyers and Hinnov, 2010], suggesting that the deterministic nature of the climate response to orbital variations is coupled to ice-dynamics. Resolving whether the threshold in ice-sheet dynamics crossed during the MPT involved bedrock interactions [Clark and Pollard, 1998], the merger of previously distinct ice-sheets [Bintanja and van de Wal, 2008], sea-ice dynamics [Gildor and Tziperman, 2000] or simply the capacity of expanded ‘large’ ice-sheets to withstand weak summer insolation maxima [Imbrie *et al.*, 1993] is outside the scope of the present discussion.

Addressing the question of what defined the ‘period’ of the ~100kyr ‘cycles’ is extremely challenging given the existence of only five to seven (depending on where one draws the boundary of the 100kyr world) such oscillations, the significant differences in both duration and structure existing between each of these and the circular assumptions involved in conventional orbital tuning methods [Huybers and Wunsch, 2005]. It does appear, however, that the timing of glacial terminations in the 100kyr world was phase-locked in some way to bundles of either precession [Imbrie *et al.*, 1993; Raymo *et al.*, 1997] and/or obliquity [Huybers and Wunsch, 2005; Liu *et al.*, 2008] cycles. The present thesis cannot discriminate between these two views but does suggest that the low-latitude ocean/atmosphere circulation system became more sensitive to precession forcing in the 100kyr world, which may plausibly have played a role, through changes in low- to high-latitude heat and moisture export, in the pacing of ice-sheet growth and melting.

Regardless of the pacing issue, any conceptual model of climate in which the sensitivity of northern hemisphere ice-sheets to orbital forcing causes the 100kyr mode deglaciations to occur also implies that the timing of de-glacial changes in pCO₂ would have lagged those in global ice-volume. In such a view, the pCO₂ changes would have arisen as a consequence of relatively rapid ocean/atmosphere teleconnection processes communicating the northern high-latitude response into the Southern Ocean and then acted as a significant feedback on warming and ice-sheet melting [Imbrie *et al.*, 1993; Ruddiman, 2003]. The approach taken throughout the present thesis, of comparing the amplitudes, structures and spectral properties of various proxy signals representing different aspects of the climate system response, supports the general form of these models and hence, a lead of northern hemisphere climate and global ice-volume records over southern hemisphere climate and carbon-cycle records during 100kyr world glacial terminations [Alley *et al.*, 2002].

In contrast, the opposite conclusion, namely that pCO₂ and low-latitude SST leads global ice-volume at glacial terminations, has been arrived at in several studies based on directly studying the phase relations of the various proxies at glacial terminations [Lea *et al.*, 2000; Tachikawa *et al.*, 2009; Shackleton, 2000; Toggweiler and Lea, 2010]. Whilst it is not possible to say unequivocally which approach is more reliable, it is argued that the latter approach, as a consequence of focusing on 1kyr time-scale lead/lag relationships rather than 10-100kyr features, is likely to much more prone to errors arising from age-model uncertainties. The observation that both ice-core pCO₂ and low-latitude Pacific SST lead $\delta^{18}\text{O}_{\text{benthic}}$ by several kyr at middle/late Pleistocene glacial terminations, whilst replicated in many studies (including the MD06-3018 data itself, as may be seen in *Figure 6.5A*, although in general the present reconstructions are not at sufficiently high resolution), may be a consequence of not only these age-model uncertainties but also of proxy rectification effects [Ashkenazy and Tziperman, 2006]. In neither case would the observation necessarily imply a 'true' climatic lead of pCO₂ over ice-volume. Furthermore, the apparent de-glacial lead of pCO₂ over global ice-volume is also removed when the rate of change of ice-volume with time, rather than ice-volume itself, is considered [Roe, 2006].

The data and analysis presented in this thesis certainly cannot unequivocally resolve these questions. However, the opinion of the author is that the general view of the Milankovitch paradigm as outlined in *Imbrie et al.* [1992,1993], in which the 100kyr mode arises through the non-linear response of northern hemisphere ice-sheets to orbital forcing and the carbon-cycle acts as a radiative forcing feedback, remains viable and not in need of fundamental revision, although some slight reformulations may be required regarding the parameterization of both the orbital forced changes in insolation [*Huybers, 2006*] and ice-volume terms [*Roe, 2006*]. More significant questions do remain regarding both the pacing of the 100kyr ‘cycles’ and what the 100kyr mode may represent in terms of the Myr time-scale evolution of the climate system [*Crowley and Hyde, 2008; Meyers and Hinnov, 2010*].

7.8 Inter-hemispheric asymmetry in the glacial/interglacial climate response across the Mid-Pleistocene Transition

Although the model for the middle/late Pleistocene 100kyr mode of climate variability, as discussed in the previous section, does not support the existence of a ‘true’ climatic lead of the carbon-cycle over northern hemisphere ice-volume during glacial terminations, it is consistent with the presence of significant inter-hemispheric asymmetry in the 10-100kyr time-scale climate response [*Shackleton, 2000; Tachikawa et al., 2009*]. The MD06-3018 SST reconstruction clearly shows the same characteristic ‘southern hemisphere’ features that are seen in previous reconstructions from across both the low-latitudes and the wider southern hemisphere [*Martinez-Garcia et al., 2009; Tachikawa et al., 2009; Toggweiler and Lea, 2010*], namely early glacial cooling and the attainment of glacial maxima conditions. These same features are also shared, to some extent, with Antarctic ice-core pCO₂ records but differ from the more saw-toothed signal seen in both stacked $\delta^{18}\text{O}_{\text{benthic}}$ records and proxy reconstructions of northern high-latitude climate (*Fig 6.5* and see chapter 6, §5.1 for discussion). Such inter-hemispheric asymmetry has been previously documented on millennial time-scales during both glacial stages

[Blunier and Brook, 2001] and glacial terminations [Toggweiler and Lea, 2010]. On the orbital time-scales now considered here, it is proposed to have arisen within the 100kyr world because the southern hemisphere and low-latitude climate response is closely coupled, through greenhouse gas forcing, to that of the carbon-cycle and hence the effect of the orbital obliquity cycle, whereas the northern hemisphere response is dominated by the 100kyr mode in ice-sheet dynamics.

Resolving whether this asymmetry has been a feature only of the 100kyr world or whether it has persisted across the MPT is rendered difficult by the absence of ice-core $p\text{CO}_2$ records extending beyond $\sim 800\text{ka}$. However, the arguments presented in §5 suggest that low-latitude SST reconstructions, such as that for MD06-3018, provide an acceptable, albeit indirect, guide to carbon-cycle variability across the transition. Thus, if $\delta^{18}\text{O}_{\text{benthic}}$ is assumed to proxy variability in global ice-volume and reconstructions of low-latitude SST, that in $p\text{CO}_2$ during the 40kyr world, then both the ice-sheet (occurring mainly, but not necessarily exclusively, in the northern hemisphere [Raymo *et al.*, 2006]) and the carbon-cycle (driven mainly by southern hemisphere processes) responses are seen to have been at the 40kyr period and to have been in-phase with the orbital obliquity cycle. As insolation changes arising from the obliquity cycle are in-phase between the two hemispheres, it is proposed that the response of the carbon-cycle in the 40kyr world may have arisen, at least in part, directly from obliquity forcing of southern high-latitude insolation rather than indirectly through teleconnections arising from northern high-latitude ice-sheet dynamics [Imbrie *et al.*, 1992]. In any case, the arguments presented here lead to the testable hypothesis that inter-hemispheric climate variability on the orbital time-scale has only been a feature of the 100kyr world and was not present in the 40kyr world.

In summary, the MPT clearly represented a protracted and complex period of non-linearity in the response of the global climate system to orbital forcing. Current data constraints are not adequate to fully characterize the changes occurring in all aspects of the climate system over the transition, but it is argued here that the two key features of the transition, namely the expansion of global ice-volume and the

emergence of the ~100kyr glacial/interglacial mode, are both best explained as a result of northern high-latitude processes. The early Pleistocene intensification of NHG may, however, have been a consequence of >100kyr time-scale changes in the low-latitude ocean/atmosphere circulation regime. In any case, this expansion of northern hemisphere ice-sheets probably then led ultimately to the emergence of the more non-linear ~100kyr mode. During the middle/late Pleistocene the global climate response has represented a complex blend of the continued obliquity dominated influence from the southern high-latitude carbon-cycle response and the powerful new ~100kyr northern high-latitude ice-sheet response. The low-latitude ocean/atmosphere circulation system also acted to amplify the effects of the precession cycle over this interval. Thus, whilst ~100kyr periodicities are present as a dominant spectral feature of climate records from all latitudes and both hemispheres, the second-order features of the 10-100kyr climatic response is seen to vary significantly as a function of both.

7.9 Research questions arising from this thesis

As a consequence of the relatively scarcity of previous ocean drilling campaigns in the subtropical southern Pacific, the down-core reconstructions presented in this thesis are, in many cases, the first that span the MPT at comparable resolution from a relatively large area of the global ocean. It is, therefore, entirely unsurprising that the analysis of the MD06-3018 records has led to at least as many, if not more, future research directions than those addressed in the initial aims of the thesis. A summary of the key opportunities arising from the work is given below:

- The MD06-3018 SST reconstruction has clearly demonstrated important spatial variability in the pattern of Pacific warm pool contraction on the >100kyr time-scale. More SST reconstructions from areas peripheral or outside the modern warm pool, in both hemispheres, are needed in order to better describe this pattern and constrain its impact on the wider ocean/atmosphere system. Furthermore, a core from ~10°S in the western Pacific would also allow more detailed evaluation of any orbital time-scale fluctuations in the southern extent of the warm pool.
- More modelling studies are required to evaluate whether the documented >100kyr low-latitude ocean/atmosphere circulation changes could indeed, as is suggested here, have plausibly limited the intensification of NHG and if so, by what specific mechanism (i.e. heat or moisture transport) this might have been occurred. As concluded in chapter 5, such modelling studies must carefully consider the choice of SST boundary conditions and in all likelihood, experiment with a range of distributions bounded by the existing paleo-data constraints.

- Given the likely importance of the >100kyr mean-state of the low-latitude Pacific ocean/atmosphere system in global climate over the Pliocene-Pleistocene boundary, other subtropical reconstructions, of longer temporal duration than MD06-3018 are also required. A picture of the late Pliocene warm pool region is now emerging [*Medina-Elizalde and Lea, 2010*], but this needs to be complimented with subtropical reconstructions at similar resolutions from both hemispheres in order to constrain meridional heat and moisture fluxes over the onset of NHG.
- The major limitation inherent in the deep water aspect of this work is the absence of any proxy for flow speed in either the NCT itself or the Tasman Sea, which means that only upper and lower limits could be placed on the influence of different water masses. The acquisition of sortable silt, or maybe ϵ_{Nd} , data would allow for some evaluation of the potential role played by flow changes on the $\delta^{13}C_{benthic}$ proxy system.
- The deep water circulation component of this study has also led to the directly testable hypothesis that the influence of the relict northern source deep water signal that is apparently present in the NCT should also be present, indeed even more strongly, in the northern Tasman Sea. The acquisition of a Pleistocene record from 2000-3000m water depth in this location would allow the evaluation of this idea and further constrain the vertical and spatial distribution of water masses in the region.
- The Mg/Ca proxy system, especially the influence of salinity on the incorporation of Mg into foraminiferal calcite, is still not yet well enough understood. This situation, whilst improving rapidly, requires both more controlled condition culture studies and, crucially from a paleoceanographic perspective, more single-core multi-proxy SST reconstructions, such as *Dekens et al. [2008]*, to allow better evaluation of the relative performances of the proxy systems. In the specific case of MD06-3018, the acquisition of radiocarbon dates for the core-top (which is currently in progress) will at least

allow for evaluation of whether the calibration offset described in chapter 4, §3.1 is a consequence of core-top age.

- If the role played by coral reef systems in the global carbon-cycle on glacial/interglacial time-scales is to be better understood, more studies using techniques that offer sub-orbital resolution to date the onset and expansion of reef development during the middle Pleistocene are required. Furthermore, the MD06-3018 SST reconstruction suggests that future millennial time-scale reconstructions of seasonal SST variability in the Coral Sea SST, especially if focused on the MIS 15 – MIS 11 interval, have the potential to significantly refine understanding of the exact relationship between the timing of reef expansion and regional climatic change.

7.10 Future directions in Pleistocene paleoceanography

A single, consistent and complete explanation for orbital time-scale climate variability across the Plio-Pleistocene remains elusive at the time of writing this thesis. Advances over the past decade in both proxy reconstructions and system modelling on these time-scales have, however, led to significant progress and coalescence of opinion, on some aspects of the problem at least. It is likely that over the coming decade further progress will be made, with the clearest opportunities increasingly focused around the interaction of the proxy data and modelling fields. Given that no simple general orbital theory of climate is able to address all of the key problems within the Milankovitch paradigm and in particular those of the ~100kyr cycles and the MPT, it follows that understanding of at least some aspects of the ‘real’ system dynamics is required. However, it is also indubitably the case that paleoceanography remains a ‘data-poor’ science and that limitations imposed by both the availability of proxies for key environmental variables and the coverage of those that are already established seriously limits both model development and evaluation at present.

Bearing this in mind, three particular exciting directions seem to be open to the general field at the present time. Firstly, and closely aligned to the fundamental contribution of this thesis itself, is the expansion of the spatial coverage of down-core proxy records of key climatic variables, such as SST, so as to allow better dynamical understanding of spatial processes such as ocean circulation in the past. This is crucially important because the role of meridional heat and moisture fluxes within the ocean/atmosphere system on orbital and >100kyr time-scales remains poorly understood. These fluxes may, as has been discussed at some length in this thesis, potentially have constituted an extremely important component of the global climate system response, especially on the >100kyr time-scale. This is true not only for the early Pleistocene intensification of NHG but also for the transition from the Pliocene into the Pleistocene and the onset of that glaciation and for understanding the warm climates of the early Cenozoic, which may provide the most appropriate analogue for an anthropogenic future. Progress in this area is dependent on both the

increasing availability of global ocean/atmosphere circulation and intermediate complexity models, which can adequately resolve the relevant ocean/atmosphere dynamics and upon the acquisition of spatially targeted, down-core proxy records of variables such as SST to both constrain model boundary conditions and evaluate model performance.

Secondly, the emergence of geochemical proxies for quantifying aspects of the inorganic carbon cycle within the oceans, such as foraminiferal calcite boron isotopes and B/Ca ratios, provide the potential to quantitatively reconstruct atmospheric $p\text{CO}_2$ and ocean carbon chemistry on orbital time-scales over the entire Plio-Pleistocene. Such work will allow rapid development of understanding of how the climate to carbon-cycle relationship evolved across the MPT and thus of the carbon-cycle response to orbital forcing in general. As such, these methods provide clear opportunities to test and develop many of the ideas presented in this thesis.

Thirdly, the relationship between orbital forcing, carbon-cycle variability and the climate system response is clearly not the same for all orbital periods and there is evidence for significant decoupling, at least at the ~400kyr eccentricity cycle period [Wang *et al.*, 2004; Russon *et al.*, 2010b]. Establishing which processes, whether geological or biogeochemical, act on these 'long' orbital time-scales to effect this decoupling may provide essential insights on the orbital response at other periods. In this case, only simple carbon-cycle models are likely to be appropriate, but considerable work remains on improving and testing such models and as for the previous case, the absence of spatially distributed proxy records of carbon-cycle and climate variability hamper this.

In little over half a century, paleoceanography has expanded scientific understanding of the past state of the Earth's ocean/atmosphere systems from being virtually non-existent to a state where much is understood about both the natural modes of variability and the system dynamics on time-scales ranging from the inter-annual to Myrs. Whilst very significant gaps remain in this understanding, as has been outlined above, and research will certainly continue with an aim to better

developing this core understanding, it is also likely that the bulk of paleoceanographic effort for the coming decades will become focused more on the concept of ‘climate-services’ - research targeted to improving understanding of the likely system response to the current anthropogenic carbon-cycle perturbation. In the context of the definition of the 100kyr world used in this thesis, the Holocene represents the latest of five interglacial periods and within the Pleistocene as a whole, it represents but one amongst many. However, the coming millennia will likely *not* constitute the start of another long cooling into a future glacial maximum, as a consequence of the anthropogenic carbon-cycle perturbation. Thus, whilst developing the orbital theory of climate remains of underlying importance to the field, the greatest requirements are now the acquisition of the data required to constrain and quantify ocean circulation and carbon-cycle variability on the ‘background’ time-scales to the anthropogenic excursion. In doing this, paleoceanography will have contributed greatly to collective understanding of both the past and future behaviour of the complex system upon which we all depend.

8.2 Marine sediment core MD06-3018 as an archive for subtropical southwest Pacific paleoceanography

- The sedimentary mode at the core-site of giant piston core MD06-3018 (2470m water depth and 23°S in the NCT) whilst not purely pelagic, is always dominated by the pelagic component. Carbonate preservation within the core is excellent and does not vary as a function of core depth, meaning that the geochemical signatures housed within the core have the potential to provide reliable paleoceanographic proxies.

8.3 Deep water circulation in the subtropical southwest Pacific on orbital and >100kyr time-scales

- Glacial stage deep water $\delta^{13}\text{C}$ values in the NCT over the past 1100ka, reconstructed through MD06-3018 *C. wuellerstorfi* $\delta^{13}\text{C}_{\text{benthic}}$ measurements, cannot be explained entirely from a purely open Pacific deep water source. Instead, a significantly enhanced relative influence from glacial Tasman Sea deep waters, compared to those from the open Pacific, is required in comparison to the interglacial stage regime. This implies a relatively enhanced glacial stage influence of isotopically-depleted mid-depth deep waters of Southern Ocean origin in the Pacific DWBC, as compared to the Tasman Sea. The glacial stage Southern Ocean is hence shown to contain significant spatial chemical gradients at depths (~2500m) well above the sea floor topography.
- On the >100kyr time-scale, the influence of the chemically younger Tasman Sea deep waters on the subtropical southwest Pacific mixing regime is seen to be a persistent feature of at least the past 1100ka. The spatial $\delta^{13}\text{C}$ gradient between the mid-depth deep waters of the Tasman Sea and the Pacific DWBC was, however, generally reduced during the MPT interval, consistent with this having been a period of reduced deep water ventilation in both hemispheres.

8.4 The paleoceanography of the southern Coral Sea on orbital and >100kyr time-scales

- The MD06-3018 *G. ruber* Mg/Ca-derived reconstruction of SST in the southern Coral Sea reveals a very stable long-term paleoclimatic history over the past 1500ka, with variability of <0.5°C on the >100kyr time-scale.
- Glacial/interglacial variability in the subtropical SST reconstruction lies in the amplitude range 2-3°C and shows a clear MPT from dominant 40kyr to 100kyr modes, with the latter periodicity becoming more significant at ~500ka.
- Reconstructed subtropical SST variability is seen to have remained coherent and in-phase with the orbital obliquity cycle across the past 1600ka and this sensitivity must have arisen from the high-latitude, rather than the local insulative effects of the orbital variations. Within the 100kyr world, the SST reconstruction shows the same, obliquity paced, early glacial stage cooling pattern seen in records of southern high-latitude climate. This suggests that the southern, rather than northern high-latitudes were the source of the obliquity signal seen in low-latitude SST.
- Reconstructed regional hydrological cycle variability (based on the extraction of the local component of calculated $\delta^{18}\text{O}_{\text{sw}}$ variability, derived in turn from coupled *G. ruber* $\delta^{18}\text{O}$ -Mg/Ca measurements) does not show significant spectral power at the ~100kyr period over the past 1600ka, but patchy intervals of significant spectral power are present in the 20-40kyr band across the record. This variability shows patchy coherence with the precession cycle over the duration of the record but only limited coherence with the obliquity cycle and no significant relationship with the latter after ~1000ka

8.5 Limitations of the Mg/Ca paleothermometer in reconstructing southern Coral Sea paleoceanography: implications for the causes of middle Pleistocene reef expansion

- The sample reproducibility error for the Mg/Ca paleothermometer does not always provide a realistic estimate of the true proxy uncertainty. A method for better estimating the ‘combined uncertainty’ associated with the reconstructed southern Coral Sea SST values has been developed, based on proposed corrections for the effects of past variations in both salinity and Mg/Ca_(sw). The value of the combined uncertainty is seen to be up to twice as large during glacial, as opposed to interglacial, stages.
- Comparison of the MD06-3018 *G. ruber* Mg/Ca-derived SST values with planktic foraminiferal transfer function derived estimates of past seasonal SST variability suggests that no significant bias away from mean-annual SST is present in the down-core Mg/Ca reconstruction.
- Although reconstructed glacial/interglacial amplitudes of southern Coral Sea mean-annual SST variability increased by ~1°C (~40%) over the MPT, the combined proxy uncertainty is such that no statistically significant change in these values is detectable on the >100kyr time-scale, or even between individual interglacial MIS. This suggests that regional climatic change probably did not constitute a significant cause of middle Pleistocene reef expansion. The paleothermometry proxy limitations, especially as regards past changes in seasonality, are, however, such that this question cannot be unequivocally addressed at present.

8.6 Subtropical Pacific constraints on >100kyr time-scale variability in the low-latitude ocean/atmosphere circulation system: implications for the origins of the Mid-Pleistocene Transition

- The reconstructed SST gradient across the southern boundary of the Pacific warm pool is shown to have remained stable, on the >100kyr time-scale, over at least the past 1500ka. It follows that no significant meridional fluctuations in the southern extent of the warm pool have occurred over this interval, in contrast to both the northern and eastern warm pool boundaries, both of which underwent contraction during the early Pleistocene. The early Pleistocene warm pool is therefore shown to have been more meridionally asymmetric than its modern configuration, which was established by ~1000ka.
- If it is assumed that the position of maximal atmospheric convergence in the western Pacific followed the centre of the warm pool, then this would have migrated southward over the interval 1200-1000ka (with an uncertainty not exceeding ± 100 kyr on both the start and end age values), consistent with a strengthening of the northern branch of the atmospheric Hadley circulation at that time.
- The relative timings of the early Pleistocene intensification of NHG and changes in the >100kyr time-scale state of the low-latitude ocean/atmosphere circulation system, as seen in the reconstructed SST patterns, are consistent with the latter having potentially been the origin of the former, through changes in the meridional atmospheric fluxes of heat and moisture to the northern high-latitudes.

8.7 Subtropical Pacific constraints on orbital time-scale variability in the low-latitude ocean/atmosphere circulation system and the carbon-cycle: implications for the structure of the Mid-Pleistocene Transition

- The spatial pattern of reconstructed glacial/interglacial SST variability in the low-latitude western Pacific is consistent with pCO₂ forcing having dominated the SST response across the MPT. The carbon-cycle was the main communicator of the southern high-latitude obliquity signal seen in the subtropical SST reconstruction. Furthermore, the relationship between the amplitudes of glacial/interglacial variability seen in subtropical Pacific SST and ice-core pCO₂ is close to being linear, implying that paleoclimate records can provide useful upper-bound estimates of the equilibrium climate sensitivity to pCO₂ forcing.
- Comparison of orbital time-scale variability in western Pacific SST reconstructions with those from the EEP demonstrates that the importance of upper-ocean ventilation changes as an alternative mechanism for the communication of the high-latitude obliquity signal into low-latitude Pacific SST declined over the MPT, at the same time as the amplitude of glacial/interglacial pCO₂ forcing increased.
- The response of the low-latitude ocean/atmosphere circulation system on orbital time-scales is complex. No coherent fluctuations of significant amplitude in either the southern extent of warm pool influence or the subtropical southwest Pacific hydrological cycle are detectable at the ~100kyr period. At the obliquity cycle period, 'super-ENSO' fluctuations significantly affected the climate of the EEP and may also be weakly detectable in the subtropical southwest Pacific hydrological cycle. The relative importance of this mechanism apparently declined over the MPT (1000-700ka), such that by the end of the transition glacial/interglacial SST amplitudes did not significantly differ zonally across the low-latitude Pacific.

- The constraints presented here on the plausible global climate impacts of orbital time-scale variability in the low-latitude ocean/atmosphere circulation system mean that the emergence of the ~100kyr mode during the MPT cannot realistically have originated principally in that system.
- Although the carbon-cycle constraints presented here are more indirect than those for the low-latitude ocean/atmosphere circulation system, they similarly suggest that the MPT did not represent a fundamental shift in the mode of carbon-cycle response to orbital forcing. This is based principally on the persistence of a strong southern high-latitude obliquity signal, communicated by greenhouse gas forcing, in subtropical SST variability across the MPT. Within this interpretation, the higher amplitude pCO₂ cycles seen over the past ~500ka are potentially a consequence of enhanced de-glacial neritic calcification arising from global changes in glacial/interglacial sea-level variability during the MPT.
- Whilst not allowing direct evaluation of the competing hypotheses, the subtropical data presented in this thesis favour a version of the traditional ‘northern hemisphere ice-sheet dynamics’ hypothesis as the most likely solution to the ‘100kyr problem’. Within such a model, the early Pleistocene intensification of NHG, which may have been driven by long-term changes in the low-latitude ocean/atmosphere circulation system, led ultimately to the emergence of the higher amplitude and more non-linear 100kyr glacial/interglacial mode. The inter-hemispheric asymmetry in the 10-100kyr climate response present within the 100kyr world is seen as a consequence of the interaction of this northern high-latitude mode with the southern high-latitude carbon-cycle response to obliquity forcing, which was maintained across the MPT. Such an inter-hemispheric asymmetry is predicted to have not been present during the 40kyr world.

Blank Page

Very deep, very deep is the well of the past.

Should we not call it bottomless?

Thomas Mann

Blank Page

References

- Achituv, Y., and Z. Dubinsky (1990), Evolution and zoogeography of coral reefs in *Ecosystems of the World 25: Coral Reefs*, edited by Z. Dubinsky, Elsevier, Amsterdam.
- Alexander, I., Andres, M.S., Braithwaite, C.J.R., Braga, J.C., Cooper, M.J., Davies, P.J., Elderfield, H., Gilmour, M.A., Kay, R.L.F., Kroon, D., McKenzie, J.A., Montaggioni, L.F., Skinner, A., Thompson, R., Vasconcelos, C., Webster, J., and Wilson, P.A. (2001), New constraints on the origin of the Australian Great Barrier Reef: Results from an international project of deep coring, *Geology*, 29(6), 483-486.
- Alley, R. B., E. J. Brook, and S. Anandkrishnan (2002), A northern lead in the orbital band: north-south phasing of ice-age events, *Quaternary Science Reviews.*, 21(1-3), 431-441
- Alory, G., A. Vega, A. Ganachaud, and M. Despinoy (2006), Influence of upwelling, subsurface stratification, and heat fluxes on coastal sea surface temperature off southwestern New Caledonia, *Journal of Geophysical Research*, 111(C7), C07023.
- Anand, P., H. Elderfield, and M. H. Conte (2003), Calibration of Mg/Ca thermometry in planktonic foraminifera from a sediment trap time series, *Paleoceanography*, 18(2), 1050.
- Archer, D., A. Winguth, D. Lea, and N. Mahowald (2000), What caused the glacial/interglacial atmospheric pCO₂ cycles?, *Reviews of Geophysics*, 38(2), 159-189.
- Ashkenazy, Y., and E. Tziperman (2004), Are the 41 kyr glacial oscillations a linear response to Milankovitch forcing?, *Quaternary Science Reviews.*, 23, 1879-1890.
- Barker, S., M. Greaves, and H. Elderfield (2003), A study of cleaning procedures used for foraminiferal Mg/Ca paleothermometry, *Geochemistry Geophysics Geosystems*, 4(9), 8407.
- Barreiro, M., G. Philander, R. Pacanowski, and A. Fedorov (2006), Simulations of warm tropical conditions with application to middle Pliocene atmospheres, *Climate Dynamics*, 26(4), 349-365.
- Bartoli, G., M. Sarnthein, M. Weinelt, H. Erlenkeuser, D. Garbe-Schonberg, and D. W. Lea (2005), Final closure of Panama and the onset of northern hemisphere glaciation, *Earth Planet. Sci. Lett.*, 237(1-2), 33-44.

- Beaufort, L., T. de Garidel-Thoron, A. C. Mix, and N. G. Pisias (2001), ENSO-like forcing on oceanic primary production during the Late Pleistocene, *Science*, 293(5539), 2440-2444.
- Barrows, T. T., and S. Juggins (2005), Sea-surface temperatures around the Australian margin and Indian Ocean during the Last Glacial Maximum, *Quaternary Science Reviews*., 24, 1017-1047.
- Bemis, B. E., H. J. Spero, J. Bijma, and D. W. Lea (1998), Re-evaluation of the oxygen isotopic composition of planktonic foraminifera: Experimental results and revised paleotemperature equations, *Paleoceanography*, 13(2), 150-160.
- Berger, W., and E. Jansen (1994), Mid-Pleistocene climate shift - the Nansen connection, in *The Polar Oceans and Their Role in Shaping the Global Environment*, edited by O. M. Johannessen, *et al.*, pp. 295-313, AGU.
- Berger, W. H., T. Bickert, M. K. Yasuda, and G. Wefer (1996), Reconstruction of atmospheric CO₂ from ice-core data and the deep-sea record of Ontong Java plateau: The Milankovitch chron, *Geologische Rundschau*, 85(3), 466-495.
- Berner, R. A., A. C. Lasaga, and R. M. Garrels (1983), The carbonate-silicate geochemical cycle and its effect on atmospheric carbon-dioxide over the past 100 million years, *American Journal of Science*, 283(7), 641-683.
- Bickert, T., W. H. Berger, S. Burke, H. Schmidt, and G. Wefer (1993), Late Quaternary stable isotope record of benthic foraminifera: Sites 805 and 806, Ontong Java Plateau *Proceedings of the Ocean Drilling Program, Scientific Results*, 130, 411-420.
- Bijma, J., W. W. Faber, and C. Hemleben (1990), Temperature and salinity limits for growth and survival of some planktonic foraminifera in laboratory cultures, *Journal of Foraminiferal Research*, 20(2), 95-116.
- Bintanja, R., and R. S. W. van de Wal (2008), North American ice-sheet dynamics and the onset of 100,000-year glacial cycles, *Nature*, 454(7206), 869-872.
- Bostock, H. C., B. N. Opdyke, M. K. Gagan, and L. K. Fifield (2004), Carbon isotope evidence for changes in Antarctic Intermediate Water circulation and ocean ventilation in the southwest Pacific during the last deglaciation, *Paleoceanography*, 19(4), PA4013.
- Bostock, H. C., B. N. Opdyke, M. K. Gagan, A. E. Kiss, and L. K. Fifield (2006), Glacial/Interglacial changes in the East Australian Current, *Climate Dynamics*, 26, 645-659.

- Braithwaite, C. J., H. Dalmaso, M. A. Gilmour, D. D. Harkness, G. M. Henderson, R. L. F. Kay, D. Kroon, L. F. Montaggioni, and P. A. Wilson (2004), The Great Barrier Reef: The chronological record from a new borehole, *Journal of Sedimentary Research*, 74(2), 298-310.
- Brierley, C. M., and A. V. Fedorov (2010), The relative importance of meridional and zonal SST gradients for the onset of the ice ages and Pliocene-Pleistocene climate evolution., *Paleoceanography*, 25, PA2214.
- Brierley, C. M., A. V. Fedorov, Z. H. Liu, T. D. Herbert, K. T. Lawrence, and J. P. LaRiviere (2009), Greatly Expanded Tropical Warm Pool and Weakened Hadley Circulation in the Early Pliocene, *Science*, 323(5922), 1714-1718.
- Broccoli, A. J. (2000), Tropical cooling at the last glacial maximum: An atmosphere-mixed layer ocean model simulation, *Journal of Climate*, 13(5), 951-976.
- Broccoli, A. J., K. A. Dahl, and R. J. Stouffer (2006), Response of the ITCZ to Northern Hemisphere cooling, *Geophysical Research Letters*, 33, L01702.
- Cabioch, G., L. Montaggioni, N. Thouveny, N. Frank, T. Sato, V. Chazottes, H. Dalmaso, C. Payri, M. Pichon, and A. M. Semah (2008), The chronology and structure of the western New Caledonian barrier reef tracts, *Palaeogeography Palaeoclimatology Palaeoecology*., 268(1-2), 91-105.
- Cande, S. C., and D. V. Kent (1995), Revised calibration of the geomagnetic Polarity timescale for the late Cretaceous and Cenozoic, *Journal of Geophysical Research-Solid Earth*, 100(B4), 6093-6095.
- Cavalier-Smith, T. (2003), Protist phylogeny and the high-level classification of Protozoa, *European Journal of Protistology*, 39(4), 338-348.
- Charles, C. D., and R. G. Fairbanks (1992), Evidence from Southern-Ocean sediments for the effect of North-Atlantic Deep-Water flux on climate, *Nature*, 355(6359), 416-419.
- Chave, K. E. (1954), Aspects of the Biogeochemistry of Magnesium .1. Calcareous Marine Organisms, *Journal of Geology*, 62(3), 266-283.
- Clark, P. U., D. Archer, D. Pollard, J. D. Blum, J. A. Rial, V. Brovkin, A. C. Mix, N. G. Pisias, and M. Roy (2006), The middle Pleistocene transition: characteristics. mechanisms and implications for long-term changes in atmospheric pCO₂, *Quaternary Science Reviews*., 25(23-24), 3150-3184.
- Clark, P. U., and D. Pollard (1998), Origin of the middle Pleistocene transition by ice sheet erosion of regolith, *Paleoceanography*, 13(1), 1-9.

- Clement, A. C., R. Seager, and M. A. Cane (1999), Orbital controls on the El Niño/Southern Oscillation and the tropical climate, *Paleoceanography*, 14(4), 441-456.
- Correge, T., and P. De Deckker (1997), Faunal and geochemical evidence for changes in intermediate water temperature and salinity in the western Coral Sea (northeast Australia) during the Late Quaternary, *Palaeogeography Palaeoclimatology Palaeoecology*, 131(3-4), 183-205.
- Crowley, T. J. (1995), Ice-age terrestrial carbon changes revisited, *Global Biogeochemical Cycles*, 9(3), 377-389.
- Crowley, T. J., and W. T. Hyde (2008), Transient nature of late Pleistocene climate variability, *Nature*, 456(7219), 226-230.
- Crundwell, M., G. Scott, T. Naish, and L. Carter (2008), Glacial-interglacial ocean climate variability from planktonic foraminifera during the Mid-Pleistocene transition in the temperate Southwest Pacific, ODP Site 1123, *Palaeogeography Palaeoclimatology Palaeoecology*, 260(1-2), 202-229.
- Curry, W. B., J.-C. Duplessy, L. Labeyrie, and N. J. Shackleton (1988), Changes in the distribution of $\delta^{13}\text{C}$ of deep water ΣCO_2 between the last glaciation and the Holocene, *Paleoceanography*, 3, 317-341.
- Curry, W. B., and G. P. Lohmann (1982), Carbon isotopic changes in benthic foraminifera from the western South-Atlantic - reconstruction of glacial abyssal circulation patterns, *Quaternary Research*, 18(2), 218-235.
- de Garidel-Thoron, T., Y. Rosenthal, F. Bassinot, and L. Beaufort (2005), Stable sea surface temperatures in the western Pacific warm pool over the past 1.75 million years, *Nature*, 433, 294-298.
- de Villiers, S., M. Greaves, and H. Elderfield (2002), An intensity ratio calibration method for the accurate determination of Mg/Ca and Sr/Ca of marine carbonates by ICP-AES, *Geochemistry Geophysics Geosystems*, 3(1), 1001.
- De Deckker, P. (1997), The significance of the oceans in the Australasian region with respect to global paleoclimates: future directions, *Palaeogeography Palaeoclimatology Palaeoecology*, 131, 511-515.
- Dekens, P. S., D. W. Lea, D. K. Pak, and H. J. Spero (2002), Core top calibration of Mg/Ca in tropical foraminifera: Refining paleotemperature estimation, *Geochemistry Geophysics Geosystems*, 3, 1022.
- Dekens, P. S., A. C. Ravelo, M. D. McCarthy, and C. A. Edwards (2008), A 5 million year comparison of Mg/Ca and alkenone paleothermometers, *Geochemistry Geophysics Geosystems*, 9, Q10001.

- Delcroix, T., and O. Lenormand (1997), ENSO signals in the vicinity of New Caledonia, South Western Pacific, *Oceanologica Acta*, 20(3), 481-491.
- Denton, G. H. (2000), Does an asymmetric thermohaline–ice-sheet oscillator drive 100 000-yr glacial cycles?, *Journal of Quaternary Science*, 15 (4), 301–318.
- Dowsett, H., J. Barron, and R. Poore (1996), Middle Pliocene sea surface temperatures: A global reconstruction, *Marine Micropaleontology*, 27(1-4), 13-25.
- Dowsett, H. J., and M. M. Robinson (2009), Mid-Pliocene equatorial Pacific sea surface temperature reconstruction: a multi-proxy perspective, *Philosophical Transactions of the Royal Society a-Mathematical Physical and Engineering Sciences*, 367(1886), 109-125.
- Dubois, N., P. Kindler, S. Spezzaferri, and C. S. (2008), The initiation of the southern central Great Barrier Reef: New multiproxy data from Pleistocene distal sediments from the Marion Plateau (NE Australia), *Marine Geology*, 250, 223-233.
- Dunbar, G. B., and G. R. Dickens (2003), Massive siliciclastic discharge to slopes of the Great Barrier Reef Platform during sea-level transgression: constraints from sediment cores between 15°S and 16°S latitude and possible explanations, *Sedimentary Geology*, 162(1-2), 141-158.
- Duplessy, J. C., N. J. Shackleton, R. G. Fairbanks, L. Labeyrie, D. W. Oppo, and N. Kallel (1988), Deepwater source variations during the last climatic cycle and their impact on the global deepwater circulation, *Paleoceanography*, 3(3), 343-360.
- Duplessy, J. C., N. J. Shackleton, R. K. Matthews, W. Prell, W. F. Ruddiman, M. Caralp, and C. H. Hendy (1984), ¹³C record of benthic foraminifera in the last interglacial ocean - implications for the carbon-cycle and the global deep water circulation, *Quaternary Research*, 21(2), 225-243.
- Elderfield, H., and G. Ganssen (2000), Past temperature and $\delta^{18}\text{O}$ of surface ocean waters inferred from foraminiferal Mg/Ca ratios, *Nature*, 405(6785), 442-445.
- Elderfield, H., M. Greaves, S. Barker, I. R. Hall, A. K. Tripathi, P. Ferretti, S. Crowhurst, L. Booth, and C. Daunt (2010), A record of bottom water temperature and seawater $\delta^{18}\text{O}$ for the Southern Ocean over the past 440kyr based on Mg/Ca of benthic foraminifera *Uvigerina* spp, *Quaternary Science Reviews*, 29, 160-169.

- Elkibbi, M., and J. A. Rial (2001), An outsider's review of the astronomical theory of the climate: is the eccentricity-driven insolation the main driver of the ice ages?, *Earth-Sci Rev*, 56, 161-177.
- Elliot, M., L. Labeyrie, and J. C. Duplessy (2002), Changes in North Atlantic deep-water formation associated with the Dansgaard-Oeschger temperature oscillations (60-10 ka), *Quaternary Science Reviews*., 21(10), 1153-1165.
- Emiliani, C. (1954), Depth habitats of some species of pelagic foraminifera as indicated by oxygen isotope ratios, *American Journal of Science*, 252(3), 149-158.
- Emiliani, C. (1955), Pleistocene temperatures, *Journal of Geology*, 63(6), 538-578.
- Falkowski, P. G., P. L. Jokiel, and R. A. K. III (1990), Irradiance and corals, in *Ecosystems of the World 25: Coral Reefs*, edited by Z. Dubinsky, Elsevier, Amsterdam.
- Fantle, M. S., and D. J. DePaolo (2005), Variations in the marine Ca cycle over the past 20 million years, *Earth and Planetary Science Letters*, 237(1-2), 102-117.
- Fantle, M. S., and D. J. DePaolo (2006), Sr isotopes and pore fluid chemistry in carbonate sediment of the Ontong Java Plateau: Calcite recrystallization rates and evidence for a rapid rise in seawater Mg over the last 10 million years, *Geochimica Cosmochimica Acta*, 70(15), 3883-3904.
- Fedorov, A. V., P. S. Dekens, M. McCarthy, A. C. Ravelo, P. B. deMenocal, M. Barreiro, R. C. Pacanowski, and S. G. Philander (2006), The Pliocene paradox (mechanisms for a permanent El Nino), *Science*, 312(5779), 1485-1489.
- Foucher, J. P., J. L. Charlou, F. Harmegnies, D. Wirrmann, A. M. Sémah, C. Chaduteau, and E. Roussel (2006), Rapport des travaux de la campagne ZoNéCo 12, Campagne AUSFAIR/ZoNéCo 12 à bord du N/O Marion Dufresne (12 au 26 février 2006).
- Gibbard, P.L., S. Boreham, K. M. Cohen and A. MoscarIELLO (2005), Global chronostratigraphical correlation table for the last 2.7 million years, *Boreas*, 34(1), unpaginated.
- Gildor, H., and E. Tziperman (2000), Sea ice as the glacial cycles' climate switch: Role of seasonal and orbital forcing, *Paleoceanography*, 15(6), 605-615.
- Gordon, A. L. (1975), An Antarctic oceanographic section along 170E, *Deep-Sea Research*, 22, 357-377.

- Gourdeau, L., W. S. Kessler, R. E. Davis, J. Sherman, C. Maes, and E. Kestenare (2008), Zonal jets entering the Coral Sea, *Journal of Physical Oceanography*, 38(3), 715-725.
- Gouriou, Y., and T. Delcroix (2002), Seasonal and ENSO variations of sea surface salinity and temperature in the South Pacific Convergence Zone during 1976-2000, *Journal of Geophysical Research*, 107(C12), SRF 12-11.
- Gradstein, F., J. Ogg, and A. Smith (2004), *A Geological Time Scale 2004*, Cambridge University Press.
- Greaves, M., S. Barker, C. Daunt, and H. Elderfield (2005), Accuracy, standardization, and interlaboratory calibration standards for foraminiferal Mg/Ca thermometry, *Geochemistry Geophysics Geosystems*, 6, Q02D13.
- Greaves, M., Caillon, N., Rebaubier, H., Bartoli, G., Bohaty, S., Cacho, I., Clarke, L., Cooper, M., Daunt, C., Delaney, M., deMenocal, P., Dutton, A., Eggins, S., Elderfield, H., Garbe-Schoenberg, D., Goddard, E., Green, D., Groeneveld, J., Hastings, D., Hathorne, E., Kimoto, K., Klinkhammer, G., Labeyrie, L., Lea, D. W., Marchitto, T., Martínez-Botí, M. A., Mortyn, P. G., Ni, Y., Nuernberg, D., Paradis, G., Pena, L., Quinn, T., Rosenthal, Y., Russell, A., Sagawa, T., Sosdian, S., Stott, L., Tachikawa, K., Tappa, E., Thunell, R., Wilson, P. A. (2008), Interlaboratory comparison study of calibration standards for foraminiferal Mg/Ca thermometry, *Geochemistry Geophysics Geosystems*, 9, Q08010.
- Grinsted, A., J. C. Moore, and S. Jevrejeva (2004), Application of the cross wavelet transform and wavelet coherence to geophysical time series, *Nonlinear Processes in Geophysics*, 11(5-6), 561-566.
- Hall, I. R., I. N. McCave, N. J. Shackleton, G. P. Weedon, and S. E. Harris (2001), Intensified deep Pacific inflow and ventilation in Pleistocene glacial times, *Nature*, 412(6849), 809-812.
- Hays, J. D., J. Imbrie, and N. J. Shackleton (1976), Variations in earths orbit - pacemaker of ice ages, *Science*, 194(4270), 1121-1132.
- Hayward B. W., G. H. Scott, M. P. Crundwell, J. P. Kennett, L. Carter, H. L. Neil, A. T. Sabaa, K. Wilson, J. S. Rodger, G. Schaefer, H. R. Grenfell, Q. Li (2008), The effect of submerged plateaux on Pleistocene gyral circulation and sea-surface temperatures in the Southwest Pacific, *Global and Planetary Change*, 63(4), 309-316.
- Head, M. J., and P. L. Gibbard (2005), Early-Middle Pleistocene Transitions: and overview and recommendation for the defining boundary in *Early-Middle Pleistocene Transitions: The Land-Ocean Evidence*, edited by M. J. Head and P. L. Gibbard, pp. 1-18, Geological Society.

- Hemleben, C., M. Spindler, and O. R. Anderson (1989), *Modern Planktonic Foraminifera*, Springer Verlag, New York.
- Henin, C., and G. R. Cresswell (2005), Upwelling along the western barrier reef of New Caledonia, *Marine and Freshwater Research*, 56(7), 1005-1010.
- Hodell, D. A., K. A. Venz, C. D. Charles, and U. S. Ninnemann (2003), Pleistocene vertical carbon isotope and carbonate gradients in the South Atlantic sector of the Southern Ocean, *Geochemistry, Geophysics, Geosystems*, 4(1), 1004.
- Honisch, B., N. G. Hemming, D. Archer, M. Siddall, and J. F. McManus (2009), Atmospheric carbon dioxide concentration across the Mid-Pleistocene Transition, *Science*, 324(5934), 1551-1554.
- Hut, G. (1987), Consultant's group meeting on stable isotope reference samples of geochemical and hydrological investigations, 42 pp, IAEA report, Vienna.
- Huybers, P. (2006), Early Pleistocene glacial cycles and the integrated summer forcing, *Science*, 313(5786), 405.
- Huybers, P. (2007), Glacial variability over the last two million years: an extended depth-derived agemodel, continuous obliquity pacing, and the Pleistocene progression, *Quaternary Science Reviews*, 26(1-2), 37-55.
- Huybers, P., and C. Wunsch (2005), Obliquity pacing of the late Pleistocene glacial terminations, *Nature*, 434, 491-494.
- Imbrie, J. Boyle, E. A., Clemens, S. C., Duffy, A., Howard, W. R., Kukla, G., Kutzbach, J., Martinson, D. G., McIntyre, A., Mix, A. C., Molfino, B., Morley, J. J., Peterson, L. C., Pisias, N. G., Prell, W. L., Raymo, M. E., Shackleton, N. J. and Toggweiler, J. R. (1992), On the structure and origin of major glaciation cycles .1. Linear responses to Milankovitch forcing, *Paleoceanography*, 7(6), 701-738.
- Imbrie, J. Boyle, E. A., Berger, A., Clemens, S. C., Duffy, A., Howard, W. R., Kukla, G., Kutzbach, J., Martinson, D. G., McIntyre, A., Mix, A. C., Molfino, B., Morley, J. J., Peterson, L. C., Pisias, N. G., Prell, W. L., Raymo, M. E., Shackleton, N. J. and Toggweiler, J. R., On the structure and origin of major glaciation cycles. 2. The 100,000-year cycle, *Paleoceanography*, 8(6), 699-735.
- Imbrie, J., and J. Z. Imbrie (1980), Modeling the climatic response to orbital variations, *Science*, 207(4434), 943-953.

- Imbrie, J., and N. G. Kipp (1971), A new micropaleontological method for quantitative paleoclimatology: application to a late Pleistocene Caribbean core, in *The Late Cenozoic Glacial Ages*, edited by K. K. Turekian, pp. 71-181, Yale University Press, New Haven.
- Isern, A. R., J. A. McKenzie, and D. A. Feary (1996), The role of sea-surface temperature as a control on carbonate platform development in the western Coral Sea, *Palaeogeography Palaeoclimatology Palaeoecology*, 124(3-4), 247-272.
- Jansen, E., Overpeck, J., Briffa, K. R., Duplessy, J. C., Joos, F., Masson-Delmotte, V., Olago, D., Otto-Bliesner, B., Peltier, W. B., Rahmstorf, S., Ramesh, R., Raynaud, R., Rind, R., Solomina, O., Villalba, R. and Zhang, D (2007), Palaeoclimate, in *Climate Change 2007: The Physical Science Basis. Contribution of Working Group I to the Fourth Assessment Report of the Intergovernmental Panel on Climate Change*, edited by S. Solomon *et al.*, Cambridge University Press, Cambridge, United Kingdom and New York, NY, USA.
- Jia, G. D., F. J. Chen, and P. A. Peng (2008), Sea surface temperature differences between the western equatorial Pacific and northern South China Sea since the Pliocene and their paleoclimatic implications, *Geophysical Research Letters*, 35(18), L18609.
- Jochum, M., B. Fox-Kemper, P. H. Molnar, and C. Shields (2009), Differences in the Indonesian seaway in a coupled climate model and their relevance to Pliocene climate and El Nino, *Paleoceanography*, 24, PA1212.
- Johnson, G. C., P. E. Robbins, and G. E. Hufford (2001), Systematic adjustments of hydrographic sections for internal consistency, *Journal of Atmospheric and Oceanic Technology*, 18(7), 1234-1244.
- Jouzel, J., V. Masson-Delmotte, O. Cattani, G. Dreyfus, S. Falourd, G. Hoffmann, B. Minster, J. Nouet, J.M. Barnola, J. Chappellaz, H. Fischer, J.C. Gallet, S. Johnsen, M. Leuenberger, L. Loulergue, D. Luethi, H. Oerter, F. Parrenin, G. Raisbeck, D. Raynaud, A. Schilt, J. Schwander, E. Selmo, R. Souchez, R. Spahni, B. Stauffer, J.P. Steffensen, B. Stenni, T.F. Stocker, J.L. Tison, M. Werner, and E.W. Wolff. (2007), Orbital and millennial Antarctic climate variability over the past 800,000 years, *Science*, 317(5839), 793-796.
- Juggins, S. (2007), C2: Software for ecological and palaeoecological data analysis and visualisation.
- Kawagata, S. (2001), Tasman Front shifts and associated paleoceanographic changes during the last 250,000 years: foraminiferal evidence from the Lord Howe Rise, *Marine Micropaleontology*, 41(3-4), 167-191.

- Kawahata, H., A. Nishimura and M. Gagan (2002), Seasonal change in foraminiferal production in the western equatorial Pacific warm pool: evidence from sediment trap experiments, *Deep Sea Research Part II: Topical Studies in Oceanography*, 49, 2783-2800.
- Kisakurek, B., A. Eisenhauer, F. Bohm, D. Garbe-Schonberg, and J. Erez (2008), Controls on shell Mg/Ca and Sr/Ca in cultured planktonic foraminiferan, *Globigerinoides ruber* (white), *Earth and Planetary Science Letters*, 273(3-4), 260-269.
- Keigwin, L. D. (1998), Glacial-age hydrography of the far northwest Pacific Ocean, *Paleoceanography*, 13(4), 323-339.
- Key, R. M., A. Kozyr, C. L. Sabine, K. Lee, R. Wanninkhof, J. L. Bullister, R. A. Feely, F. J. Millero, C. Mordy, and T. H. Peng (2004), A global ocean carbon climatology: Results from Global Data Analysis Project (GLODAP), *Global Biogeochemical Cycles*, 18(4).
- Kievman, C. M. (1998), Match between late Pleistocene Great Bahama Bank and deep-sea oxygen isotope records of sea level, *Geology*, 26(7), 635-638.
- Kisakurek, B., A. Eisenhauer, F. Bohm, D. Garbe-Schonberg, and J. Erez (2008), Controls on shell Mg/Ca and Sr/Ca in cultured planktonic foraminiferan, *Globigerinoides ruber* (white), *Earth and Planetary Science Letters*, 273(3-4), 260-269.
- Kleypas, J. A., J. W. McManus, and L. A. B. Menez (1999), Environmental limits to coral reef development: Where do we draw the line?, *American Zoologist*, 39(1), 146-159.
- Kohler, P., and R. Bintanja (2008), The carbon cycle during the Mid-Pleistocene Transition: the Southern Ocean Decoupling Hypothesis, *Climate of the Past*, 4, 311-322.
- Kroopnick, P. M. (1985), The distribution of ^{13}C of ΣCO_2 in the world oceans, *Deep-Sea Research Part A - Oceanographic Research Papers*, 32(1), 57-84.
- Koutavas, A., and J. Lynch-Stieglitz (2004), Variability of the marine ITCZ over the eastern Pacific during the past 30,000 years: regional perspective and global context, in *The Hadley Circulation: Past, Present and Future*, edited by H. F. Diaz and R. S. Bradley, pp. 347-369, Kluwer Academic Publishers.
- Koutavas, A., J. Lynch-Stieglitz, and T. M. Marchitto (2002a), El Nino-La Nina pattern of glacial-interglacial transitions: Evidence from geochemical proxies in foraminifera, *Geochimica Cosmochimica Acta*, 66(15A), A413-A413.

- Koutavas, A., J. Lynch-Stieglitz, T. M. Marchitto, and J. P. Sachs (2002), El Niño-like pattern in ice age tropical Pacific sea surface temperature, *Science*, 297(5579), 226-230.
- Lafoy, Y., I. Brodien, R. Vially, and N. F. Exon (2005), Structure of the basin and ridge system west of New Caledonia (southwest Pacific): A synthesis, *Marine Geophysical Researches*, 26(1), 37-50.
- Laskar, J., P. Robutel, F. Joutel, M. Gastineau, A. C. M. Correia, and B. Levrard (2004), A long-term numerical solution for the insolation quantities of the Earth, *Astronomy & Astrophysics*, 428(1), 261-285.
- Laj, C., and J. E. T. Channell (2007), Geomagnetic Excursions, in *Geomagnetism*, edited by M. Kono, pp. 373-416, Elsevier.
- Lawrence, K. T., Z. H. Liu, and T. D. Herbert (2006), Evolution of the eastern tropical Pacific through Plio-Pleistocene glaciation, *Science*, 312(5770), 79-83.
- Lawrence, K. T., and T. D. Herbert (2005), Late quaternary sea-surface temperatures in the western Coral Sea: Implications for the growth of the Australian Great Barrier Reef, *Geology*, 33(8), 677-680.
- Lea, D. W., D. K. Pak, and H. J. Spero (2000), Climate impact of late quaternary equatorial Pacific sea surface temperature variations, *Science*, 289(5485), 1719-1724.
- Lea, D. W. (2004), The 100,000-yr cycle in tropical SST, greenhouse forcing, and climate sensitivity, *Journal of Climate*, 17(11), 2170-2179.
- LeGrande, A. N., and G. A. Schmidt (2006), Global gridded data set of the oxygen isotopic composition in seawater, *Geophysical Research Letters*, 33(12), L12604.
- Linsley, B. K., Y. Rosenthal, and D. W. Oppo (2010), Holocene evolution of the Indonesian throughflow and the western Pacific warm pool, *Nature Geoscience*, advance online publication.
- Lisiecki, L. E. (2010), Links between eccentricity forcing and the 100,000-year glacial cycle, *Nature Geoscience*, 3(5), 349-352.
- Lisiecki, L. E., and M. E. Raymo (2005), A Pliocene-Pleistocene stack of 57 globally distributed benthic $\delta^{18}\text{O}$ records, *Paleoceanography*, 20(1), PA1003.
- Lisiecki, L. E., and M. E. Raymo (2009), Diachronous benthic $\delta^{18}\text{O}$ responses during late Pleistocene terminations, *Paleoceanography*, 24, PA3210.

- Liu, Z., and T. D. Herbert (2004), High-latitude influence on the eastern equatorial Pacific climate in the early Pleistocene epoch, *Nature*, 427, 720-724.
- Liu, Z. H., L. C. Cleaveland, and T. D. Herbert (2008), Early onset and origin of 100-kyr cycles in Pleistocene tropical SST records, *Earth and Planetary Science Letters*, 265(3-4), 703-715.
- Liu, Z. Y., S. I. Shin, B. Otto-Bliesner, J. E. Kutzbach, E. C. Brady, and D. E. Lee (2002), Tropical cooling at the last glacial maximum and extratropical ocean ventilation, *Geophysical Research Letters*, 29(10), 1409.
- Locarnini, R. A., A. V. Mishonov, J. I. Antonov, T. P. Boyer, and H. E. Garcia (2006), World Ocean Atlas 2005, Volume 1, 182 pp, U.S. Government Printing Office, Washington, D.C.
- Lowemark, L., W. L. Hong, T. F. Yui, and G. W. Hung (2005), A test of different factors influencing the isotopic signal of planktonic foraminifera, in surface sediments from the northern South China Sea, *Marine Micropaleontology*, 55(1-2), 49-62.
- Lüthi, D., M. Le Floch, B. Bereiter, T. Blunier, J-M. Barnola, U. Siegenthaler, D. Raynaud, J. Jouzel, H. Fischer, K. Kawamura and T. F. Stocker, High-resolution carbon dioxide concentration record 650,000-800,000 years before present, *Nature*, 453(7193), 379-382.
- Lyle, M., J. Barron, T. J. Bralower, M. Huber, A. O. Lyle, A. C. Ravelo, D. K. Rea, and P. A. Wilson (2008), Pacific ocean and Cenozoic evolution of climate, *Reviews of Geophysics*, 46(2), RG2002.
- Maasch, K. A., and B. Saltzman (1990), A low-order dynamic-model of global climatic variability over the full Pleistocene, *Journal of Geophysical Research*, 95(D2), 1955-1963.
- Mackensen, A., H. W. Hubberten, T. Bickert, G. Fischer, and D. K. Futterer (1993), The $\delta^{13}\text{C}$ in benthic foraminiferal tests of *Fontbotia wuellerstorfi* (Schwager) relative to the $\delta^{13}\text{C}$ of dissolved inorganic carbon in Southern-Ocean deep-water - implications for glacial ocean circulation models, *Paleoceanography*, 8(5), 587-610.
- Marchitto, T. M., S. P. Bryan, W. B. Curry, and D. C. McCorkle (2007), Mg/Ca temperature calibration for the benthic foraminifer *Cibicidoides pachyderma*, *Paleoceanography*, 22(1), PA1203.
- MARGO Project Members (2009), Constraints on the magnitude and patterns of ocean cooling at the Last Glacial Maximum, *Nature Geoscience*, 2(2), 127-132.

- Marlow, J. R., C. B. Lange, G. Wefer, and A. Rosell-Mele (2000), Upwelling intensification as part of the Pliocene-Pleistocene climate transition, *Science*, 290(5500), 2288-2291.
- Martinez, J. I. (1994), Late Pleistocene paleoceanography of the Tasman Sea - implications for the dynamics of the warm pool in the western Pacific, *Palaeogeography Palaeoclimatology Palaeoecology*, 112(1-2), 19-62.
- Martinez, J. I. (1997), Decreasing influence of subantarctic mode water north of the Tasman Front over the past 150kyr, *Palaeogeography Palaeoclimatology Palaeoecology*, 131(3-4), 355-364.
- Martinez-Garcia, A., A. Rosell-Mele, W. Geibert, R. Gersonde, P. Masque, V. Gaspari, and C. Barbante (2009), Links between iron supply, marine productivity, sea surface temperature, and CO₂ over the last 1.1 Ma, *Paleoceanography*, 24, PA1207.
- Maslin, M. A., and A. J. Ridgwell (2005), Mid-Pleistocene revolution and the "eccentricity myth", in *Early-Middle Pleistocene Transitions: The Land-Ocean Evidence*, edited by M. J. Head and P. L. Gibbard, pp. 19-34, Geological Society.
- Mathien-Blard, E., and F. Bassinot (2009), Salinity bias on the foraminifera Mg/Ca thermometry: Correction procedure and implications for past ocean hydrographic reconstructions, *Geochemistry Geophysics Geosystems*, 10, Q12011.
- Matsumoto, K., J. Lynch-Stieglitz, and R. F. Anderson (2001), Similar glacial and Holocene Southern Ocean hydrography, *Paleoceanography*, 16(5), 445-454.
- Matsumoto, K., T. Oba, J. Lynch-Stieglitz, and H. Yamamoto (2002), Interior hydrography and circulation of the glacial Pacific Ocean, *Quaternary Science Reviews*, 21(14-15), 1693-1704.
- Mazaud, A. (2005), User-friendly software for vector analysis of the magnetization of long sediment cores, *Geochemistry Geophysics Geosystems*, 6, Q12006.
- McCave, I. N., L. Carter, and I. R. Hall (2008), Glacial-interglacial changes in water mass structure and flow in the SW Pacific Ocean, *Quaternary Science Reviews*, 1886-1908.
- McClymont, E. L., and A. Rosell-Mele (2005), Links between the onset of modern Walker circulation and the mid-Pleistocene climate transition, *Geology*, 33(5), 389-392.

- McConnell, M. C., and R. C. Thunell (2005), Calibration of the planktonic foraminiferal Mg/Ca paleothermometer: sediment trap results from the Guaymas Basin, Gulf of California, *Paleoceanography*, 20(2), PA2016.
- McCorkle, D. C., and L. D. Keigwin (1994), Depth profiles of $\delta^{13}\text{C}$ in bottom water and core top *C. wuellerstorfi* on the Ontong Java Plateau and Emperor seamounts, *Paleoceanography*, 9(2), 197-208.
- McTaggart, K. E., and G. C. Johnson (1997), CTD/O₂ measurements collected on a Climate and Global Change cruise (WOCE Sections P14S and P15S) during January-March, 1996, 485 pp. NOAA Data Report.
- Medina-Elizalde, M., and D. W. Lea (2005), The Mid-Pleistocene Transition in the tropical Pacific, *Science*, 310(5750), 1009-1113.
- Medina-Elizalde, M., and D. W. Lea (2010), Late Pliocene equatorial Pacific, *Paleoceanography*, 25(2), PA2208.
- Medina-Elizalde, M., D. W. Lea, and M. S. Fantle (2008), Implications of seawater Mg/Ca variability for Plio-Pleistocene tropical climate reconstruction, *Earth and Planetary Science Letters*, 269(3-4), 584-594.
- Meyers, S. R., and L. A. Hinnov (2010), Northern Hemisphere glaciation and the evolution of Plio-Pleistocene climate noise, *Paleoceanography*, 25, PA3207.
- Michel, E., L. D. Labeyrie, J. C. Duplessy, N. Gorfti, M. Labracherie, and J. L. Turon (1995), Could deep sub-Antarctic convection feed the world deep basins during the Last Glacial Maximum, *Paleoceanography*, 10(5), 927-941.
- Milankovitch, M. (1948), Ausbau Und Gegenwartiger Stand Der Astronomischen Theorie Der Erdgeschichtlichen Klimate, *Experientia*, 4(11), 413-418.
- Mix, A. C., N. G. Pisias, W. Rugh, J. Wilson, A. Morey, and T. Hagelberg (1995), Benthic foraminiferal stable isotope record from site 849, 0-5Ma: Local and global climate changes, *Proceedings of the Ocean Drilling Program, Scientific Results*, 138, 371-412.
- Molnar, P. (2008), Closing of the Central American seaway and the ice age: a critical review, *Paleoceanography*, 23(1), PA2201.
- Moore, T. C., N. G. Pisias, and D. A. Dunn (1982), Carbonate time-series of the Quaternary and late Miocene sediments in the Pacific-Ocean - a spectral comparison, *Marine Geology*, 46(3-4), 217-233.

- Moy, A. D., W. R. Howard, and M. K. Gagan (2006), Late Quaternary palaeoceanography of the Circumpolar Deep Water from the South Tasman Rise, *Journal of Quaternary Science*, 21(7), 763-777.
- Mudelsee, M., and M. E. Raymo (2005), Slow dynamics of the Northern Hemisphere glaciation, *Paleoceanography*, 20(4), PA4022.
- Mudelsee, M., and M. Schulz (1997), The Mid-Pleistocene climate transition: onset of 100 ka cycle lags ice volume build-up by 280 ka, *Earth and Planetary Science Letters*, 151(1-2), 117-123.
- Mudelsee, M., and K. Statterger (1997), Exploring the structure of the mid-Pleistocene revolution with advanced methods of time-series analysis, *Geologische Rundschau*, 86, 499-511.
- Nees, S. (1997), Late Quaternary palaeoceanography of the Tasman Sea: the benthic foraminiferal view, *Palaeogeography Palaeoclimatology Palaeoecology*, 131(3-4), 365-389.
- Nicet, J. B., and T. Delcroix (2000), ENSO-related precipitation changes in New Caledonia, southwestern tropical Pacific: 1969-98, *Monthly Weather Review*, 128(8), 3001-3006.
- Ninnemann, U. S., and C. D. Charles (2002), Changes in the mode of Southern Ocean circulation over the last glacial cycle revealed by foraminiferal stable isotopic variability, *Earth and Planetary Science Letters*, 201(2), 383-396.
- Nurnberg, D., J. Bijma, and C. Hemleben (1996), Assessing the reliability of magnesium in foraminiferal calcite as a proxy for water mass temperatures (vol 60, pg 803, 1995), *Geochimica Cosmochimica Acta*, 60(13), 2483-2483.
- Opdyke, B. N., and J. C. G. Walker (1992), Return of the coral reef hypothesis: basin to shelf partitioning of CaCO₃ and its effect on atmospheric CO₂, *Geology*, 20, 733-736.
- Otto-Bliesner, B. L., and A. Clement (2005), The sensitivity of the Hadley circulation to past and future forcings in two climate models, in *The Hadley Circulation: Past, Present and Future*, edited by H. F. Diaz and R. S. Bradley, pp. 437-464, Springer, New York.
- Pahnke, K., and R. Zahn (2005), Southern hemisphere water mass conversion linked with North Atlantic climate variability, *Science*, 307(5716), 1741-1746.
- Paillard, D. (1998), The timing of Pleistocene glaciations from a simple multiple-state climate model, *Nature*, 391, 378-382.

- Paillard, D. (2001), Glacial cycles: Toward a new paradigm, *Reviews of Geophysics*, 39(3), 325-346.
- Paillard, D., L. Labeyrie, and P. Yiou (1996), Macintosh program performs time-series analysis, *Eos Transactions AGU*, 77, 379.
- Palike, H., R. D. Norris, J. O. Herrle, P. A. Wilson, H. K. Coxall, C. H. Lear, N. J. Shackleton, A. K. Tripathi, and B. S. Wade (2006), The heartbeat of the Oligocene climate system, *Science*, 314(5807), 1894-1898.
- Peerdeman, F. M., P. J. Davies, and A. R. Chivas (1993), The stable oxygen isotope signal in shallow-water upper-slope sediments off the Great Barrier Reef (Hole 820A), *Proceedings of the Ocean Drilling Program, Scientific Results*, 133, 162-172.
- Pelletier, B. (2006), Geology of the New Caledonia region and its implications for the study of the New Caledonian biodiversity, paper presented at *Forum Biodiversité des Ecosystèmes Coralliens*, Nouméa, Nouvelle Calédonie.
- Petit, J. R., J. Jouzel, D. Raynaud, N. I. Barkov, J.-M. Barnola, I. Basile, M. Bender, J. Chappellaz, M. Davis, G. Delaygue, M. Delmotte, V. M. Kotlyakov, M. Legrand, V. Y. Lipenkov, C. Lorius, L. Pepin, C. Ritz, E. Saltzman and M. Stievenard (1999), Climate and atmospheric history of the past 420,000 years from the Vostok ice core, Antarctica, *Nature*, 399(6735), 429-436.
- Philander, S. G., and A. V. Fedorov (2003), Role of tropics in changing the response to Milankovich forcing some three million years ago, *Paleoceanography*, 18(2), 1045.
- Piotrowski, A. M., S. L. Goldstein, S. R. Hemming, and R. G. Fairbanks (2005), Temporal relationships of carbon cycling and ocean circulation at glacial boundaries, *Science*, 307(5717), 1933-1938.
- Prell, W. L. (1985), The stability of low-latitude sea surface temperatures: an evaluation of the CLIMAP reconstruction with emphasis on the positive SST anomalies, US Department of Energy, Washington, DC.
- Quinn, T. M., and D. E. Sampson (2002), A multiproxy approach to reconstructing sea surface conditions using coral skeleton geochemistry, *Paleoceanography*, 17(4), 1062.
- Ravelo, A. C., D. H. Andreasen, M. Lyle, A. O. Lyle, and M. W. Wara (2004), Regional climate shifts caused by gradual global cooling in the Pliocene epoch, *Nature*, 429(6989), 263-267.
- Ravelo, A. C., P. S. Dekens, and M. McCarthy (2006), Evidence for El Niño-like conditions during the Pliocene, *GSA Today*, 16, 4-11.

- Raymo, M. E. (1994), The initiation of northern-hemisphere glaciation, *Annual Review of Earth and Planetary Sciences*, 22, 353-383.
- Raymo, M. (1997), The timing of major climate transitions, *Paleoceanography*, 12(4), 577-585.
- Raymo, M. E., D. W. Oppo, and W. Curry (1997), The mid-Pleistocene climate transition: A deep sea carbon isotopic perspective, *Paleoceanography*, 12(4), 546-559.
- Raymo, M. E., and W. F. Ruddiman (1992), Tectonic forcing of late Cenozoic climate, *Nature*, 359(6391), 117-122.
- Raymo, M. E., L. E. Lisiecki, and K. H. Nisancioglu (2006), Plio-pleistocene ice volume, Antarctic climate, and the global $\delta^{18}\text{O}$ record, *Science*, 313(5786), 492-495.
- Reid, J. L. (1997), On the total geostrophic circulation of the Pacific Ocean: flow patterns, tracers, and transports, *Progress in Oceanography*, 39(4), 263-352.
- Rickaby, R. E. M., H. Elderfield, N. Roberts, C. D. Hillenbrand, and A. Mackensen (2010), Evidence for elevated alkalinity in the glacial Southern Ocean, *Paleoceanography*, 25, PA1209.
- Ridgway, K. R., and J. R. Dunn (2003), Mesoscale structure of the mean East Australian Current System and its relationship with topography, *Progress in Oceanography*, 56, 189-222.
- Ridgwell, A. J., A. J. Watson, M. A. Maslin, and J. O. Kaplan (2003), Implications of coral reef buildup for the controls on atmospheric CO_2 since the Last Glacial Maximum, *Paleoceanography*, 18(4), 1083.
- Rind, D., and J. Perlwitz (2004), The response of the Hadley circulation to climate changes, past and future, in *The Hadley Circulation: Past, Present and Future*, edited by H. F. Diaz and R. S. Bradley, pp. 399-435, Kluwer Academic Publishers.
- Rintoul, S. R. (1998), On the origin and influence of Adelie Land Bottom Water, in *Ocean, Ice and Atmosphere: Interactions at the Antarctic Continental Margin*, edited by S. S. Jacobs and R. F. Weiss, pp. 151-171.
- Roe, G. (2006), In defense of Milankovitch, *Geophysical Research Letters*, 33(24), L24703.
- Ruddiman, W. F. (2003), Orbital insolation, ice volume, and greenhouse gases, *Quaternary Science Reviews*, 22(15-17), 1597-1629.

- Ruddiman, W. F., M. E. Raymo, D. G. Martinson, B. M. Clement, and J. Backman (1989), Pleistocene evolution: Northern Hemisphere ice sheets and North Atlantic Ocean, *Paleoceanography*, 4(4), 353-412.
- Russon, T., M. Elliot, C. Kissel, G. Cabioch, P. De Deckker, and T. Correge (2009), Middle-Late Pleistocene deep water circulation in the southwest subtropical Pacific, *Paleoceanography*, 24, PA4205.
- Russon, T., M. Elliot, A. Sadekov, T. Correge, G. Cabioch, and P. De Deckker (2010a), Inter-hemispheric asymmetry in the early Pleistocene Pacific warm pool, *Geophysical Research Letters*, 37, L11601.
- Russon, T., M. Elliot, A. Sadekov, T. Correge, G. Cabioch, and P. De Deckker (2011) The Mid-Pleistocene Transition in the subtropical southwest Pacific, *Paleoceanography*, in press.
- Russon, T., D. Paillard, and M. Elliot (2010b), Potential origins of 400-500kyr periodicities in the ocean carbon cycle: a box model approach, *Global Biogeochemical Cycles*, 24, GB2013.
- Sadekov, A., S. M. Eggins, P. De Deckker, and D. Kroon (2008), Uncertainties in seawater thermometry deriving from intratest and intertest Mg/Ca variability in *Globigerinoides ruber*, *Paleoceanography*, 23(1), PA1215.
- Saltzman, B. (1982), Stochastically-driven climatic fluctuations in the sea-ice, ocean temperature, CO₂ feedback-system, *Tellus*, 34(2), 97-112.
- Sarachik, E. S., and M. A. Cane (2010), *The El-Nino Southern Oscillation Phenomenon*, Cambridge University Press, Cambridge.
- Sato, K., M. Oda, S. Chiyonobu, K. Kimoto, H. Domitsu, and J. C. Ingle Jr (2008), Establishment of the western Pacific warm pool during the Pliocene: Evidence from planktic foraminifera, oxygen isotopes, and Mg/Ca ratios, *Palaeogeography Palaeoclimatology Palaeoecology*, 265(1-2), 140-147.
- Schefuss, E., J. S. S. Damste, and J. H. F. Jansen (2004), Forcing of tropical Atlantic sea surface temperatures during the mid-Pleistocene transition, *Paleoceanography*, 19(4).
- Schlitzer, R. (2007), Ocean Data View, <http://odv.awi.de>.
- Schmieder, F., T. von Dobeneck, and U. Bleil (2000), The Mid-Pleistocene climate transition as documented in the deep South Atlantic Ocean: initiation, interim state and terminal event, *Earth and Planetary Science Letters*, 179(3-4), 539-549.

- Shackleton, N. J. (1974), Attainment of isotopic equilibrium between ocean water and benthonic foraminifera genus *Uvigerina*: Isotopic changes in the ocean during the last glacial, in *Les methodes quantitatives d'etude des variations du climat au cours du Pleistocene*, edited, pp. 203-209, Centre National de la Recherche Scientifique, Gif-sur Yvette, France.
- Shackleton, N. J. (1977), Carbon-13 in *Uvigerina*: tropical rainforest history and the Equatorial Pacific carbonate dissolution cycles, in *The Fate of Fossil Fuel CO₂ in the Oceans New York*, edited by N. R. Andersen and A. Malahoff, pp. 401-427, Plenum Press, New York.
- Shackleton, N. J. (2000), The 100,000-year ice-age cycle identified and found to lag temperature, carbon dioxide, and orbital eccentricity, *Science*, 289(5486), 1897-1902.
- Shackleton N.J., J. Backman, H. Zimmerman, D. V. Kent, M. A. Hall, D. G. Roberts, D. Schnitker, J. G. Baldauf, A. Desprairies, R. Homrighausen, P. Huddleston, J. B. Keene, A. J. Kaltenback, K. A. O. Krumsiek, A. C. Morton, J. W. Murray and J. Westberg-Smith (1984), Oxygen isotope calibration of the onset of ice-rafting and history of glaciation in the North-Atlantic region, *Nature*, 307, 620-623.
- Shackleton, N. J., A. Berger, and W. R. Peltier (1990), An alternative astronomical calibration of the lower Pleistocene timescale based on ODP site 677, *Trans. Roy. Soc. Edin. - Earth Sci.*, 81, 251-261.
- Shackleton, N. J., and B. N. Opdyke (1973), Oxygen isotope and palaeomagnetic stratigraphy of equatorial Pacific core V28-238: oxygen isotope temperatures and ice volumes on a 105 and 106 year scale, *Quaternary Research* 3, 39-55.
- Sigman, D. M., and E. A. Boyle (2000), Glacial/interglacial variations in atmospheric carbon dioxide, *Nature*, 407(6806), 859-869.
- Skinner, L. C., and N. J. Shackleton (2005), An Atlantic lead over Pacific deep-water change across Termination I: implications for the application of the marine isotope stage stratigraphy, *Quaternary Science Reviews.*, 24(5-6), 571-580.
- Sokolov, S., and S. Rintoul (2000), Circulation and water masses of the southwest Pacific: WOCE Section P11, Papua New Guinea to Tasmania, *Journal of Marine Research*, 58(2), 223-268.
- Sosdian, S., and Y. Rosenthal (2009), Deep-sea temperature and ice volume changes across the Pliocene-Pleistocene climate transitions, *Science*, 325(5938), 306-310.

- Spero, H. J., J. Bijma, D. W. Lea, and B. E. Bemis (1997), Effect of seawater carbonate concentration on foraminiferal carbon and oxygen isotopes, *Nature*, 390(6659), 497-500.
- Spero, H. J., K. M. Mielke, E. M. Kalve, D. W. Lea, and D. K. Pak (2003), Multispecies approach to reconstructing eastern equatorial Pacific thermocline hydrography during the past 360 kyr, *Paleoceanography*, 18(1).
- Steinke, S., H. Y. Chiu, P. S. Yu, C. C. Shen, L. Lowemark, H. S. Mii, and M. T. Chen (2005), Mg/Ca ratios of two *Globigerinoides ruber* (white) morphotypes: Implications for reconstructing past tropical/ subtropical surface water conditions, *Geochemistry Geophysics Geosystems*, 6, Q11005.
- Stott, L., C. Poulsen, S. Lund, and R. Thunell (2002), Super ENSO and global climate oscillations at millennial time scales, *Science*, 297(5579), 222-226.
- Tachikawa, K., L. Vidal, C. Sonzogni, and E. Bard (2009), Glacial/interglacial sea surface temperature changes in the Southwest Pacific ocean over the past 360 ka, *Quaternary Science Reviews*., 28(13-14), 1160-1170.
- Talley, L. D. (2007), Hydrographic atlas of the World Ocean Circulation Experiment (WOCE): Volume 2: Pacific Ocean, International WOCE Project Office, Southampton, U.K.
- Thiede, J., S. Nees, H. Schulz, and P. De Deckker (1997), Oceanic surface conditions recorded on the sea floor of the southwest Pacific Ocean through the distribution of foraminifers and biogenic silica, *Palaeogeography Palaeoclimatology Palaeoecology*., 131(3-4), 207-239.
- Thompson, P. R., A. W. H. Bé, J. C. Duplessy, and N. J. Shackleton (1979), Disappearance of pink-pigmented *Globigerinoides ruber* at 120,000yr bp in the Indian and Pacific Oceans, *Nature*, 280(5723), 554-558.
- Toggweiler, J. R. (1999), Variation of atmospheric CO₂ by ventilation of the ocean's deepest water, *Paleoceanography*, 14(5), 571-588.
- Toggweiler, J. R. (2008), Origin of the 100,000-year timescale in Antarctic temperatures and atmospheric CO₂, *Paleoceanography*, 23(2), PA2211.
- Toggweiler, J. R., and D. W. Lea (2010), Temperature differences between the hemispheres and ice age climate variability, *Paleoceanography*, 25, PA2212.

- Toggweiler, J. R., J. L. Russell, and S. R. Carson (2006), Midlatitude westerlies, atmospheric CO₂, and climate change during the ice ages, *Paleoceanography*, *21*(2), PA2005.
- Trenberth, K. E., and A. Solomon (1994), The global heat-balance- heat transports in the atmosphere and ocean, *Climate Dynamics*, *10*, 107-134.
- Tsimplis, M. N., S. Bacon, and H. L. Bryden (1998), The circulation of the subtropical South Pacific derived from hydrographic data, *Journal of Geophysical Research*, *103*(C10), 21,443-421,468.
- Tziperman, E., and H. Gildor (2003), On the mid-Pleistocene transition to 100-kyr glacial cycles and the asymmetry between glaciation and deglaciation times, *Paleoceanography*, *18*(1), 1001.
- Urey, H. C. (1947), The thermodynamic properties of isotopic substances, *Journal of the Chemical Society*, (May), 562-581.
- Vecsei, A., and W. H. Berger (2004), Increase of atmospheric CO₂ during deglaciation: Constraints on the coral reef hypothesis from patterns of deposition, *Global Biogeochemical Cycles*, *18*(1), GB1035.
- Venuti, A., F. Florindo, E. Michel, and I. R. Hall (2007), Magnetic proxy for the deep (Pacific) western boundary current variability across the mid-Pleistocene climate transition, *Earth and Planetary Science Letters*, *259*(1-2), 107-118.
- Venz, K. A., and D. A. Hodell (2002), New evidence for changes in Plio-Pleistocene deep water circulation from Southern Ocean ODP Leg 177 Site 1090, *Palaeogeography Palaeoclimatology Palaeoecology*, *182*, 197-220.
- Visser, K., R. Thunell, and L. Stott (2003), Magnitude and timing of temperature change in the Indo-Pacific warm pool during deglaciation, *Nature*, *421*(6919), 152-155.
- Vizcaíno, M., S. Rupper, and J. C. H. Chiang (2010), Permanent El Niño and the onset of Northern Hemisphere glaciations: mechanism and comparison with other hypotheses, *Paleoceanography*, *25*(2), PA2205.
- Wang, L. J. (1994), Sea-surface temperature history of the low-latitude western Pacific during the last 5.3 Million Years, *Palaeogeography Palaeoclimatology Palaeoecology*, *108*(3-4), 379-436.
- Wang, L. J. (2000), Isotopic signals in two morphotypes of *Globigerinoides ruber* (white) from the South China Sea: implications for monsoon climate change during the last glacial cycle, *Palaeogeography Palaeoclimatology Palaeoecology*, *161*(3-4), 381-394.

- Wang, P. X., J. Tian, X. R. Cheng, C. L. Liu, and J. Xu (2004), Major Pleistocene stages in a carbon perspective: The South China Sea record and its global comparison, *Paleoceanography*, 19, PA4005.
- Wara, M. W., A. C. Ravelo, and M. L. Delaney (2005), Permanent El Nino-like conditions during the Pliocene warm period, *Science*, 309(5735), 758-761.
- Warren, B. A. (1973), Transpacific hydrographic sections at latitudes 43°S and 28°S - Scorpio Expedition. Vol. 2. Deep-water, *Deep-Sea Research*, 20(1), 9-38.
- Warren, B. A. (1981), Deep circulation of the world ocean, in *Evolution of Physical Oceanography*, edited by B. A. Warren and C. Wunsch, pp. 6-41, MIT Press, Cambridge.
- Warren, B. A., T. Whitworth, M. I. Moore, and W. D. Nowlin (1994), Slight northwestward inflow to the deep South Fiji Basin, *Deep-Sea Research Part I-Oceanographic Research Papers*, 41(5-6), 953-956.
- Weaver, P. P. E., H. Neil, and L. Carter (1997), Sea surface temperature estimates from the Southwest Pacific based on planktonic foraminifera and oxygen isotopes, *Palaeogeography Palaeoclimatology Palaeoecology*, 131(3-4), 241-256.
- Whitworth, T., B. A. Warren, W. D. Nowlin, S. B. Rutz, R. D. Pillsbury, and M. I. Moore (1999), On the deep western-boundary current in the Southwest Pacific Basin, *Progress in Oceanography*, 43(1), 1-54.
- Wijffels, S. E., J. M. Toole, and . Davis (2001), Revisiting the South Pacific subtropical circulation: A synthesis of World Ocean Circulation Experiment observations along 32 degrees S, *Journal of Geophysical Research*, 106(C9), 19481-19513.
- WOCE (2002), World Ocean Circulation Experiment: Global Data, Version 3.0, WOCE International Project Office, Southampton, UK.
- Wunsch, C. (2004), Quantitative estimate of the Milankovitch-forced contribution to observed Quaternary climate change, *Quaternary Science Reviews*, 23, 1001-1012.
- Wyrtki, K. (1961), The flow of water into the deep sea basins of the western south Pacific Ocean., *Australian Journal of Marine and Freshwater Research*, 12, 1-16.
- Xiong, S. F., Z. L. Ding, W. Y. Jiang, S. L. Yang, and T. S. Liu (2003), Initial intensification of East Asian winter monsoon at about 2.75 Ma as seen in the Chinese eolian loess-red clay deposit, *Geophysical Research Letters*, 30(10), 1524.

- Yamamoto, K., Y. Iryu, T. Sato, S. Chiyonobu, K. Sagae, and E. Abe (2006), Responses of coral reefs to increased amplitude of sea-level changes at the Mid-Pleistocene climate transition, *Palaeogeography Palaeoclimatology Palaeoecology*, 241(1), 160-175.
- Zachos, J., M. Pagani, L. Sloan, E. Thomas, and K. Billups (2001a), Trends, rhythms, and aberrations in global climate 65 Ma to present, *Science*, 292(5517), 686-693.
- Zachos, J. C., N. J. Shackleton, J. S. Revenaugh, H. Palike, and B. P. Flower (2001b), Climate response to orbital forcing across the Oligocene-Miocene boundary, *Science*, 292(5515).
- Zahn, R., K. Winn, and M. Sarnthein (1986), Benthic foraminiferal $\delta^{13}\text{C}$ and accumulation rates of organic carbon: *Uvigerina peregina* group and *Cibicidoides wuellerstorfi*, *Paleoceanography*, 1(1), 27-42.
- Zeebe, R. E., and P. Westbroek (2003), A simple model for the CaCO_3 saturation state of the ocean: The "Strangelove", the "Neritan", and the "Cretan" Ocean, *Geochemistry Geophysics Geosystems*, 4(12), 1104.
- Zeebe, R. E., and D. A. Wolf-Gladrow (2001), *CO₂ in seawater: equilibrium, kinetics, isotopes*, Elsevier.

Blank Page

Appendix 1: Principles of the foraminiferal stable isotope and Mg/Ca trace-metal proxy systems

A1.1 Stable oxygen isotopes in foraminiferal calcite

Oxygen exists in three stable isotopes; ^{18}O (relative abundance, 0.2%), ^{17}O (0.04%) and ^{16}O (99.8%). Measurements of the relative abundances of the two most common isotopes, ^{16}O and ^{18}O , may be expressed in ‘ δ ’ notation, defined as follows:

Equation A1.1
$$\delta^{18}\text{O} = \left(\frac{(^{18}\text{O}/^{16}\text{O})_{\text{sample}}}{(^{18}\text{O}/^{16}\text{O})_{\text{reference}}} - 1 \right) \times 1000 \text{ (‰)}$$

Calcareous marine organisms, such as foraminifera, build their shells through the incorporation of Ca^{2+} and the DIC species CO_3^{2-} and HCO_3^- . The stable isotopic composition of oxygen in the resulting biogenic calcite ($\delta^{18}\text{O}_{\text{calcite}}$) thus depends directly upon the isotopic composition of the DIC species. However, the number of oxygen atoms contained in H_2O itself is four orders of magnitude greater than that in all of the DIC species combined, meaning that it is the isotopic composition of the seawater ($\delta^{18}\text{O}_{\text{sw}}$) that principally controls the signal incorporated into calcite [Zeebe and Wolf-Gladrow, 2001]. As a consequence of the ‘ δ ’ definition (as in equation A1.1), $\delta^{18}\text{O}$ measurements are necessarily given relative to a reference material. For $\delta^{18}\text{O}_{\text{calcite}}$, this is normally that of the Vienna Pee Dee Belemnite (VPDB) and this is assumed throughout the thesis unless specifically stated otherwise.

In addition to the direct control exerted by $\delta^{18}\text{O}_{\text{sw}}$ on $\delta^{18}\text{O}_{\text{calcite}}$, there exists a well established temperature dependent fractionation of oxygen isotopes between H_2O and CaCO_3 [Zeebe and Wolf-Gladrow, 2001]. Unifying these two factors leads to the prediction of a relationship between $\delta^{18}\text{O}_{\text{calcite}}$, the calcification temp (T_{calc}) and $\delta^{18}\text{O}_{\text{sw}}$ which dates back to the work of Harold Urey and constitutes the most well used of all paleoceanographic proxy systems. The first experimental determination of this relationship, known as the ‘isotopic paleotemperature equation’, was undertaken

in the 1950s and is normally given in the form of equation A1.2, where both $\delta^{18}\text{O}_{\text{calcite}}$ and $\delta^{18}\text{O}_{\text{sw}}$ are on the VPDB scale. All the $\delta^{18}\text{O}_{\text{sw}}$ values presented in this thesis are derived from this equation and are hence also presented on the VPDB scale. For seawater measurements of $\delta^{18}\text{O}_{\text{sw}}$, the reference is generally that of Vienna Standard Mean Ocean Water (VSMOW), but these may be linearly ‘converted’ into the VPDB reference frame, using equation A1.3 [Hut, 1987].

$$\text{Equation A1.2} \quad T_{\text{calc}} = a + b(\delta^{18}\text{O}_{\text{calcite}} - \delta^{18}\text{O}_{\text{sw}}) + c(\delta^{18}\text{O}_{\text{calcite}} - \delta^{18}\text{O}_{\text{sw}})^2$$

$$\text{Equation A1.3} \quad \delta^{18}\text{O}_{\text{sw(VPDB)}} = \delta^{18}\text{O}_{\text{sw(SMOW)}} - 0.27$$

The three empirical constants a , b and c in equation A1.2 are only weakly dependent on the taxa and size fraction used and the magnitude of c is very small compared to those of a and b such that the equation is often made linear [Bemis *et al.*, 1998]. Crucially the sensitivity of $\delta^{18}\text{O}_{\text{calcite}}$ to changes in T_{calc} (i.e. the magnitude of b) is of the order of 0.2‰/°C. The analytical precision for measurements of $\delta^{18}\text{O}_{\text{calcite}}$ is generally less than 0.1‰, meaning that changes in T_{calc} of ~0.5°C are potentially resolvable with the method if $\delta^{18}\text{O}_{\text{sw}}$ is known. However, constant $\delta^{18}\text{O}_{\text{sw}}$ cannot be safely assumed on most paleoceanographic time-scales.

Variability in $\delta^{18}\text{O}_{\text{sw}}$ at a given location is controlled both by fluctuations in the local and regional hydrological cycle, due ultimately to the mass dependent fractionation of oxygen during precipitation and evaporation, and by global fluctuations in $\delta^{18}\text{O}_{\text{sw}}$. The latter effect is highly significant on glacial/interglacial time-scales with the waxing and waning of large ice-sheets which store significant amounts of water enriched in the light ^{16}O isotope. This effect is clearly closely coupled to global sea-level fluctuations such that the sensitivity of $\delta^{18}\text{O}_{\text{calcite}}$ to changes in sea-level is of the order of -0.01‰/m. On time-scales exceeding that of deep ocean mixing (i.e. > ~1kyr), the global-ice volume contribution to $\delta^{18}\text{O}_{\text{calcite}}$ variability should be spatially homogenous, providing the basis for the use of such measurements as a stratigraphic correlation tool.

The relationship between $\delta^{18}\text{O}_{\text{sw}}$ and salinity is nearly linear on the regional scale, but across the globe the values of the slope of this relationship range from 0.2 to 1.0 ‰, with the tropical Pacific values lying towards the lower end [*LeGrande and Schmidt, 2006*]. Thus, the sensitivity of $\delta^{18}\text{O}_{\text{calcite}}$ to plausible salinity fluctuations arising from regional hydrological cycle fluctuations on the glacial/interglacial time-scale is of the order of 0.1‰, an order of magnitude smaller than both the ice-sheet and temperature contributions. However, regional hydrological cycle induced changes in the $\delta^{18}\text{O}_{\text{calcite}}$ signal may still be detectable in regions with dynamic hydrological systems, provided that careful assumptions are made to remove the other effects. .

An additional complexity in the $\delta^{18}\text{O}$ proxy system arises from the fact that oxygen isotopes also exhibit fractionation between different DIC species within seawater. The relative abundances of these species are a function of seawater pH, which in turn relates to $[\text{CO}_3^{2-}]$, such that $\delta^{18}\text{O}_{\text{calcite}}$ also depends on $[\text{CO}_3^{2-}]$ [*Zeebe and Wolf-Gladrow, 2001*]. The strength of this effect is of the order of -0.002 ‰/($\mu\text{mol}/\text{kg}$) [*Spero et al., 1997*] however, meaning that glacial/interglacial shifts in mean ocean alkalinity of $\sim 100 \mu\text{mol}/\text{kg}$ could potentially account for only $\sim 0.2\%$ of the change in $\delta^{18}\text{O}_{\text{calcite}}$. The carbonate chemistry control is thus relatively modest and is generally neglected in glacial/interglacial time-scale paleoceanographic reconstructions.

The dominant controls on $\delta^{18}\text{O}_{\text{calcite}}$ on the glacial/interglacial time-scale are local T_{calc} and global ice-volume fluctuations, except in areas with very strong regional hydrological cycle responses. Both of these two main effects act in the same direction, such that during glacial stages, which are both colder and associated with greater global ice-volume, have relatively enriched (positive) $\delta^{18}\text{O}_{\text{calcite}}$ signatures compared to interglacial stages. The great advantages of the $\delta^{18}\text{O}_{\text{calcite}}$ proxy are its relative ease of measurement and the high signal / analytical error ratio (generally > 10) on the glacial/interglacial time-scale. However, the known significance of two semi-independent environmental controls provides a serious limitation to its use as a quantitative reconstructive proxy for past temperature (or indeed ice-volume)

variability. One approach to minimize this effect is to use the $\delta^{18}\text{O}$ records of benthic foraminifera ($\delta^{18}\text{O}_{\text{benthic}}$) as a guide to global ice-volume variability, based on the assumptions that the fluctuations in DWT, unlike SST, on these time-scales are relatively small. An additional refinement is the used of “stacked” $\delta^{18}\text{O}_{\text{benthic}}$ records, such as the SPECMAP project [Imbrie and Imbrie, 1980] or the LR04 stack [Lisiecki and Raymo, 2005] which, through spatial averaging, may act to further remove any DWT signal. However, work over the past decade has demonstrated that the effect of DWT on $\delta^{18}\text{O}_{\text{benthic}}$ is also more significant than previously assumed and that it is variable on a basin scale [Shackleton, 2000; Skinner and Shackleton, 2005; Lisiecki and Raymo, 2009]. Thus, whilst $\delta^{18}\text{O}_{\text{calcite}}$ measurements remain the workhorse of modern paleoceanography, both as a paleotemperature proxy and as a stratigraphic correlation tool in the creation of core-age models, there remain considerable assumptions and uncertainties inherent in both techniques.

A1.2 Stable carbon isotopes in foraminiferal calcite

Carbon has only two stable isotopes ^{13}C (relative abundance, 1.1%) and ^{12}C (98.9%). The $\delta^{13}\text{C}$ notation is defined analogously to $\delta^{18}\text{O}$ (equation A1.1) and $\delta^{13}\text{C}_{\text{calcite}}$ measurements are also quoted relative to VPDB. As a proxy system, $\delta^{13}\text{C}$ in foraminiferal calcite possesses certain similarities, but also many very important differences to that of $\delta^{18}\text{O}_{\text{calcite}}$. The similarities arise from the fact that the origin of the carbon atoms in the biogenic calcite, as for the oxygen ones, is from DIC species in seawater. Unlike for oxygen, however, very little temperature dependant fraction occurs during calcification [Zeebe and Wolf-Gladrow, 2001], meaning that $\delta^{13}\text{C}_{\text{calcite}}$ is primarily sensitive to the isotopic composition of the DIC species ($\delta^{13}\text{C}_{\text{DIC}}$), but not to changes in T_{calc} .

Were it the case that $\delta^{13}\text{C}_{\text{DIC}}$ variability at a given water depth and location was dominated by a single process on a given time-scale, then the $\delta^{13}\text{C}_{\text{calcite}}$ proxy should in principle be simpler to interpret than $\delta^{18}\text{O}$. This is not the case as, unlike $\delta^{18}\text{O}_{\text{sw}}$, $\delta^{13}\text{C}_{\text{DIC}}$ is strongly influence by biological processes through the carbon isotope fractionation occurring during photosynthesis and the formation of organic

matter. This means that, unlike temperature, salinity and $\delta^{18}\text{O}_{\text{sw}}$, $\delta^{13}\text{C}_{\text{DIC}}$ cannot be viewed as a “conservative” water-mass proxy. Within the upper-ocean, where photosynthesis occurs, the biological effects dominate the fluctuations in $\delta^{13}\text{C}_{\text{DIC}}$ on most time-scales, meaning that paleoceanographic $\delta^{13}\text{C}_{\text{planktic}}$ records tend to be very noisy and very difficult to interpret. Indeed, the $\delta^{13}\text{C}_{\text{planktic}}$ record for the sediment core considered in this thesis is presented for reference only (appendices 4 and 6) and is not discussed in detail.

In areas without very large systematic fluctuations in overlying primary productivity on the time-scales of interest, the $\delta^{13}\text{C}_{\text{DIC}}$ of deep water masses may, however, behave as a pseudo-conservative tracer of water mass origin. This effect arises through the differences in the $\delta^{13}\text{C}_{\text{DIC}}$ signatures of the surface waters in the areas of deep water formation, which is then retained within the deep water mass. Given that modern deep water formation occurs only in a few locations, which are characterized by very different surface ocean $\delta^{13}\text{C}_{\text{DIC}}$ values, namely the North Atlantic and parts of the Southern Ocean, measurements of $\delta^{13}\text{C}_{\text{benthic}}$ may potentially be used to identify the relative influences of such water masses [*Charles and Fairbanks, 1992*]. The biological effect also remains important for deep water masses through the “aging-effect” caused by the progressive addition of isotopically light, remineralized organic carbon from the upper-ocean into the deep waters. This has the effect of progressively lightening the $\delta^{13}\text{C}_{\text{DIC}}$ values as a function of cumulative overlying productivity, which relates both to the rate of flow of the deep water mass and on the productivity regime itself.

The sensitivity of $\delta^{13}\text{C}_{\text{DIC}}$ to changes in $[\text{CO}_3^{2-}]$ is much greater than that for $\delta^{18}\text{O}_{\text{sw}}$, to the extent that a significant fraction of measured glacial/interglacial $\delta^{13}\text{C}_{\text{calcite}}$ change may represent shifts in $[\text{CO}_3^{2-}]$ and whole ocean alkalinity [*Spero et al., 1997*]. Because changes in $[\text{CO}_3^{2-}]$ are broadly inversely correlated to shifts in atmospheric pCO_2 , it follows that mean-ocean changes in $\delta^{13}\text{C}_{\text{DIC}}$ also relate to changes in atmospheric pCO_2 . Stable carbon isotopes, particularly as measured in benthic foraminifera, therefore have the potential to yield information about water mass origin and ventilation rate, primary productivity and ocean/atmosphere carbon

chemistry. They are thus a highly valuable and versatile proxy system, but the multiple and spatially variable nature of the controlling factors means that very great care is required in their interpretation.

A1.3 Mg/Ca ratios in foraminiferal calcite

Of all the conservative properties of seawater few, if any, is as important for our understanding of global climate as the temperature of the water mass. As was discussed above, measurements of $\delta^{18}\text{O}_{\text{calcite}}$ are sensitive to changes in T_{calc} , but the additional and co-varying control from $\delta^{18}\text{O}_{\text{sw}}$ means that quantification of temperature changes using that system alone is rendered difficult. Thus, a major goal in paleoceanography over the past two decades has been the development of alternative, quantitative proxies for T_{calc} . One such technique involves measurement of the Mg/Ca ratio within foraminiferal calcite. The principle that the incorporation of Group II metals other than calcium into the biogenic calcite lattice may be temperature dependent was suggested as early as the 1950s [*Chave, 1954*], but paleoceanographic calibrations of the proxy have only become available from the mid 1990s onwards [*Nurnberg et al., 1996; Elderfield and Ganssen, 2000*]. One very great attraction of an ‘inorganic’ paleothermometer, such as Mg/Ca, is that coupled measurements of $\delta^{18}\text{O}$ and Mg/Ca may be made on the same material allowing quantification of two of the three variables in equation A1.2 and hence the calculation of $\delta^{18}\text{O}_{\text{sw}}$. The form of the relationship between Mg/Ca and T_{calc} is empirically determined to be exponential, as shown in equation A1.4.

Equation A1.4
$$\text{Mg} / \text{Ca} = ae^{bT_{\text{calc}}}$$

(Mg/Ca is given in units of mmol/mol and a and b are the pre-exponential and exponential calibration coefficients respectively)

Most calibrations for planktic foraminifera yield a value for b of ~ 0.1 , meaning that the sensitivity of Mg/Ca to changes in T_{calc} is $\sim 10\%/^{\circ}\text{C}$. Standard error propagation formulae mean that the error on T_{calc} , $\sigma_{(T_{\text{calc}})}$, resulting from the error on Mg/Ca, $\sigma_{(\text{Mg/Ca})}$, is as given in equation A1.5.

$$\text{Equation A1.5} \quad \sigma_{(T_{\text{calc}})} = \sigma_{(\text{Mg/Ca})} / b(\text{Mg/Ca})$$

The form of this equation means that the error in T_{calc} increases with decreasing Mg/Ca (or indeed temperature itself) and also that the value and uncertainty of the exponential constant b is also important in the T_{calc} error. Given that planktic foraminiferal Mg/Ca values generally lie within the range 1-5 mmol/mol and analytical precision for measurements (which are principally achieved via Inductively Coupled Plasma – Optical Emission Spectroscopy, ICP-OES) is better than 0.1mmol/mol, it follows that the Mg/Ca system offers the potential to resolve T_{calc} differences of the order of 0.2°C . In reality, however, the sample reproducibility error tends to greatly exceed this analytical error, as is discussed in the case of the MD06-3018 measurements in chapter 4, §3.1.

A wide range of calibration curves now exist for the planktic Mg/Ca proxy system, based on sediment trap [Anand *et al.*, 2003; McConnell and Thunell, 2005], core-top [Elderfield and Ganssen, 2000; Lea *et al.*, 2000] and culture [Kisakurek *et al.*, 2008] studies. All support the general form of equation A1.4 but provide differing estimate of the values for a and b . The pre-exponential constant in particular varies significantly as a function of taxa, size fraction and cleaning methodology used. The uncertainty on T_{calc} arising from the calibration uncertainties in a and b is of the order of several $^{\circ}\text{C}$, meaning that the relative error in down-core temperature reconstructions is always much less than that for single absolute value temperature reconstructions, or the comparison between reconstructions made on different calibrations. A much more limited number of benthic foraminiferal calibrations exist [Marchitto *et al.*, 2007; Elderfield *et al.*, 2010], potentially allowing the reconstruction of DWT and the separation of this from the global ice-volume contribution to $\delta^{18}\text{O}_{\text{benthic}}$ [Sosdian and Rosenthal, 2009].

As with all proxies, other environmental factors exert secondary controls on the recorded Mg/Ca ratios. At present the most important such controls are thought to be exerted by salinity and $[\text{CO}_3^{2-}]$ [Kisakurek *et al.*, 2008; Sadekov *et al.*, 2008]. The proposed salinity control varies widely between calibration studies but potentially implies that some form of correction is required before coupled $\delta^{18}\text{O}$ -Mg/Ca measurements may be used to resolve the isotopic paleotemperature equation [Mathien-Blard and Bassinot, 2009]. Furthermore, calcite dissolution has been shown to preferentially remove Mg-enriched material from the tests meaning that empirical corrections are required for core-sites affected by dissolution [Dekens *et al.*, 2002]. A final uncertainty stems from the tacit assumption in equation A1.3 that the Mg/Ca ratio of the surrounding seawater ($\text{Mg}/\text{Ca}_{(\text{sw})}$) remains constant on the time-scale of interest. Unlike for $\delta^{18}\text{O}_{\text{sw}}$, this assumption is reasonable on glacial/interglacial timescales given the relatively long residence times of Mg and Ca in the ocean. However, modelling studies suggest that this may not be the case on longer (i.e. >100kyr) time-scales [Fantle and DePaolo, 2005, 2006] and that reconstructions beyond the past ~1000ka in particular may need to be corrected for the evolution of $\text{Mg}/\text{Ca}_{(\text{sw})}$ [Medina-Elizalde *et al.*, 2008]. The effect of these factors on the combined proxy uncertainty is discussed in chapter 4.

At present, Mg/Ca paleothermometry is the most established tool for reconstructing T_{calc} from planktonic marine carbonates. The method offers a high signal/analytical error ratio (generally >20) and, whilst significantly more complex than stable isotope analysis, a relatively simple sample preparation protocol. However, the proxy remains relatively ‘young’ compared to the stable isotope methods and is the subject of much ongoing work to better constrain both the non-temperature related factors affecting the system as well as intra- and inter-test variability [Barker *et al.*, 2005; Sadekov *et al.*, 2008].

Appendix 2: Laboratory method, ICP-OES settings, calibration standards, reference materials and sample rejection criteria used for trace-metal analysis

A2.1 Trace metal sample preparation methodology

The following method is based closely on the non-reductive ('Mg/Ca') method outlined in *Barker et al.*, 2003. Comparison of ICP measured sample calcium concentrations to initial, un-cleaned, sample weights, suggests a cumulative mass loss of 40-60% during trace metal cleaning. All work was undertaken in clean box, except for initial picking (normal lab conditions) and the preparation of reagents (blank acid, leach acid, oxidising solution) which was undertaken in a trace-metal clean lab. The blank/dissolution acids were stored in acid-cleaned Teflon bottles and other reagents were stored in acid-cleaned PPE bottles. The micro-centrifuge vials used were PPE (VWR Brand). 'Acid-cleaning' of plastics involved at least 3 days on a hot plate in both Mucasol detergent and then 1M trace-metal grade HNO₃, followed by rinsing in milli-Q water.

Initial preparation stage (each sample handled individually)

- 35-40 *G. ruber* (*G. ruber ruber* morphotype, as discussed in chapter 4, §3.1) were picked from the 250-315µm size fraction
- Samples crushed under glass plates and transferred to acid cleaned 500µL micro-centrifuge vials.
- 3 * 1min rinse in de-ionised water (all rinse steps follow the *Barker et al.*, 2003 methodology)
- 2 * 1min rinse in methanol
- 2 * rinse with de-ionised water
- Checked for contaminant grains under the microscope

Oxidative cleaning stage (samples handled in batches of 20-30)

- Oxidization of organic matter achieved through: 10mins in $>80^{\circ}\text{C}$ water bath with $250\mu\text{L}$ $\text{H}_2\text{O}_2/\text{NaOH}$ solution, ultrasonicated briefly after 5mins
- Oxidizing solution replaced and repeated
- 2 * rinse with milli-Q water, including vial caps

Acid leaching stage (each sample handled individually)

- 20s ultrasonic bath with $250\mu\text{L}$ 0.001M HNO_3 , prepared from dilution of the blank acid
- Rapid replacement with milli-Q water
- 2 * rinse with milli-Q water
- Removal of all remaining supernatant
- Samples checked under microscope for any contamination introduced during cleaning

Dissolution stage (samples handled in batches of 20-30)

- $500\mu\text{L}$ of 0.1M HNO_3 added (blank acid) to sample and ultrasonicated till fully dissolved ($\sim 10\text{mins}$)
- Centrifuged for 10mins at 6000rpm
- Transfer top $450\mu\text{L}$ to acid cleaned fresh vial
- Take $50\mu\text{L}$ for pilot sample with $450\mu\text{L}$ of blank acid (pilot sample prepared in new but un-cleaned micro-centrifuge tube)
- Dilute remaining sample to 60ppm Ca and analyse (final sample prepared in fresh acid cleaned micro-centrifuge tube)

A2.2 Operating conditions for the Varian VISTA (Axial) ICP-OES

EM coil power	1.2	kW
Plasma Ar Flow	15	L/min
Auxiliary Ar Flow	1.5	L/min
Nebulizer Ar Flow	0.85	L/min
Peristaltic pump rate	37	rpm
Stabilisation time	15	s
Uptake delay	30	s
Replicates per sample	5	
Integration time per replicate	6	s

The peristaltic pump rate was chosen such that the delivery rate of sample to the micro-mist nebulizer used was $\sim 400\mu\text{L}/\text{min}$ (derived using calculation offered online by Glass-Expansion Ltd). The uptake delay was determined empirically. Choice of EM coil power and gas flow rates follows *de Villiers et al.* [2002].

A2.3 Choice of ICP-OES spectral lines

The following spectral lines were measured for each sample and standard solution:

- Ca: 315.887 and 317.933 nm
- Mg: 280.270 and 285.213 nm
- Sr: 421.104 nm
- Al: 396.152 nm
- Fe: 238.204 nm
- Mn: 294.291 nm

The Mg₂₈₀/Ca₃₁₅ ratio was selected for the Mg/Ca intensity ratio calibration, as although Mg₂₈₅ is somewhat less sensitive to the Ca matrix effect [*de Villiers et al.*, 2002], the present study yielded significantly better long-term machine stability for Mg₂₈₀. However, the difference in calculated Mg/Ca (for measurements at [Ca]=60ppm) arising from choice of line was less than 0.01 mmol/mol for samples in the ratio range (3 – 6 mmol/mol) investigated here.

A2.4 Trace-metal analysis calibration standards

Three sets of standards were used. The first was based on ten dilutions of carbonate reference material ECRM-521 to standard Ca concentrations in the range 1 – 200ppm. These standards were used only to ascertain the [Ca] in the samples. The six calibration standards were made up gravimetrically from commercially available single element solutions of Ca, Mg and Sr (at 1000ppm) to [Ca]=60ppm but with varying Mg/Ca and Sr/Ca ratios in the range 1 -10 mmol/mol and 0.8 -1.5 mmol/mol respectively. This set of standards is now the in-house Edinburgh Mg/Ca calibration set and was cross-calibrated to material provided by Cambridge University ($r^2=0.998$) to ensure inter-laboratory precision.

Mg/Ca and Sr/Ca ratios were then calculated using the intensity-ratio calibration method which has the effect of minimizing the Ca matrix effect [*de Villiers et al.*, 2002]. The final standard set comprises dilutions of a commercially available multi-element ICP standard solution and was used to measure [Al], [Fe] and [Mn] in the range 0.01-0.50ppm. Fe/Mg ratios were calculated from [Fe] and [Mg] rather than an intensity ratio calibration. In general, Al and Mn concentrations were close to the machine detection limits, meaning that contamination based on these elements was identified by intensities significantly ($>3\sigma$) above the background levels, rather than concentration or ratio based criteria. All standards were stored in 30ml acid-cleaned PPE bottles during the period of analysis. To minimize any matrix effect arising from the acid, all standard dilutions were made with 0.1M HNO₃, the same blank acid as used for the samples.

A2.5 Trace-metal reference materials and long-term reproducibility

Two reference materials were used. The first was based on solid-state carbonate reference material ECRM-521 which was dissolved in 0.1M HNO₃, the same acid as used for sample blanks and standard dilutions, centrifuged and stored at 1000ppm [Ca] in an acid-cleaned Teflon bottle. Dilutions of this material to 60ppm [Ca] were made prior into an acid-cleaned PPE bottle prior to analysis. This material was measured prior to the beginning of each run, in-between every six samples (including pilot samples) and at the end of each run. Samples were analyzed using the Varian VISTA Pro ICP-OES (Axial) in the School of Geosciences, University of Edinburgh. Over the period of analysis (May 2009 to November 2009) the following long-term average values and standard deviations, based on 166 measurements of ECRM-521, were found (all units are mmol/mol):

Mg/Ca	1 σ_a	Sr/Ca	1 σ_a	Al/Ca	1 σ_a	Fe/Ca	1 σ_a	Mn/Ca	1 σ_a
3.7626	0.0176	0.1636	0.0069	0.4507	0.0356	0.0939	0.0078	0.1335	0.0054

These values are highly consistent with previous characterization and inter-laboratory comparison studies on this reference material [*Greaves et al.*, 2005; *Greaves et al.*, 2008]. An in-house check solution was prepared gravimetrically from single element solutions to [Ca]=60ppm and Mg/Ca=4.10mmol/mol and stored in a single acid-cleaned Teflon bottle. This solution was measured twice per run (post-calibration and at the end of analysis) to monitor for any inter-run drift in the values found for ECRM-521 that might have arisen from bottle contamination of the reference material.

A2.6 Trace-metal sample rejection criteria

Samples were rejected if they fulfilled any of the following criteria:

- [Ca] in final sample <30ppm or >90ppm
- Fe/Mg ratio > 1 mol/mol
- Intensities of Al or Mn >3 σ above the running average level
- Sample repeated $n \geq 3$ times and one value significantly discrepant from the others (probable contamination of sample vial)

Where multiple samples from the same depth remained un-rejected, these values were averaged to give the presented value.

Appendix 3: Laboratory method, reference materials and sample rejection criteria used for stable isotope analysis

A3.1 Stable isotope sample preparation methodology

Initial preparation stage (each sample handled individually)

- 12-15 *G. ruber* (*G. ruber ruber* morphotype, as discussed in chapter 4, §3.1) individuals were picked from the 250-315 μm size fraction
- 3-6 *C. wuellerstorfi* individuals were picked from the >315 μm size fraction

Cleaning stage (each sample handled individually)

- Samples were ultrasonicated in methanol for 5-10s with tests unbroken
- The majority of the supernatant was lifted off with a pipette before samples being left to dry under a flow hood
- Samples were returned to the microscope and screened for contamination prior to transfer to glass mass spec vials

Comparison of measured individual shell weights pre and post cleaning suggests a cumulative mass loss of 5-10% during stable isotope cleaning, presumed to arise principally from the removal of surficial coccolith material from the tests (see *Figure 2.5*).

A3.2 Stable isotope reference materials and long-term reproducibility

Samples were analyzed with a Thermo Electron Delta+ Mass Spectrometer with Kiel Preparation Device in the School of GeoSciences, University of Edinburgh for both $\delta^{18}\text{O}_{\text{calcite}}$ and $\delta^{13}\text{C}_{\text{calcite}}$. Long term accuracy (against one internal standard calibrated to NBS19 and an in-house reference material) of the device over the period of analysis (May 2006 to October 2008) was $1\sigma_{\text{a}}=0.09\text{‰}$ for $\delta^{18}\text{O}$ and $1\sigma_{\text{a}}=0.08\text{‰}$ for $\delta^{13}\text{C}$.

A3.3 Stable isotope sample rejection criteria

Samples were rejected if, after being repeated $n \geq 3$ times, one value was significantly discrepant from the others (probable contamination of sample vial). Where multiple samples from the same depth remained un-rejected, these values were averaged to give the presented value.

Appendix 4: Down-core MD06-3018 stable isotope and trace-metal data

Data includes correction to *G. ruber* $\delta^{13}\text{C}_{\text{planktic}}$ of +0.94‰ [Spero *et al.*, 2003] and to *C. wuellerstorfi* $\delta^{18}\text{O}_{\text{benthic}}$ of +0.64‰ [Shackleton and Opdyke, 1973]. ‘N/A’ indicates no measurement made/accepted. In the age model column, ‘*’ indicates the disturbed interval of sedimentation, as discussed in chapter 2, §11 and chapter 3, §7.

Depth in core (Raw)	Depth in core (CCD)	Age model	$\delta^{18}\text{O}_{\text{planktic}}$	$\delta^{13}\text{C}_{\text{planktic}}$ (corrected)	$\delta^{18}\text{O}_{\text{benthic}}$ (corrected)	$\delta^{13}\text{C}_{\text{benthic}}$	Mg/Ca	Sr/Ca
cm	cm	ka	‰	‰	‰	‰	mmol/mol	mmol/mol
0	0	0.0	-1.201	1.694	3.385	0.539	4.6003	N/A
5	5	1.5	N/A	N/A	N/A	N/A	4.4960	1.5050
10	10	2.9	-1.257	1.530	3.228	0.739	4.6535	N/A
15	15	4.4	N/A	N/A	N/A	N/A	4.7406	1.4852
20	20	5.8	-1.247	2.425	3.143	0.942	4.7910	N/A
25	25	7.2	N/A	N/A	N/A	N/A	4.7495	1.5021
30	30	8.7	-0.743	1.606	4.021	0.804	4.3911	1.4753
35	35	10.1	N/A	N/A	N/A	N/A	4.4363	1.4691
40	40	11.6	-0.972	1.184	3.725	-0.021	4.7101	1.4741
45	45	13.0	N/A	N/A	N/A	N/A	4.3926	1.4625
50	50	14.5	-0.623	1.395	4.520	-0.022	4.4396	1.4602
55	55	15.9	N/A	N/A	N/A	N/A	4.2025	1.4506
60	60	17.4	-0.199	1.065	4.594	0.044	4.3339	1.4664
65	65	18.8	N/A	N/A	N/A	N/A	4.1934	1.4386
70	70	20.3	-0.226	1.456	4.746	0.129	3.7855	N/A
75	75	22.7	N/A	N/A	N/A	N/A	3.5279	1.4205
80	80	25.2	-0.156	1.034	4.871	0.132	4.0286	1.4360
85	85	27.7	-0.051	0.318	N/A	N/A	N/A	N/A
90	90	30.3	-0.290	1.743	4.652	0.373	3.5552	1.4171
100	100	35.5	-0.303	1.561	4.587	0.361	3.9804	1.4571
110	110	40.6	-0.203	1.832	4.349	0.298	3.7014	1.4454
120	120	45.8	-0.116	1.538	4.586	0.479	3.5150	1.4234
130	130	50.9	-0.199	1.630	4.480	0.604	3.6947	1.4418
140	140	56.1	-0.428	1.772	4.117	0.566	3.8787	1.4209
150	150	61.2	-0.149	1.625	4.564	0.366	3.8757	1.4218
160	160	66.3	-0.312	1.349	4.637	0.193	3.7671	1.4227
170	170	71.0	-0.666	1.406	4.551	0.315	3.3129	1.4156
180	180	75.8	-0.474	2.003	4.151	0.585	3.5291	N/A
190	190	80.6	-0.726	1.384	4.186	0.320	3.7625	1.4106
200	200	85.3	-0.771	1.487	4.159	0.409	3.7922	1.4171
210	210	90.1	-0.472	1.527	3.889	0.533	3.4820	1.4197
220	220	94.9	-0.695	1.666	4.056	0.519	3.7988	1.4445
230	230	99.6	-0.547	1.656	3.884	0.437	3.9304	1.4195
240	240	104.4	-0.799	1.510	4.009	0.260	3.9425	1.4504

Depth in core (Raw)	Depth in core (CCD)	Age model	$\delta^{18}\text{O}_{\text{planktic}}$	$\delta^{13}\text{C}_{\text{planktic}}$ (corrected)	$\delta^{18}\text{O}_{\text{benthic}}$ (corrected)	$\delta^{13}\text{C}_{\text{benthic}}$	Mg/Ca	Sr/Ca
cm	cm	ka	‰	‰	‰	‰	mmol/mol	mmol/mol
250	250	109.4	-0.925	1.505	4.191	0.369	4.3402	N/A
260	260	115.0	-0.794	1.573	3.592	0.448	4.6245	1.4605
265	265	117.7	-1.261	0.896	3.856	0.447	4.3947	1.4533
270	270	120.5	-1.033	1.877	N/A	N/A	4.6082	1.4474
275	275	123.3	N/A	N/A	3.775	0.488	N/A	N/A
280	280	126.1	-0.686	1.579	3.571	0.447	4.6155	1.4791
290	290	131.6	-0.805	1.775	4.254	0.171	4.7439	1.4734
300	300	134.0	-0.448	1.013	4.605	0.024	4.1885	1.4569
305	305	135.2	N/A	N/A	N/A	N/A	4.6084	1.4707
310	310	136.4	-0.119	1.569	4.776	0.104	3.9230	1.4517
320	320	138.9	0.056	1.403	4.849	-0.188	3.8201	1.4319
330	330	142.2	-0.302	1.275	4.971	-0.044	3.9597	1.4259
340	340	147.7	0.077	1.325	4.664	-0.222	3.7377	1.4285
345	345	150.4	0.147	0.620	N/A	N/A	N/A	N/A
350	350	153.2	-0.220	1.082	4.641	0.050	4.0697	N/A
360	360	158.7	-0.078	1.218	4.908	-0.109	3.6155	N/A
370	370	164.2	-0.437	0.956	4.581	0.049	3.7924	N/A
380	380	169.7	-0.120	1.578	4.482	-0.001	3.4425	N/A
390	390	175.2	-0.474	0.752	4.621	-0.051	3.7521	N/A
400	400	180.7	-0.132	1.552	4.239	-0.071	3.6936	N/A
410	410	186.2	-0.259	1.642	4.678	0.069	3.4613	N/A
420	420	190.2	-0.772	1.516	4.092	-0.115	3.4428	N/A
430	430	193.9	-0.787	1.999	4.335	0.189	3.5073	N/A
440	440	197.6	-0.745	1.715	3.957	0.418	3.9310	N/A
450	450	201.4	-0.817	1.658	3.863	0.390	3.9023	1.4380
460	460	205.1	-0.996	1.683	3.829	0.421	4.0317	N/A
470	470	208.8	-0.685	1.656	3.950	0.418	4.2246	N/A
480	480	212.5	-0.438	1.776	3.719	0.566	4.2775	N/A
490	490	215.8	-0.581	1.261	3.673	0.397	4.4305	N/A
500	500	218.7	-0.721	0.844	4.172	0.080	4.3721	N/A
510	510	221.6	-0.279	1.196	4.254	0.158	3.7906	N/A
520	520	231.1	-0.438	1.714	4.290	0.163	3.9178	N/A
530	530	240.5	-0.663	1.393	4.066	0.169	4.1384	N/A
540	540	246.9	-0.466	1.683	4.519	0.159	4.4816	N/A
550	550	253.3	-0.170	1.305	4.432	0.090	4.0746	N/A
560	560	259.7	-0.293	1.177	4.440	-0.055	3.7738	N/A
570	570	266.1	0.022	1.707	4.585	-0.058	3.5335	1.4597
580	580	271.9	0.355	1.910	4.692	-0.041	3.8214	N/A
590	590	274.2	0.170	1.665	4.590	-0.013	3.9618	N/A
600	600	276.4	-0.023	1.578	4.222	-0.008	3.6798	N/A
610	610	278.7	-0.235	2.089	4.388	0.561	3.5506	N/A
620	620	281.0	-0.194	1.541	4.277	0.379	3.6185	N/A

Depth in core (Raw)	Depth in core (CCD)	Age model	$\delta^{18}\text{O}_{\text{planktic}}$	$\delta^{13}\text{C}_{\text{planktic}}$ (corrected)	$\delta^{18}\text{O}_{\text{benthic}}$ (corrected)	$\delta^{13}\text{C}_{\text{benthic}}$	Mg/Ca	Sr/Ca
cm	cm	ka	‰	‰	‰	‰	mmol/mol	mmol/mol
630	630	283.3	-0.404	1.911	4.014	0.752	3.9673	N/A
640	640	286.0	-0.258	1.934	3.776	0.493	4.0687	N/A
650	650	290.8	-0.204	1.475	4.478	0.165	3.8642	N/A
660	660	295.6	-0.253	1.728	4.297	0.234	3.4476	1.4026
670	670	300.4	-0.489	1.858	4.389	0.225	3.8392	N/A
680	680	305.1	-0.272	1.837	4.275	0.300	3.9884	N/A
690	690	309.9	-0.631	1.641	3.955	0.414	3.9552	N/A
700	700	314.7	-0.633	1.530	3.651	0.219	3.7608	N/A
710	710	319.5	-0.800	1.500	3.737	0.294	4.1696	N/A
720	720	324.3	-0.694	1.868	3.708	0.450	4.2814	N/A
730	730	329.1	-0.970	1.743	3.617	0.330	4.4333	N/A
740	740	330.5	-0.962	1.818	3.831	0.387	4.5385	N/A
750	750	*	-0.493	1.552	4.147	0.259	N/A	N/A
760	760	*	0.173	1.760	3.619	0.696	N/A	N/A
770	770	*	-0.228	1.189	4.220	0.650	N/A	N/A
780	780	*	-0.174	1.194	4.570	0.374	N/A	N/A
790	790	*	-0.555	1.751	4.703	0.203	N/A	N/A
800	800	*	0.009	1.427	4.246	0.314	N/A	N/A
810	810	*	-0.545	1.577	4.359	0.320	N/A	N/A
820	820	*	-0.415	1.416	4.098	0.196	N/A	N/A
830	830	*	-0.325	1.680	4.313	0.233	N/A	N/A
840	840	*	-0.145	0.525	4.511	0.222	N/A	N/A
850	850	*	0.129	1.346	4.516	0.212	N/A	N/A
870	855	342.0	-0.389	1.745	4.064	0.366	4.5298	N/A
880	865	343.0	-0.091	1.955	4.287	0.228	4.5313	N/A
890	875	344.6	0.286	1.614	4.611	0.002	4.1051	1.4311
900	885	350.7	0.245	1.447	4.691	-0.059	3.8198	N/A
910	895	356.8	-0.053	1.306	4.591	-0.068	3.6429	N/A
920	905	363.0	-0.119	1.284	4.616	-0.107	3.3513	1.4269
930	915	369.1	-0.039	1.856	4.587	-0.121	3.6490	N/A
940	925	375.2	-0.238	1.893	4.115	0.315	3.2879	1.3948
950	935	381.3	-0.319	1.701	4.123	0.362	3.3122	1.4005
960	945	387.4	-0.713	1.717	4.026	0.343	3.4231	1.4061
970	955	393.6	-0.419	1.545	4.121	0.075	3.5839	N/A
980	965	399.7	-0.563	2.053	3.746	0.490	3.9931	N/A
990	975	405.7	-1.061	1.491	3.212	0.573	4.5912	N/A
1000	985	411.3	-1.090	1.693	3.339	0.565	4.5355	N/A
1005	990	414.0	N/A	N/A	N/A	N/A	4.4829	1.4295
1010	995	416.8	-0.905	1.476	3.515	0.873	4.4161	N/A
1015	1000	419.6	N/A	N/A	N/A	N/A	4.4072	1.4503
1020	1005	422.3	-0.372	0.858	4.001	0.571	4.1464	N/A
1025	1010	425.1	N/A	N/A	N/A	N/A	4.0766	1.4414

Depth in core (Raw)	Depth in core (CCD)	Age model	$\delta^{18}\text{O}_{\text{planktic}}$	$\delta^{13}\text{C}_{\text{planktic}}$ (corrected)	$\delta^{18}\text{O}_{\text{benthic}}$ (corrected)	$\delta^{13}\text{C}_{\text{benthic}}$	Mg/Ca	Sr/Ca
cm	cm	ka	‰	‰	‰	‰	mmol/mol	mmol/mol
1030	1015	427.9	0.171	1.355	4.618	0.075	3.9854	1.4518
1035	1020	430.6	N/A	N/A	N/A	N/A	3.7307	1.4309
1040	1025	433.4	0.711	1.593	4.961	0.027	3.7770	N/A
1050	1027	434.5	0.470	1.482	4.827	0.029	4.0800	1.4328
1055	1032	437.3	0.502	1.472	5.073	-0.277	3.7224	1.3978
1070	1037	440.0	0.389	1.649	4.613	-0.006	3.8182	N/A
1080	1047	445.5	0.112	1.619	4.869	-0.234	3.8886	N/A
1090	1057	451.0	0.127	1.693	4.724	-0.027	3.6350	N/A
1100	1067	456.5	0.183	1.268	4.421	0.053	3.7163	1.4137
1110	1077	462.0	0.263	1.770	4.385	0.035	3.3989	1.3953
1120	1087	467.5	-0.116	1.798	4.245	0.206	3.7791	1.3937
1130	1097	473.0	-0.299	1.346	4.646	0.093	3.5956	N/A
1140	1107	478.5	-0.687	1.562	3.864	0.468	3.6166	N/A
1150	1117	484.0	-0.803	1.450	3.808	0.558	3.6407	1.3929
1160	1127	489.9	-0.684	1.741	3.643	0.808	3.8139	1.4032
1170	1137	497.6	-0.453	1.956	3.817	0.743	3.8525	N/A
1180	1147	505.3	-0.474	1.804	3.578	0.778	3.8210	N/A
1190	1157	513.0	-0.365	1.709	4.056	0.902	3.5726	1.4062
1200	1167	520.7	-0.310	1.529	4.157	0.586	3.5112	1.4062
1210	1177	528.4	-0.288	1.156	4.093	0.526	3.9117	1.4159
1220	1187	536.1	-0.429	0.950	4.157	0.149	4.0000	N/A
1230	1197	543.7	-0.328	1.723	4.448	0.218	3.8805	1.4168
1240	1207	551.5	-0.628	1.144	4.483	0.028	3.5504	1.4047
1250	1217	559.5	-0.540	1.586	3.927	0.379	3.6448	1.3959
1260	1227	567.4	-0.755	1.373	3.863	0.432	4.0483	1.4261
1270	1237	575.5	-0.797	1.358	3.821	0.406	4.6189	1.4507
1280	1247	586.3	-0.875	1.251	3.891	0.283	4.3564	N/A
1290	1257	597.1	-0.728	0.853	4.250	0.082	4.3542	N/A
1300	1267	607.9	-0.758	1.657	3.884	0.202	4.5834	N/A
1310	1277	616.8	-1.003	1.166	3.911	0.421	4.2622	1.4262
1320	1287	623.0	-0.320	1.043	4.549	0.138	3.9634	1.4424
1330	1297	629.2	0.260	1.552	4.824	-0.090	3.7461	1.4385
1340	1307	639.3	-0.082	0.776	4.828	-0.033	3.7050	1.4112
1350	1317	651.7	-0.242	0.925	4.539	0.075	3.9447	1.4222
1360	1327	664.1	-0.004	1.419	4.353	-0.119	3.7149	1.3998
1370	1337	676.5	-0.634	0.821	4.225	0.083	3.7040	1.3936
1380	1347	688.9	-0.661	1.470	4.036	0.040	3.5742	1.3900
1390	1354	697.2	-0.873	1.408	3.819	0.416	4.0760	1.4126
1400	1364	703.6	-0.677	1.500	4.358	0.262	4.2101	1.4446
1410	1374	709.9	-0.363	1.153	4.132	0.380	4.1664	1.4288
1420	1384	716.2	-0.154	1.334	4.531	0.021	3.9974	1.4247
1430	1394	726.1	-0.358	1.001	4.542	-0.081	3.8669	1.4187

Depth in core (Raw)	Depth in core (CCD)	Age model	$\delta^{18}\text{O}_{\text{planktic}}$	$\delta^{13}\text{C}_{\text{planktic}}$ (corrected)	$\delta^{18}\text{O}_{\text{benthic}}$ (corrected)	$\delta^{13}\text{C}_{\text{benthic}}$	Mg/Ca	Sr/Ca
cm	cm	ka	‰	‰	‰	‰	mmol/mol	mmol/mol
1440	1404	740.2	-0.536	1.101	4.336	0.010	3.9279	1.4111
1450	1414	748.4	-0.173	1.256	4.549	-0.149	3.8880	1.3992
1460	1424	757.2	-0.205	1.626	4.371	-0.292	3.4599	1.3827
1470	1434	766.1	-0.015	1.900	4.150	0.110	3.8185	1.3916
1480	1444	774.9	-1.012	1.412	4.024	0.241	3.7754	1.4033
1490	1454	783.2	-0.683	1.763	3.925	0.182	4.0366	1.3889
1500	1464	786.9	-0.576	1.443	4.042	0.099	4.2395	1.4145
1510	1474	790.6	-0.221	0.789	4.087	-0.209	4.2362	1.4064
1520	1484	794.3	0.006	1.297	4.347	-0.207	3.9816	1.4256
1530	1494	798.0	-0.082	1.276	4.414	-0.100	3.9159	1.3939
1540	1504	808.7	-0.587	1.179	4.393	-0.096	3.8734	1.3944
1550	1514	819.9	-0.829	1.195	3.763	-0.002	4.0764	1.4134
1560	1524	831.1	-0.973	1.094	4.007	0.079	4.1279	1.4234
1570	1534	842.3	-0.779	1.219	3.780	0.123	4.0642	1.4209
1580	1544	853.5	-0.994	1.030	3.740	0.192	4.2565	1.4199
1590	1554	861.3	-0.761	0.902	3.816	0.153	4.3939	1.4394
1600	1564	867.1	-0.743	0.986	4.023	0.052	4.6048	1.4443
1605	1569	869.9	-0.238	1.363	N/A	N/A	4.4579	1.4428
1610	1574	872.8	-0.129	0.923	4.607	-0.042	3.8373	1.4347
1620	1584	880.2	0.035	1.028	4.632	-0.047	3.8247	1.4108
1630	1594	889.9	-0.117	1.531	4.435	-0.029	3.8682	1.4102
1640	1604	899.5	-0.469	1.031	4.439	0.061	4.0556	1.4590
1645	1609	904.4	-0.332	1.317	4.069	-0.260	N/A	N/A
1650	1614	909.2	-0.528	1.383	4.112	-0.269	4.0349	1.4282
1655	1619	914.0	N/A	N/A	4.238	-0.344	N/A	N/A
1660	1624	918.9	-0.134	1.013	4.203	0.032	4.0183	1.3853
1670	1634	928.5	-0.432	1.292	4.088	0.012	3.7894	1.4033
1680	1644	938.2	-0.746	1.254	3.901	0.109	4.2971	1.4028
1690	1654	947.8	-0.709	1.621	3.810	0.261	4.1508	1.4221
1700	1664	956.6	-0.768	1.686	3.573	0.321	4.2063	1.4220
1710	1674	962.5	-0.535	1.403	4.094	0.177	4.1065	1.4303
1720	1684	968.4	-0.152	1.865	4.324	0.206	3.6077	1.3951
1730	1694	974.2	-0.572	2.066	4.146	0.212	3.7075	1.4014
1740	1704	980.1	-0.358	2.027	4.037	0.312	3.8628	1.4175
1750	1714	985.9	-0.571	2.047	4.253	0.257	3.7006	1.3780
1760	1724	991.8	-0.504	1.650	4.108	0.338	3.7489	1.3937
1770	1734	997.6	-0.380	1.644	4.252	0.172	3.5888	1.3578
1780	1744	1003.5	-0.406	1.904	4.109	0.364	3.4747	1.4061
1790	1754	1009.3	-0.508	1.652	3.978	0.458	3.8677	1.4114
1800	1759	1012.3	-0.692	1.550	4.071	0.300	4.0196	1.4414
1805	1764	1015.2	-0.462	1.870	3.842	0.475	N/A	N/A
1810	1769	1018.1	-0.732	1.369	3.922	0.353	3.8708	1.4291

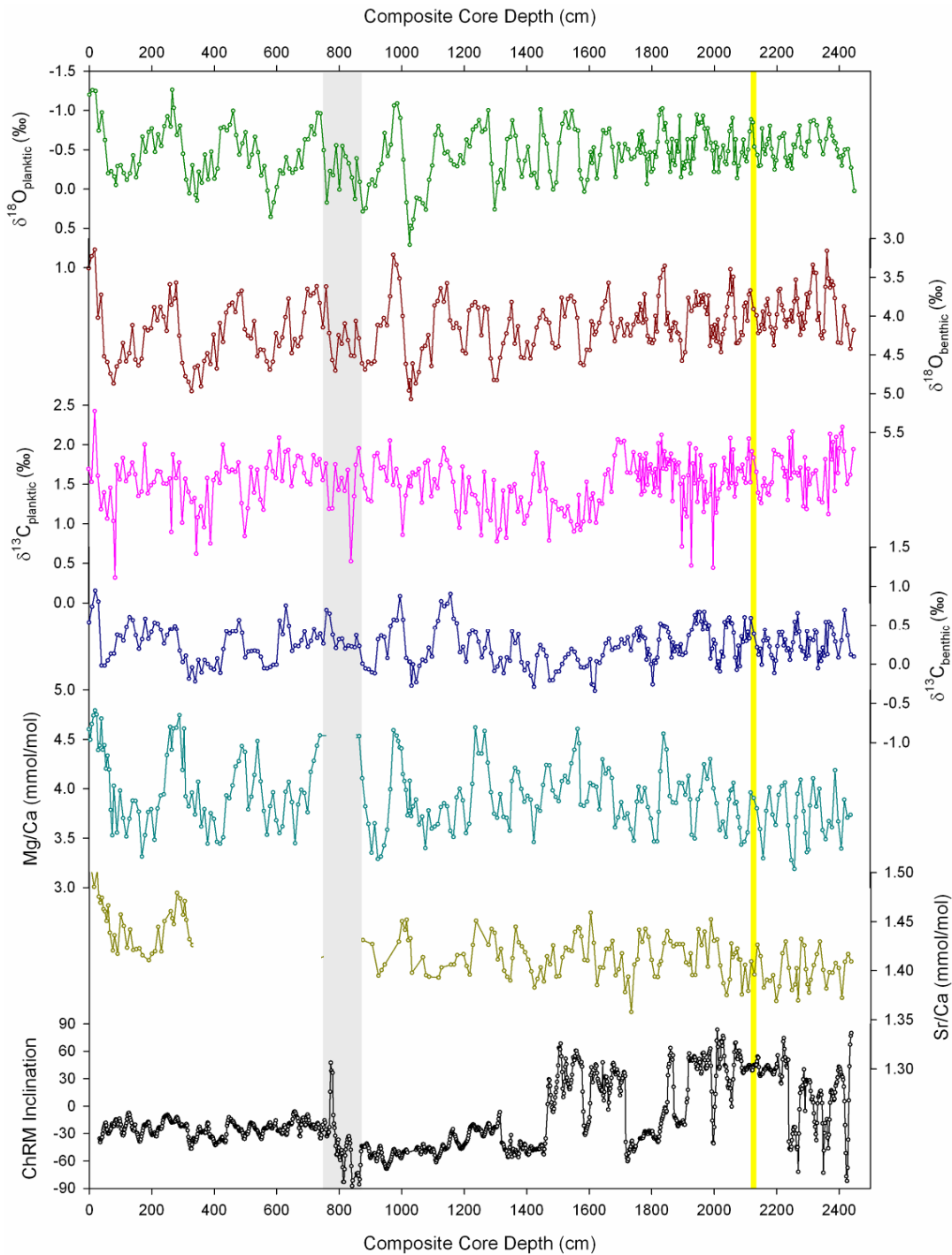
Depth in core (Raw)	Depth in core (CCD)	Age model	$\delta^{18}\text{O}_{\text{planktic}}$	$\delta^{13}\text{C}_{\text{planktic}}$ (corrected)	$\delta^{18}\text{O}_{\text{benthic}}$ (corrected)	$\delta^{13}\text{C}_{\text{benthic}}$	Mg/Ca	Sr/Ca
cm	cm	ka	‰	‰	‰	‰	mmol/mol	mmol/mol
1815	1774	1020.9	-0.568	1.824	4.088	0.341	N/A	N/A
1820	1779	1023.7	-0.447	1.414	3.717	0.326	4.0064	1.4425
1825	1784	1026.2	-0.064	1.889	4.042	0.054	N/A	N/A
1830	1789	1028.7	-0.379	1.495	4.257	0.190	3.8130	1.4342
1835	1794	1031.1	-0.466	1.697	4.336	0.117	N/A	N/A
1840	1799	1033.6	-0.218	1.752	4.303	-0.002	3.6983	1.4109
1845	1804	1036.7	-0.254	1.646	4.351	-0.261	N/A	N/A
1850	1809	1039.7	-0.471	1.401	4.310	0.039	3.4654	1.3938
1855	1814	1044.5	-0.408	1.692	3.999	0.015	N/A	N/A
1860	1819	1049.4	-0.600	1.458	4.202	0.081	3.4664	1.3934
1865	1824	1054.2	-0.942	2.018	3.742	0.309	3.7657	1.4058
1870	1829	1059.0	-1.010	1.358	3.510	0.520	4.1760	1.4095
1875	1834	1063.9	-1.025	2.125	N/A	N/A	N/A	N/A
1880	1839	1068.7	-0.755	1.699	3.405	0.493	4.5565	1.4278
1885	1844	1074.0	-0.836	1.915	3.352	0.487	N/A	N/A
1890	1849	1079.2	-0.599	1.692	4.103	0.474	4.3971	1.4402
1895	1854	1084.5	-0.465	1.815	3.963	0.405	N/A	N/A
1900	1859	1089.8	-0.219	1.752	4.194	0.333	3.9247	1.4300
1905	1864	1095.1	-0.635	1.885	4.311	0.081	N/A	N/A
1910	1869	1100.4	-0.362	1.286	4.156	0.274	3.8605	1.4247
1915	1874	1104.9	-0.303	1.801	4.084	0.159	N/A	N/A
1920	1879	1109.4	-0.610	1.649	4.093	0.224	3.8558	1.4268
1925	1884	1113.0	-0.474	1.751	4.214	0.219	N/A	N/A
1930	1889	1116.6	-0.930	1.773	4.228	0.125	4.0595	1.4269
1935	1894	1120.2	-0.150	1.504	4.314	0.249	N/A	N/A
1940	1899	1123.8	-0.332	0.712	4.578	0.114	4.0539	1.4269
1945	1904	1127.9	-0.262	1.587	N/A	N/A	N/A	N/A
1950	1909	1131.9	-0.349	1.182	4.467	0.142	3.9381	1.4083
1955	1914	1136.2	-0.632	1.091	N/A	N/A	N/A	N/A
1960	1919	1140.4	-0.355	1.612	3.766	0.367	4.1293	1.4060
1965	1924	1144.6	-0.198	2.013	N/A	N/A	3.8906	1.4175
1970	1929	1148.8	-0.633	0.471	3.935	0.439	3.5328	1.3954
1975	1934	1153.1	-0.387	1.762	N/A	N/A	N/A	N/A
1980	1939	1157.3	-0.665	1.513	3.867	0.629	3.4949	1.3955
1985	1944	1161.5	-0.946	1.952	3.686	0.524	N/A	N/A
1990	1949	1165.7	-0.826	1.277	3.855	0.670	3.8915	1.4423
1995	1954	1169.9	-0.844	1.557	3.857	0.671	N/A	N/A
2000	1959	1174.2	-0.845	1.868	3.741	0.551	3.9795	1.4259
2005	1964	1178.4	-0.930	1.602	3.820	0.441	N/A	N/A
2010	1969	1182.6	-0.766	1.149	3.726	0.672	4.2459	1.4397
2015	1974	1186.5	-0.512	1.531	3.888	0.530	N/A	N/A
2020	1979	1190.3	-0.772	1.276	3.975	0.445	4.0998	1.4039

Depth in core (Raw)	Depth in core (CCD)	Age model	$\delta^{18}\text{O}_{\text{planktic}}$	$\delta^{13}\text{C}_{\text{planktic}}$ (corrected)	$\delta^{18}\text{O}_{\text{benthic}}$ (corrected)	$\delta^{13}\text{C}_{\text{benthic}}$	Mg/Ca	Sr/Ca
cm	cm	ka	‰	‰	‰	‰	mmol/mol	mmol/mol
2025	1984	1194.1	N/A	N/A	3.738	0.500	N/A	N/A
2030	1989	1197.9	-0.586	1.372	4.385	0.067	4.2993	1.4522
2035	1994	1200.8	-0.488	1.735	4.138	0.195	N/A	N/A
2040	1999	1203.8	-0.218	0.443	4.274	0.306	4.0029	1.4304
2045	2004	1206.8	-0.590	1.742	4.113	0.256	N/A	N/A
2050	2009	1209.7	-0.530	1.141	4.325	-0.052	3.8516	1.4318
2055	2014	1212.7	-0.216	1.319	4.046	0.031	N/A	N/A
2060	2019	1215.7	-0.404	1.429	4.341	-0.096	3.5794	1.4052
2065	2024	1218.6	N/A	N/A	4.465	0.155	N/A	N/A
2070	2029	1221.6	-0.551	1.515	4.234	0.092	3.6656	1.3870
2075	2034	1224.6	-0.344	1.833	4.166	0.541	N/A	N/A
2080	2039	1227.5	-0.315	1.685	3.993	0.472	3.5099	1.3750
2085	2044	1230.5	-0.481	1.666	3.885	0.568	N/A	N/A
2090	2049	1233.4	-0.736	1.452	3.713	0.600	3.8936	1.3909
2095	2054	1236.0	-0.805	2.085	3.397	0.535	3.9801	1.4277
2100	2058	1238.1	-0.905	1.515	3.722	0.523	3.9910	1.4135
2105	2063	1240.7	-0.327	1.940	3.496	0.399	4.0578	1.4167
2110	2068	1243.2	-0.632	1.343	4.024	0.081	3.8507	1.4182
2115	2073	1245.8	-0.138	1.502	4.351	-0.076	3.8635	1.4224
2120	2078	1248.4	-0.293	1.697	4.350	0.233	3.7138	1.4116
2125	2083	1252.1	N/A	N/A	4.316	-0.029	3.6054	1.4110
2130	2088	1255.8	-0.465	1.665	4.212	0.351	3.4332	1.3758
2135	2093	1259.5	-0.627	1.747	4.247	0.282	N/A	N/A
2140	2098	1263.2	-0.414	1.576	3.875	0.603	3.4629	1.4058
2145	2103	1266.8	-0.351	1.518	3.829	0.294	N/A	N/A
2150	2108	1270.5	-0.502	1.823	4.062	0.409	3.5562	1.3793
2155	2113	1274.2	-0.733	2.076	3.721	0.325	N/A	N/A
2160	2118	1277.9	-0.886	1.525	3.671	0.593	3.9606	1.4093
2165	2123	1281.3	-0.848	1.916	N/A	N/A	N/A	N/A
2170	2128	1284.8	-0.538	1.836	3.911	0.383	3.9039	1.3960
2175	2133	1288.2	N/A	N/A	N/A	N/A	N/A	N/A
2180	2138	1291.7	-0.434	1.656	3.992	0.212	3.8007	1.4262
2185	2143	1295.2	-0.291	1.393	4.220	0.118	N/A	N/A
2190	2148	1298.8	-0.300	1.317	4.195	0.194	3.5915	1.4147
2195	2153	1302.9	-0.770	1.260	4.113	-0.011	N/A	N/A
2200	2158	1307.0	-0.506	1.477	3.942	0.297	3.2951	1.3827
2205	2163	1311.3	-0.443	1.572	4.170	0.439	N/A	N/A
2210	2168	1315.5	-0.567	1.481	3.865	0.302	3.7757	1.3905
2215	2173	1320.0	-0.635	1.382	3.781	0.324	N/A	N/A
2220	2178	1324.6	-0.804	1.365	3.977	0.223	4.0119	1.3894
2225	2183	1329.1	-0.511	1.501	4.143	0.113	N/A	N/A
2230	2188	1333.6	-0.412	1.525	4.224	0.072	3.7370	1.3954

Depth in core (Raw)	Depth in core (CCD)	Age model	$\delta^{18}\text{O}_{\text{planktic}}$	$\delta^{13}\text{C}_{\text{planktic}}$ (corrected)	$\delta^{18}\text{O}_{\text{benthic}}$ (corrected)	$\delta^{13}\text{C}_{\text{benthic}}$	Mg/Ca	Sr/Ca
cm	cm	ka	‰	‰	‰	‰	mmol/mol	mmol/mol
2235	2193	1337.8	-0.249	1.933	4.377	-0.117	N/A	N/A
2240	2198	1341.9	-0.363	1.882	4.160	0.040	3.6326	1.3690
2245	2203	1345.9	N/A	N/A	3.979	0.227	N/A	N/A
2250	2208	1349.8	-0.651	1.873	3.672	0.404	3.9372	1.3838
2255	2213	1353.8	N/A	N/A	3.651	0.373	N/A	N/A
2260	2218	1357.7	-0.676	1.845	3.858	0.407	4.0269	1.4175
2265	2223	1361.6	-0.708	1.703	3.928	0.235	N/A	N/A
2270	2228	1365.6	-0.401	1.596	4.050	0.310	4.0632	1.4296
2275	2233	1369.6	-0.292	1.665	4.139	0.173	N/A	N/A
2280	2238	1373.6	-0.354	1.300	4.051	0.197	3.6296	1.4027
2285	2243	1378.0	-0.424	2.086	4.043	0.050	N/A	N/A
2290	2248	1382.4	-0.260	1.574	3.931	0.174	3.2769	1.3800
2295	2253	1386.8	-0.563	2.167	4.072	0.274	N/A	N/A
2300	2258	1391.2	-0.533	1.647	3.812	0.544	3.1873	1.3857
2305	2263	1395.7	N/A	N/A	3.531	0.388	3.7110	1.4024
2310	2268	1400.1	-0.692	1.644	3.775	0.655	3.9473	1.3696
2315	2273	1404.6	-0.806	1.609	3.986	0.413	N/A	N/A
2320	2278	1409.2	-0.526	1.710	4.243	0.215	4.0898	1.4322
2325	2283	1412.9	N/A	N/A	3.966	0.164	N/A	N/A
2330	2288	1416.6	-0.441	1.220	4.167	0.157	3.7715	1.4256
2335	2293	1419.9	-0.418	1.841	4.082	0.064	3.5500	1.4014
2340	2298	1423.2	-0.598	1.186	3.718	0.418	3.3562	1.3862
2345	2303	1426.4	-0.607	1.694	3.887	0.106	3.3833	1.3776
2350	2308	1429.7	-0.858	1.501	3.698	0.324	3.8284	1.3906
2360	2318	1436.3	-0.873	1.632	3.339	0.302	4.1038	1.4056
2365	2323	1440.1	N/A	N/A	3.441	0.434	N/A	N/A
2370	2328	1443.9	-0.810	1.674	3.445	0.403	3.8186	1.4169
2375	2333	1447.7	N/A	N/A	4.052	-0.056	N/A	N/A
2380	2338	1451.4	-0.607	1.312	3.967	0.145	3.9984	1.4296
2385	2343	1455.3	N/A	N/A	4.246	0.036	N/A	N/A
2390	2348	1459.1	-0.443	1.271	4.288	0.205	3.5796	1.4006
2395	2353	1463.0	N/A	N/A	4.197	0.104	N/A	N/A
2400	2358	1466.9	-0.637	1.816	3.624	0.541	3.4877	1.3818
2405	2363	1470.8	N/A	N/A	3.159	0.124	N/A	N/A
2410	2368	1474.8	-0.892	1.122	3.515	0.544	3.6711	1.3983
2415	2373	1478.3	-0.794	2.136	3.635	0.518	N/A	N/A
2420	2378	1481.7	-0.677	1.812	3.552	0.466	3.6089	1.3979
2425	2383	1484.7	-0.606	2.035	3.602	0.377	N/A	N/A
2430	2388	1487.7	-0.583	1.415	3.771	0.285	4.1875	1.4077
2435	2393	1490.7	-0.502	2.098	N/A	N/A	N/A	N/A
2440	2398	1493.7	-0.405	1.641	4.342	0.082	3.6675	1.4026
2445	2403	1497.4	-0.415	1.954	N/A	N/A	N/A	N/A
2450	2408	1501.2	-0.297	2.139	4.348	0.300	3.3936	1.3722
2455	2413	1508.2	-0.433	2.225	N/A	N/A	N/A	N/A
2460	2418	1515.3	-0.501	1.916	3.877	0.696	3.8890	1.4090

Depth in core (Raw)	Depth in core (CCD)	Age model	$\delta^{18}\text{O}_{\text{planktic}}$	$\delta^{13}\text{C}_{\text{planktic}}$ (corrected)	$\delta^{18}\text{O}_{\text{benthic}}$ (corrected)	$\delta^{13}\text{C}_{\text{benthic}}$	Mg/Ca	Sr/Ca
cm	cm	ka	‰	‰	‰	‰	mmol/mol	mmol/mol
2470	2428	1529.4	-0.508	1.504	4.113	0.365	3.7061	1.4168
2480	2438	1543.5	-0.270	1.619	4.423	0.119	3.7350	1.4092
2490	2448	1557.6	0.026	1.944	4.183	0.094	N/A	N/A

Appendix 5: Plots of stable isotope, trace-metal and magnetic inclination data versus core depth



Grey bar indicates interval of disturbed sedimentation excluded from age-model development and yellow bar indicates interval of <60 weight% CaCO_3 and hence, potential carbonate dissolution, as discussed in chapter 2, §10.3.

Appendix 6: High resolution stable isotope and trace-metal data for selected glacial terminations

As for appendix 4, data includes correction to *G. ruber* $\delta^{13}\text{C}_{\text{planktic}}$ of +0.94‰ [Spero *et al.*, 2003] and to *C. wuellerstorfi* $\delta^{18}\text{O}_{\text{benthic}}$ of +0.64‰ [Shackleton and Opdyke, 1973]. ‘N/A’ indicates no measurement made/accepted.

A6.1 LGM/Hol

Depth in core (Raw)	Depth in core (CCD)	Age model	$\delta^{18}\text{O}_{\text{planktic}}$	$\delta^{13}\text{C}_{\text{planktic}}$ (corrected)	$\delta^{18}\text{O}_{\text{benthic}}$ (corrected)	$\delta^{13}\text{C}_{\text{benthic}}$	Mg/Ca	Sr/Ca
cm	cm	ka	‰	‰	‰	‰	mmol/mol	mmol/mol
0	0	0.0	-1.201	1.694	3.385	0.539	4.6003	N/A
1	1	0.3	-1.221	1.689	3.585	0.881	N/A	N/A
5	5	1.5	N/A	N/A	N/A	N/A	4.4960	1.5050
10	10	2.9	-1.257	1.530	3.228	0.739	4.6535	N/A
15	15	4.4	-1.358	1.427	3.296	0.778	4.7406	1.4852
17	17	4.9	-1.072	1.393	3.359	0.745	N/A	N/A
18	18	5.2	-1.282	1.206	3.499	0.681	N/A	N/A
20	20	5.8	-1.247	2.425	3.143	0.942	4.7910	N/A
21	21	6.1	-1.142	1.365	3.672	0.721	N/A	N/A
23	23	6.7	-1.299	1.410	N/A	N/A	N/A	N/A
25	25	7.2	-1.080	1.751	N/A	N/A	4.7495	1.5021
27	27	7.8	-1.245	1.488	3.806	0.482	N/A	N/A
29	29	8.4	-1.013	1.367	4.355	0.571	N/A	N/A
30	30	8.7	-0.743	1.606	4.021	0.804	4.3911	1.4753
31	31	9.0	-0.955	1.361	N/A	N/A	N/A	N/A
33	33	9.6	-0.725	1.018	3.951	0.378	N/A	N/A
35	35	10.1	-0.914	1.118	4.098	0.604	4.4363	1.4691
37	37	10.7	-0.864	1.439	3.761	0.643	N/A	N/A
39	39	11.3	-0.722	1.381	N/A	N/A	N/A	N/A
40	40	11.6	-0.972	1.184	3.725	-0.021	4.7101	1.4741
41	41	11.9	-0.816	1.205	N/A	N/A	N/A	N/A
43	43	12.4	-0.528	0.884	3.855	0.861	N/A	N/A
45	45	13.0	-0.799	0.967	4.166	0.500	4.3926	1.4625
47	47	13.6	-0.508	1.146	4.472	0.323	N/A	N/A
49	49	14.2	-0.397	1.806	N/A	N/A	N/A	N/A
50	50	14.5	-0.623	1.395	4.520	-0.022	4.4396	1.4602
51	51	14.8	-0.395	1.546	4.197	0.537	N/A	N/A
53	53	15.3	-0.343	1.622	4.127	0.498	N/A	N/A
55	55	15.9	-0.189	1.494	4.560	0.393	4.2025	1.4506
57	57	16.5	-0.183	1.372	4.579	0.149	N/A	N/A
59	59	17.1	N/A	N/A	4.894	0.179	N/A	N/A

Depth in core (Raw)	Depth in core (CCD)	Age model	$\delta^{18}\text{O}_{\text{planktic}}$	$\delta^{13}\text{C}_{\text{planktic}}$ (corrected)	$\delta^{18}\text{O}_{\text{benthic}}$ (corrected)	$\delta^{13}\text{C}_{\text{benthic}}$	Mg/Ca	Sr/Ca
cm	cm	ka	‰	‰	‰	‰	mmol/mol	mmol/mol
60	60	17.4	-0.199	1.065	4.594	0.044	4.3339	1.4664
61	61	17.6	-0.056	1.420	N/A	N/A	4.2321	1.4658
63	63	18.2	N/A	N/A	4.828	0.247	4.0568	1.4209
65	65	18.8	-0.016	1.151	N/A	N/A	4.1934	1.4386
67	67	19.4	-0.142	1.133	4.749	0.095	N/A	N/A
69	69	20.0	-0.043	1.367	4.769	0.197	3.8547	1.4169
70	70	20.2	-0.226	1.456	4.746	0.129	3.7855	N/A
71	71	20.7	-0.043	1.648	N/A	N/A	N/A	N/A
73	73	21.7	-0.090	1.707	4.757	0.290	3.7215	1.4298
75	75	22.7	-0.017	1.441	4.718	0.234	3.5279	1.4205
77	77	23.7	-0.048	1.258	4.526	0.319	4.0122	1.4220
79	79	24.7	-0.065	1.346	4.619	0.247	N/A	N/A
80	80	25.2	-0.156	1.034	4.871	0.132	4.0286	1.4360
81	81	25.7	-0.374	1.276	4.613	0.144	N/A	N/A
83	83	26.7	-0.345	1.698	4.618	0.483	3.7899	1.4088
85	85	27.7	-0.051	0.318	N/A	N/A	N/A	N/A
90	90	30.3	-0.290	1.743	4.652	0.373	3.5552	1.4171
100	100	35.5	-0.303	1.561	4.587	0.361	3.9804	1.4571
110	110	40.6	-0.203	1.832	4.349	0.298	3.7014	1.4454
120	120	45.8	-0.116	1.538	4.586	0.479	3.5150	1.4234
130	130	50.9	-0.199	1.630	4.480	0.604	3.6947	1.4418
140	140	56.1	-0.428	1.772	4.117	0.566	3.8787	1.4209
150	150	61.2	-0.149	1.625	4.564	0.366	3.8757	1.4218

A6.2 MIS 12/11

Depth in core (Raw)	Depth in core (CCD)	Age model	$\delta^{18}\text{O}_{\text{planktic}}$	$\delta^{13}\text{C}_{\text{planktic}}$ (corrected)	$\delta^{18}\text{O}_{\text{benthic}}$ (corrected)	$\delta^{13}\text{C}_{\text{benthic}}$	Mg/Ca	Sr/Ca
cm	cm	ka	‰	‰	‰	‰	mmol/mol	mmol/mol
950	935	381.3	-0.319	1.701	4.123	0.362	3.3122	1.4005
960	945	387.4	-0.713	1.717	4.026	0.343	3.4231	1.4061
970	955	393.6	-0.419	1.545	4.121	0.075	3.5839	N/A
980	965	399.7	-0.563	2.053	3.746	0.490	3.9931	N/A
981	966	400.3	-1.045	1.390	3.863	0.698	N/A	N/A
983	968	401.5	-0.785	1.632	3.761	0.572	N/A	N/A
985	970	402.7	-1.099	1.931	3.592	0.752	N/A	N/A
987	972	403.9	-0.847	1.486	3.451	0.751	N/A	N/A
989	974	405.1	-0.838	2.040	3.482	0.663	N/A	N/A
990	975	405.7	-1.061	1.491	3.337	0.597	4.5912	N/A
991	976	406.3	-1.244	1.646	3.690	0.548	N/A	N/A
993	978	407.4	-0.889	1.813	3.547	0.686	N/A	N/A
995	980	408.5	-0.911	1.611	3.329	0.671	N/A	N/A
997	982	409.6	-1.175	1.535	3.839	0.417	N/A	N/A
999	984	410.7	-0.691	1.779	3.564	0.550	N/A	N/A
1000	985	411.3	-1.090	1.693	3.339	0.565	4.5355	N/A
1001	986	411.8	-0.979	1.365	3.513	0.534	N/A	N/A
1003	988	412.9	-0.764	1.871	3.269	0.638	N/A	N/A
1005	990	414.0	-0.981	1.601	3.403	0.753	4.4829	1.4295
1006	991	414.6	-0.934	1.502	N/A	N/A	N/A	N/A
1007	992	415.1	-1.172	1.691	3.676	0.603	N/A	N/A
1008	993	415.7	-1.025	1.934	N/A	N/A	N/A	N/A
1009	994	416.3	-0.833	1.555	3.534	0.494	N/A	N/A
1010	995	416.8	-0.905	1.476	3.515	0.873	4.4161	N/A
1011	996	417.4	-0.657	1.448	3.421	0.671	N/A	N/A
1012	997	417.9	-1.086	1.555	N/A	N/A	N/A	N/A
1013	998	418.5	-1.027	1.350	3.734	0.685	N/A	N/A
1014	999	419.0	-0.788	1.788	N/A	N/A	N/A	N/A
1015	1000	419.6	-0.823	1.174	3.647	0.746	4.4072	1.4503
1016	1001	420.1	-0.706	1.389	N/A	N/A	N/A	N/A
1017	1002	420.7	-0.552	1.375	4.294	0.509	N/A	N/A
1018	1003	421.2	-0.931	1.434	N/A	N/A	N/A	N/A
1019	1004	421.8	-0.115	1.561	4.144	0.488	N/A	N/A
1020	1005	422.3	-0.372	0.858	4.001	0.571	4.1464	N/A
1021	1006	422.9	-0.334	1.559	4.093	0.450	N/A	N/A
1022	1007	423.4	-0.171	1.509	N/A	N/A	N/A	N/A
1023	1008	424.0	-0.197	1.237	4.022	0.321	N/A	N/A
1024	1009	424.6	-0.183	1.377	N/A	N/A	N/A	N/A
1025	1010	425.1	-0.302	1.187	3.949	0.377	4.0766	1.4414
1026	1011	425.7	-0.137	0.931	N/A	N/A	N/A	N/A
1027	1012	426.2	-0.056	1.292	4.262	0.181	4.2460	1.4566
1028	1013	426.8	-0.192	1.300	N/A	N/A	N/A	N/A

Depth in core (Raw)	Depth in core (CCD)	Age model	$\delta^{18}\text{O}_{\text{planktic}}$	$\delta^{13}\text{C}_{\text{planktic}}$ (corrected)	$\delta^{18}\text{O}_{\text{benthic}}$ (corrected)	$\delta^{13}\text{C}_{\text{benthic}}$	Mg/Ca	Sr/Ca
cm	cm	ka	‰	‰	‰	‰	mmol/mol	mmol/mol
1029	1014	427.3	-0.033	1.106	3.911	0.023	N/A	N/A
1030	1015	427.9	0.007	0.446	4.618	0.075	3.9854	1.4518
1031	1016	428.4	-0.167	1.493	4.380	0.230	N/A	N/A
1032	1017	429.0	0.155	1.470	N/A	N/A	N/A	N/A
1033	1018	429.5	0.183	1.268	4.681	0.017	4.1191	1.4383
1034	1019	430.1	0.206	1.831	N/A	N/A	N/A	N/A
1035	1020	430.6	0.210	1.634	5.115	0.009	3.7307	1.4309
1037	1022	431.8	0.397	1.459	4.792	0.032	3.9488	1.4351
1039	1024	432.9	0.953	1.536	5.189	-0.174	N/A	N/A
1040	1025	433.4	0.711	1.593	4.961	0.027	3.7770	N/A
1041	1026	434.0	0.674	1.542	5.070	0.030	3.6555	1.4234
1050	1027	434.5	0.470	1.482	4.827	0.029	4.0800	1.4328
1051	1028	435.1	0.265	1.204	5.260	-0.049	3.9960	1.4335
1053	1030	436.2	0.838	1.649	5.051	-0.158	3.5156	1.3864
1055	1032	437.3	0.502	1.472	5.073	-0.277	3.7224	1.3978
1057	1034	438.4	0.670	1.646	4.718	-0.109	3.6159	1.4084
1070	1037	440.0	0.389	1.649	4.613	-0.006	3.8182	N/A
1080	1047	445.5	0.112	1.619	4.869	-0.234	3.8886	N/A
1090	1057	451.0	0.127	1.693	4.724	-0.027	3.6350	N/A
1100	1067	456.5	0.183	1.268	4.421	0.053	3.7163	1.4137
1110	1077	462.0	0.263	1.770	4.385	0.035	3.3989	1.3953

A6.3 MIS 38/37

Depth in core (Raw)	Depth in core (CCD)	Age model	$\delta^{18}\text{O}_{\text{planktic}}$	$\delta^{13}\text{C}_{\text{planktic}}$ (corrected)	$\delta^{18}\text{O}_{\text{benthic}}$ (corrected)	$\delta^{13}\text{C}_{\text{benthic}}$	Mg/Ca	Sr/Ca
cm	cm	ka	‰	‰	‰	‰	mmol/ mol	mmol/ mol
2070	2029	1221.6	-0.551	1.515	4.234	0.092	3.6656	1.3870
2075	2034	1224.6	-0.344	1.833	4.166	0.541	N/A	N/A
2080	2039	1227.5	-0.315	1.685	3.993	0.472	3.5099	1.3750
2085	2044	1230.5	-0.481	1.666	3.885	0.568	N/A	N/A
2090	2049	1233.4	-0.736	1.452	3.713	0.600	3.8936	1.3909
2095	2054	1236.0	-0.805	2.085	3.397	0.535	3.9801	1.4277
2097	2056	1237.1	-0.858	2.040	N/A	N/A	N/A	N/A
2100	2058	1238.1	-0.905	1.515	3.722	0.523	3.9910	1.4135
2102	2060	1239.1	-0.399	1.954	3.445	0.469	N/A	N/A
2105	2063	1240.7	-0.327	1.940	3.496	0.399	4.0578	1.4167
2107	2065	1241.7	-0.448	1.637	3.793	0.182	3.9898	1.4230
2110	2068	1243.2	-0.632	1.343	3.992	0.161	3.8507	1.4182
2112	2070	1244.2	-0.105	1.469	3.943	0.165	4.0681	1.4287
2115	2073	1245.8	-0.138	1.502	4.351	-0.076	3.8635	1.4224
2117	2075	1246.9	0.029	1.726	4.254	0.121	3.6046	1.4081
2120	2078	1248.5	-0.293	1.697	4.350	0.233	3.7138	1.4116
2122	2080	1249.9	N/A	N/A	4.250	0.116	3.4985	1.4044
2125	2083	1252.1	-0.584	1.456	4.250	-0.079	3.6054	1.4110
2127	2085	1253.6	-0.191	1.736	4.378	-0.035	3.2934	1.3792
2130	2088	1255.8	-0.465	1.665	4.212	0.351	3.4332	1.3758
2135	2093	1259.5	-0.627	1.747	4.247	0.282	N/A	N/A
2140	2098	1263.2	-0.414	1.576	3.875	0.603	3.4629	1.4058
2145	2103	1266.8	-0.351	1.518	3.829	0.294	N/A	N/A
2150	2108	1270.5	-0.502	1.823	4.062	0.409	3.5562	1.3793
2155	2113	1274.2	-0.733	2.076	3.721	0.325	N/A	N/A
2160	2118	1277.9	-0.886	1.525	3.671	0.593	3.9606	1.4093
2165	2123	1281.3	-0.848	1.916	N/A	N/A	N/A	N/A

Appendix 7: MD06-3018 planktic foraminiferal faunal counts

Species lists followed are from *Imbrie and Kipp* 1971 and taxonomy is based upon that of *Hemleben et al.* 1989.

Depth CCD (cm)	Age (ka)	G.falconensis	G.rubescens	T.humilis	T.quiqueloba	N.pachyderma (left)	N.pachyderma (right)
0	0	5	5	0	0	0	0
35	10.1	3	5	0	0	0	0
51	14.8	0	0	0	0	0	0
75	19.4	17	5	0	1	0	3
67	22.7	2	1	0	6	0	0
85	27.7	23	8	0	10	0	2
100	35.5	13	6	0	2	0	0
991	406.3	9	6	2	3	0	0
1035	430.6	20	3	1	4	0	8
1053	436.2	17	0	0	6	0	12
2100	1238.1	11	0	0	19	0	0
2120	1248.5	9	0	0	32	0	0
2127	1252.1	13	0	0	7	0	0

Depth CCD (cm)	Age (ka)	N.dutertrei	G.conglomerata	G.hexagonus	O.universa	G.conglobatus	G.ruber (pink)
0	0	7	0	17	3	4	0
35	10.1	6	4	3	4	2	0
51	14.8	21	0	4	6	8	0
75	19.4	13	0	1	6	6	0
67	22.7	11	1	11	6	2	0
85	27.7	4	0	6	8	0	0
100	35.5	17	0	5	7	1	0
991	406.3	3	1	8	9	5	3
1035	430.6	13	1	13	11	6	0
1053	436.2	1	0	8	12	5	0
2100	1238.1	4	0	18	9	1	0
2120	1248.5	13	1	6	9	0	0
2127	1252.1	19	0	6	5	2	1

Depth CCD (cm)	Age (ka)	G.ruber (white)	G.tenellus	G.sacculifer	G.sacculifer (with sac)	S.debiscens	G.aequilateris
0	0	95	1	36	7	1	12
35	10.1	110	1	38	1	0	11
51	14.8	103	0	46	10	3	9
75	19.4	98	0	70	3	2	6
67	22.7	77	3	38	4	4	16
85	27.7	100	2	51	1	4	5
100	35.5	108	1	57	3	3	9
991	406.3	167	1	88	3	2	13
1035	430.6	150	2	88	3	4	1
1053	436.2	114	4	76	5	0	1
2100	1238.1	94	0	69	6	2	10
2120	1248.5	110	0	93	1	0	2
2127	1252.1	72	0	53	2	2	3

Depth (cm)	Age (ka)	G.calida	G.bulloides	G.inflata	P.obliquic- olata	G.truncatul- inoides (left)	G.truncatul- inoides (right)
0	0	15	12	11	0	0	1
35	10.1	10	9	10	2	0	0
51	14.8	8	6	12	0	1	1
75	19.4	12	35	27	1	0	2
67	22.7	7	21	19	1	1	1
85	27.7	15	52	37	1	0	1
100	35.5	8	50	24	2	3	8
991	406.3	14	46	9	4	0	7
1035	430.6	9	67	34	3	1	4
1053	436.2	10	54	43	0	0	14
2100	1238.1	12	43	4	2	0	10
2120	1248.5	16	66	25	1	1	6
2127	1252.1	9	46	18	1	1	5

Depth CCD (cm)	Age (ka)	G.crassaformis	G.hirsuta	G.scitula	D.anfracta	G.menardii	G.tumida
0	0	4	2	0	0	0	2
35	10.1	4	1	1	1	0	0
51	14.8	8	4	1	1	4	0
75	19.4	7	8	4	0	2	2
67	22.7	7	3	1	0	2	1
85	27.7	10	4	0	0	3	5
100	35.5	8	3	2	0	7	4
991	406.3	3	1	0	0	0	2
1035	430.6	6	0	0	0	2	3
1053	436.2	2	1	0	0	2	16
2100	1238.1	1	0	0	0	2	3
2120	1248.5	9	4	2	0	1	3
2127	1252.1	6	3	2	0	4	1

Depth CCD (cm)	Age (ka)	G.glutinata	G.theyeri	Benthics	UID	TOTAL
0	0	31	1	0	3	272
35	10.1	16	0	0	1	242
51	14.8	17	4	4	0	277
75	19.4	44	4	1	1	381
67	22.7	16	3	1	1	267
85	27.7	38	0	1	0	391
100	35.5	48	5	2	3	409
991	406.3	43	0	1	0	453
1035	430.6	50	0	4	4	515
1053	436.2	34	4	6	4	451
2100	1238.1	45	2	2	4	373
2120	1248.5	39	0	1	4	454
2127	1252.1	18	1	2	1	303

Fin